

# **Detection and Monitoring of Arid Grazing Land Vegetation using ATSR-2 and Geometric Optical Modelling**

Thesis submitted for the degree of  
**Doctor of Philosophy**  
at the University of Leicester



**Marianne Clare Edwards**

Department of Geography

University of Leicester

February 1999



# **Detection and Monitoring of Arid Grazing Land Vegetation using ATSR-2 and Geometric Optical Modelling**

**Marianne Clare Edwards**

## **ABSTRACT**

This study focused on the Badia region of Jordan and examined how low spatial resolution Along Track Scanning Radiometer (ATSR-2) and Advanced Very High Resolution Radiometer (AVHRR) data can be used to detect and monitor changes in grazing land vegetation in semi-arid environments. Comparisons were made between a wide range of different vegetation indices calculated using the red and near-infrared wavebands of both ATSR-2 and AVHRR imagery and field data collected at a series of sampling sites exhibiting a wide range of percentage vegetation covers. For the ATSR-2 data both the nadir and forward sensor view angles were considered. Poor correlations were found between the vegetation indices and field-measured vegetation cover for the Badia region. It was found that highly reflective soils, very sparse vegetation, and the xerophytic nature of vegetation in arid regions limited the use of such indices. Furthermore, due to factors such as angle of view, spatial resolution and problems in geo-location, the forward view of ATSR-2 was not found to add any advantages in terms of the ability to detect and monitor the sparsely vegetated surfaces. As an alternative to vegetation indices, a hybrid geometric optical/empirically based model was developed for the area. Using the information given in the red/near-infrared scattergram of a satellite image, the model allowed percentage vegetation cover to be predicted from the remotely sensed data. Strong correlations ( $r^2 = 0.91$ ) were found between the model-predicted percentage vegetation cover and that measured at the field sites. The estimates of percentage vegetation cover derived using the model were similar for both the ATSR-2 and the AVHRR imagery, suggesting that the model results are independent of sensor type. These results suggest that the geometric optical/ empirical model can improve the ability to map vegetation resources in arid environments, and that the consistency of the results from the two different sensors should enable long term monitoring of the region.



# CONTENTS

<b>Abstract</b>	<b>i</b>
<b>Contents</b>	<b>ii</b>
<b>List of Figures</b>	<b>vii</b>
<b>List of Tables</b>	<b>x</b>
<b>List of Plates</b>	<b>xii</b>
<b>Acronyms</b>	<b>xiii</b>
<b>Acknowledgements</b>	<b>xvi</b>
<b>Chapter 1: Introduction</b>	<b>1</b>
1.1 Rangeland Degradation in Jordan	2
1.2 The Jordan Badia Research and Development Programme	3
1.2.1 Geology and Topography	5
1.2.2 Geomorphology	7
1.2.3 Climate, hydrology and water resources	10
1.2.4 Biogeography	12
1.3 Remote sensing of arid land vegetation	15
1.3.1 Vegetation Indices	18
1.3.2 A modelling approach	19
1.4 Sensors	20
1.5 Research aims and objectives	24
1.6 Thesis structure	25
<b>Chapter 2: Field data collection and analysis</b>	<b>26</b>
2.1 Introduction	27
2.2 Fieldwork aims and objectives	27
2.3 Field site selection and location	27
2.4 Vegetation survey	32
2.4.1 Sampling strategy	33
2.4.2 Species	34
2.4.3 Plant dimensions and shape	36



2.4.4	Biomass	37
2.4.5	Percentage vegetation cover	40
2.5	Ground radiometric measurements	43
2.5.1	Instrumentation	43
2.5.2	Measurements taken	46
2.6	Soil	47
2.7	Meteorological data	51
2.7.1	Precipitation	51
2.7.2	Wind speed and direction	54
2.7.3	Soil and air temperature	55
2.8	The relationship between vegetation, soil moisture and precipitation	56
2.9	The relationship between ground radiometry, vegetation and soil	58
2.10	Limitations of field work	64
2.11	Summary and conclusions	64
<b>Chapter 3: Satellite image acquisition and processing</b>		<b>67</b>
3.1	Introduction	68
3.2	ATSR-2 history and specifications	68
3.2.1	ERS launch and payload	68
3.2.2	Instrument specifications	70
3.2.3	The dual look	72
3.3	Image acquisition	74
3.3.1	Image retrieval	77
3.3.2	The image header	77
3.3.3	Calibration and error codes	77
3.4	Image processing	79
3.4.1	Atmospheric correction	79
3.4.1.1	Limitations of the atmospheric correction procedure	84
3.4.2	Geometric correction	86
3.5	NOAA AVHRR	88
3.5.1	History and specifications	89
3.5.2	Image acquisition	91



3.5.3	Image retrieval and processing	92
3.5.3.1	Atmospheric correction	94
3.5.3.2	Geometric correction	95
3.6	Problems associated with the use of imagery	95
3.6.1	ATSR-2	95
3.6.2	NOAA AVHRR	96
3.7	Summary and conclusions	97
 <b>Chapter 4: Bi-directional effects and the dual view</b>		<b>98</b>
4.1	Introduction	99
4.2	Bi-directional Reflection Distribution Function (BRDF)	99
4.3	Geometric optical modelling	100
4.3.1	Model design	103
4.3.2	Model assumptions	105
4.3.3	Input parameters	106
4.4	Effect of changes in view angle	106
4.4.1	Change in view angle with relative azimuth	106
4.4.2	Change in view angle with solar zenith	117
4.5	Model limitations	119
4.6	Summary and conclusions	121
 <b>Chapter 5: Arid land vegetation analysis: comparing ground and satellite measurements using vegetation indices</b>		<b>124</b>
5.1	Introduction	125
5.2	Vegetation Indices	125
5.3	Comparing vegetation characteristics and satellite imagery	132
5.3.1	The relationship between individual wavebands and percentage vegetation cover	134
5.3.1.1	The relationship between reflected middle infrared and percentage vegetation cover	138
5.3.2	Frequently used vegetation indices	141
5.3.3	The use of 'new' vegetation indices	144



5.4	Seasonal variations detected using vegetation indices	146
5.5	Problems associated with the use of vegetation indices	149
5.6	Summary and conclusions	156
<b>Chapter 6: Arid land vegetation analysis: a modelling approach</b>		<b>158</b>
6.1	Introduction	159
6.2	Modelling	159
6.3	Understanding surface-energy interactions using the red/near-infrared scattergram	162
6.3.1	Model design	162
6.3.2	Parameter estimation	165
6.3.2.1	Estimation of the sub-pixel fractional shadow cover	165
6.3.2.2	Estimation of the reflectance terms	167
6.3.3	Estimation of sub-pixel fractional canopy cover and inversion	175
6.4	Model validation	179
6.5	Seasonal variations detected using the model	184
6.6	Model assumptions and limitations	190
6.7	Summary and conclusions	193
<b>Chapter 7: Arid land vegetation detection in Jordan using ATSR-2</b>		<b>195</b>
7.1	Introduction	196
7.2	Information held in the forward bands of ATSR-2	196
7.2.1	ATSR-2 as applied to the geometric model	196
7.2.1.1	Regridding and Resampling	196
7.2.1.2	Geolocation	198
7.2.2	Principal components analysis	201
7.2.2.1	Methodology	202
7.2.2.2	Visible channels	203
7.2.2.3	Visible plus thermal band	207
7.2.2.4	Forward and nadir bands combined	210
7.2.2.5	Summary and conclusions	213
7.3	A comparison of ATSR-2 with other sensors	214
7.3.1	The importance of spectral resolution	214



7.3.1.1	The spectral wavebands of ATSR-2 compared to TM and AVHRR	215
7.3.1.2	Methodology to compare sensor waveband responses	217
7.3.1.3	Results and discussion	217
7.3.2	The importance of spatial resolution	223
7.3.3	The importance of temporal resolution	225
7.3.4	Other advantages of ATSR-2	226
7.4	Summary and conclusions	227
<b>Chapter 8:</b>	<b>Conclusions</b>	<b>229</b>
8.1	Introduction	230
8.2	Summary	230
8.2.1	Arid land vegetation detection	230
8.2.2	ATSR-2 as a tool for arid land vegetation detection	232
8.3	Application to the Jordan Badia Research and Development Programme	233
8.3.1	Integration of data sources	233
8.3.2	Remote sensing in development	234
8.4	Problems associated with arid land vegetation detection and monitoring	236
8.5	Suggestions for further work	238
<b>Appendix 1:</b>	<b>Minimum transect lengths and species-area curves for two field sites, <i>Feidat ed Dihikiya</i> and <i>Buqayawiyya</i></b>	<b>241</b>
<b>Appendix 2:</b>	<b>IDL code used to read raw ATSR-2 files</b>	<b>243</b>
<b>Appendix 3:</b>	<b>Example of header data from an ATSR-2 image</b>	<b>268</b>
<b>Appendix 4:</b>	<b>ATSR-2 and AVHRR imagery obtained</b>	<b>270</b>
<b>Appendix 5:</b>	<b>C programme used to run the simple geometric optical model</b>	<b>271</b>
<b>Appendix 6:</b>	<b>Splitting the 3.7 <math>\mu\text{m}</math> band</b>	<b>279</b>
<b>Appendix 7:</b>	<b>Full list of vegetation indices correlated against percentage vegetation cover estimates</b>	<b>281</b>
<b>References</b>		<b>283</b>

## List of Figures

1.1	Location of the Jordan Badia Research and Development Programme	4
1.2	Major geological divisions of the Badia (after Burdon 1959)	6
1.3	Location of the main qa'as and fans within the JBRDP area (Source: Allison <i>et al.</i> 1998)	9
1.4	The Biogeographic zones of Zohary (source: Al-Eisawi 1985)	13
2.1	Location of field sites within Jordan	30
2.2	Shapes of plants measured along line transects in the 1996 and 1997 field campaigns	37
2.3	Bi-directional measurements taken using field radiometers	47
2.4	Mean volumetric soil moisture content at different field sites across Jordan	50
2.5	Precipitation distribution in Jordan (source: Al-Fataftah 1991)	52
2.6	Mean monthly rainfall (mm) recorded by automatic weather stations at two sites in the Badia Research and Development Programme area	53
2.7	Wind direction as recorded by the automatic weather station at <i>Salma</i>	55
2.8	Monthly variations in maximum soil and air temperature as recorded by the automatic weather station at <i>Salma</i>	56
2.9	Relationship between soil moisture and percentage vegetation cover at fields sites in the Badia and the Jordan Valley	58
2.10	Spectral signature of soils in the Badia, measured using the ASD in the spring 1996 (nadir viewing)	59
2.11	Soil reflectance in the Badia and Jordan Valley, measured using the Milton Multiband Radiometer in the autumn 1997	60
2.12	Spectral signatures of vegetation in the Badia (nadir viewing) compared to green grass from a temperate region	61
2.13	Spectral response curves for soil and vegetation for sites in the Badia	63
3.1	Scan geometry for the ATSR-2 instrument	72
3.2	Quality of ATSR-2 images acquired in terms of data rate and the presence/absence of cloud	75
4.1	Canopy model structure (source: Jupp <i>et al.</i> , 1986)	103



4.2	Forward and backward scatter	107
4.3	Changes in pixel reflectance with changes in relative azimuth for different view angles, and a solar zenith angle of 30°	108
4.4	Directional reflectance at non-vegetated sites in the Badia as measured by the ASD	110
4.5	The proportions of illuminated and shaded soil and vegetation seen as the sensor looks at different view angles, at a relative azimuth of 0° and a solar zenith angle of 30°	113
4.6	Directional reflectance measurements for the background soil at <i>Feidat ed Dihikiya</i> , taken with the ASD	115
4.7	Vegetation reflectance at <i>Wassad</i> at two view angles taken with the ASD	115
4.8	Changes in NDVI with changing relative azimuth and view angle, and a solar zenith angle of 30°	116
4.9	Changes in pixel reflectance with changes in relative azimuth for different view angles and a solar zenith of 50°	118
5.1	The relation of the PVI to the soil line	128
5.2	NDVI variation over time as recorded by ATSR-2 data at different field sites	147
5.3	NDVI variation over time as recorded by AVHRR data at different field sites	147
6.1	Schematic diagram showing canopy and soil reflectance model (source: Jasinski, 1996)	164
6.2	Position of the soil line and 100 % cover line within the red/near-infrared scattergram	169
6.3	Red/near-infrared scattergram for the 06/09/95 ATSR-2 image, overlain with lines of constant percentage vegetation cover	177
6.4	Percentage vegetation cover map derived from 06/09/95 ATSR-2 image using model inversion	178
6.5	Predicted percentage vegetation cover derived from the model for the 10/09/97 ATSR-2 image, plotted against actual percentage vegetation cover values taken in the field	182
6.6	Percentage vegetation change over time as predicted by the model using	184

	ATSR-2 imagery	
6.7	Percentage vegetation change over time as predicted by the model using AVHRR imagery	185
6.8	Percentage vegetation cover change over time, as predicted by the model for ATSR-2 and AVHRR imagery, for selected field sites in the Jordan Valley	186
6.9	Difference in percentage vegetation cover as predicted by the model for ATSR-2 and AVHRR imagery, for months in which both imagery was collected	187
6.10	Difference in NDVI as predicted by ATSR-2 and AVHRR imagery, for months in which both image types were acquired	188
6.11	Difference in percentage vegetation cover as predicted by ATSR-2 and AVHRR from NDVI values	189
7.1	Subset of the 05/09/97 ATSR-2 image with <i>qa</i> 's highlighted in white (bands 2,3 and 4)	199
7.2	Red and near-infrared bandwidth responses of the ATSR-2, AVHRR and Landsat TM sensors	215
7.3	Red and near infrared reflectances for soil and vegetation at 6 different field sites, as measured by the ATSR-2, AVHRR and Landsat TM wavebands	218
7.4	Simulated NDVI of soil (s) and vegetation (v) at 6 field sites, calculated for the ATSR-2, AVHRR and Landsat TM wavebands using ASD field radiometry data	219
7.5	NDVI simulated for the ATSR-2, AVHRR and Landsat TM sensors, for different fractional covers, using the simple geometric optical model (Chapter 4) and field data from <i>Qattafi</i>	220
7.6	The spectral response of <i>Salsola vermiculata</i> and the background soil at Qattafi superimposed on the waveband responses of the ATSR-2, AVHRR and Landsat TM sensors.	221



## List of Tables

1.1	Specifications of the ATSR-2 and AVHRR sensors	21
2.1	Field site locations and descriptions	31
2.2	Dominant species found at field sites in the Badia, and details of their family, life-form and palatability	34
2.3	Correlation of biomass with plant volume for the main species encountered across the field sites	39
2.4	Percentage vegetation cover estimates measured in the field	42
2.5	Milton Multiband Radiometer 'K' values	46
2.6	Soil properties of soils at field sites across Jordan	49
3.1	Characteristics of the ATSR-2 sensor	70
3.2	Characteristics of the NOAA 14 AVHRR sensor	90
4.1	Parameters used as input to the simple geometric model	106
5.1	Images used to assess the relationship between percentage vegetation cover and vegetation indices	133
5.2	Pearson's product moment correlation coefficients calculated for reflectance in the bands of ATSR-2 correlated against percentage vegetation cover	135
5.3	Pearson's product moment correlation coefficients calculated for reflectance in the bands of the AVHRR correlated against percentage vegetation cover	136
5.4	Pearson's product moment correlation coefficients calculated for the correlation between percentage vegetation cover and the 1.6 $\mu$ m band, the full 3.7 $\mu$ m band and the reflected part of the 3.7 $\mu$ m band of ATSR-2	139
5.5	Soil line coefficients calculated from ATSR-2 and AVHRR images	142
5.6	Pearson's product moment correlation coefficients calculated for selected vegetation indices from ATSR-2 correlated against percentage vegetation cover	142
5.7	Pearson's product moment correlation coefficients calculated for selected vegetation indices from AVHRR correlated against percentage vegetation cover	143

5.8	Pearson's product moment correlation coefficients calculated for 'new' indices from ATSR-2 data correlated against percentage vegetation cover	145
6.1	Parameter estimation derived from the model for ATSR-2 images	174
6.2	Parameter estimation derived from the model for AVHRR images	175
6.3	Pearson's product moment correlation coefficient calculated for theoretical percentage vegetation cover as predicted by the model for ATSR-2 data correlated against percentage vegetation cover values taken in the field	179
6.4	Pearson's product moment correlation coefficient calculated for theoretical percentage vegetation cover as predicted by the model for AVHRR data correlated against percentage vegetation cover values taken in the field	180
6.5	Mean squared residuals and lines of best fit for predicted versus actual percentage vegetation cover, for imagery for which field validation was available	183
7.1	Geo-locational differences for selected sites between the geometric model of ATSR-2 and GPS measurements taken in the field	200
7.2	Results of the PCA carried out for two areas (Jordan Valley and Badia desert) within the 09/05/97 ATSR-2 image, using visible bands	204
7.3	Results of the PCA carried out for two areas (Jordan Valley and Badia desert) within the 06/09/95 ATSR-2 image, using visible bands	205
7.4	Results of the PCA carried out for two areas (Jordan Valley and Badia desert) within the 09/05/97 ATSR-2 image, using visible and thermal bands	208
7.5	Results of the PCA carried out for two areas (Jordan Valley and Badia desert) within the 06/09/95 ATSR-2 image, using visible and thermal bands	209
7.6	Results of the PCA carried out for two areas (Jordan Valley and Badia desert) within the 09/05/97 ATSR-2 image, using visible and thermal bands, forward and nadir bands together	210
7.7	Results of the PCA carried out for two areas (Jordan Valley and Badia	212



	desert) within the 06/09/95 ATSR-2 image, using visible and thermal bands, forward and nadir bands together	
7.8	A comparison of the red and near-infrared bandwidths of the ATSR-2, AVHRR and Landsat TM sensors	216

**List of Plates**

1.1	The qa’a at <i>Qa’a Salma</i>	8
1.2	<i>Marab al Buqayawiyya</i>	8
1.3	An irrigated banana plantation in the Jordan Valley	15
5.1	<i>Salsola vermiculata</i> , taken at <i>Qattafi</i> in the autumn of 1997	152
5.2	Grass at <i>Buqayawiyya</i> , in the spring 1996	153

## **List of Acronyms**

<b>5S</b>	<b>Simulation of the Satellite Signal in the Solar Spectrum</b>
<b>AATSR</b>	<b>Advanced Along Track Scanning Radiometer</b>
<b>AOD</b>	<b>Aerosol Optical Depth</b>
<b>ASAR</b>	<b>Advanced Synthetic Aperture Radar</b>
<b>ASD</b>	<b>Analytical Spectral Devices (spectroradiometer)</b>
<b>ATSR-2</b>	<b>Along Track Scanning Radiometer</b>
<b>AVHRR</b>	<b>Advanced Very High Resolution Radiometer</b>
<b>AWAS</b>	<b>Amman Water and Sewerage Authority</b>
<b>AWS</b>	<b>Automatic Weather Station</b>
<b>BRDF</b>	<b>Bi-directional Reflection Distribution Function</b>
<b>BRF</b>	<b>Bi-directional Reflectance Factor</b>
<b>CDA</b>	<b>Command and Data Acquisition</b>
<b>CEOS</b>	<b>Committee on Earth Observation Satellites</b>
<b>CORD</b>	<b>Centre for Overseas Research and Development</b>
<b>DERA</b>	<b>Defence Research Agency</b>
<b>EOS</b>	<b>Earth Observing System</b>
<b>ERS</b>	<b>European Remote Sensing Satellite</b>
<b>ESA</b>	<b>European Space Agency</b>
<b>ESOC</b>	<b>Earth Space Operations Centre</b>
<b>ESRIN</b>	<b>European Space Research Institute</b>
<b>FLIM</b>	<b>Forest Light Interaction Model</b>
<b>FTP</b>	<b>File Transfer Process</b>
<b>GAC</b>	<b>Global Area Coverage</b>
<b>GBROWSE</b>	<b>Gridded Browse</b>
<b>GBT</b>	<b>Gridded Brightness Temperature</b>
<b>GCP</b>	<b>Ground Control Point</b>
<b>GEMI</b>	<b>Global Environmental Monitoring Index</b>
<b>GIS</b>	<b>Geographical Information System</b>
<b>GOME</b>	<b>Global Environmental Monitoring Experiment</b>
<b>GPS</b>	<b>Global Positioning System</b>



GSST	Gridded Sea Surface Temperature
HRPT	High Resolution Picture Transfer
IDL	Iterative Data Language
JBRDP	Jordan Badia Research and Development Programme
LAC	Local Area Coverage
LAI	Leaf Area Index
MERIS	Medium Resolution Imaging Spectrometer
MIR	Middle Infrared
MISR	Multiangle Imaging SpectroRadiometer
MMR	Milton Multiband Radiometer
MODIS	MODerate resolution Imaging Spectroradiometer
MSS	Multispectral Scanner
NASA	National Aeronautics and Space Administration
NDVI	Normalised Difference Vegetation Index
NERC EPFS	Natural Environment Research Council Equipment Pool for Field Spectroscopy
NESDIS	National Environmental Satellite Data and Information Service
NIR	Near Infrared
NOAA	National Oceanic and Atmospheric Administration
PAF	Processing and Archiving Facility
PCA	Principal Components Analysis
PI	Principal Investigator
POD	Polar Orbiter Data
POLDER	POLarisation and Directionality of Earth Reflectance
PVI	Perpendicular Vegetation Index
RAL	Rutherford Appleton Laboratories
RVI	Ratio Vegetation Index
SAA	Satellite Active Archive
SAR	Synthetic Aperture Radar
SAVI	Soil Adjusted Vegetation Index
SAVI <sub>2</sub>	Soil Adjusted Ratio Index
SPOT XS	Le Systeme Pour l’Observation de la Terre (Multispectral)

SWIR	Short-Wave Infrared
TIROS	Television Infrared Observation Satellite
TM	Thematic Mapper
TSAVI	Transformed Soil Adjusted Vegetation Index
USGS	United States Geological Survey
UK	United Kingdom
WGS84	World Geodetic System 1984



## Acknowledgements

This thesis could not have been completed without the help and support of many people. I would particularly like to thank my supervisors, Dr Jane Wellens and Professor Andrew Millington of the University of Leicester, for their endless support and encouragement.

The work was funded through a Leicester University studentship, and satellite imagery was obtained through an ESA PI to Dr Kevin White and Professor Andrew Millington (UK.A02.125). I would like to acknowledge NERC EPFS for the use of their field radiometers and RAL for their help and advice about the use of ATSR-2 imagery.

Field work formed a significant component of the work and I would like to thank everyone who helped make the field campaigns so successful - Mohammed Shabbaz and the staff at the Higher Council for Science and Technology in Jordan, Professor Dawud Al-Eisawi at the University of Jordan, all at the Safawi Research Centre, the Royal Geographic Society, Roderic Dutton and everyone involved in running the project at CORD. My gratitude also extends to Dr Kevin White and Dr George Mackay for their help with field data collection, and to my colleague and friend, Kevin Tansey who shared many weeks spent in the desert and counted numerous plants with enthusiasm and goodwill.

Regarding programming and the use of models, I am indebted to Dr Michael Jasinski at the NASA Goddard Space Flight Centre for his assistance and patience in answering all my questions, and Dr George Mackay and Dr Fraser Gemmell for their help and advice. I would also like to acknowledge the support of all the staff at the Geography Department, particularly Bill Hickin and the technical staff, and Ruth Pollington who helped me with map production.

Finally thanks must go to my family and friends for listening to my stories of Bedouin in the desert and being there when it mattered most.

## **Dedication**

**'Now, to Him who sits on the throne and to the Lamb,  
be praise and honour and glory and power,  
for ever and ever. Amen'**

**Revelation 5: v.13.**



## **1.0 Introduction**

### **1.1 Rangeland Degradation in Jordan**

### **1.2 The Jordan Badia Research and Development Programme**

#### **1.2.1 Geology and Topography**

#### **1.2.2 Geomorphology**

#### **1.2.3 Climate, hydrology and water resources**

#### **1.2.4 Biogeography**

### **1.3 Remote sensing of arid land vegetation**

#### **1.3.1 Vegetation Indices**

#### **1.3.2 A modelling approach**

### **1.4 Sensors**

### **1.5 Research aims and objectives**

### **1.6 Thesis structure**

## 1.1 Rangeland Degradation in Jordan

Jordan has one of the highest rates of natural population increase in the world. In the mid 1990's, the population doubling rate was only 18 years (Maani *et al.*, 1998). A growing population puts pressure on resources particularly in terms of the availability and distribution of food and water. The need for land to remain productive becomes increasingly important.

90 % of the land area of Jordan can be described as rangeland - land which supports vegetation useful for the grazing of livestock (Abu-Irmaileh, 1994). In recent years these rangelands have been suffering from degradation as a result of desertification brought about by factors such as drought, wind erosion and overgrazing (Abu-Irmaileh, 1994). With a growing human population, there is a need to address this situation and safeguard the future of both the environment and the pastoral economy.

The Jordan Badia Research and Development Programme was set up in 1992 under the joint auspices of the Higher Council for Science and Technology in Jordan and the Royal Geographic Society in the UK, to address the problems of land degradation, desertification and overgrazing in the region of north-east Jordan known as the Badia. Due to run over several years, the project aimed to bring together researchers from different disciplines, formulating a body of information about the area, addressing some of the issues and in turn providing the means to make informed decisions about future management of the area.

An important requirement of the Badia Research Programme was to obtain information on the extent of natural resources in the Programme area and their spatial and temporal variations. As part of the Jordan Badia Research and Development Programme, the work outlined in this thesis aimed to meet this need with respect to the vegetation resources through the use of satellite imagery and ground data collection. Using the Badia as a study area, the work examines the way that vegetation in arid areas can be detected and monitored using remote sensing. It considers some of the ways in which arid land vegetation has been studied in the past and the problems



that have been encountered, and in an attempt to address some of these difficulties, evaluates the utility of data from a new sensor, the Along Track Scanning Radiometer (ATSR-2).

This introductory chapter details the Jordan Badia Research and Development Programme and provides information on the geography of the Badia Programme area. The problems and potential of remote sensing as a tool for the study of arid land vegetation are then discussed before the specifications of the Along Track Scanning Radiometer are introduced and outlined. Finally Sections 1.5 and 1.6 outline research aims and objectives and the thesis structure.

This thesis does not contain a traditional literature review in the form of large detailed review at the beginning of the study. Each individual chapter is considered as a unit and literature is reviewed throughout as concepts are introduced, explained and used. It was considered that the use of literature in this way was more appropriate and avoided extensive repetition.

## **1.2 The Jordan Badia Research and Development Programme**

Figure 1.1 indicates the location of the Jordan Badia Research and Development Programme area. Bordered by Syria, Saudi Arabia and Iraq, it lies in the north-eastern region of Jordan between 31° 30' and 32° 45' N and 36° 30' and 38° 10' E, and covers an area of 11,210 km<sup>2</sup>.

The Badia area was delimited in the 1920's as a result of the drawing of national boundaries after the First World War. The area was previously inhabited solely by Bedouin nomadic tribespeople but the region underwent significant development in the 1930's after the construction of a pipeline by the Iraq Petroleum Company (IPC). Settlements grew up round oil pumping stations and today although some Bedouin tribespeople do retain a traditional nomadic lifestyle of full mobility with their sheep, goats and camels, many have settled in hamlets and villages and adopted a fully or partially sedentary lifestyle (Dutton, 1998).



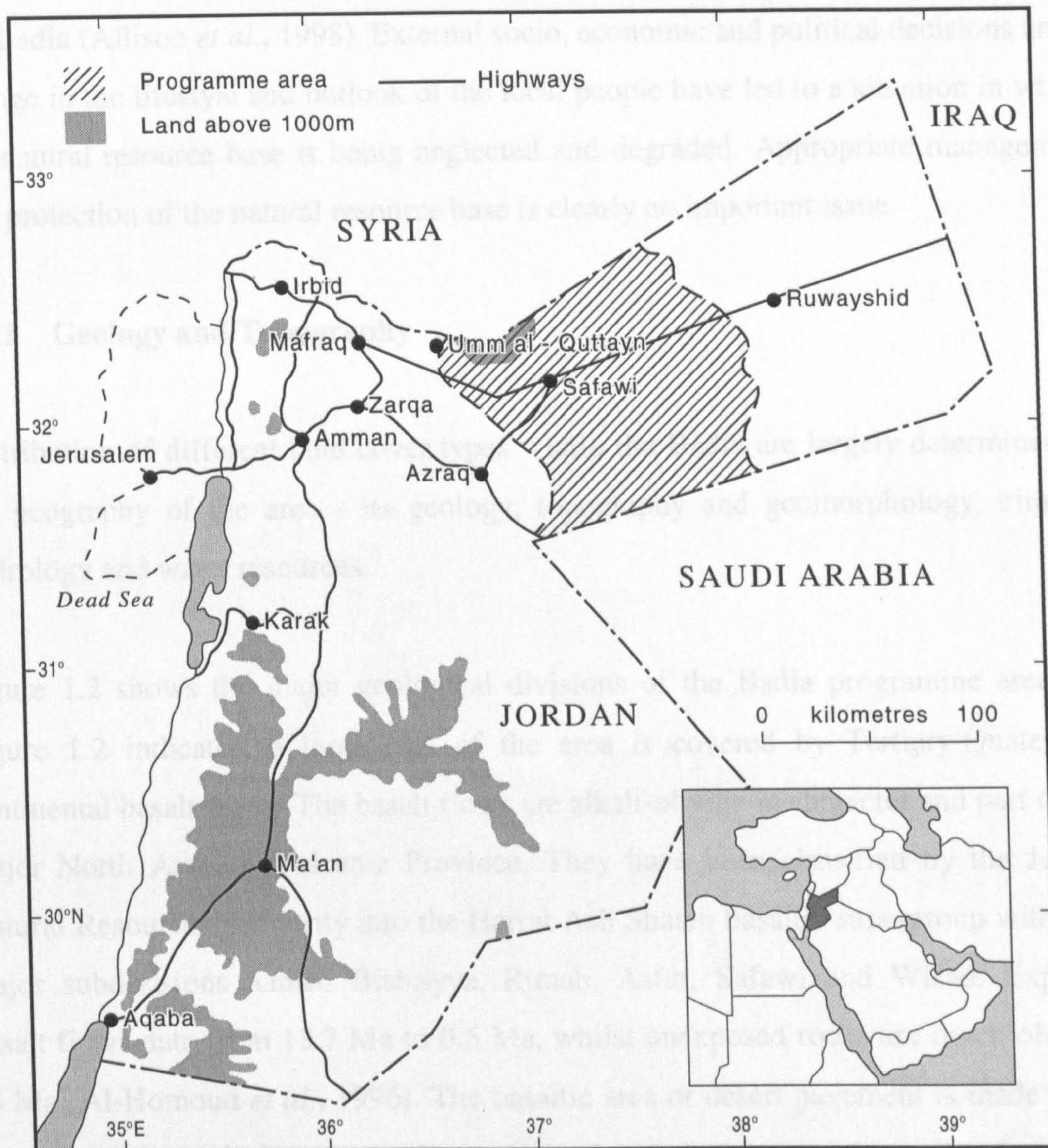


*Figure 1.1: Location of the Jordan Badia Research and Development Programme*  
*The Programme area covers 11,210 km<sup>2</sup> and is bounded by Syria to the north and Saudi Arabia to the south.*

With development and settlement, there has been a movement away from traditional nomadism and a rise in human population levels. In terms of natural resources, the Badia provides an extensive area of rangeland. It has some areas which have been cultivated and used for agriculture, and there is evidence in the region for mineral extraction. The Badia is home to less than 2.5 % of the total population of Jordan but its resources help support the population of Jordan as a whole. Water in the Badia is drained and pumped to the capital, Amman and livestock raised in the area are sold in



the larger towns and cities. Around 70 % of Jordan's animal products are produced in the Badia (Allison *et al.*, 1998). External socio, economic and political decisions and a change in the lifestyle and outlook of the local people have led to a situation in which the natural resource base is being neglected and degraded. Appropriate management and protection of the natural resource base is clearly an important issue.

### **1.2.1 Geology and Topography**

Distribution of different land cover types within the Badia are largely determined by the geography of the area - its geology, topography and geomorphology, climate, hydrology and water resources.

Figure 1.2 shows the major geological divisions of the Badia programme area. As Figure 1.2 indicates, a large part of the area is covered by Tertiary-Quaternary continental basalt flows. The basalt flows are alkali-olivine in character and part of the major North Arabian Volcanic Province. They have been classified by the Jordan Natural Resources Authority into the Harrat Ash Shaam basaltic supergroup with five major subdivisions named Bishriyya, Rimah, Asfar, Safawi and Wisad. Exposed basalt flows date from 13.7 Ma to 0.5 Ma, whilst unexposed rocks are much older at 23 Ma (Al-Homoud *et al.*, 1996). The basaltic area or desert pavement is made up of basalt boulders whose size is dictated by the underlying geology. Basalt in the northern part of the area tends to be increasingly covered with lichen indicating increased precipitation and higher water availability.



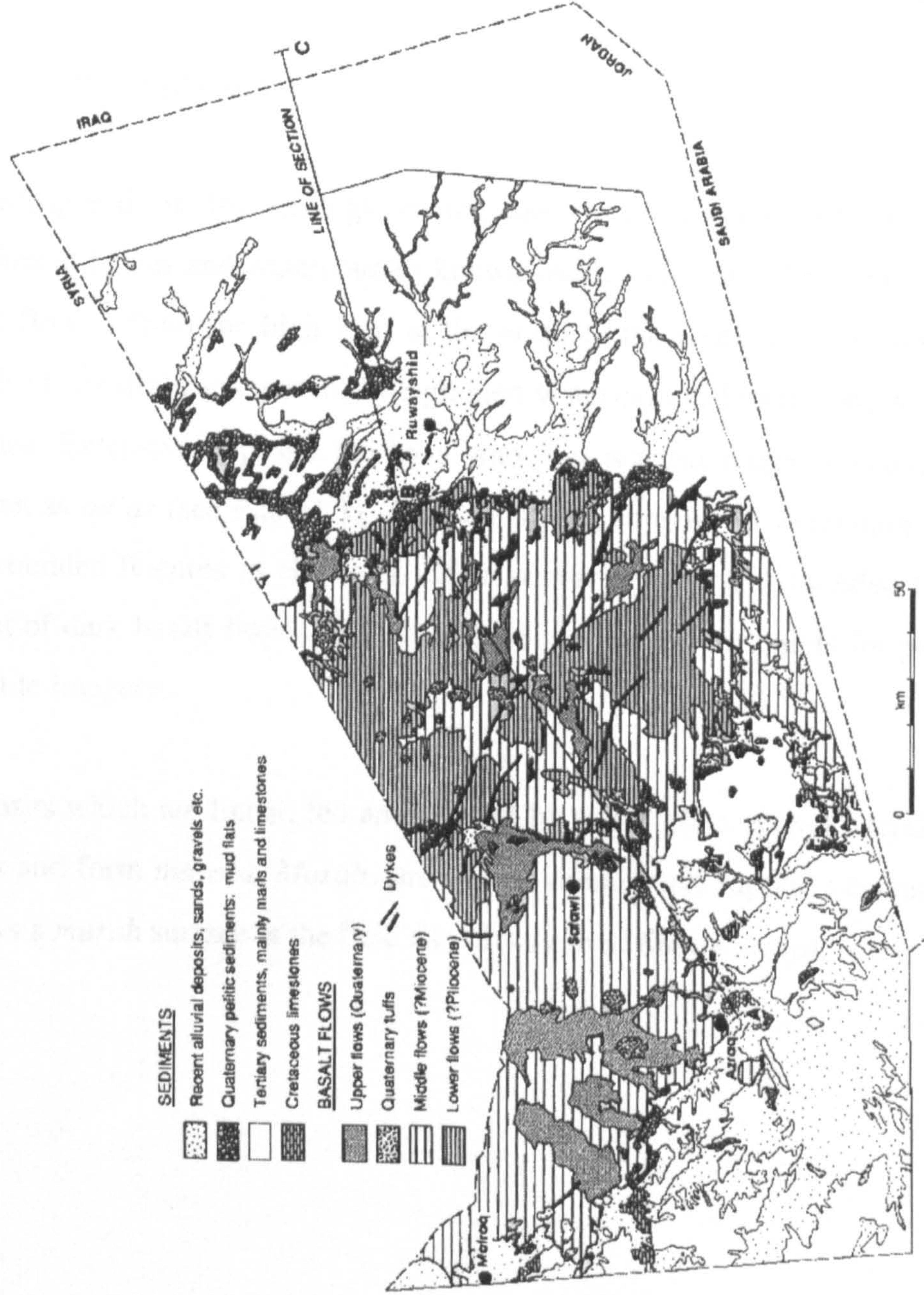


Figure 1.2: Major geological divisions of the Badia (after Burdon 1959). Basalt flows dominate the northern part of the area whilst the southwest is characterised by sedimentary rocks. The east is covered with marls and limestones. The geology affects the distribution of vegetation.



In terms of topography, in the programme area as a whole, the mean altitude is 700 m above sea level with an altitudinal range of approximately 800 m above sea level. The highest ground is around 1,150 m above sea level found in the north-west on the footslopes of the Jabal-al-Arab, whilst the lowest ground is in the south along the Saudi Arabian border at 400 m above sea level (Allison *et al.*, 1998). In general, the region is dominated by gently undulating low hills with extensive flat regions.

### 1.2.2 Geomorphology

Superimposed on the geology of the area is a drainage system comprising of catchment basins and watercourses known locally as wadis. The general direction of wadi flow is from the high land in the north to the south and the south-west. As a result of the drainage system, fine grained water-lain sediments are deposited on the surface. Extensive deposits fed by a wadi but without major outward drainage are known as *qa'as* (see Plate 1.1). They are saline, support no vegetation and appear as flat rounded features in character. Often occurring as bright rounded features in the midst of dark basalt flows, they form good ground control points for geo-referencing satellite imagery.

Deposits which are linear, fed and drained by wadis often spread laterally over larger areas and form *marabs*. *Marabs* are of low salinity and support vegetation. Plate 1.2 shows a *marab* surface at the field site of *Marab al Buqayawiyya*.



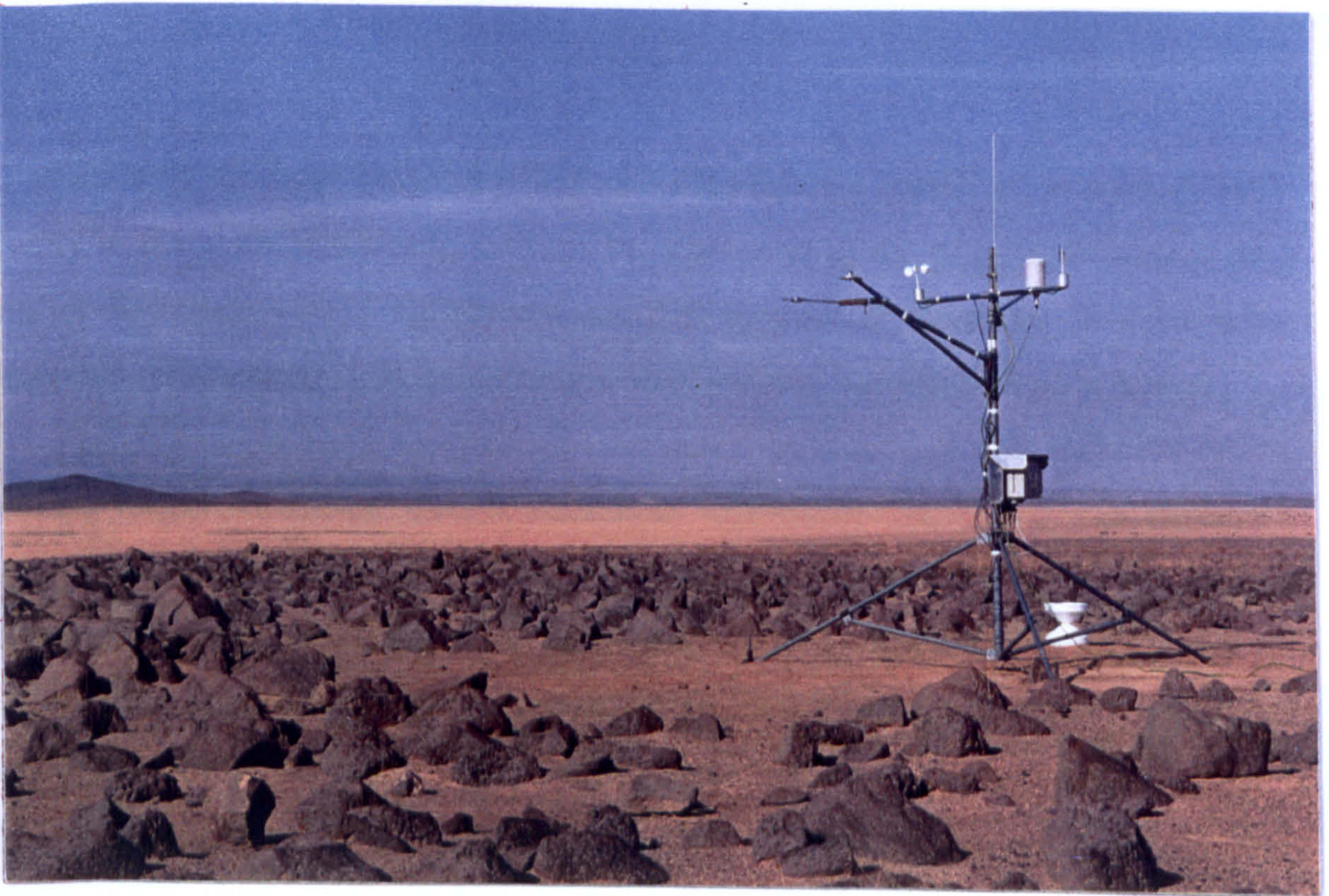


*Plate 1.1: The qa'a at Qa'a Salma. Qa'as are very flat and bright in soil colour. This plate shows Qa'a Salma in the background. In the foreground, an automatic weather station has been set up on a basalt lava flow.*



*Plate 1.2: Marab al Buqayawiyya. Marab surfaces vary in the amount of vegetation cover. They occur where wadis flow out into outwash plains. This plate show field radiometry taking place at Marab al Buqayawiyya.*



In addition to the large basalt regolith pavement (known locally as *harrat*), found mainly in the north of the area, towards the south-east of the programme area is an area of limestone with a surface characterised by angular fragments of chert and limestone (*el hammad*). This has numerous wadi systems but very few *qa'a* deposits.

Moving further south-east towards the border with Saudi Arabia, the soils become highly gypsiferous presenting a white well-developed gypsum crust on the extensive alluvial outwash plain. In the south-west, by contrast, the surface is covered with a thin aeolian sediment, orange-brown in colour, that extends in thickness as one moves across the border. Location of the main *qa'as* and fans that are found in the Programme area are shown in Figure 1.3.

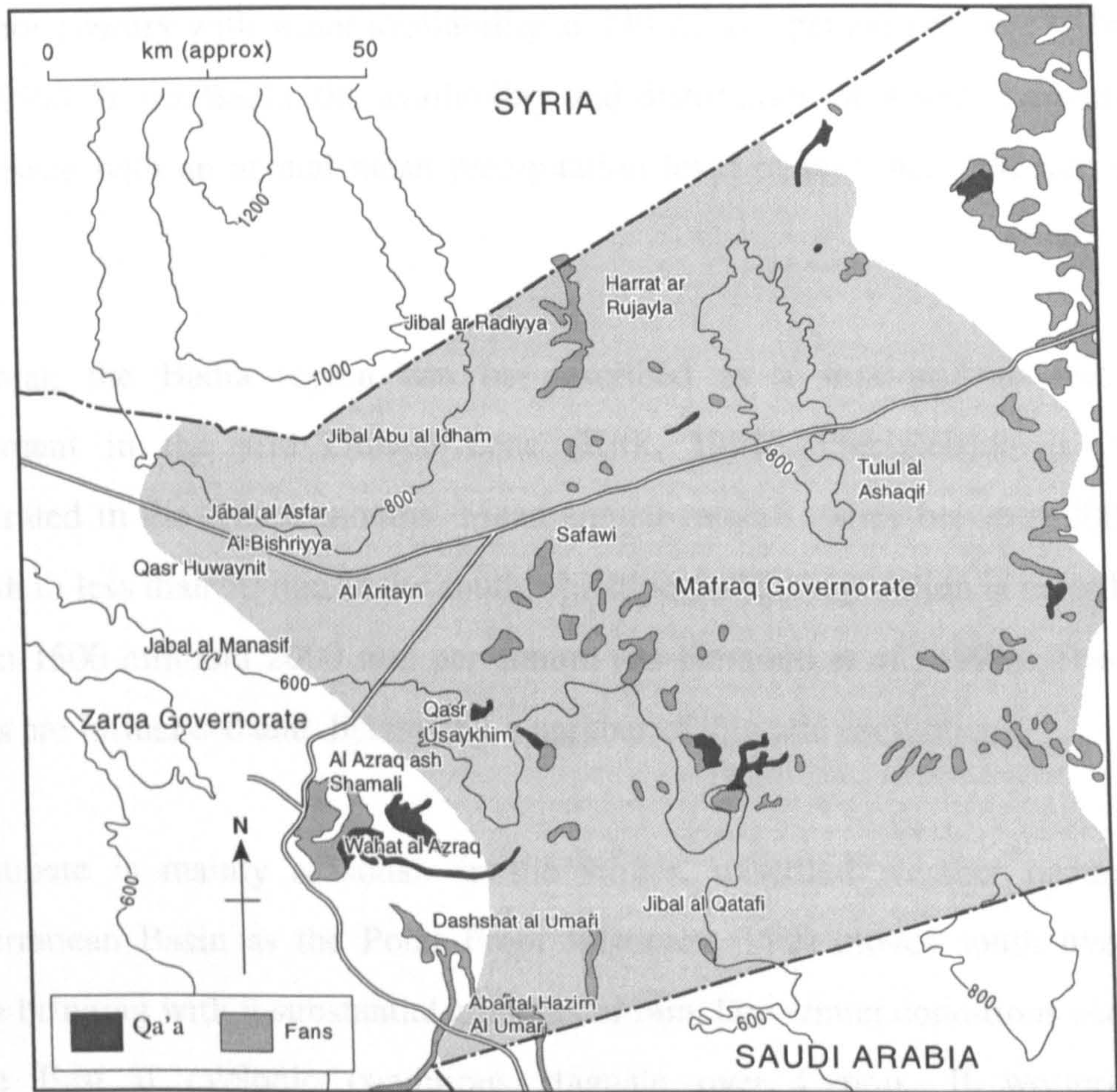


*Figure 1.3: Location of the main qa'as and fans within the JBRDP area. (Source: Allison et al., 1998). There are many others but these are smaller and have not been mapped.*



Descriptions of the geology, topography and geomorphology illustrate the wide range of surface types within the programme area - dark basalt, bright *qa'as*, *wadis* and vegetated *marabs* are all evident. Although these features are all important in the remote sensing of the Earth's surface, this thesis is concerned with the way in which arid land vegetation can be detected and monitored using remote sensing and therefore concentrates largely on the *marab* areas.

### **1.2.3 Climate, hydrology and water resources**

In addition to the underlying topography and geomorphology, a critical factor affecting the spatial and temporal distribution of vegetated areas within the Badia region is the distribution and availability of water. Jordan has been described as a water-poor country with water availability at 240 m<sup>3</sup> per person per year (Abu-Taleb *et al.*, 1992). In the Badia, the availability and distribution of water is a particularly critical issue with an annual mean precipitation level of less than 100 mm in most areas.

In general, the Badia region can be described as a semi-arid to arid steppe environment in the arid climate zone (Kirk, 1998). Precipitation is low and concentrated in the winter months. Mean annual rainfall varies between 200 mm in the north to less than 50 mm in the south whilst potential evaporation is recorded to be between 1500 mm and 2000 mm per annum (Al-Homoud *et al.*, 1996). The weather patterns are influenced and dictated by a number of climatic oscillations.

The climate is mainly seasonal. In the winter, unsettled weather occurs in the Mediterranean Basin as the Polar Front Jetstream (PFJ) moves south over central Europe bringing with it substantial amounts of rain. Dry winter conditions occur in the Middle East if cyclonic conditions stagnate over Cyprus. If westerly winds predominate, the cyclonic conditions move eastwards and the Middle East experiences some precipitation, mainly corresponding to orographic features (Kirk, 1998). During the spring the PFJ moves further northwards pushed by the sub-tropical Jetstream and precipitation is reduced. In the summer months, subtropical ridges of high pressure in

the Mediterranean lead to dry settled conditions (Perry, 1981). Pressure differentials over continental Asia and the effect of the Indian Monsoonal System also contribute to the widespread subsidence with easterly jetstreams moving over Southern Arabia and East Africa leading to upper air convergence (Kirk, 1998).

Despite low annual precipitation, north-eastern Badia benefits from large volumes of surface water draining the Jabal al-Arab in Syria (Dotteridge, 1998). Unfortunately, much of this water is presently lost due to evaporation from the *qa'a* areas and has little influence on vegetation. Some attempts are being made to conserve water through techniques of water harvesting. The water harvesting techniques in use involve exploiting the soil crust formation characteristic of arid and semi-arid soils to act as a means by which water can be channelled as runoff into storage basins (Abu-Awwad and Shatanawi, 1997). Storage basins can be found in the Badia, for example, at *Buqayawiyya*, but their use and efficiency are still in the early stages of development and to date they have had little influence on the distribution of vegetation.

In terms of ground water, the Badia region has substantial ground water resources. One of the problems however, is that much of the water is abstracted for public use and irrigation outside the region in Amman, Zarqa and Mafraq. In 1994, the Amman Water and Sewerage Authority (AWAS) extracted 19.2 million m<sup>3</sup> from the Badia region whereas only 0.87 million m<sup>3</sup> was used for local supplies (Dotteridge and Gibbs, 1998).

This brief summary of the water resources in the Badia area indicates that precipitation in the area is low and seasonal. Ground and surface water resources are relatively high but 'astonishingly, the water is taken from the arid zone to the wetter areas' (Barham and Menshing, 1988). Implications of poor water resources are likely to be low vegetation growth that responds seasonally to winter rainfall events and consequent runoff.

#### 1.2.4 Biogeography

Semi-natural vegetation in the Badia is found in *marab* areas in and around the *wadi* systems. There are some areas of agricultural land, for example, in villages close to the Syrian border but these are not the focus of this study.

One of the most comprehensive studies of the vegetation of Jordan was done by Zohary in 'Plant Life of Palestine' (1962) and 'Geobotanical Foundation of the Middle East' (1973). He classifies vegetation into four regions - the Mediterranean region, the Irano-Turanian region, the Saharo Arabian region and the Sudanian region. The extent of these are shown in Figure 1.4.

The main region of interest in this study area is the Saharo-Arabian region which encompasses the majority of Jordan and all of the Badia. Mean rainfall within this zone is 50 mm and the soils are poor or non-existent. Within the Saharan Arabian region, Al-Eisawi (1985) considers vegetation in the Badia to fall into three main categories - hammada vegetation, saline (halophytic) vegetation and non-vegetated mud flats.

The hammada vegetation category is found across the Badia region. It can be divided into three subgroups - run-off hammada, pebble and gravel hammada and sandy hammada:-

- a) Runoff hammada is confined to wadis and areas of water accumulation. Dominant species include *Atriplex halimus*, *Artemisia herba-alba*, *Achillea fragrantissima*, *Anabasis articulata* and *Tamarix* spp.
- b) Pebble and gravel hammada includes lichen-covered black pebbles with a white-grey lichen growth and annuals of the species *Anthemis deserti*, *Trigonella stellata* and *Herniaria hirsuta*
- c) Sandy hammada is found along the borders with Iraq and Saudi Arabia. Dominant species include *Seidlitzia rosmarinus*, *Artemisia herba-alba*, *Achillea fragrantissima*, *Zilla spinosa* and *Halocnemus strobilaceum*



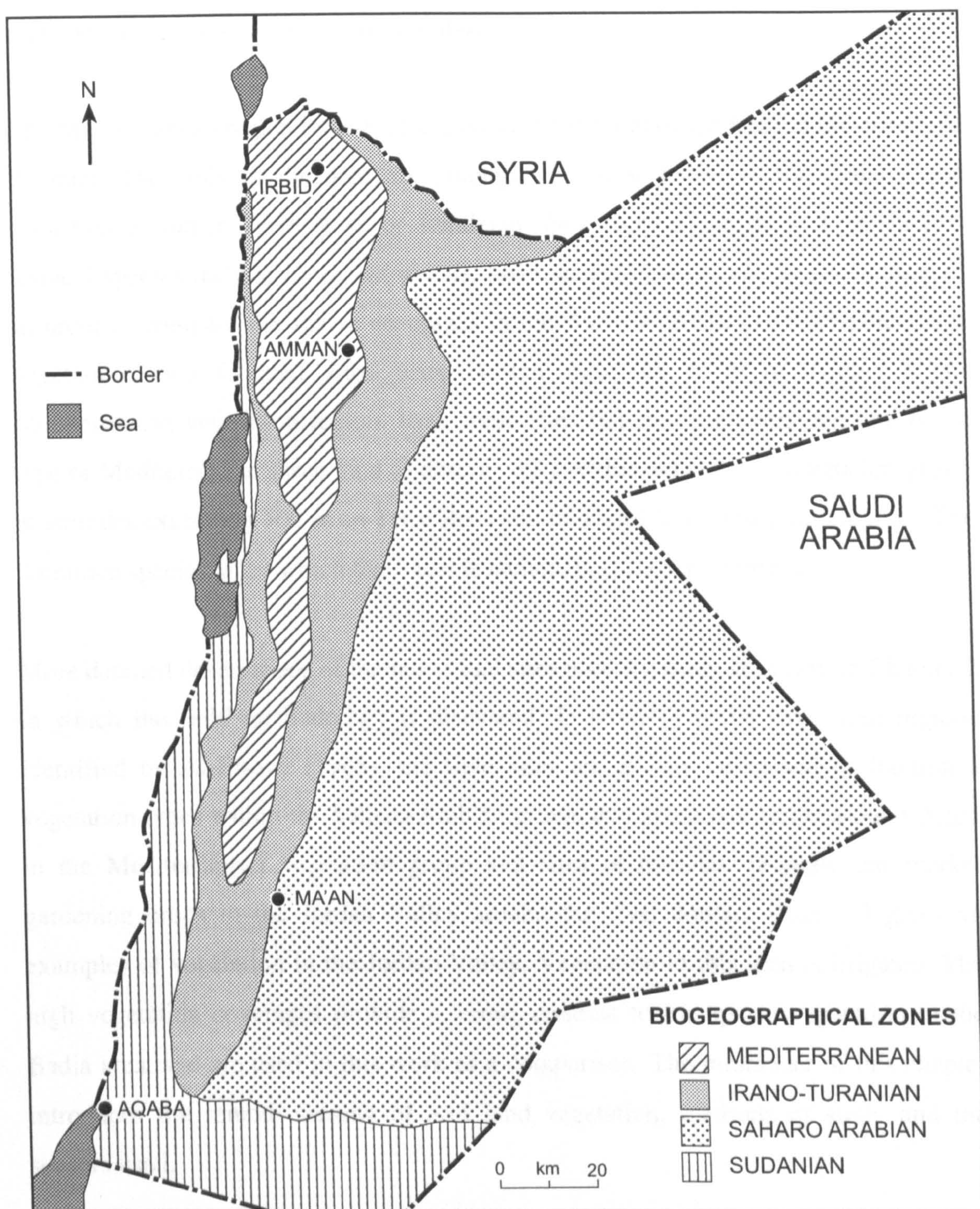


Figure 1.4: The Biogeographic zones of Zohary (source: Al-Eisawi 1985). The JBRDP area falls in the Irano-Turanian area.

Saline vegetation occurs around the Azraq Oasis, in the Jordan Rift Valley around the Dead Sea and around the River Jordan. Species vary depending on their tolerance to



salinity. Mud flats represent *qa'a* areas. Soils on these areas are made up of very fine particles of clay and silt. Vegetation is absent.

The Mediterranean region includes the mountain ranges between Irbid in the north and Amman. The soils in the area are amongst the most fertile in the country and classified as either Terra Rosa or Rendzina, they support the densest vegetation. Typical species include *Pinus halepensis*, *Quercus caliprinus* and *Ceratonia siliqua*. In order to compare the sparse coverages in the Badia with sites of high percentage vegetation, two forested sites were chosen near the town of Ajlun in the Mediterranean vegetation region. Both these sites fall into the evergreen oak forest type or Mediterranean shrub land as described by Al-Eisawi (1985). Vegetation grows at altitudes exceeding 700 m on Terra Rosa soil of a hard limestone parental rock. The dominant species, after which the forest is named, is *Quercus caliprinus*.

More detailed descriptions of the individual sites used for study are given in Chapter 2 in which the field methodology is discussed. In relation to the vegetation regions identified by Al-Eisawi (1985), the field sites are mainly composed of hammada vegetation types within the Saharo-Arabian group, evergreen oak forest around Ajlun in the Mediterranean vegetation group and sites of bananas, oranges and market gardening crops in the Jordan Valley around the river Jordan. Plate 1.3 gives an examples of vegetation in the Jordan Valley. Vegetation in this area is irrigated. The high vegetation coverages provide a strong contrast to the sparse vegetation in the Badia area, and are used in this work as a comparison. The remainder of this chapter introduces the remote sensing of arid land vegetation, methods of study and the sensors used.





*Plate 1.3: An irrigated banana plantation in the Jordan Valley. Vegetation coverages are high (70-100%,) and the area provides a good comparison to the sparse coverages in the Badia region.*

### **1.3 Remote sensing of arid land vegetation**

By their nature and definition, rangelands often cover wide areas of many thousands of hectares. Ground based surveying and mapping techniques for monitoring change are inappropriate because of their spatial and temporal limitations and high cost in terms of resources (Pickup, 1989). Remote sensing and the use of satellite data however, offer a relatively low cost means by which these large areas can be studied at frequent temporal intervals.

A considerable body of research has been carried out using remote sensing in arid regions. Many authors recognise the unique challenge that arid land remote sensing



offers from both a scientific and a management point of view (Tueller, 1987). Much work has been carried out in the semi-arid rangelands of Australia (Foran, 1987, Graetz, 1987, Graetz and Gentle, 1982, Pech *et al.*, 1986, Paltridge and Mitchell, 1990). Graetz and Gentle (1982) and Pech *et al.* (1986) for example, discuss the application of imagery from the Landsat MSS sensor to rangeland management in Australian semi-arid shrublands. They found that whilst post-rain vegetation showed a typical green photosynthetically active vegetation response, the reflectance of perennial shrubs for the rest of the year was low in all wavebands. Soil reflectance was generally high whilst the influence of shadow complicated vegetation cover and greenness prediction. Similarly Foran (1987) studied the use of Landsat MSS for cover monitoring in central Australia, and found that total plant cover could only be predicted in particular areas at certain times of the year. In some landscapes, plant cover prediction was hampered by the fact that rainfall was localised at sub-pixel levels. These studies indicate that the time of year can be a critical issue in remote sensing studies concerned with vegetation detection. The spectral response of vegetation may only be distinct from soil in periods after seasonal rainfall when it is at its greenest.

Other studies have concentrated on land cover mapping and monitoring in Africa. For example, Ringrose and Matheson (1987) applied imagery from the Landsat Thematic Mapper to the analysis of semi-arid vegetation cover in Botswana whilst Kennedy (1989) considered the phenology of grazing lands in Tunisia using the Advanced Very High Resolution Radiometer. Tucker *et al.* (1985) studied the satellite remote sensing of herbaceous biomass production in the Senegalese Sahel also using imagery from the Advanced Very High Resolution Radiometer. They found finding a strong correlation between the satellite data and end-of-season above-ground dry biomass.

Marsh *et al.* (1992) applied data from two sensors, the Advanced Very High Resolution Radiometer and the SPOT XS sensor, to the question of mapping land cover dynamics in the west African Sahel. Their results highlighted the utility of using imagery with different spatial resolutions. The 20 m resolution of SPOT XS proved good for mapping land cover classes on a local scale, whilst the 1.1 km resolution of



the Advanced Very High Resolution Radiometer was better for vegetation mapping on a larger scale such as along the course of a river. These studies indicate that the choice of sensor must be appropriate to the scale of the study.

Huete and Jackson (1987) and Wilson and Tueller (1987) provide examples of studies undertaken considering remote sensing of the arid rangelands in Arizona. Huete and Jackson (1987) studied arid rangeland vegetation in Tucson, Arizona using the Landsat TM sensor, and found that senesced grass and weathered litter that were incorporated into the soil background hampered green phytomass level detection using band ratioing techniques. Wilson and Tueller (1987) examined rangeland communities in Nevada using ground measurements and reflectance data collected on board a low flying aircraft. Soil accounted for 30-80 % of the received radiance and vegetation lowered the spectral signature of an otherwise bright soil surface. The lowering of reflectance in the red and near-infrared parts of the electromagnetic spectrum that occurs across surfaces of areas with a low vegetation cover is known as the darkening effect (Ringrose and Matheson, 1987). This response is common to many arid areas, particularly those in the Middle East, and is a result of the effects of both the vegetation itself and shadow.

In terms of the Middle East, relatively little is known about the spectral characteristics of semi-arid regions in the Saharo-Arabian phytogeographic zone (Pinker and Karnieli, 1995). The work that has been done has concentrated on the difference between the overgrazed area of the Gaza Strip and Northern Sinai and land protected from grazing in the adjacent area of the Western Negev (Otterman *et al.*, 1975, Otterman, 1981, Otterman, 1996, Pinker and Karnieli, 1995). All these studies highlight the 'darkening' effect of vegetation on an otherwise bright soil surface.

Common to many of the papers written about the remote sensing of arid land vegetation are comments about the problems of distinguishing the spectral reflectance of low levels of vegetation cover from the background soil at the scale of a pixel. It is generally recognised that where the surface is made up of a mixture of soil and vegetation, prediction of cover estimates are very difficult to achieve (Satterwhite and

Henley, 1987). A high soil reflectance, in addition to sparse vegetation that is not very green and photosynthetically active, results in a situation where the vegetation is very difficult to detect. Changing illumination/viewing geometries, the high occurrence of shadow and a variable soil background spectral response as a consequence of changing soil colour, mineralogy, texture, salinity and moisture, all affect surface reflectance and exacerbate an already difficult problem.

This thesis concentrates on the detection and monitoring of vegetation in arid regions using optical wavelengths. It is recognised that a number of studies have been done that study vegetation using wavelengths in the microwave region of the electromagnetic spectrum (for example, Grover and Quegan, 1999, Ribbles and Le Toan, 1999). These have been mainly carried out for forest applications. Microwave remote sensing is not considered here (see Tansey, 1999, for details of microwave remote sensing of the Badia region).

### 1.3.1 Vegetation Indices

Arid land vegetation detection and monitoring has been approached in different ways. One of the most common is the use of vegetation indices or band ratioing techniques. Typically vegetation gives low reflection in the red wavelengths due to absorption by chlorophyll and high reflection in the near-infrared wavelengths due to the internal structure of the leaf and high levels of transmission and reflection (Belward, 1991). By combining data from these two wavelengths, this difference can be used to indicate the presence or absence of vegetation (Townshend, 1984, Tucker and Sellers, 1986) .

The Normalised Difference Vegetation Index (NDVI), is an index defined as:-

$$\text{NDVI} = \frac{\text{near infrared band} - \text{red band}}{\text{near infrared band} + \text{red band}} \quad (1.1)$$

The NDVI ranges between -1 and +1 with vegetation typically being in the range 0 to 1. Studies have found that the NDVI correlates well to estimates of biophysical



parameters such as percentage vegetation cover, biomass and Leaf Area Index (for example, Tucker *et al.*, 1985, Kennedy, 1989, Wylie *et al.*, 1991).

Choudbury and Tucker (1987) studying the Kalahari, the Great Victoria and the Great Sandy deserts found that in an arid environment, the influence of the background soil at the pixel scale means the use of the NDVI is limited for estimating very low levels of vegetation cover. Soil and vegetation do not differ sufficiently in red/near-infrared spectral response for the small amounts of vegetation to be detected. One method to help overcome this problem is to use an index where attempts have been made to take the influence of the soil into account. One such index is the Soil Adjusted Vegetation Index, SAVI (Huete 1988).

SAVI was developed by Huete (1988) to address the problem of the background soil. For an experimental site in Phoenix, Arizona, Huete found that by knowing the reflectance of the soil, red and near-infrared reflectances of vegetated areas could be adjusted to take account of the background soil. Soil noise was reduced and relationships between vegetation and spectral data were improved.

Additional indices that attempt to relate vegetation cover to background soil include the Perpendicular Vegetation Index (Richardson and Wiegand, 1977), the Transformed Soil Adjusted Vegetation Index (Baret *et al.*, 1989) and the soil adjusted ratio index, SAVI<sub>2</sub> (Major *et al.*, 1990). Formulae for the different indices and further discussion are presented in Chapter 5 when vegetation indices in relation to the ATSR-2 sensor are discussed.

### **1.3.2 A modelling approach**

An alternative to the study of rangeland vegetation using the method of vegetation indices, is to adopt a modelling approach. The use of physically and empirically based models move beyond the information derived simply from different wavebands and pixels in a satellite image to consider processes occurring on a sub-pixel scale. In particular, they consider the way in which energy is interacting with different facets of



the earth's surface to produce the reflectance recorded by the sensor. They allow one to examine the effects of changing illumination and sun-sensor geometry.

A number of models have been formulated for vegetated landscapes in arid areas (for example Jupp *et al.*, 1986, Franklin and Turner, 1992). In an arid area, a model can be simplified in that the landscape can be considered as a composition of two basic elements - vegetation and background soil. The assignment of reflectance values to these components, the significance of shadow, the shape and distribution of the plants modelled and the question of the vegetation parameters that are estimated, are parameters which vary between models and can be difficult to determine. Chapter 6 considers ways in which the arid land vegetation of the Badia can be detected and monitored using a modelling approach. Further discussion reviewing the literature concerning models is given in Chapter 6.

## **1.4 Sensors**

Sensors chosen for this research were those with the spatial and temporal resolution necessary to cover the large Badia programme area. and record seasonal change. The work also aimed to use sensors which would have features which would offer a new approach in terms of the study of arid land vegetation.

Table 1.1 shows the specifications of two sensors, the Advanced Very High Resolution Radiometer, (AVHRR) and the Along Track Scanning Radiometer, (ATSR-2).



Table 1.1: Specifications of the ATSR-2 and AVHRR sensors.

	ATSR-2	AVHRR
Orbit	near polar, sun synchronous	near polar, sun synchronous
Altitude	777 km	833-870 km
Coverage cycle	6 days	9 days
Swath width	500 km	2700 km
Spatial resolution	1 * 1 km at nadir	1.16 * 1.16 km at nadir
View zenith angle	nadir, 55 ° forward	± 55.4 °
Spectral bands (µm)	0.545 - 0.565 green 0.649 - 0.669 red 0.855 - 0.875 near-infrared 1.58 - 1.64 shortwave infrared 3.55 - 3.93 mir/thermal 10.4-11.3 thermal 11.5-12.5 thermal	0.580 - 0.680 red 0.725 - 1.10 near-infrared 3.55-3.93 mir/thermal 10.3-11.3 thermal 11.5-12.5 thermal

NB: The information given for AVHRR is particular for NOAA-14

AVHRR sensors have been launched on board the National Oceanic and Atmospheric Administration (NOAA) series of satellites from 1978. With a wide swath width of 2700 km, a spatial resolution of 1.1 km and high temporal coverage with a nadir repeat cycle of 9 days, they have provided data for approximately 20 years. These data have been extensively used for land cover mapping and monitoring over wide areas. The AVHRR sensor has five wavebands located in the red, near-infrared and thermal parts of the electromagnetic spectrum (Table 1.1). Red and near-infrared wavebands make the AVHRR ideal for the study of vegetation. The AVHRR has been widely used and studies have covered a range of different environments which have included desert and semi-arid conditions. For example, Tucker *et al.* (1985b) applied AVHRR imagery to the study of total herbaceous biomass production in the Senegalese Sahel. Using imagery collected over five years between 1980 and 1984, they found that the NDVI showed a high correlation with end-of-season above-ground green biomass. Hobbs (1995) similarly, used the AVHRR to assess herbage production in the arid rangelands of Central Australia. Whilst temporal sums of NDVI over a growing



season showed poor correlations with herbage biomass, maximum NDVI values adjusted for the influence of the background soil showed a significant positive relationship.

The wavebands of AVHRR are relatively wide. For land based studies, the position and width of the wavebands are critical issues (Elvidge *et al.*, 1993, 1995). One of the problems with the use of vegetation indices for studying arid land vegetation is that vegetation cannot be distinguished from the background soil. One of the main reasons for this is because desert vegetation, under extreme heat and water stress, often does not show the same big red/near-infrared differences that are common in green photosynthetically active vegetation of wetter regions. There may be a difference between the red and near-infrared reflectance of arid vegetation but it is small and indices formed from the wavebands of broad band sensors such as the AVHRR do not detect it.

This thesis is concerned with assessing the usefulness of the Along Track Scanning Radiometer, ATSR-2, to the problem of vegetation detection and monitoring in arid areas. ATSR-2, is a relatively new sensor, launched by the European Space Agency in 1995. From Table 1.1, it can be seen that the ATSR-2 is comparable to the AVHRR in terms of its temporal and spatial resolution but spectrally, the wavebands (particularly in the red and near-infrared) are much narrower. The ATSR-2 was designed specifically for vegetation studies by providing narrow wavebands in the visible and near-infrared wavelengths that should be able to detect more easily the red/near-infrared reflectance differences characteristic of vegetation (Mason and Delderfield, 1990).

An additional feature of the ATSR-2 sensor is that it has a dual view. Every point on the Earth's surface is viewed twice, once at nadir and once at a forward view angle of 55°. In respect to the study of vegetation, viewing off-nadir at 55° provides the opportunity to study the bi-directional properties of vegetated regions. Vegetated surfaces reflect incident radiation unequally in different directions (i.e. are non-Lambertian) as a function of the optical properties of the surface component elements,



the spatial and geometric arrangement of these elements and the spectral and angular distribution of incident radiation and view angle (Li and Strahler, 1986, Barnsley *et al.*, 1997). By interpreting the magnitude of radiance in a particular direction, information about the physical characteristics of the surface can be ascertained (Kimes *et al.*, 1984). With respect to a sparsely vegetated surface such as that found in the Badia, as the solar/viewing geometry and the amount of shadowed ground changes, viewing the ground off-nadir at 55° may enable the detection of vegetation not visible at nadir viewing.

The novel features of ATSR-2 (its narrow wavebands and dual view) indicate that it may be advantageous for the mapping and monitoring of the vegetation of the Badia. In order to assess its usefulness, this thesis compares the ability of ATSR-2 to detect arid land vegetation with that of the more commonly used AVHRR data. Further information about AVHRR and ATSR-2 are given in Chapter 3 when methods of image data collection and analysis are explained.

It would have been useful to compare the use of ATSR-2 and AVHRR data with that of data from the Landsat Thematic Mapper (TM). Landsat TM has a 30m spatial resolution, and would have provided a good intermediary between ground data, 1.1 km AVHRR data and 1 km ATSR-2 data. Unfortunately Landsat TM data for the area was unavailable for the time of the project. It would, however, make a useful comparison for further work



## **Research aims and objectives**

The broad aim of this research was to assess the utility of the ATSR-2 for the detection and monitoring of arid land vegetation in Jordan. More specifically, the research had the following objectives:-

1. To investigate and compare the use of multi-temporal ATSR-2 and AVHRR data for arid land vegetation detection and monitoring using vegetation indices and modelling approaches.
2. To assess the utility of the forward view of the ATSR-2 for the detection and monitoring of arid land vegetation by modelling the bi-directional effect of the desert surfaces and applying principles from the model to imagery taken in the forward view.
3. To consider the narrow bandwidths of the ATSR-2 and assess the importance of band width in the remote sensing of arid land vegetation.

These objectives were set within the context of the Jordan Badia Research and Development Programme.



## **1.6 Thesis structure**

This thesis takes the form of eight chapters. Following this introductory chapter, Chapter two outlines the fieldwork undertaken in Jordan, presenting methodologies employed and some initial analysis. Fieldwork is an essential component of remote sensing studies and is needed to acquire information about the biophysical parameters necessary for comparison with the reflectance data received by the satellite. Chapter three focuses on the satellite data. The ATSR-2 and AVHRR sensors are described, and image acquisition and processing techniques discussed. Problems associated with image use are considered. In order to understand the forward view of the ATSR-2, Chapter four presents an optical model to examine the way in which ground reflectance varies as a result of changes in viewing and illumination geometry. These results are used to interpret the results of Chapter five where the detection and monitoring of arid land vegetation is attempted using ATSR-2 and AVHRR imagery and vegetation indices. As an alternative method of arid land vegetation detection, Chapter six adopts a modelling approach. A number of models are discussed before the most suitable is chosen and applied to the Badia environment. The forward and nadir views of the ATSR-2 and AVHRR are compared. Building on the results of the previous chapters, Chapter seven takes a broad view of the ATSR-2 sensor and its ability to detect and monitor arid land vegetation. Information in the forward view is analysed using principal component analysis and the spatial, spectral and temporal resolution of the instrument are considered. Finally, concluding remarks are given in Chapter eight. The study is placed within the context of the overall Jordan Badia Research and Development Programme and suggestions for further work are made.



## **2.0 Field data collection and analysis**

### **2.1 Introduction**

### **2.2 Field work aims and objectives**

### **2.3 Field site selection and location**

### **2.4 Vegetation survey**

#### **2.4.1 Sampling strategy**

#### **2.4.2 Species**

#### **2.4.3 Plant dimensions and shape**

#### **2.4.4 Biomass**

#### **2.4.5 Percentage vegetation cover**

### **2.5 Ground radiometric measurements**

#### **2.5.1 Instrumentation**

#### **2.5.2 Measurements taken**

### **2.6 Soil**

### **2.7 Meteorological data**

#### **2.7.1 Precipitation**

#### **2.7.2 Wind speed and direction**

#### **2.7.3 Soil and air temperature**

### **2.8 The relationship between vegetation, soil moisture and precipitation**

### **2.9 The relationship between ground radiometry, vegetation and soil**

### **2.10 Problems associated with field data collection**

### **2.11 Summary and conclusions**



## **2.1 Introduction**

Field data collection is an essential part of studies aiming to examine relationships between remotely sensed data and ground based biophysical parameters. This chapter describes field work carried out in Jordan over three field seasons - November-December 1995, March-May 1996 and November-December 1997. During the first two field seasons, data were collected in the Badia only, the main area of interest, whilst in the third, the study was extended to include sites with higher percentage vegetation covers in and around the Jordan Valley. All field work in the Badia was carried out from Safawi Field Centre - a research centre set up by the Jordan Higher Council for Science and Technology specifically for the Jordan Badia Research and Development Programme. This chapter discusses the criteria for field site selection, the procedures used for data collection and processing and a brief analysis of the results.

## **2.2 Fieldwork aims and objectives**

The aim of the field work was to visit the study area and make measurements that would characterise areas in terms of vegetation, soil and radiometric properties. Visits in November-December 1995 and March-May 1996, before and after the period of winter rains, were designed to capture any seasonal variability in vegetation whilst a return visit two years later in November-December 1997 was carried out to monitor any intra-annual changes.

## **2.3 Field site selection and location**

One of the advantages of using remotely sensed data to examine issues of natural resource management is their ability to monitor phenomenon over a wide geographical area as a result of their spatial resolution. A single ATSR-2 image can cover an area up to 500 km in width. One of the difficulties this presents however, is the collection of ground data on such a scale as to represent a significant sample of the area covered. Time and other resource limitations mean that researchers are often



restricted in the amount of field work that can be undertaken. Using AVHRR data, Diallo *et al.* (1991) sampled 0.01 % of the area of sites in Senegal whilst Wylie *et al.* (1991) sampled only 0.03 % of each of 23 sites in Niger. 0.03 % seems a very small fraction of a study area percentage but, having said this, results from studies such as these have found strong empirical relationships between the vegetation characteristics and remotely sensed data.

In Jordan, an ideal number of sites in statistical terms was overshadowed by the need to find sites that would be ‘useful’ in terms of relating to remotely sensed imagery. Site selection was limited by the need for sites to fulfil a number of criteria.

Firstly, sites need to be flat and homogenous in land cover type. A flat area means the radiometric signal is not altered as a result of changing slope, aspect and relief whilst homogeneity allows the radiometric characterisation of a specific land cover type. Justice (1978) recognised that it is very difficult to find areas of homogeneity and suggested this definition could be modified so that, a site could be regarded as homogeneous if there was one surface cover for more than 85 % of the site or a spatially uniform distribution of surface cover types. Justice (1978) also recommends that the site shows no more than 22.5 % variation either side of the dominant aspect and 20 % of the site area varies not more than 25 % variation from the dominant slope angle.

Secondly the site should be at least 3.3 km<sup>2</sup> in area. This follows the formula set out by Justice and Townshend (1981);

$$A = P(1+2L) \tag{2.1}$$

where:-

A is the minimum distance of the sampling area (km)

P is the dimension of the pixel (km)

L is the accuracy of location (in terms of the number of pixels)



Adhering to this formula and assuming a location accuracy of one pixel, the use of ATSR-2 imagery with 1 km resolution at nadir dictates that sampling sites should be at least 3 km<sup>2</sup> whilst the site should be 3.3 km<sup>2</sup> for use with AVHRR imagery. In the Badia it was this second criteria that proved to be the most problematic. As the vegetation naturally occurs where wadis flow out onto *qa'a* surfaces, areas of vegetation tend to be elongated and fan-shaped. Many possible sites had to be rejected because although they were sufficiently long, they were too narrow to cover more than one ATSR-2 pixel at nadir. As is discussed in Section 7.2.1, the larger pixel sizes in the forward view of ATSR-2 means that ideally field sites need to be even larger. In an arid area such as Jordan with localised vegetation this proved problematic.

After consideration of the above criteria, field sites in the Badia were chosen as a result of reconnaissance trips to the study area using a hard copy false colour composite TM image as a reference. Similarly, study sites in the Jordan valley were selected after reconnaissance visits in the autumn of 1997.

Table 2.1 details the field sites chosen giving their location, a brief description and the field seasons when data were collected. Figure 2.1 shows their location with respect to Jordan as a whole. Field sites in the Jordan Valley were only visited during the final field visit in 1997 as it became apparent during data analysis that measurements in an area of high percentage vegetation cover were required for comparison with those of the Badia.

As can be seen from Table 2.1, not all of the field sites were visited on every occasion. Unfortunately time limitations, weather conditions and the logistical problems encountered whilst working in Jordan meant that some omissions were unavoidable. However despite these, it was considered at the end of 1997 that the data collected would form a good basis with which to make field data/image comparisons.



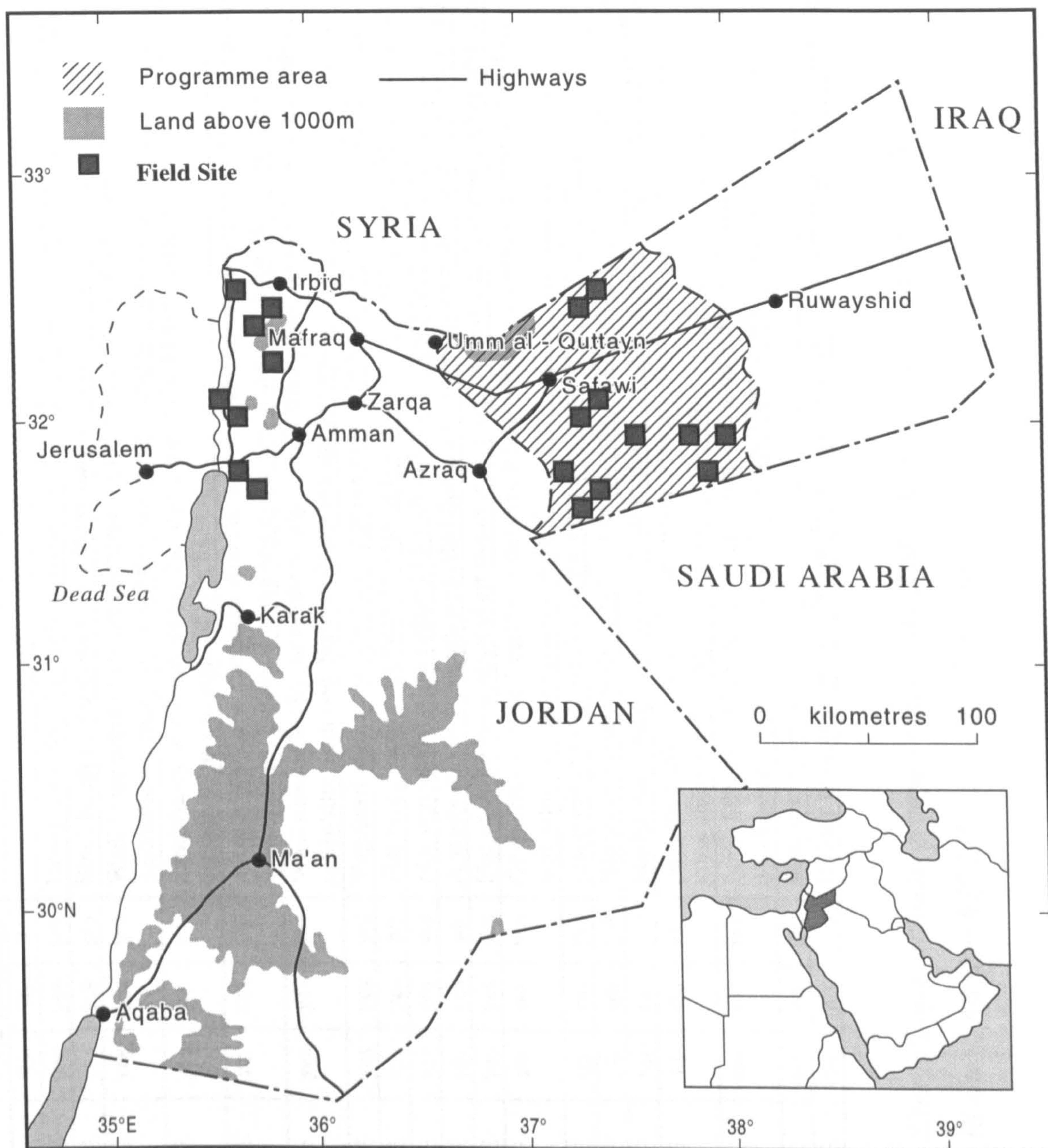


*Figure 2.1: Location of field sites within Jordan. Field Sites fall into two distinct groupings, those in the Jordan Valley to the west and those in the Jordan Badia Research and Development Programme Area (hashed lines) in the East.*



Field Site Name	Location	Field campaign			Site Description
		95	96	97	
<i>Qa'a</i> Abu-Goudie	32.1252 N 37.1793 E	yes	yes	yes	Unvegetated flat clay surface. Relatively smooth and compact with desiccation cracks
B1, Fahda Vesicular basalt	32.3302 N 37.1828 E	yes	yes	yes	Black basalt boulders with a sand/clay matrix. Unvegetated.
Marab <i>Salma</i>	32.4379 N 37.2697 E	yes	yes	yes	Wadi in the north of the area near the Syrian border. Moderate/densely vegetated. Site of the automatic weather station and Bedouin police camp site. Limited grazing.
Marab <i>Qattafi</i>	31.8593 N 37.4321 E	yes	yes	yes	Sandy/stony wadi surrounded by large basalt hills. Moderate-sparsely vegetated. Bedouin encampments and signs of grazing.
Wadi el <i>Hazim</i>	31.5928 N 37.2457 E	no	yes	yes	A sandy wadi near the Saudi Arabian border. Significantly vegetated sand dunes and mound wadi systems. Evidence of grazing by camels, goats and sheep. Some date palms.
<i>Feidat ed Dihikiya</i>	31.5656 N 37.1477 E	yes	yes	yes	Wadi surrounded by limestone escarpment, dominated by Tamarix trees on mounds in sandy/silty wadi bed. Signs of heavy grazing by camels.
Marab al <i>Wassad</i>	31.8866 N 37.9926 E	yes	yes	yes	Vegetated marab near the <i>Wassad</i> police post. Fine reddish sand overlying gravel.
Marab al <i>Wutaydat</i>	31.8247 N 37.7479 E	yes	yes	no	Flat sandy marab surrounded by volcanic cones. Sparse-moderately vegetated.
Marab al <i>Buqayawiyya</i>	32.0397 N 37.1245 E	yes	yes	yes	Flat vegetated mud/salt plain 13 km from Safawi. Moderately vegetated.
<i>Shumaysaniyyat</i>	31.7592 N 37.7543 E	yes	yes	no	A sandy area to the south-west. Red fine grain sand with a surface covering of small stones.
<i>Azraq hammada</i>	31.7119 N 36.9718 E	yes	yes	yes	Flat site with loose black chert stones over compact sand. Small scattered Chenopod clumps
Lower Jordan Valley: Dead Sea A	31.7549 N 35.5950 E	no	no	yes	On the banks of the Dead Sea extending inland. Moderate/heavily vegetated. Sand/silty site with white saltcrusting at the surface
Lower Jordan Valley: Dead Sea B	31.7730 N 35.5900 E	no	no	yes	Just north of the Dead Sea - a flat open site, moderately vegetated. Sheep/camel grazing
Middle Jordan Valley: Bananas	31.9132 N 35.6327 E	no	no	yes	Banana plantation with large fields of bananas at different growth stages. Irrigated and green.
Middle Jordan Valley: Low crops	31.9630 N 35.5767 E	no	no	yes	Market gardening crops symmetrical in fields - onions, lettuces, barley, aubergines. Irrigated
Upper Jordan Valley: Oranges	32.6047 N 35.6107 E	no	no	yes	Near the border with Israel in the north. Plantations of trees - oranges, lemons and limes, with a grass understorey. Irrigated and heavily farmed.
<i>Ajlun A</i>	32.3536 N 35.7485 E	no	no	yes	In the hills near <i>Ajlun</i> castle - large expanse of semi-natural woodland - coniferous and deciduous trees. Red soils covered with small limestones pebbles and larger rocks.
<i>Ajlun B</i>	32.4454 N 35.7379 E	no	no	yes	Similar to <i>Ajlun A</i>
Olive	32.2986 N 35.8723 E	no	no	yes	Hillside of olive trees near Jerash. Dark/red brown soil cleared of stones. No grass understorey.

Table 2.1 : Field site locations and descriptions. Sites fall into two main groups - those in the Badia (first 11 listed) and those in the Jordan Valley (8 sites). All sites fulfilled the specified criteria.



## 2.4 Vegetation survey

As discussed in Section 1.3, the remote sensing of vegetation is an important part of many ecological/environmental studies. Although it is well established that vegetation has a characteristic spectral response particularly in the red and near-infrared, this is related to photosynthetically active vegetation. In terms of field data collection one must still decide which ground based parameter relating to the biophysical description 'photosynthetically active vegetation' is the most appropriate to measure. Some authors choose to measure Leaf Area Index (e.g. Price, 1992), whilst others measure biomass (Kennedy, 1989, Justice and Hiernaux, 1986) or percentage vegetation cover (Ringrose and Matheson, 1987).

There are numerous ways of describing vegetation (Kent and Coker, 1994, Pears, 1985). For the purposes of this study priority was given to recording the physiognomy of the vegetation - the plant morphology and density, as this would be useful in modelling and estimating the proportions of shadow that vegetation casts on the soil surface. Shadow is an important parameter because it directly affects the spectral response of a pixel. In terms of the floristics, an attempt was made to identify the main species present. A visit was made to the field with Professor Dawud Al-Eisawi, Professor of Botany at the University of Jordan, one of the leading authorities in the vegetation of Jordan and this indicated that in the time available it would be a realistic aim to identify the species that were dominant in cover but leave the others unnamed. Raunkier's J curve suggests that many communities contain several dominant species of a high frequency and cover and a number of species with much lower frequencies and cover, and few in-between (Kent and Coker, 1994). By identifying the dominant species it is possible to encompass most of the plant population. Estimations of the biomass and percentage vegetation cover were also attempted. A good estimation of biomass from remotely sensed data would be particularly useful in relation to the issues of desertification and overgrazing, but, as is discussed later, percentage vegetation proved much easier to measure.



### 2.4.1 Sampling strategy

On the first visit to field sites at *Feidat ed Dihikiya* and *Buqayawiyya*, species-area curves were constructed following the method described by Pears (1985) to determine the sampling size needed to capture species variability, and hence give an accurate representation of the type and form of plants present. Transects were also laid out and the total length of transect needed to accurately represent percentage vegetation cover calculated. The results showed that good percentage cover estimates were obtained at the two field sites using transect lengths of approximately 140 m at both *Feidat ed Dihikiya* and *Buqayawiyya*. Furthermore, species variability was captured using quadrat areas of 130 m<sup>2</sup> at *Feidat ed Dihikiya* and 80 m<sup>2</sup> at *Buqayawiyya*. The graphs showing the minimum transect lengths and species area curves can be found in Appendix 1.

The results of the species area curves were considered when determining the sampling strategy at each field site. It was decided that within each study site, the central 1 km<sup>2</sup> would be used as the main study area. 1 km<sup>2</sup> represents the size of an ATSR-2 pixel and locating the field site in the centre means that if imagery is subject to a 1 pixel geo-location error, sampling will still lie within the 3.3 km<sup>2</sup> chosen study area. Within this central 1 km<sup>2</sup>, three 30 \* 30 m areas were then randomly located and laid out using 30 m measuring tapes. 30 \* 30 m should encompass all species present based on the results of the species area curves. Within each 30 \* 30 m area, ten 20 m transects were then laid out starting from randomly located x,y co-ordinates and orientated in a bearing derived from random numbers. Ten 20m transects gives a total transect length for each quadrat of 200 m exceeding the results of the minimum transect length assessments made at *Buqayawiyya* and *Feidat ed Dihikiya*. Random location of the quadrats and the transects means the sample is not biased in any way and parametric statistical tests are therefore applicable. The transects were used as a basic sampling unit from which subsequent measurements were made. Measurements of plant width, height and length, and shape were made of every plant encountered along each transect were made. Observations were also made of species type.



This sampling strategy was used at all sites in the Badia desert region in 1995, 1996 and 1997. It was also adopted in the areas of semi-natural vegetation in the Jordan Valley such as sites at the Dead Sea and in the Ajlun region. In the cultivated areas of the Jordan Valley - those covered by olive trees, oranges, bananas and market gardening crops, an alternative strategy was adopted. Crops at these sites are planted in a regimental pattern in rows at equal widths apart. Measurements of all the plants within a 30 \* 30 m area were taken by laying out a 30 \* 30 m area with tape measures and walking along the plants row by row. This strategy was adopted because with a standard planting pattern, every plant within the quadrat can be positioned and measured.

### 2.4.2 Species

To date, 322 species in 46 vascular plant families have been found in the Badia (Cope and Al-Eisawi, 1998). A list of the dominant species found at field sites in the Badia is given in Table 2.2 below. These were identified with help of botanists working in Safawi and through use of the herbarium at Safawi field station.

Table 2.2: Dominant species found at field sites in the Badia, and details of their family, life-form and palatability.

Field site	Landscape Feature	Dominant species	Family	Life-form	Palatable
Marab Salma	Marab	<i>Achillea fragrantissima</i>	Compositae	Bush	palatable
		<i>Artemisia herba-alba</i>	Compositae	Bush	palatable
Marab Qattafi	Marab	<i>Seidlitzia rosmarinus</i>	Chenopodiaceae	Bush	palatable
		<i>Salsola vermiculata</i>	Chenopodiaceae	Bush	palatable
Wadi el Hazim	Marab	<i>Atriplex halimus</i>	Chenopodiaceae	Shrub	palatable
		<i>Hammada eigii</i>	Chenopodiaceae	Bush	palatable
Feidat ed Dihikiya	Marab	<i>Achillea fragrantissima</i>	Compositae	Bush	palatable
		<i>Tamarix tetragyna</i>	Tamaricaceae	Shrub	palatable
Marab al Wassad	Marab	<i>Anabasis articulata</i>	Chenopodiaceae	Bush	palatable
		<i>Zilla spinosa</i>	Cruciferae	Herb	unpalatable
Marab al Wutaydat	Marab	<i>Anabasis syriaca</i>	Chenopodiaceae	Bush	palatable
Marab al Bugayawiyya	Marab	<i>Capparis ovata</i>	Capparaceae	Herb	unpalatable
		<i>Achillea fragrantissima</i>	Compositae	Bush	palatable
Shumaysaniyyat	Marab	<i>Anabasis articulata</i>	Chenopodiaceae	Bush	palatable
Azraq hammada	Marab	<i>Anabasis articulata</i>	Chenopodiaceae	Bush	palatable
		<i>Salsola vermiculata</i>	Chenopodiaceae	Bush	palatable



As Table 2.2 shows, most field sites are similar in their species composition. With similar soils over the Saharo-Arabian region (saline, sandy hammadas and mud flats) and with water as a common limiting factor, this is not surprising.

Many of the main species shown in Table 2.2 are those typical of hammada vegetation in the Saharo-Arabian vegetation region (i.e. the Badia) as described in Chapter 1. Within the three subdivisions described by Al-Eisawi (1985), run-off hammada, pebble and gravel hammada and sandy hammada, vegetation at *Qattafi*, *Hazim*, *Wassad* and *Shumaysaniyyat* is typical of sandy hammada vegetation whilst that at *Salma*, *Feidat ed Dihikiya*, *Buqayawiyya* and *Azraq hammada* is typical of run-off hammada vegetation. *Wutaydat* appears to be intermediate between the two types.

The majority of the species listed in Table 2.2 are palatable to grazing stock. The effect that grazing has on the vegetation is extremely significant. Where fencing and protection of areas have been established in Jordan, an increase of 200-300 % in vegetation height, cover, phytomass, diversity and total number of macrophyte species has been observed, indicating the extent of overgrazing in unprotected areas elsewhere (Hatough *et al.*, 1986). As grazing increases, species composition changes and plants with defence mechanisms such as thorns or poison replace more palatable species. Kasapligil (1956) studied the range reserves of Surra and Khanasri near Mafraq in Jordan and observed that palatable species, *Artemisia* and *Poa* disappeared in overgrazed areas, whilst they flourished in the reserves. Livestock trampling can also have direct and indirect effects on vegetation as hooves cause mechanical injury and loss of vegetation as well as compaction of the soil.

A typical protected area is the Shaumari reserve which is situated 10 km south-west of Azraq within the Badia area (31.758 N, 36.757 E). This area was initiated in 1958 by the Ministry of Agriculture in Jordan, to be used as a range-land reserve. It was handed over to the Royal Society for the Conservation of Nature in 1967 as a centre for wildlife protection. Covering 22 km<sup>2</sup>, the reserve falls within the Saharo-Arabian biogeographical region. With a maximum elevation of less than 10 m, the area is



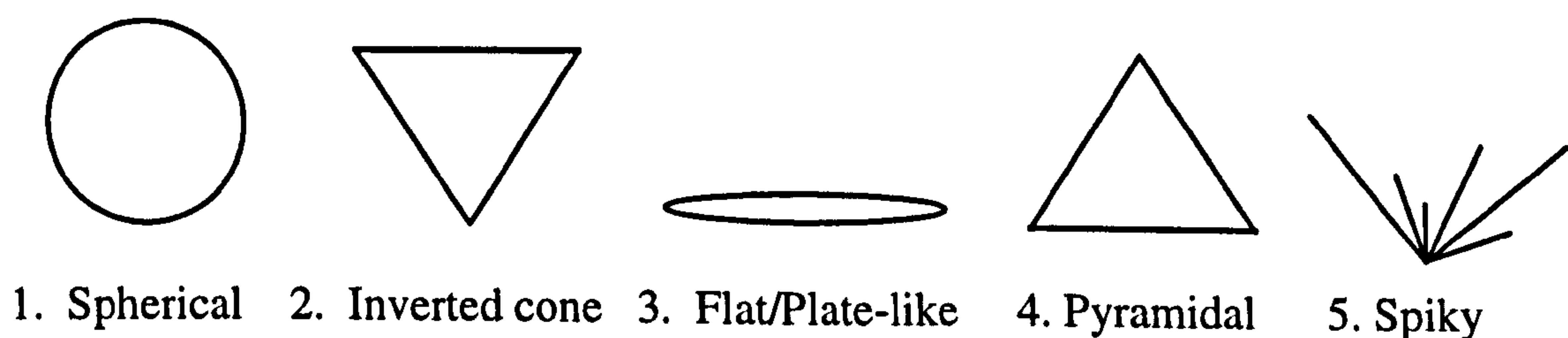
dominated by run-off water systems and wadis and hammada soil covered with fine gravels (Al-Eisawi and Hatough, 1987).

The mean height of vegetation at the Shaumari nature reserve in the autumn of 1997 was 109.5 cm. This compares to 46.5 cm in similar sites outside the reserve. Shaumari was visited to investigate the effect of protection and fencing on the vegetation but, unfortunately it was too heterogeneous to form a permanent field site for use in this study. It was also not representative of the grazing zone.

### 2.4.3 Plant dimensions and shape

A requirement for modelling vegetation is an estimate of plant dimensions and shape. The size and shape of the plant will largely dictate the shadow cast and the resultant pixel reflectance. The mean width, length and height was recorded for every plant that intersected with the transect. In this case, measurements were made of every plant that had shoots crossing the transect regardless of whether the plant roots were in the sample area.

On field visits in 1996 and 1997, every plant measured in the Badia was also given a score based on its shape. The scheme used to score the plants is illustrated below:-



Scoring was subjective and was undertaken in order to allow modelling of the plant dimensions to shape and area measurements. Plants were not scored for shape in 1995 since at this stage the modelling approach to the analysis had not been adopted.

Figure 2.2 illustrates the scores given to plants measured along line transects in 1996 and 1997. The dominant shape was a sphere with 64.1 % of plants allocated to this



group. 'Spiky' plants formed the next largest group with 28.13 % of plants. 'Spiky' referred to plants of very low densities with no discernible shape.

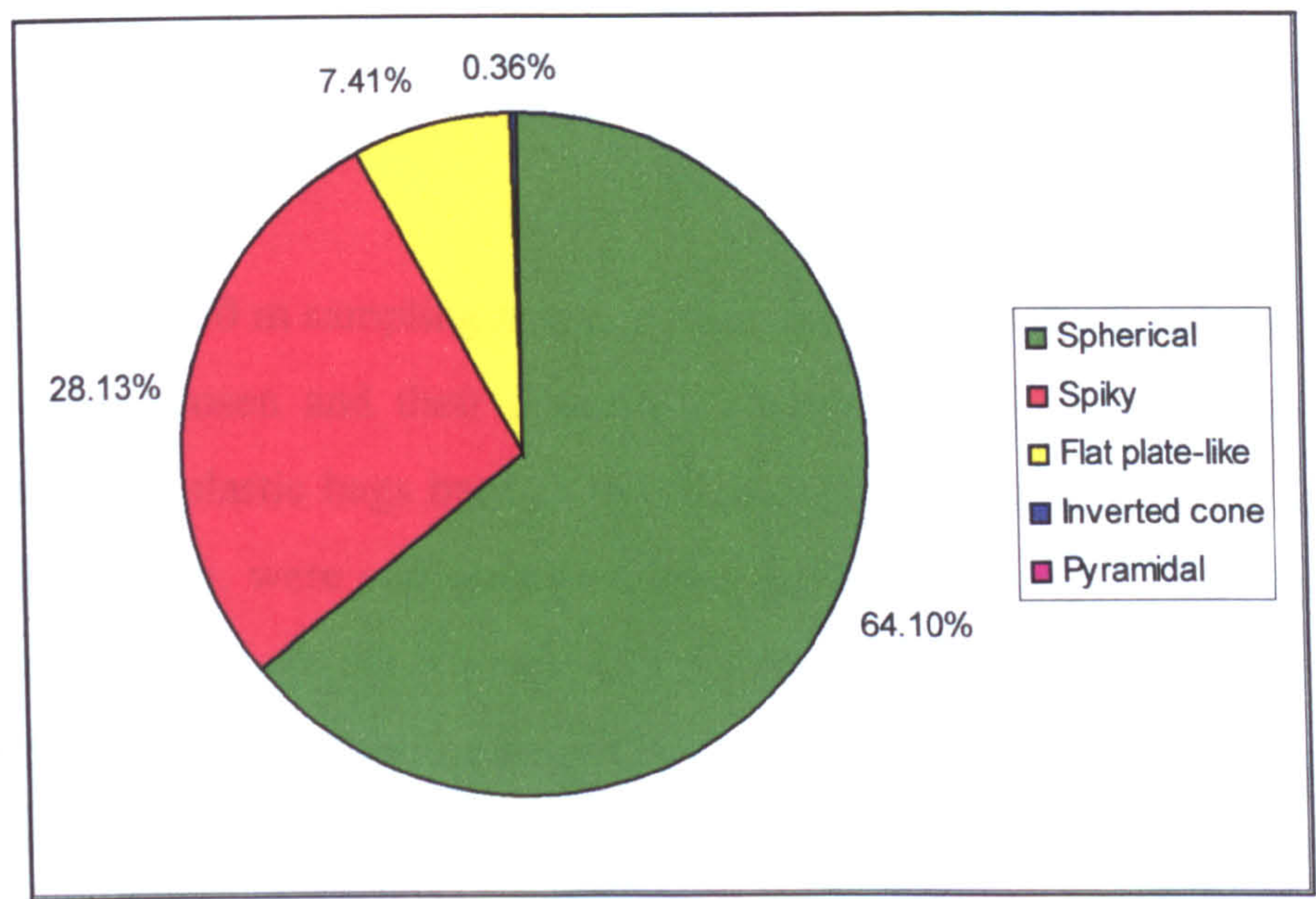


Figure 2.2: Shapes of the plants measured along line transects in the 1996 and 1997 field campaigns. The dominant shape was spherical, followed by 'spiky'.

2.4.4 Biomass

Biomass or standing crop is the weight of organic matter per unit area present in some particular component of the ecosystem at a particular instant of time (Moore and Chapman, 1986). It is generally expressed in terms of dry weight and can be obtained by clipping the above ground vegetation in a given area using shears and secateurs and drying it for 24 hours in an oven at 105 °C (Kent and Coker, 1994). For remote sensing studies in temperate areas, an estimate of biomass can be obtained by throwing a 0.5 m quadrat and clipping all the vegetation contained within it. In Jordan this is problematic. Bushes or plants are often very distinct units upon a bare soil background. Throwing a quadrat either encompasses part of a whole bush, or nothing at all. Taking this into account, the method used by Wellens (1993) for above-ground green biomass estimation in Tunisia was adopted. This method involves clipping, separating and obtaining dry weights of total shrub and shrub parts of a sample of shrubs, and taking height, length, width or volume dimension measurements of all



shrubs in the 30 \* 30m sampling quadrat including the ones harvested (Uresk *et al.*, 1977). Taking only a sample of shrubs means that the effect on the landscape is minimal. A relationship between volume and biomass is calculated using the measured plants and extrapolated to those plants where only dimensions were measured.

Within the 30 \* 30 m sampling frame, entire specimens of the dominant plant species present were chosen and their dimensions measured. They were then clipped and taken in sealed plastic bags back to the Safawi research station. Green components - leaves, shoots etc. were separated out from the brown woody components and both parts were weighed. In the absence of a drying oven, material was then laid out and left for 5 days before weighing again. Kennedy (1989) comments that in the absence of laboratory drying equipment, leaving samples to air dry for 120 hours or until an equilibrium moisture content is reached is perfectly acceptable in arid environments.

Wellens (1993) used crown and height measurements of a harvested plant to model their shape and calculate its volume. A least-squares regression analysis was then performed, and the relationship between plant volume and oven-dried green biomass established. Once a relationship has been established, the biomass of unweighed plants can be calculated from plant dimensions and biomass for the site as a whole can be calculated by using estimates of the percentage vegetation cover. The work in Jordan aimed to use the same method as that used by Wellens (1993) in Tunisia. Using dimension and shape measurements, it was established that the best approximation for the plant shape was a sphere. Table 2.3 below shows the results of correlating plant volumes against air dried biomass for the main species found at different field sites. The entries with no data indicates where it was difficult to separate green components from brown components.



Table 2.3: Correlation of biomass with plant volume for the main species encountered across the field sites. The total dry weight refers to the weight of the shrub as a whole.

The ‘green’ component refers to the plant’s leaves and shoots.

Species	Correlation coefficient	
	Total dry weight	Green component
<i>Achillea fragrantissima</i>	0.64	-0.03
<i>Anabasis articulata</i>	0.59	0.29
<i>Anabasis syriaca</i>	0.75	-0.41
<i>Seidlitzia rosmarinus</i>	0.85	no data
<i>Artemisia herba-alba</i>	0.69	0.68
<i>Atriplex halimus</i>	-0.36	-0.10
<i>Salsola vermiculata</i>	0.63	no data
<i>Hammada eigii</i>	0.59	0.73
<i>Tribulus</i> sp.	0.90	no data
<i>Cleome arabia</i>	0.30	no data
significant at the 95 % confidence interval		

As can be seen from Table 2.3, biomass does not show a consistently significant relationship with plant volume. This is in contrast to the results presented by Wellens (1993) which all show  $r^2$  values of 0.93 and above. A poor relationship means that there is no significant statistical basis from which to estimate the biomass of unweighed plants and the biomass of each site cannot be calculated.

There are a number of reasons why it was difficult to establish a relationship between biomass and plant volume. Firstly, it was difficult to separate above ground green biomass from the rest of the plant for many of the plants. Some chenopods such as *Seidlitzia rosmarinus* did not have green shoots or leaves. They were made up of thick segmented stems with dry, brown flowering shoots at the top. These flowers provide palatable food for browsers but do not fall strictly into the category of ‘green’ biomass. Typically, only the green component of vegetation gives the red/near-infrared spectral signature characteristic of vegetation. The implications of brown/grey/green leaves and stems found in arid land vegetation are discussed in Chapter 5.

Problems also arose from the practicalities of measuring, weighing and drying plants. There were difficulties transporting plants back to the field station. Safawi field



station has no drying oven. Plants were left to air dry but as is discussed by McCleary (1968) many desert plants have strategies for retaining water and deterring predators. Leaves have thick waxy leaves, thorns and spikes (e.g. *Capparis ovata*, *Zilla spinosa*). Without oven drying, some of the water may not have been lost.

As a result of the difficulties experienced, it was decided that percentage vegetation cover would be favoured over estimates of biomass. This was much easier to measure and has the advantage that estimates could also be obtained for sites in the Jordan Valley as well as in the Badia. The commercial value of market crops in the Jordan Valley meant destructive methods of estimating biomass could not be used. Smartt *et al.* (1974;1976) examining different measures of species abundance comment that measures of cover provide a good approximation to superficially more accurate measures such as frequency and biomass. Furthermore, dictating the vegetation/soil ratio viewed by the sensor, percentage cover can be considered to be the most important variable determining the spectral response of a community (Graetz and Gentle, 1982).

#### **2.4.5 Percentage vegetation cover**

Vegetation cover has been described by Greig-Smith (1983) as the portion of the ground occupied by a perpendicular projection of the aerial parts of individuals of the species under consideration. It is usually expressed as a percentage and because of the over-layering of different species, estimates of total cover can exceed 100 %.

In relation to remotely sensed data, percentage vegetation cover is taken to represent an estimate of total cover without differentiation of species. The data collected in the field recorded the coverage of different plants but areas of overlap were not considered since satellite viewing from above using optical wavelengths cannot sense vegetation cover greater than 100 %.

There are a number of different ways of measuring percentage vegetation cover such as visual estimation using a 1 \* 1 m quadrat, use of a cover pin frame or line intercept



methods. The choice of which technique to use depends on the time available, the nature of the vegetation and the accuracy of the results required. It is recognised that in an environment where vegetation is sparse, the normal square quadrat is unsuitable and it is better to use the line-intercept method instead (Kent and Coker, 1994). The line intercept method was the technique used in this study and utilised the transects laid out in the large 30 \* 30 m areas (Section 2.4.1). The distance over which vegetation intersected the line was recorded. Percentage cover is then simply calculated as the length of line covered by vegetation divided by the total length of line. Using randomly located transects this appears to work well. In some of the study areas especially in the spring period, the ground in between plants was covered in a fine hue of grass shoots. Where this was the case, a 0.5 m quadrat was thrown at the start of each line. Percentage cover was estimated visually in this quadrat and then that percentage was added to the total percentage of vegetation along the transect line. In 1995 and 1996, the presence of a field assistant meant that two independent estimates of quadrat percentage cover could be made and an average taken. In 1997, when a field assistant was unavailable, estimates were made by a single observer.

In areas of cultivated crops, transects were not laid out and percentage vegetation cover was estimated in two ways:-

- 1) For sites where plants are distinct as individual units (i.e. bananas, orange trees and olive trees), percentage vegetation cover was calculated by taking the width and length of each plant canopy in a 30 \* 30 m area and calculating its area as a circle ( $\pi r^2$ ). The areas of all the plants added together, divided by the total area of a 30 \* 30 m quadrat gives the percentage vegetation cover as a whole.
- 2) For sites where plants were distinct not as individual units but in rows (i.e. market gardening crops), the percentage vegetation coverage was calculated by multiplying the width of a row by its length. The area of an individual row was multiplied by the number of rows and then divided by the 30 \* 30 m quadrat area as whole.

Ideally, it would have been desirable to adopt the same sampling strategy for all field sites. However, what is appropriate for one site is not necessarily appropriate for the



others. It was considered that the aim should be to get the most accurate estimate for percentage vegetation coverage rather than keep sampling strategies consistent.

Percentage vegetation cover estimates are given in Table 2.4:-

*Table 2.4: Percentage vegetation cover estimates measured in the field. Jordan Valley measurements were only taken in the final field season in 1997. For sites in the Badia region, percentage vegetation cover shows very little change over time.*

Field Site Name	% Vegetation Cover		
	Autumn 95	Spring 96	Autumn 97
Marab Salma	10.7*	27.98	28.96
Marab Qattafi	3.71	7.96	7.85
Wadi el Hazim	no data	22.35	15.59
Feidat ed Dihikiya	2.98	5.2	13.61
Marab al Wassad	5.96	3.78	5.57
Marab al Wutaydat	4.73	3.97	no data
Marab al Buqayawiyya	8.2	6.17	15.05
Shumaysaniyyat	3.39	7.7	no data
Azraq hammada	2.11	1.83	1.63
Lower Jordan Valley: Dead Sea A	no data	no data	49.27
Lower Jordan Valley: Dead Sea B	no data	no data	37.51
Middle Jordan Valley: Bananas	no data	no data	34.91
Middle Jordan Valley: Low crops	no data	no data	35.0
Upper Jordan Valley: Oranges	no data	no data	100
Ajlun A	no data	no data	80.8
Ajlun B	no data	no data	70.1
Jerash: Olives	no data	no data	18.29

\* different area measured to the following two years

For the periods measured, *Azraq hammada*, *Wutaydat* and *Wassad* show very little change. As one might expect, values for autumn 1995 and 1997 are very similar - the vegetation is dominated by woody perennials able to survive in drought conditions throughout the summer, but there is no indication of a ‘greening up’ after winter rains. Spring 1996 values incorporated no inter-perennial grass covering. *Feidat ed Dihikiya*, *Shumaysaniyyat* and *Qattafi* show an increase in coverage from autumn



1995 to the spring 1996 suggesting a response to winter rainfall. *Buqayawiyya* and *Feidat ed Dihikiya* show a significant difference between autumn 1995 and autumn 1997 values suggesting that 1997 was a wetter year in these areas. This observation is supported by the soil moisture values shown in Figure 2.4.

In general, percentage vegetation cover values recorded in the Badia are very low and show little seasonal and intra-annual change. Significant percentage coverage changes are inconsistent between field sites highlighting the difference in conditions at the field sites in terms of soil type, vegetation species, grazing pressure, and variations in local rainfall and flooding.

The Jordan Valley area visited in the autumn of 1997 displayed percentage vegetation cover values of up to 100 %. As the region is geared towards high agricultural productivity and supported by irrigation this is not unexpected. The analysis in Chapters 5 and 6 utilises the field sites in this area to provide a vital comparison to those in the Badia.

## **2.5 Ground radiometric measurements**

The aim of field radiometry was to characterise the ground surface in terms of radiometric response, and to investigate its bi-directional properties. The instrumentation used and field methodology are explained here, whilst analysis of the bi-directional properties is discussed in relation to a simple geometric optical model in Chapter 4.

### **2.5.1 Instrumentation**

There are a range of different instruments designed to make radiometric measurements in the field. The Natural Environment Research Council (NERC) currently have five different high performance field spectroradiometers that they lend out to users through the equipment pool for field spectroscopy (NERC EPFS), based



in the Department of Geography at the University of Southampton. Instruments vary in spectral resolution, processing time and portability.

Ground radiometric measurements in this study were made during every field campaign using a variety of different field radiometers. The Spectron SE590 and the ASD were borrowed from NERC EPFS and used in the Autumn 1995 and Spring 1996 respectively. A Milton Multiband Radiometer was borrowed from the University of Reading and used in the final field campaign in 1997 due to problems with the ASD. Each radiometer measures spectral radiance which is then converted to surface reflectance by comparison with coincident irradiance on a reference panel. In the case of the Spectron and the ASD, conversion is done automatically whilst with the Milton Multiband Radiometer conversion is carried out manually at a later stage.

The Spectron SE590 is a lightweight, rapid scanning instrument. It measures spectral radiance in narrow bandwidths of 11 nm across the spectral range 400 - 1100 nm. The target and the reference are measured sequentially with a typical time delay of 10 seconds. Each scan takes approximately one second. The reference was provided in the form of a Labsphere Spectralon reflectance target SRT-99-100-1011 - a spectralon panel. Alternatively a second optical head, a cosine receptor, can be used. Data were collected on miniature digital tapes and downloaded to an IBM-PC.

The Analytical Spectral Device or ASD measures over a wider spectral range, 350-2500 nm. The spectral resolution is finer than the Spectron measuring in 3 nm intervals over the range 350-1000 nm and 10 nm over the 1000-2500 nm range. A typical scan takes less than a second although optimisation at the start of each set of measurements takes longer. The ASD is designed as a field radiometer and provides rapid high resolution measurements. It can be worn on a harness but, care must be taken as the fibre optic cable connecting the computer and the fore-optic and pistol grip is extremely delicate and can be easily damaged. For the work in Jordan, a fore-optic providing an 8° field of view was chosen and again the same Spectralon panel was used as a reference to convert spectral radiance to reflectance.



On the final field campaign in the autumn 1997, the ASD was taken to Jordan again. Unfortunately, despite testing before departure, on arrival the instrument failed to work due to internal electronic problems. As a surrogate the Milton Multiband Radiometer (MMR) was transported to Jordan and measurements were made using the MMR instead. Although the Series 100 MMR lacks the high radiometric resolution of the other instruments, it is lightweight and very easy to use.

The MMR is fitted with detectors and absorption filters corresponding to the bandpasses of Landsat TM. It measures spectral radiance in four bands, 400 - 500 nm (TM band 1 - visible blue), 500 - 600 nm (TM band 2 - visible green), 600 - 700 nm (TM band 3 - visible red) and 700 - 1100 nm (TM band 4 - near-infrared). The target was measured sequentially to a reference target and the surface reflectance or bi-directional reflectance factor (BRF) was calculated as a ratio between the two multiplied by a constant K, the ratio of the reflectivity standard used to a perfectly reflecting panel (Equation 2.1). The dark current offset  $V_o$  subtracted from each reading is the voltage produced when detectors are covered and no radiation is being measured.

$$BRF = \left( \frac{V_t - V_o}{V_r - V_o} \right) * K \quad (2.1)$$

where  $V_t$  = voltage from the target

$V_r$  = voltage from the reference panel

$V_o$  = dark current offset

K = in-band correction factor

In Jordan two reflectivity standards were used - a Kodak grey card and a barium sulphate panel. Both were calibrated against a perfectly reflecting target by NERC EPFS giving the K values shown in Table 2.5.



*Table 2.5 Milton Multiband Radiometer 'K' values*

	<b>K values</b>			
	<b>TM Band 1</b>	<b>TM Band 2</b>	<b>TM Band 3</b>	<b>TM Band 4</b>
Kodak Grey Card	17.27	17.46	19.96	18.88
White panel	99.33	99.4	99.41	99.43

Ideally, the same radiometer should have been used in every field season but machine availability and technical breakdown meant that this was not possible. Measurements made with different instruments do mean that whilst absolute reflectance values cannot be compared, relative differences between sites, vegetation types and soil can be examined.

**2.5.2 Measurements taken**

During all the field measurements care was taken to adhere to the guidelines set out by Milton (1987) regarding radiometric data collection. Measurements were restricted to periods when solar conditions were stable. In general, measurements made early in the morning or around solar noon were during cloud free conditions. Some sites however, could only be visited later in the afternoon when any cloud formation was noted.

Radiometric measurements were made at a constant height above the surface. The actual height used varied according to the field of view of the sensor but, in general a range of 1.5-2 m was adhered to. Mounting the radiometer on a tripod ensured it remained stable during measurements and that an exact position was kept for measurements of the surface and of the reference panel.

To sample the bi-directional hemisphere of the surface, measurements were made at viewing angles of nadir, 25 ° and 55 ° and relative azimuth angles of 0°, 45°, 90°, 135°, 180°, 225°, 270° and 315°. An angle of 0° pointed the sensor head directly into the sun and represented viewing in the forward scatter direction whilst 180 ° viewed directly away from the sun represented the hot spot and a backscatter direction. On some occasions especially at the 25° view angle, the reading at 180 ° was omitted as



the tripod contaminated the field of view with shadow. Figure 2.3 gives an indication of a set of measurements taken at any one site.

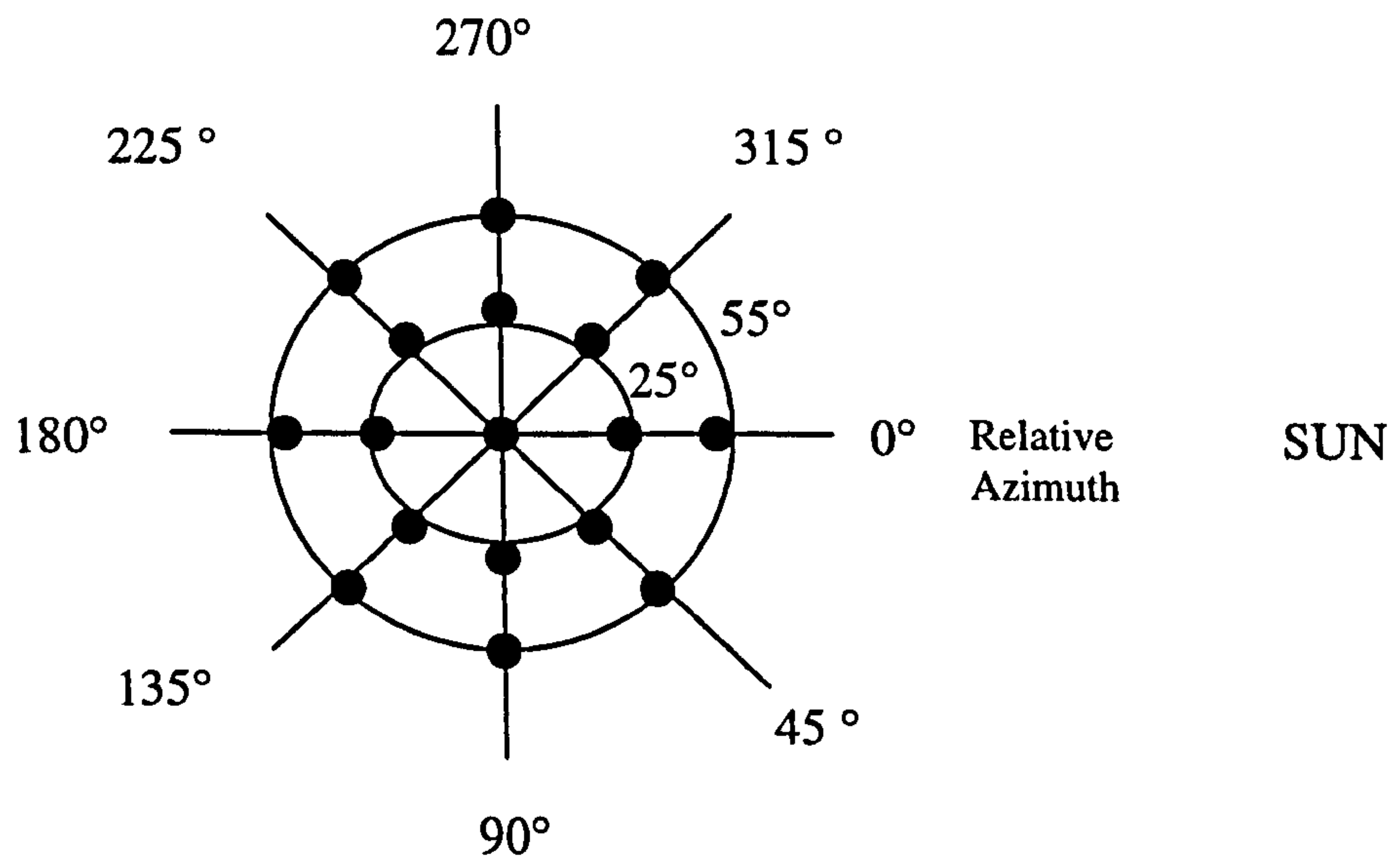


*Figure 2.3: Bi-directional measurements taken using field radiometers.*

*Measurements were taken at nadir, 25° and 55° view angles, and relative azimuth angle around the measurement sphere in increments of 45°.*

Measurements were made of the soil surface and of the vegetation. When using the Spectron and the ASD, 10 sets of measurements were made at each field site. With the Milton radiometer, three sets of three readings were made at each field site. For all sites a mean reflectance value was calculated from the series of measurements made in a particular viewing direction in order to characterise the surface and allow for any anomalies.

## 2.6 Soil

Soil type and water content have a direct control on plant distribution and performance (Ball, 1986). For sparse vegetation canopies, changes in soil type and soil optical properties are also important in influencing the spectral response of the surface and the calculation of vegetation index values (Baret *et al.*, 1993, Elvidge and Lyon, 1985).



Soils in Jordan are generally poor in terms of moisture content and nutrients. With the exception of some parts of the Mediterranean region and areas of forest, the result of erosion and low levels of vegetation mean that many soils contain only a C horizon and parent material (Al-Eisawi, 1985).

In order to ascertain the influence that background soil has in this study, a soil sample was collected at every field site and analysed for soil colour. Table 2.6 below indicates the soil type and soil colour for sites in the Badia, and soil colour for sites in the Jordan Valley. Soil particle size analysis was carried out by Kevin Tansey, a PhD colleague at the University of Jordan, Amman using standard methods. Laboratory facilities were not available during the 1997 field visit and so particle size analysis could not be carried out on soils from the Jordan Valley. Soil colour was determined for all soils with reference to a Munsell soil colour chart.

Estimates of soil moisture were made at every field site using a ThetaProbe soil moisture sensor. Primarily, soil moisture was recorded so that a complementary study to the one described here could be carried out looking at the relationship between soil moisture and radar backscatter (see Tansey, 1999). However, data from this work is included here to investigate any relationships between rainfall, percentage vegetation cover and soil moisture content. After a rainfall event one would expect soil moisture to increase and percentage vegetation cover also to increase.



*Table 2.6: Soil Properties of soils at field sites across Jordan. The sites all exhibit different soil properties. These properties are important in affecting the spectral response of the surface.*

Site name	Soil Colour		Soil texture class	Soil texture (%)		
				Sand	Silt	Clay
Salma	Yellowish brown	10 yr 5/8	silty loam	14.8	71.9	13.3
Shumaysaniyyat	Orange	7.5 yr 7/4	sand	89.7	6.0	4.3
Buqayawiyya	Dull yellow orange	10 yr 7/4	silty clay loam	15	50	35
Feidat ed Dihikiya	Light yellow orange	10 yr 8/3	clay	4.8	33.6	61.6
Hazim	Dull yellow orange	10 yr 6/4	sand	93.5	2.92	3.62
Wassad	Dull yellow orange	10 yr 7/3	sand	87.1	7.0	5.9
Wutaydat	Orange	7.5 yr 6/6	loamy sand	77.5	12.3	10.2
Qattafi	Bright yellowish brown	10 yr 6/6	sandy clay loam	60	20	20
Azraq hammada	Dull yellow orange	7.5 yr 6/6	sandy loam	46.1	48.6	5.3
Bananas	Brown	10 yr 4/6	no data			
Oranges	Dull yellowish brown	10 yr 4/3	no data			
Olives	Bright reddish brown	5 yr 5/8	no data			
Ajlun A	Dark reddish brown	5 yr 3/6	no data			
Ajlun B	Dark reddish brown	5 yr 3/6	no data			
Low crops	Pale yellow	2.5 yr 8/4	no data			
Dead sea A	Dull yellow orange	10 yr 6/3	no data			
Dead sea B	Dull yellow orange	10 yr 6/3	no data			

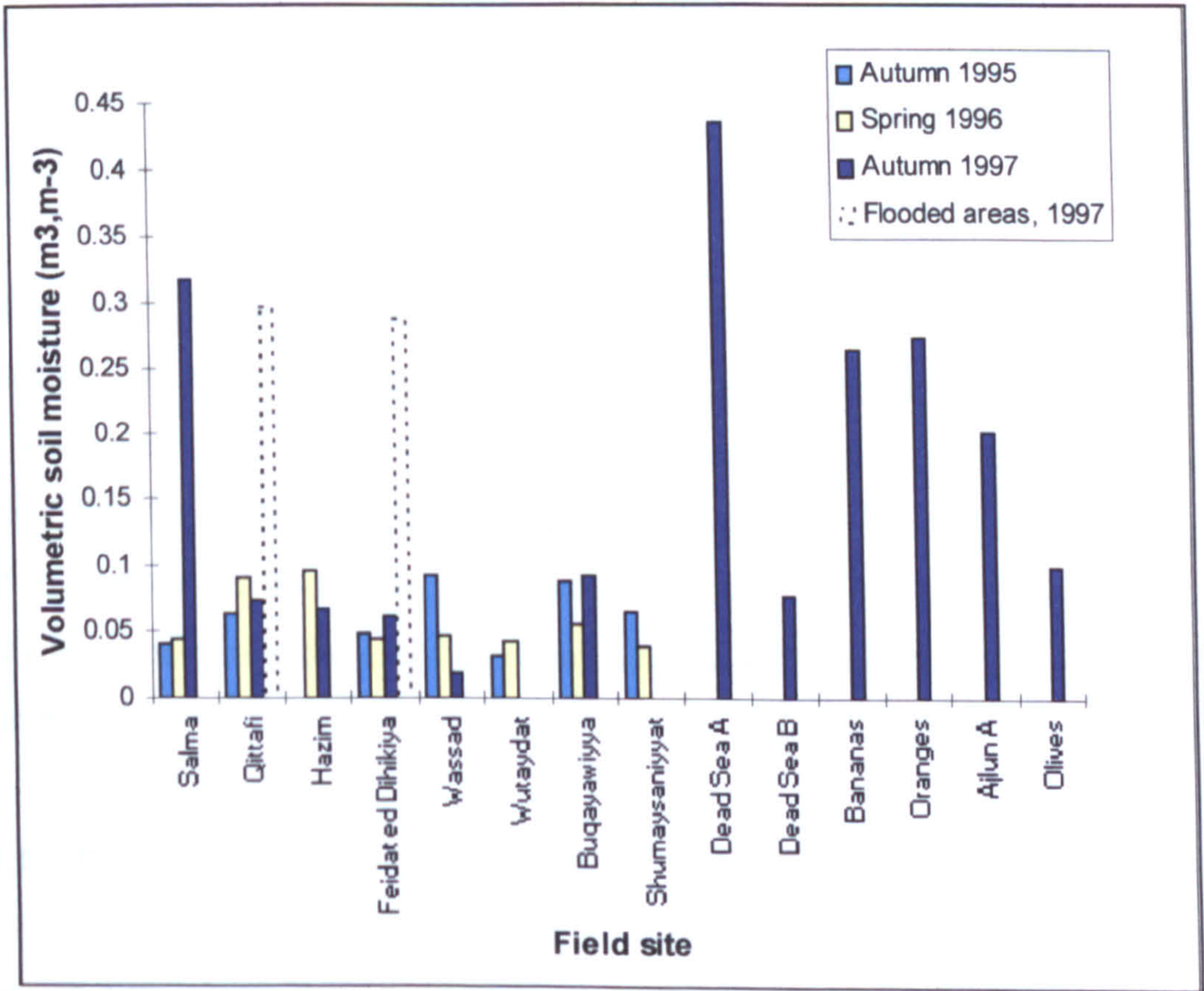
The ThetaProbe is a four pronged probe that measures volumetric water content in the top 5 cm of the soil by responding to changes in apparent dielectric content. Volumetric water content is a ratio between the water present and the total volume of the sample. 0 m<sup>3</sup>.m<sup>-3</sup> corresponds to a completely dry soil whilst 1.0 m<sup>3</sup>.m<sup>-3</sup> corresponds to pure water. At any one field site, up to 20 measurements were taken at random locations. The raw data were subsequently converted to values of volumetric soil moisture using calibration equations provided with the ThetaProbe documentation (see Delta-T Devices ThetaProbe user manual, 1995), and a mean value for each field site calculated.

Figure 2.4 shows the mean volumetric soil moisture measured at different field sites in 1995, 1996 and 1997. From the graph one can quickly appreciate the fact that at



*Feidat ed Dihikiya, Qattafi and Salma* the autumn of 1997 was very wet compared to 1995 and 1996. Volumetric soil moisture readings taken in flooded *qa'a* areas adjacent to the areas of marab at *Feidat ed Dihikiya* and *Qattafi* are indicated by a dotted line.

From Figure 2.4, it can be seen that spring 1996 values are very similar to autumn 1995 values indicating that the winter of 1995/6 was not a good year in terms of winter rainfall. Soil moisture values do not rise over the winter period as expected. As one would expect the areas in the Jordan Valley all have very high soil moisture contents. Dead Sea A also has a high reading, attributable to surface streams.



*Figure 2.4: Mean volumetric soil moisture content at different field sites across Jordan. As the graph indicates, soil moisture was much higher in the autumn 1997 than in the other two dates.*



## 2.7 Meteorological data

In 1995, an automatic weather station (AWS) was taken out from Leicester University and installed at *Qa'a Salma* (32.44027 °N, 37.27084 °E) in the north of the study area. Positioned on a flat surface slightly elevated from the *qa'a* surface, the weather station carried instrumentation to measure wind speed and direction, air temperature, humidity, solar irradiance and rainfall. Additional probes included a net pyrradiometer to monitor net all-wave radiation, thermistor probes suitable for recording soil temperature, a soil heat flux plate and aspirated hygrometers. Between 15/12/95 and 29/03/96 sensors were programmed to take readings every minute and produce a twenty minute average. Between 14/05/96 and 28/10/96 readings were taken every five minutes and averaged over one hour. The change in temporal resolution was to allow a greater time interval between battery changes. The rain gauge worked as a tipping bucket mechanism measured at a resolution of 0.5 mm and summed hourly. All data were recorded on a battery driven data logger fixed to the main mast of the weather station.

Unfortunately, although installed on the 16th December 1995, data were only collected until the 27th October 1996. This was the final date of downloading before the instrument was reported stolen by the Bedouin police patrol. Data were also unavailable for the period 29th March to 13th May 1996 - the period when batteries had to be removed and recharged. Sections 2.7.1 to 2.7.3 discuss the climate of the study area combining the data that were collected with the AWS with that from other sources.

### 2.7.1 Precipitation

Figure 2.5 illustrates the precipitation distribution across Jordan. Rainfall in Jordan is highly variable ranging from less than 50 mm yr<sup>-1</sup> in the Badia to more than 500 mm yr<sup>-1</sup> over the *Ajlun* heights. In the Badia there is a rainfall gradient from a minimum in the south on the Saudi Arabian border to a maximum near the Syrian border in the



north. Rain generally falls in the winter between the months of November and May (Al-Homoud *et al.*1996).

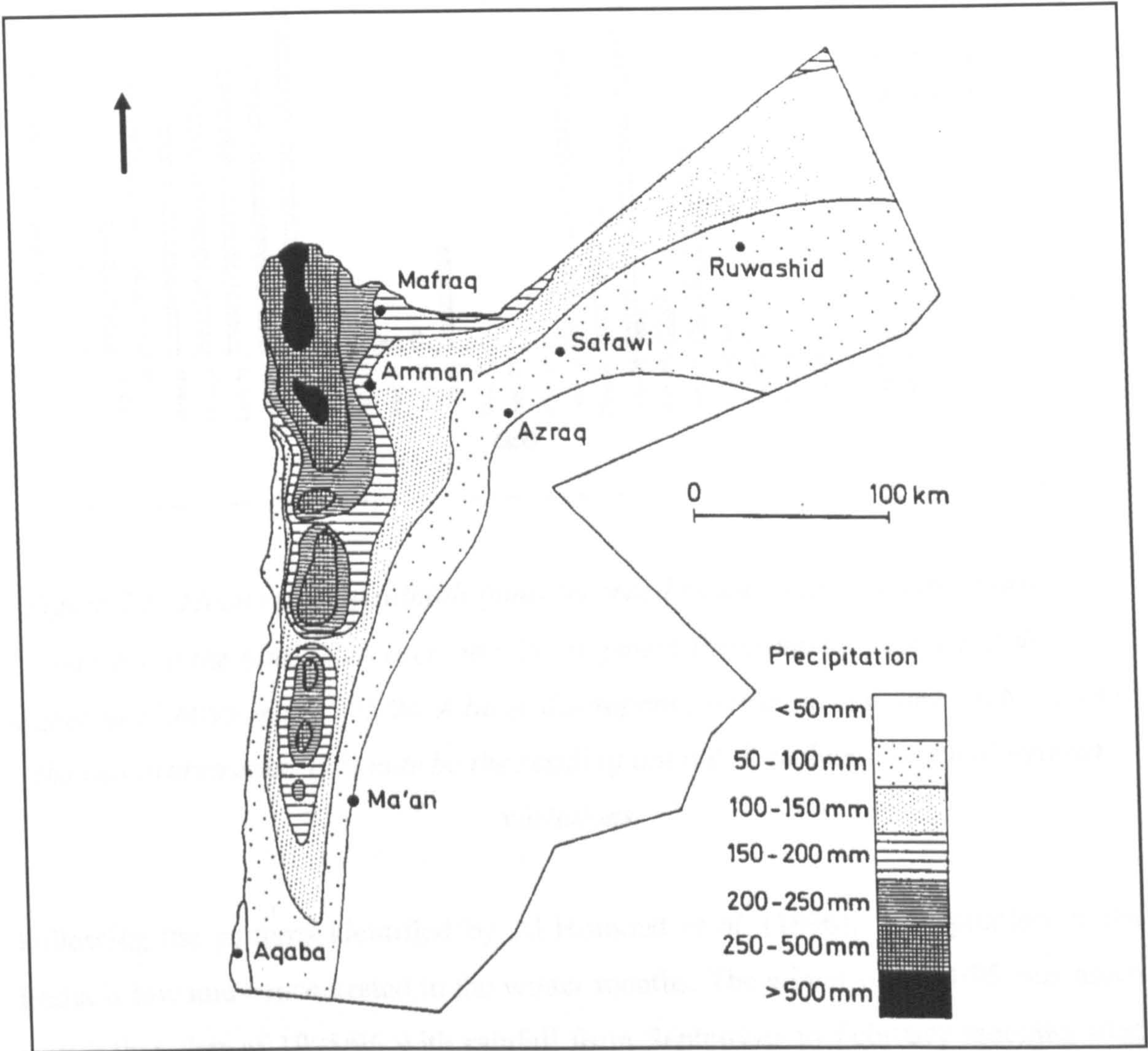


Figure 2.5: Precipitation distribution in Jordan (source: Al-Fataftah 1991) . In the Badia region around Safawi, rainfall is low (50-150 mm yr<sup>-1</sup>). By contrast, rainfall in the Jordan Valley to the west is much higher (reaching over 500 mm yr<sup>-1</sup>)

Figure 2.6 indicates rainfall in the Badia over a two year period. The measurements recorded by the AWS at *Salma* are shown alongside those recorded at another weather station situated further to the west at Lower Farm, Menara (32.2 N, 36.75 E). This was set up in conjunction with another project conducted by Kirk (1998) at the University of Durham and was in operation from August 1994 to the summer of 1996.



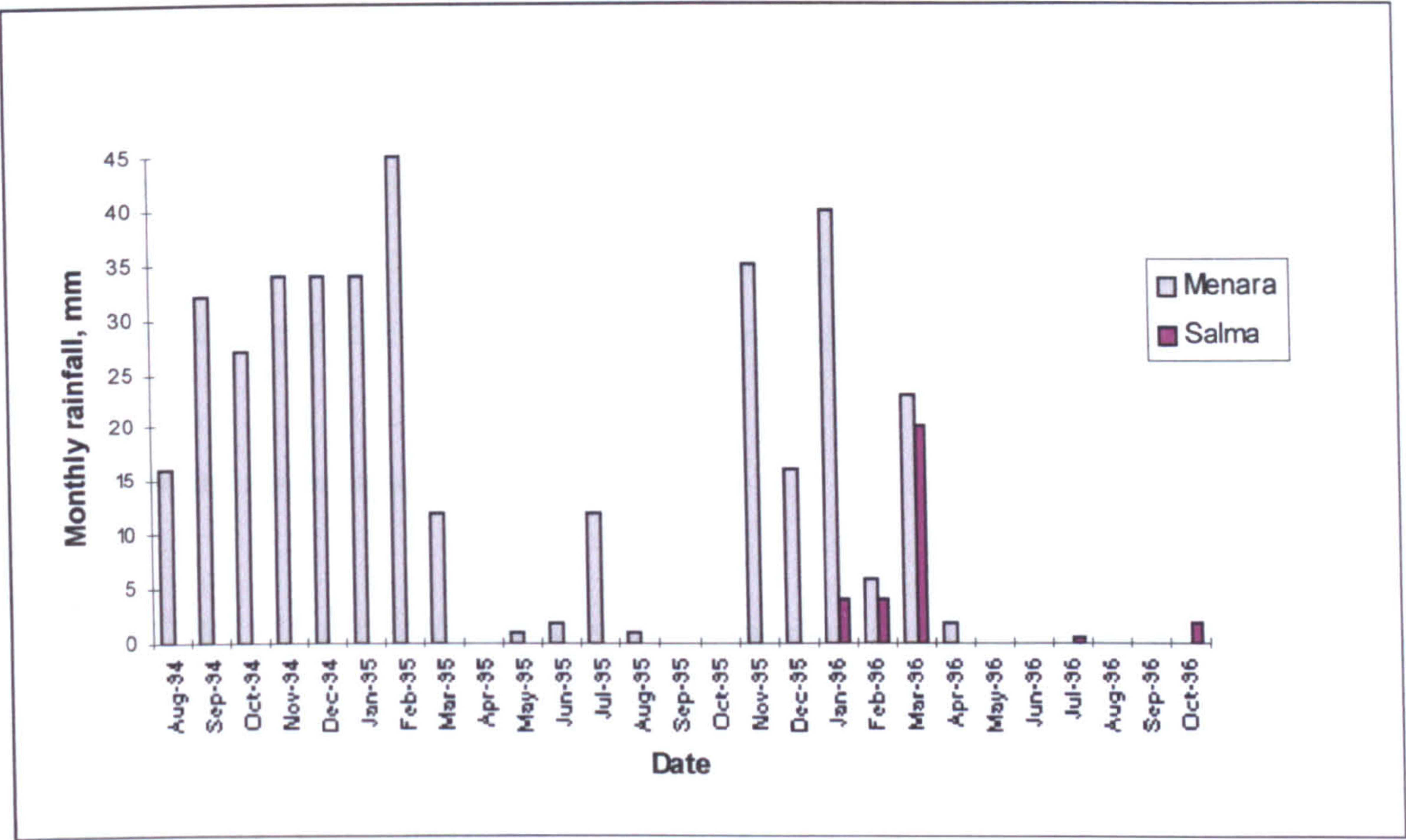


Figure 2.6: Mean monthly rainfall (mm) recorded by automatic weather stations at two sites in the Badia Research and Development Programme Area. Rainfall was higher in 1994/95 than 1995/96. A large discrepancy occurs in January 1996 between the two instruments. This may be the result of animal disturbance or local weather variations.

Following the patterns identified by Al-Homoud *et al.* (1996), precipitation in the Badia is low and concentrated in the winter months. The winter of 1994/95 was much wetter than that of 1995/96 with rainfall from September to February reaching over 200 mm compared to just 100 mm in 1995/96. For the period of concurrent data collection, the rainfall recorded at *Salma* matches in part that at *Menara*. Discrepancies could arise from the fact that the weather station at *Menara* is further to the west and at a greater elevation than the AWS at *Salma* such that rainfall will increase due to orographic influences. Furthermore, the AWS at *Salma* measures in 0.5 mm intervals. Rainfall events of less than 0.5 mm precipitation will not be recorded.

The pattern of annual rainfall can be explained with reference to the climatic oscillations outlined in Chapter 1. The pattern, frequency and intensity of rainfall events will effect the spatial and temporal distribution of vegetation. The results



indicate that rain fell in the winter months of 1995/96, and one would therefore expect vegetation cover to increase during the months immediately after rainfall, and then wilt and senesce in the drought months during the summer. Unfortunately, rainfall data were not collected during the following winter, 1996/97 and so one cannot examine the response of the vegetation to rain data during this time.

### **2.7.2 Wind speed and direction**

Al-Homoud *et al.* (1996) identify two dominant wind directions in the Badia. In the summer, north-west winds dominate due to the influence of the Indian Monsoon and seasonal troughs in the north of the country. In the winter, depressions moving along the eastern Mediterranean cause a change in wind direction to west/south-west.

Figure 2.7 shows diurnal wind direction as recorded by the AWS for the months of January, March, July and October. In all four months wind direction changes as air temperatures rise during the day. In January, dominant winds after 18:00 hours are southerly, whilst in July, they are north/north-westerly. These conform to the mean wind directions across Jordan reported by Al-Homoud *et al.* (1996) but, in general, the patterns are less obvious since they are affected by local factors and variations.



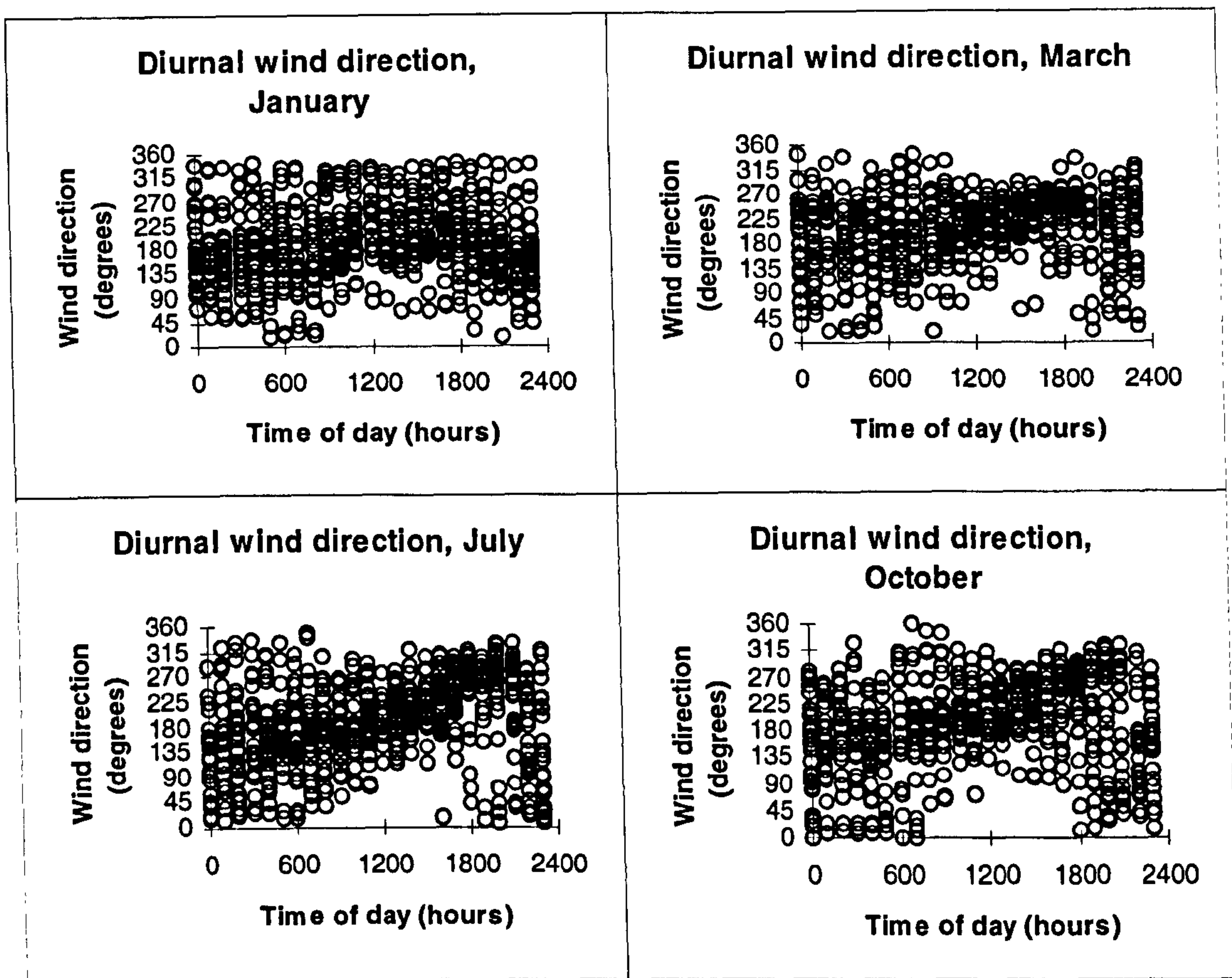


*Figure 2.7: Wind direction as recorded by the automatic weather station at Salma. Dominant wind direction after 1800 is southerly in January, and north/north-westerly in July.*

In terms of wind speed, the strongest windspeeds recorded come from the west at speeds of  $7.7 \text{ ms}^{-1}$ .

### 2.7.3 Soil and air temperature

Soil and air temperatures are important affecting microbiological activity, organic matter cycling and nutrient availability and water loss from evaporation and transpiration (Ball, 1986). Figure 2.8 shows variations in soil and air temperature as recorded by the AWS over the measurement period. As the graph indicates, soil and air temperature are highly correlated with temperatures which are at a minimum in the winter months and a maximum in the summer months. The maximum recorded air temperature was  $42.35^\circ\text{C}$  in July 1996 whilst the minimum was  $-2.47^\circ\text{C}$  in February



1996. These temperatures compare well with those reported by other authors. Al-Eisawi and Hatough (1987) present a minimum annual temperature of  $-9^{\circ}\text{C}$  and a maximum annual temperature of  $47^{\circ}\text{C}$  for the Shaumari nature reserve near Azraq whilst, Al-Homoud *et al.* (1996) comment that temperatures in the Badia can exceed  $46^{\circ}\text{C}$  and dip as low as  $-12^{\circ}\text{C}$ . The relationships of soil and air temperatures match those found by Taimeh (1985) conducting a similar study at Irbid and Rabba further to the west.

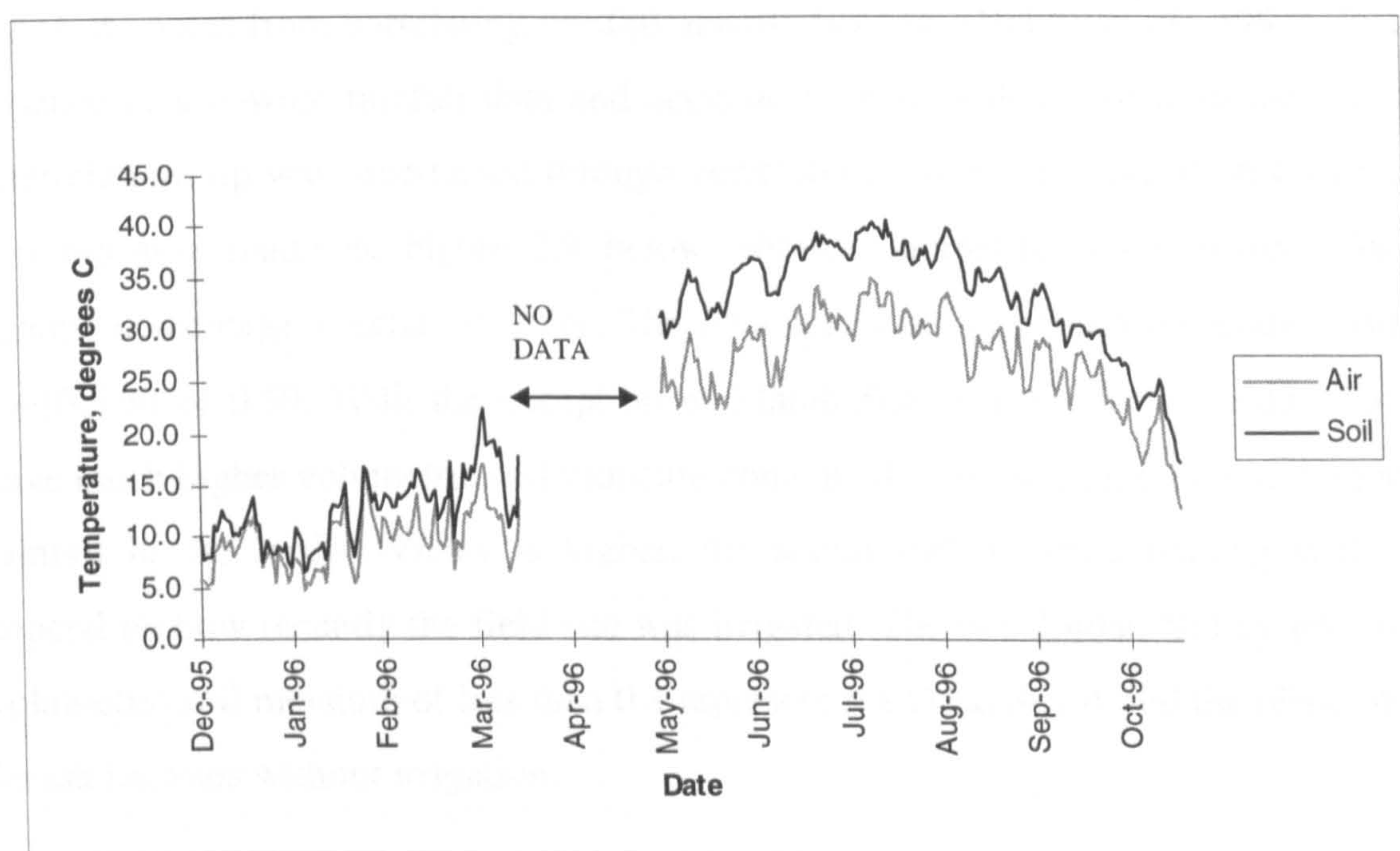


*Figure 2.8: Monthly variations in maximum soil and air temperature as recorded by the automatic weather station at Salma. Temperatures reach their maximum in the summer months (July and August) and show minimum values in January.*

With reference to Figure 2.8 it is clear that the differences between soil and air temperatures are more extreme when temperatures are hotter in the summer months than when they are colder in the winter months.

## 2.8 The relationship between vegetation, soil moisture and precipitation

In warm arid regions, the overwhelming factor determining plant growth is the availability of water (Le Houerou, 1984). The relationship between precipitation, soil



moisture and herbage production however is not a simple one and is interlinked with many other factors (Hobbs *et al.*, 1994). In arid environments high temperatures and sparsely vegetated landscapes lead to high soil surface evaporation rates. Plant productivity will depend on the moisture storage characteristics of the soil and whether water can seep down to enter soil water reserves and the plant root system before being evaporated and lost.

There are many models of soil moisture balance and herbage production but one of the simplest comes from correlating rainfall against biomass (Hobbs *et al.*, 1994). In the absence of site-wide rainfall data and accurate biomass calculations, an idea of the interrelationship was ascertained through correlating percentage vegetation cover and soil moisture readings. Figure 2.9 below, shows volumetric soil moisture plotted against percentage vegetation cover. The parameters are positively correlated with a coefficient of 0.69. With the exception of Marab *Salma*, sites in the Jordan Valley have much higher volumetric soil moisture contents than those in the Badia. Although rainfall in the Jordan Valley is higher, the actual soil moisture reading will also depend on how recently the field site was irrigated. The two Jordan Valley sites with volumetric soil moisture of less than 0.1 represent the Dead Sea A and the olive site at Jerash i.e. sites without irrigation.



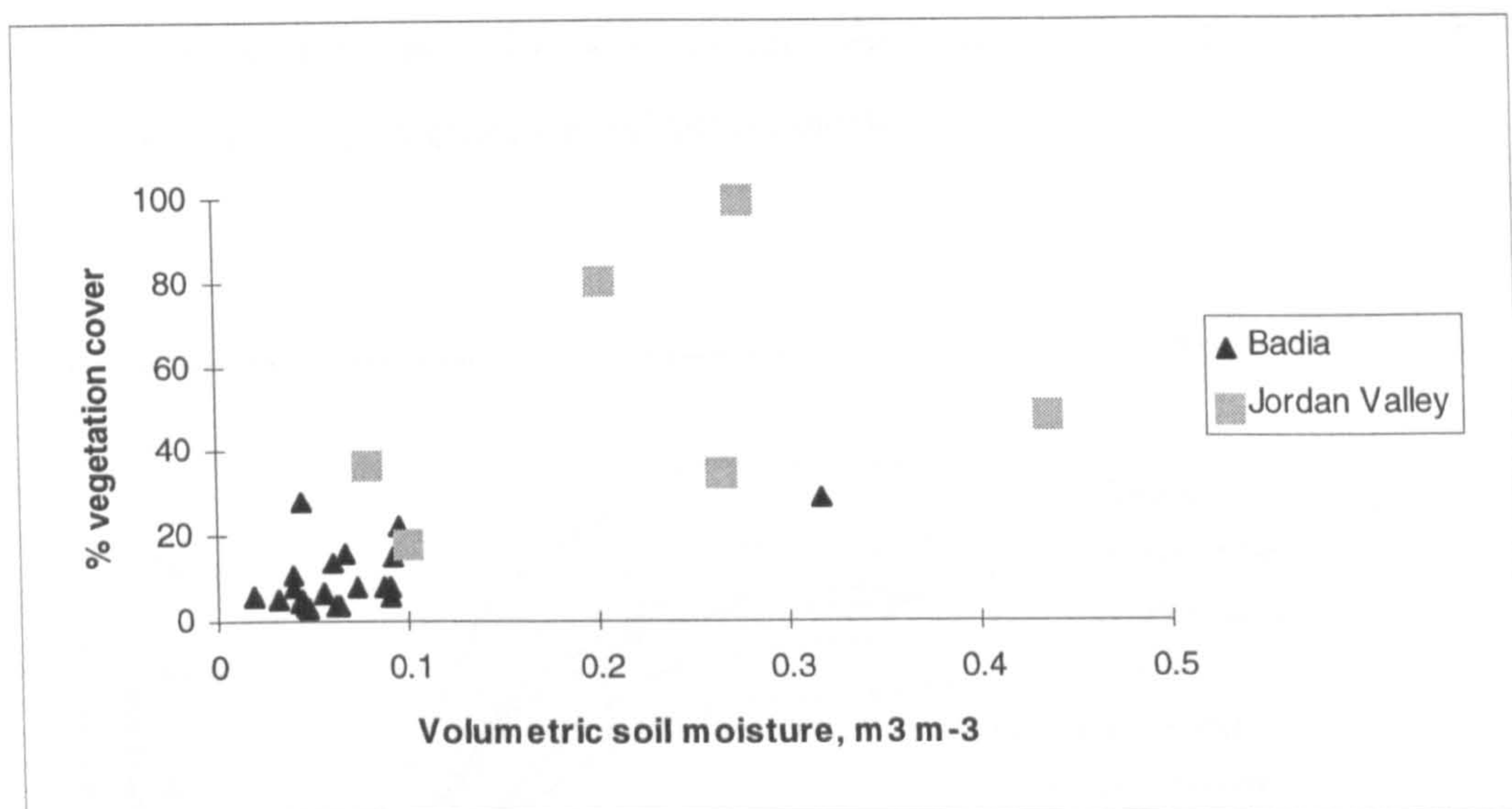


Figure 2.9: Relationship between soil moisture and percentage vegetation cover at field sites in the Badia and the Jordan Valley. When sites from the Jordan Valley are included, a positive relationship can be seen. When only sites in the Badia are considered, any relationship is much less obvious.

## 2.9 The relationship between ground radiometry, vegetation and soil

Figure 2.10 shows the spectral signatures of soil as collected by the ASD in the spring of 1996. The data for the sites at *Buqayawiyya* and *Azraq hammada* are missing from the plot since the weather, instrument failure and time constraints meant they could not be visited with the ASD.

The reflectance of a soil varies depending on a number of factors such as mineralogy and texture, the presence or absence of a thin humus layer and precipitated salts such as calcium carbonate on the surface (Ringrose *et al.*, 1989). From the samples made it appears *Feidat ed Dihikiya* has the soil with the highest reflectance in all wavebands. With reference to Table 2.6, this is a light coloured soil with a high clay content. Conversely, the soil with the lowest reflectance is that at *Wassad*, a dull coloured soil with a high sand content but a low clay content. A Pearson's product moment correlation coefficient between reflectance at 1000 nm (as an example) and percentage clay for all soils listed in Table 2.6 is high at 0.84 supporting the argument that soil



reflectance is dictated in part by soil texture. As one might expect black basalt boulders, B1, show low reflectance in all wavelengths.

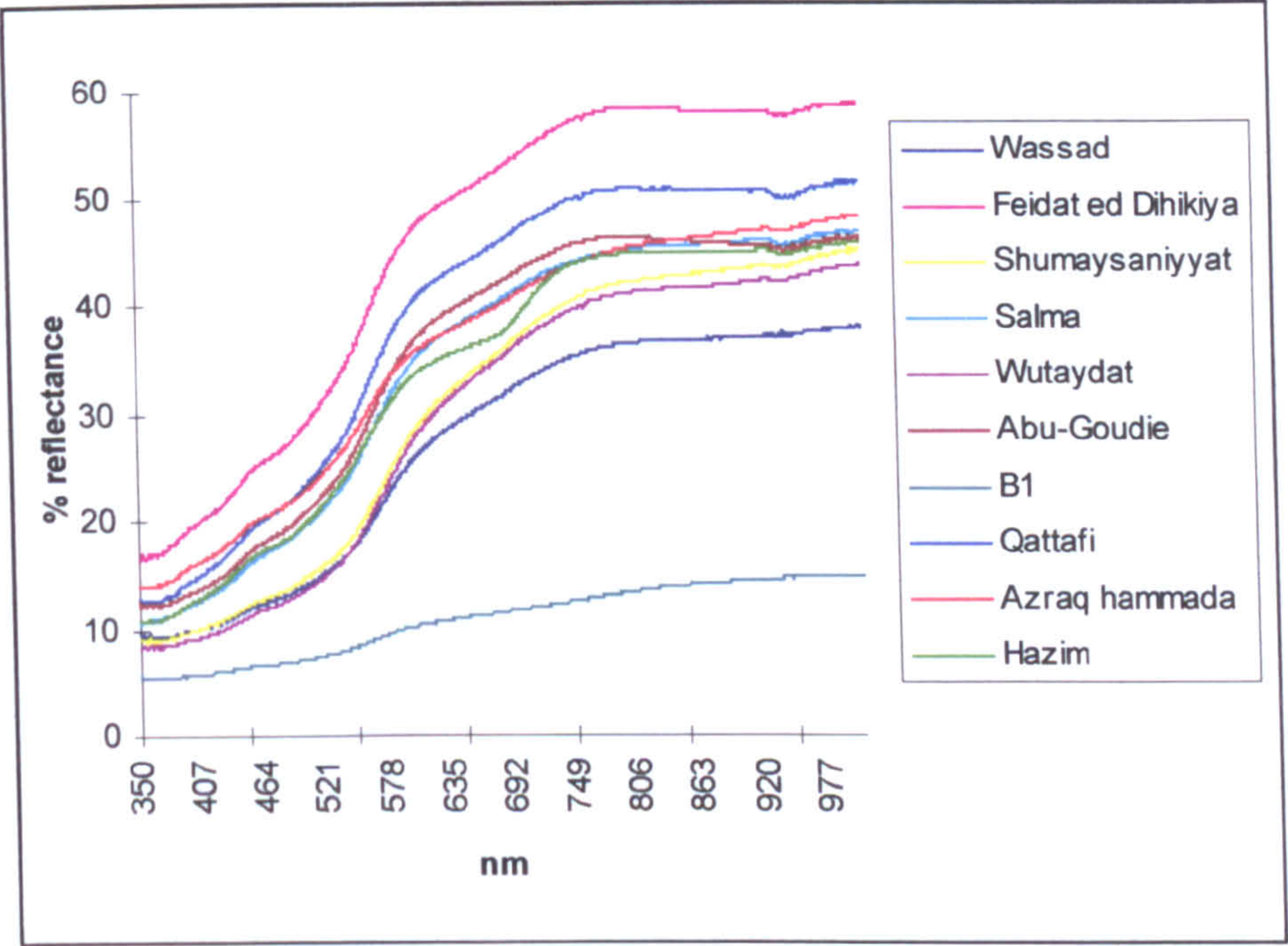


Figure 2.10: Spectral signature of soils in the Badia, measured using the ASD in the spring 1996 (nadir viewing). Soils vary in their spectral response. Feidat ed Dihikiya has the brightest soil whilst the basalt surface show the lowest reflectances.

Figure 2.11 shows the spectral signature of soils in the Badia and the Jordan Valley area as collected by the MMR in the autumn 1997.



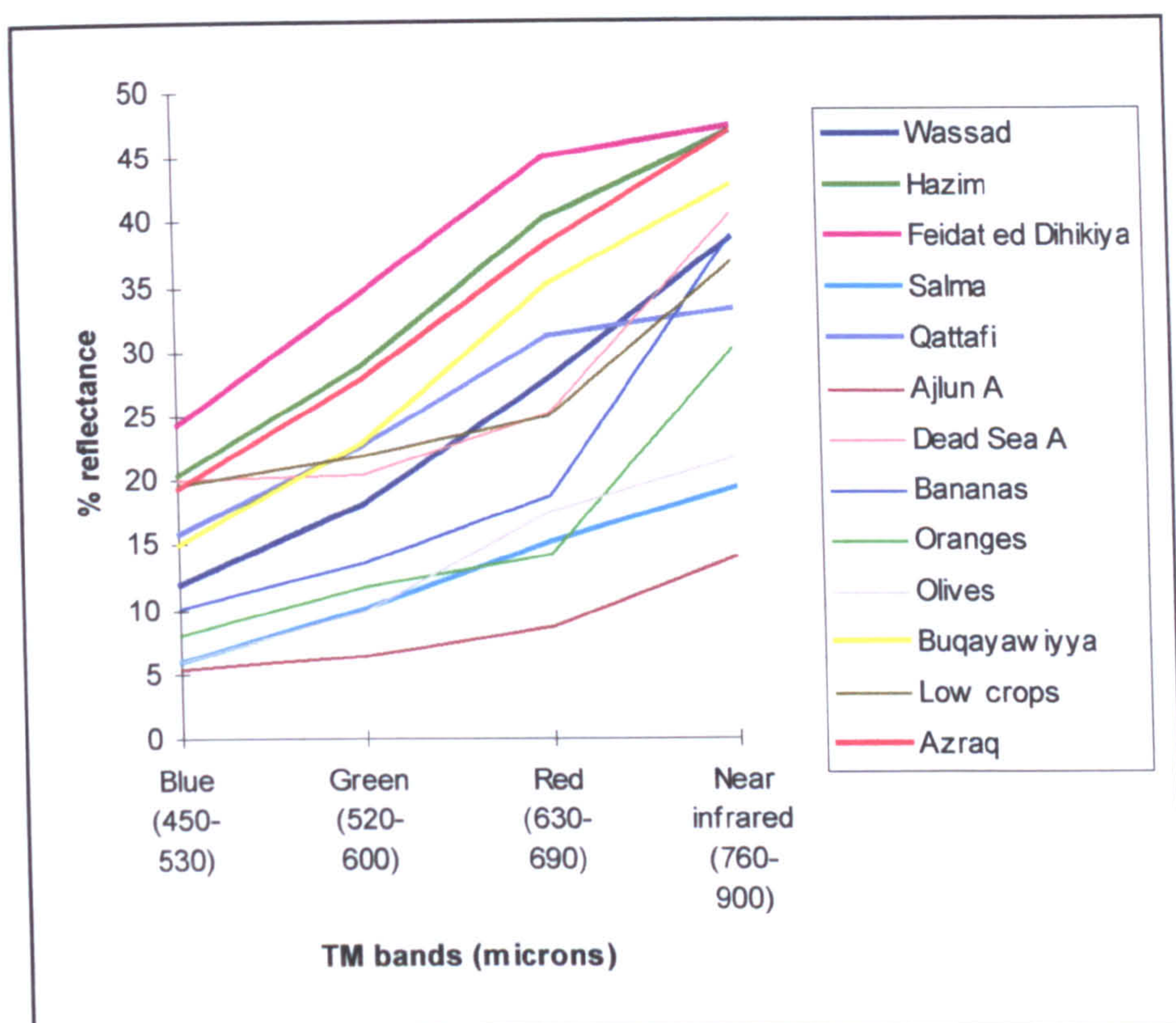
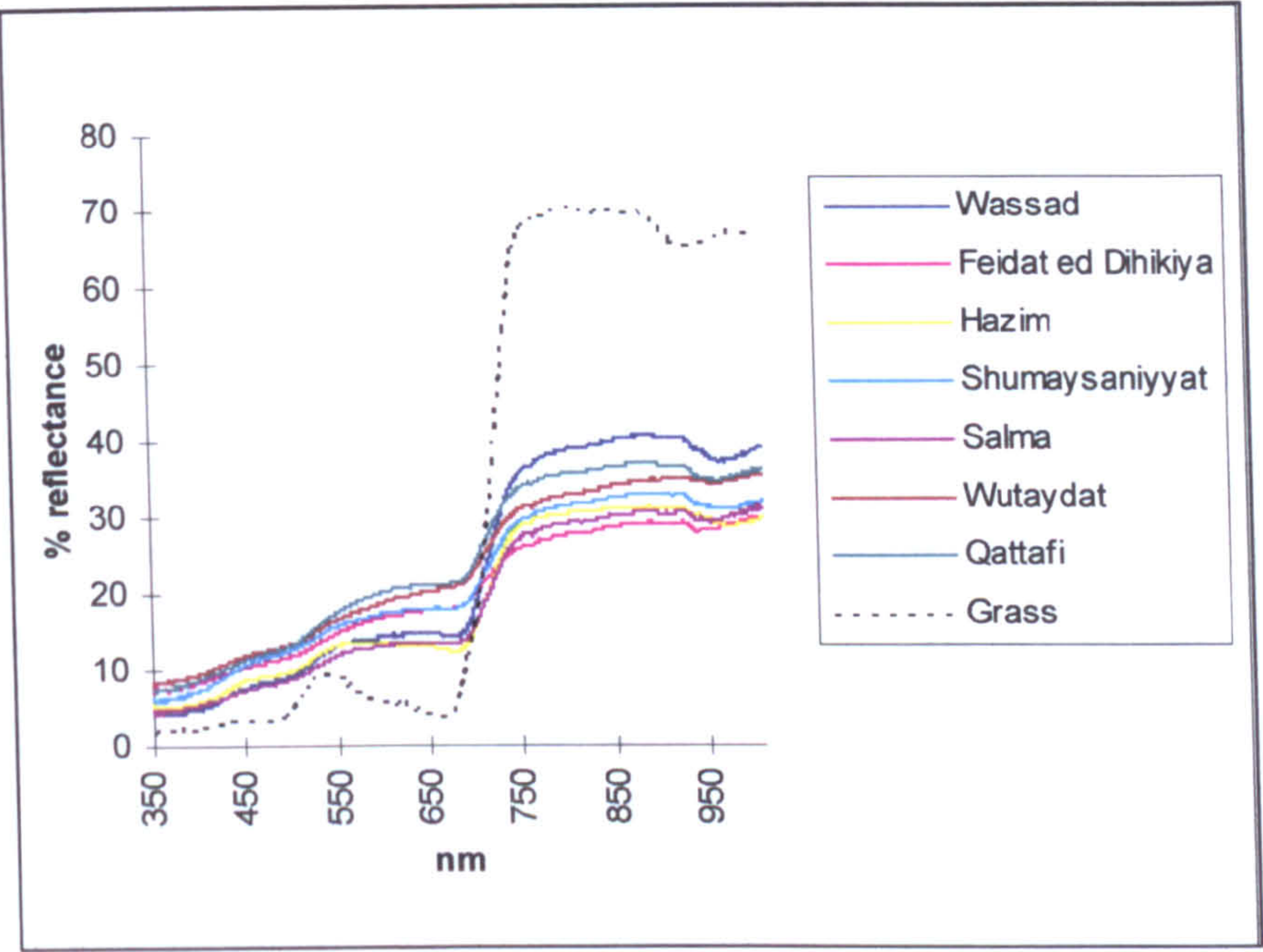


Figure 2.11: Soil reflectance in the Badia and Jordan Valley, measured using the Milton Multiband Radiometer in the autumn 1997. Reflectance of sites in the Badia appear as the thicker bold lines. With the exception of Salma, soils in the Badia have higher reflectances than those in the Jordan Valley.

Using spectral measurements from the MMR, the soil at *Feidat ed Dihikiya* again shows the highest reflectance, and with the exception of *Salma*, the lowest reflecting soil in the Badia is that at *Wassad*. The soils in the Jordan Valley and *Salma* give much lower reflectances. With reference to Table 2.6 , many of the soils in the Jordan Valley are dark in colour with a reddish tinge. The presence of a red colour suggests the presence of iron (II) and iron (III) oxides which are known to darken soils and suppress the spectral response (Ringrose *et al.*, 1989). With reference to Figure 2.4 all soils in the Jordan Valley also have high volumetric soil moisture readings. A correlation carried out between volumetric soil moisture and reflectance in the red wavelengths gave a negative coefficient of -0.67. At the surface, water will be a specular reflector, whereas water having once entered the soil darkens the surface and reduces the reflectance.



Figure 2.12 shows the spectral signatures of vegetation in the Badia compared to that of green grass. The grass signature was obtained from USGS spectral library found on the internet (reference: <http://speclab.cr.usgs.gov/browse.html>, July 1998).



*Figure 2.12: Spectral signatures of vegetation in the Badia (nadir viewing) compared to green grass from a temperate region. Vegetation in the Badia does show a red and near infrared difference but it is smaller and less well defined compared to green, photosynthetically active grass.*

For all sites measured, the spectral response of vegetation is typical of green photosynthetically active vegetation in that it shows an increase in reflectance in the near-infrared wavelengths and a ‘red-edge’. In the visible part of the spectrum (400 - 700 nm) reflectance is low as energy is absorbed by pigments in leaf chloroplasts and used in the process of photosynthesis. In the near-infrared region (700 -1300 nm) the internal structure of the leaf and spongy mesophyll tissue causes high levels of reflection and transmission (Curran, 1980, Tucker *et al.*, 1981). Vegetation at different sites varies in spectral response due to the effects of the differences in vegetation composition and structure, and the underlying soil.



Compared to green grass as found in temperate climates, however, the signatures of the Badia vegetation are very different. In the visible wavelengths the Badia vegetation generally reflects more strongly than the grass and does not show the decrease in reflection in the red wavelengths. In the near-infrared and longer wavelengths, the opposite is true. Green grass shows much higher reflectance values. These differences are attributable to a number of factors such as the influence of the background soil, leaf physiognomy and leaf water content (Wilson and Tueller, 1987).

ASD data were only collected to a maximum wavelength of 1010 nm. Dehydration of leaves causes an increase in reflectance throughout the 400-2500 nm range due to a change both in leaf internal structure and water content. Changes in leaf internal structure affect the whole wavelength range but variations due to leaf water content are most pronounced at wavelengths greater than 1300 nm where strong water absorption bands are located (Gao and Goetz, 1994, Aldakheel and Danson, 1997). Information on the spectral response of vegetation in the Badia at longer wavelengths may have helped to explain some of the patterns observed at shorter wavelengths, as well as give an indication as to how well the plant responds to drought conditions and the availability of ground water reserves.

Figure 2.13 compares the spectral response of vegetation and soil for field sites in the Badia. Seven of the plots showed were derived from ASD spectral data in Spring 1996 whilst the remaining two were constructed using data from the MMR collected in Autumn 1997. The plots highlight the constraints of using MMR data in terms of spectral resolution and signature definition. With the exception of the longer wavelengths at *Wassad*, soil at all sites shows higher reflectances than vegetation. Desert plants have the effect of darkening the surface and in many studies have been shown to have lower reflectances than the soil background (Otterman *et al.*, 1975, 1981, Wilson and Tueller, 1987, Ringrose *et al.*, 1989). Reasons for this finding include a high proportion of dead organic material combined with high soil reflectance, a high incidence of vertical shadow and low leaf vegetation cover (Ringrose and Matheson, 1987).



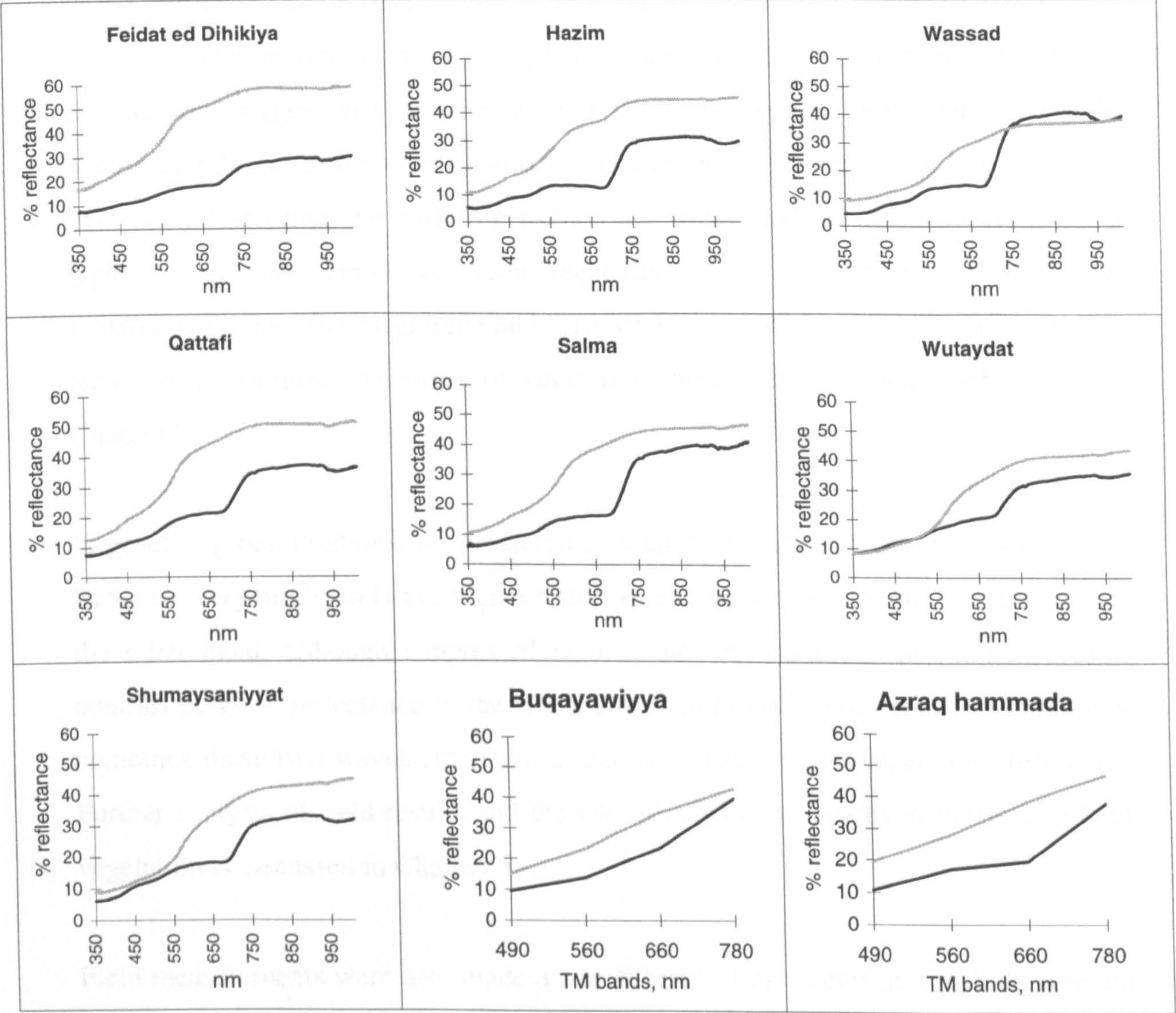


Figure 2.13: Spectral response curves for soil and vegetation for sites in the Badia



The site showing the greatest vegetation/soil contrast and the lowest 'vegetation' signal is *Feidat ed Dihikiya*. Soils are light yellow/orange in colour with a high clay content. Dominant vegetation species are *Achillea fragrantissima* and *Tamarix tetragyna*. Percentage vegetation cover information collected from this site (Table 2.4) shows that coverage between autumn 1995 and spring 1996 increased by less than 3 %. Soil moisture during the same period shows a decrease (Figure 2.4). These observations suggest that between autumn 1995 and spring 1996 there was little winter rainfall and consequent seasonal vegetation growth. Plants in spring 1996 may have been desiccated and suffering from water stress, and do not therefore show a typical 'vegetation' curve for green vegetation such as that presented at *Salma*, *Wassad* or *Hazim*. The magnitude and form of a vegetation signature is an important factor in determining the utility of vegetation indices. This is discussed further in Chapter 5.

In general, ground radiometric measurements taken at nadir indicate that soils in the Badia are very bright and have higher reflectances than the vegetation. Vegetation on the other hand, although suppressed in absolute reflectance, does show a greater contrast between reflectance in the red and near-infrared wavelengths. An index that combines these two wavebands should therefore detect a soil/vegetation difference. Further analysis of field results and the use of vegetation indices to detect arid land vegetation is discussed in Chapter 5.

Field measurements were also made using different view angles and relative azimuth angles. The results of these measurements are presented in Chapter 4 when modelling the effect of off-nadir viewing is discussed.

## **2.10 Limitations of field work**

A number of problems were encountered during field data collection, some associated with the logistics of carrying out work in Jordan and the weather, and others related to instrumentation and sampling techniques.



In terms of the vegetation survey, it was considered that the vegetation at all sites was adequately represented in terms of physiognomy, structure and composition. It would have been useful to visit sites in the Jordan Valley on all three occasions but, the value of sites in the Jordan Valley for comparative purposes only became apparent towards the latter stages of the project. Interviews with local farmers suggest that due to irrigation, the Valley is intensively farmed throughout the year with the exception of the summer months (July and August), when repairs to pumps and pipes are made. Extrapolation of percentage vegetation cover values collected in 1997 to represent conditions in 1995 and 1996 field seasons is used for analysis in Chapters 5 and 6.

Every effort was made to ensure that radiometric measurements collected over the ground represented the radiometric properties of the ground surface as accurately as possible. Unfortunately, due to the nature of the vegetation cover, measurements of background soil and vegetation had to be made individually. A radiometric estimation of a certain percentage cover could not be made. It would also have been useful to have made the radiometric readings using the ASD instrument (which has the highest spectral resolution) in all three field seasons but, due to instrument availability and technical problems, other radiometers had to be used.

In terms of the soil survey, errors in the soil moisture results could arise from the fact that measurements made by the ThetaProbe are affected by soil compressibility, air pockets round the rods, stones, roots, subsoil drainage and small scale variability in transpiration and evaporation losses (Delta-T Devices, 1995). The first two factors are particularly relevant in a desert environment where soils are often so baked that a hole has to be made using a trowel before the ThetaProbe can be inserted. This will lead to variations in readings due to air pockets rather than soil moisture differences. For this reason, average readings taken from a number of places within each field site were used to minimise this source of error.

One of the problems with the collection of meteorological data is the difficulty of correlating point measurements to areal measurements. The AWS measured atmospheric parameters at *Qa'a Salma* which can be related to parameters at the



*Marab Salma* field site but, extrapolating these observations in order to associate them with parameters at other field sites is difficult and unsubstantiated. This is especially true given the large distances between some of the field sites and the localised nature of many rainfall events. Having said that however, the ground collected meteorological data can be used to examine some of the relationships between different meteorological variables and give an indication as to whether 1995/1996 was a particularly wet year.

## **2.11 Summary and conclusions**

This chapter has described field work undertaken in Jordan. Data were collected across a number of sites on a wide range of parameters, namely the vegetation, soils, radiometric properties of the surface and meteorological conditions. Methodologies were based on standard methods or those suggested by workers in similar environments but were adapted for the Jordanian environment. The accuracy and quality of field data underpins relationships ascertained as a result of satellite imagery/field data comparisons. It is thought that the information presented here is a good data base from which to study the potential and use of ATSR-2 in the study of areas of sparse vegetation. Analysis of ATSR-2 is presented in Chapters 5 and 6. The next chapter considers the acquisition and processing of satellite imagery.



## **3.0 Satellite image acquisition and processing**

### **3.1 Introduction**

### **3.2 ATSR-2 history and specifications**

#### **3.2.1 ERS launch and payload**

#### **3.2.2 Instrument specifications**

#### **3.2.3 The dual view**

### **3.3 Image acquisition**

#### **3.3.1 Image retrieval**

#### **3.3.2 The image header**

#### **3.3.3 Calibration and error codes**

### **3.4 Image processing**

#### **3.4.1 Atmospheric correction**

##### **3.4.1.1 Limitations of the atmospheric correction procedure**

#### **3.4.2 Geometric correction**

### **3.5 NOAA AVHRR**

#### **3.5.1 History and specifications**

#### **3.5.2 Image acquisition**

#### **3.5.3 Image retrieval and processing**

##### **3.5.3.1 Atmospheric correction**

##### **3.5.3.2 Geometric correction**

### **3.6 Problems associated with the use of imagery**

#### **3.6.1 ATSR-2**

#### **3.6.2 NOAA AVHRR**

### **3.7 Summary and conclusions**



### **3.1 Introduction**

One of the main aims of this thesis was to investigate the detection and monitoring of arid land vegetation using the ATSR-2 sensor. Developing an understanding of ATSR-2 data, the acquisition of imagery and the adoption of good data processing techniques were therefore an important component in addressing this aim. This chapter describes the history and specifications of the ATSR-2 sensor and details the images acquired and the processing techniques undertaken. Attention is then turned to the characteristics of the NOAA Advanced Very High Resolution Radiometer since imagery from NOAA AVHRR were used as a comparison to ATSR-2 imagery. The NOAA AVHRR has a similar spatial and temporal resolution to the ATSR-2 and was therefore considered a good sensor to use as a comparison.

### **3.2 ATSR-2 history and specifications**

This section describes the launch history and specifications of the ATSR-2 instrument. This information was acquired through the use of the data and direct communication with the European Space Agency (ESA) and Rutherford Appleton Laboratories (RAL) in the UK. Information regarding instrument specifications and performance was mainly obtained from ESA web pages (<http://earth1.esrin.esa.it/>, July 1998).

#### **3.2.1 ERS launch and payload**

On the 17th July 1991, the European Space Agency launched ERS-1 from the Guiana Space Centre on-board an Ariane 4 rocket. Circling the Earth in a sun-synchronous orbit and with a design life-span of two years, ERS-1 carried on board a variety of instruments designed to provide measurements of sea-surface wind speed/direction, sea-surface height, wave height, sea-surface temperature, cloud-top temperature and cover, atmospheric water vapour and radar images of land, ice and ocean. These measurements were aimed at enhancing the ability of scientists to conduct environmental monitoring at global scales.



Alongside the active microwave instrument, the radar altimeter, laser retro-reflectors and precise range and range-rate equipment, was the Along Track Scanning Radiometer, ATSR. Comprising of a microwave sounder and a four band, dual view, self-calibrating infrared radiometer, ATSR was aimed specifically at oceanographic and climatological studies and provided the ability to measure cloud top temperatures, cloud cover and atmospheric water vapour content and sea surface temperatures to within  $\pm 0.5$  °K (Zavody *et al.*, 1994, Higgins, 1995).

Following the success of ERS-1, a second European Remote Sensing Satellite, ERS-2 was launched from the Guiana Space Centre on the 21st April 1995. ERS-2 was reputed to be '*the most complex satellite ever built in Europe to observe planet Earth and its environment*' (ESA web pages) and aimed to continue the work of ERS-1. Put into the same orbit as ERS-1 but displaced in phase by 24 hours, ERS-2 carried on board similar instruments to ERS-1 but included new sensors to measure ozone (GOME) and atmospheric humidity (the microwave sounder).

In terms of the Along Track Scanning Radiometer, the ATSR-2 on board ERS-2 followed similar specifications to the ATSR but was enhanced in that the number of wavebands was extended to include channels in the green, red and near-infrared parts of the electromagnetic spectrum. It was designed to facilitate land based studies and the mapping and monitoring of vegetation.



3.2.2 Instrument specifications

Table 3.1 details the general characteristics of the ATSR-2 sensor.

Table 3.1      Characteristics of the ATSR-2 sensor

Launch	21st April 1995
Orbit	near polar, sun synchronous
Altitude	777 km
Coverage cycle	6 days
Swath width	500 km
Spatial resolution	1 * 1 km at nadir
View zenith angle	nadir 55° forward
Spectral bands (µm)	0.545 - 0.565    green 0.649 - 0.669    red 0.855 - 0.875    near-infrared 1.58 - 1.64    short wave infrared 3.55 - 3.93    mir/thermal 10.4 - 11.3    thermal 11.5 - 12.5    thermal

ATSR-2 was launched on board ERS-2 on the 21st April 1995 and projected to an altitude of 777 km and a near polar sun synchronous orbit. It has a descending equatorial node crossing of 10.30 a.m. local time and a global repeat cycle of 6 days. Although the repeat cycle of ATSR-2 is 6 days, the revisit time is 35 days. A location on the Earth’s surface will be scanned once in every 6 days but, for frames to be in exactly the same orbit, an interval of 35 days is required.

ATSR-2 is a coarse spatial resolution sensor. Pixels are 1 km<sup>2</sup> at nadir extending to 3 km<sup>2</sup> at the extreme edges of the 500 km swath. Care must be taken when comparing images acquired on different dates because unless images are acquired from exactly the same orbit, differences in spatial resolution will occur for a site at the same



location on the ground. Differences in spatial resolution may mean differences in radiometric response. If the images are 35 days apart, then the same orbit is being mapped and field sites will be in the same position relative to the swath width. In the forward look, pixels are larger, 1.5 \* 2 km at the swath centre (Higgins, 1995). Regridding and resampling at RAL, maps these onto a 1 x 1 km frame. The implications this has in terms of the retrieval of radiometric properties and comparisons between forward and nadir data are discussed in Chapter 7.

The large swath and coverage cycle of 6 days means ATSR-2 is particularly well suited to temporal studies on regional or global scales. It should be ideal for examining vegetation phenologies over a large area such as the 11,210 km<sup>2</sup> of the Badia.

ATSR-2 has seven wavebands - green, red, near-infrared, shortwave infrared and three thermal channels (Table 3.1). The three channels at 3.7 µm, 11.0 µm and 12.0 µm were designed specifically for oceanographic and climatological studies, and many examples can be found of their use in sea surface temperature retrieval (Barton and Prata, 1995, Edwards *et al.*, 1990, Forrester and Challenor, 1995). The shortwave infrared or 1.6 µm channel was included for cloud detection although it has also been used for monitoring volcanic lava domes (Wooster *et al.*, 1997) and fire detection and monitoring (Perrin and Millington, 1997). It is primarily the three visible channels that are of interest in this project. ATSR-2 includes channels at 0.865 µm, 0.659 µm and 0.555 µm specifically for land based and vegetation studies (Mason and Delderfield, 1990). Channels 2 and 3 lie in the red and near-infrared regions of the spectra and correspond broadly to AVHRR channels 1 and 2 although they are narrower (see Table 1.1).



### 3.2.3 The dual view

One of the unique features of the ATSR-2 instruments is its dual view (Figure 3.1) As the satellite orbits the Earth, the detectors viewing direction sweeps out a cone in space. A scanning mirror inclined with an axis of rotation at  $23.45^\circ$  from the vertical takes measurements at a forward look angle of  $55^\circ$  from zenith and then sweeps round in a conical fashion to take a measurement at nadir. As a result of the cone being tilted forward, the along-track view is obtained within a range of  $52.7^\circ$  at the extreme edges of the swath to  $55.1^\circ$  at the sub-satellite track, and a coincident range in the nadir view of  $21.8^\circ$  to  $0^\circ$ . The two views are separated by approximately 900 km in distance.

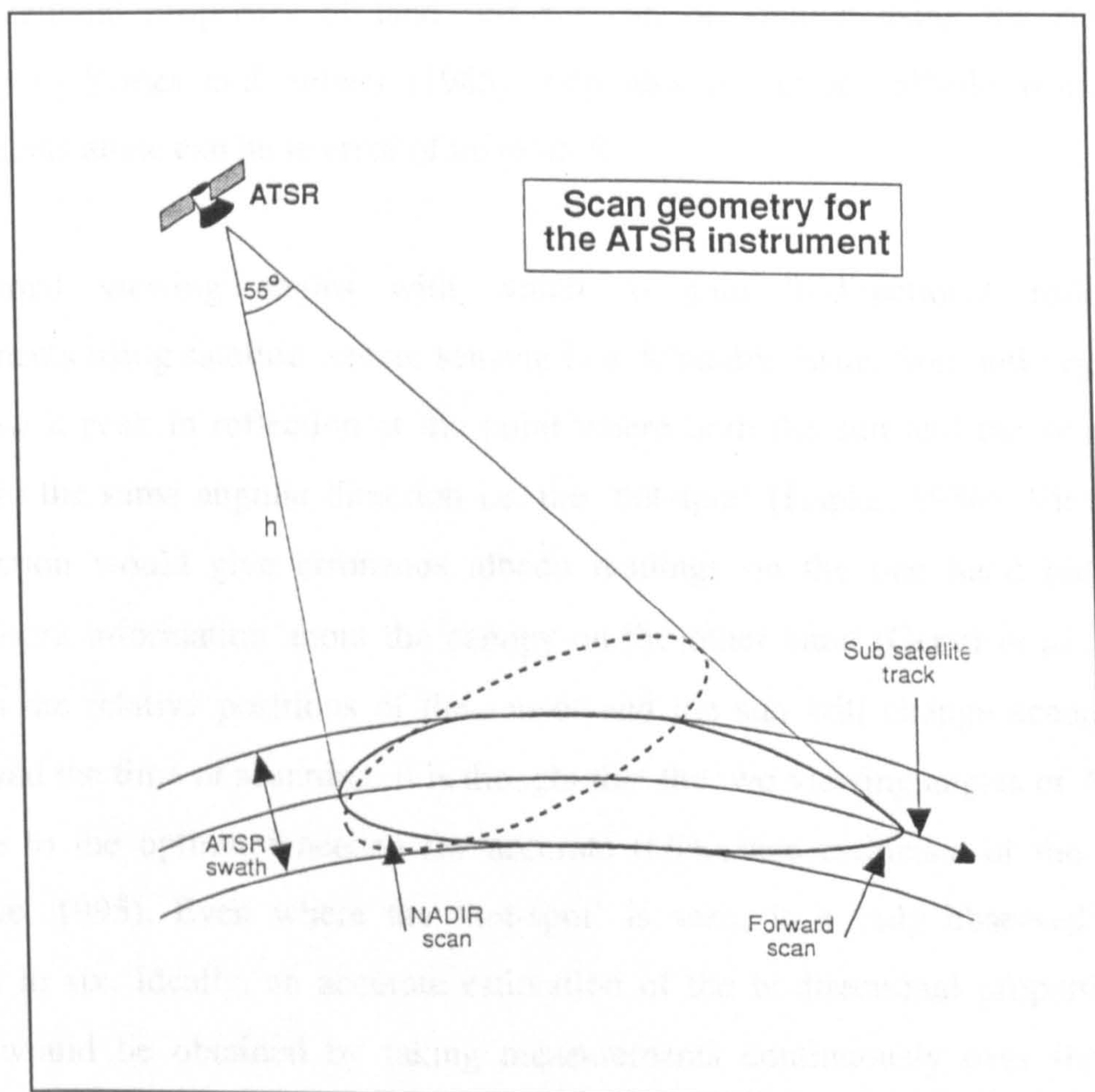


*Figure 3.1: Scan geometry for the ATSR-2 instrument. The instrument has a conical scan mechanism and takes two images, one at nadir and one at  $55^\circ$  forward.*



The primary purpose of the dual look on the ATSR was to enable the accurate determination of sea surface temperatures through calculating the effect of the atmosphere (Godslave, 1995). Viewing at nadir and at 55° means the Earth is being viewed through two different atmospheric path lengths. Assuming the atmosphere is locally horizontally stratified and stable for the two minutes it takes for both looks to be scanned, viewing through different path lengths can be compared and hence the effects of the atmosphere calculated. Mackay *et al.* (1998) describe an atmospheric correction based on the two views of ATSR-2 whilst Barton and Prata (1995) look at the implications for the determination of sea surface temperature, and comment that by using ATSR, sea surface temperature can be calculated to within half a °K.

With the addition of visible and near-infrared channels, the effects of a dual look and the bi-directional properties of land surfaces can be studied using the ATSR-2. According to Kimes and Sellers (1985), estimates of surface albedo from nadir measurements alone can be in error of up to 45 %.

The optimal viewing angles with which to gain bi-directional reflectance measurements using satellite remote sensing is a debatable issue. Soil and vegetation often show a peak in reflection at the point where both the sun and the sensor are viewing in the same angular direction i.e. the 'hot-spot' (Hapke, 1986). Viewing in this direction would give erroneous albedo readings on the one hand but might provide extra information about the canopy on the other hand (Gerstl *et al.*, 1986). Although the relative positions of the sensor and the sun will change according to latitude and the time of scanning, it is thought that the two viewing angles of ATSR-2 are close to the optimum needed for accurate reflectance estimates of the surface (Godslave, 1995). Even where the 'hot-spot' is seen, it is only observed in one overpass in six. Ideally, an accurate estimation of the bi-directional properties of a surface would be obtained by taking measurements continuously over the whole measurement hemisphere using infinitesimally small angles (Gauthier *et al.*, 1991). In practise this is hard to do at the ground level and arguably impossible to do using a space-borne sensor.



One of the aims of this study was to examine the utility of the dual look in the mapping and monitoring of sparse vegetation in arid areas. The potential of the dual look of the ATSR-2 has already been investigated in a theoretical framework and in relation to tropical forests (Gemmell and Millington, 1997). This thesis builds on that work extending it to include mid-latitude desert regions where vegetation is markedly different in terms of cover, type and structure and show a different pattern of phenological development.

### **3.3 Image acquisition**

With the launch of a new satellite, ESA commits to a vast undertaking in terms of the mission management and control, information marketing, the retrieval and distribution of data, information and support to users. To help make the job easier, tasks are disseminated to various centres throughout Europe. Overall responsibility for data acquisition, product generation and the distribution of data and products lies with the Earthnet ERS Central Facility based at ESA-ESRIN in Italy. Control and functional management of ERS-1 and ERS-2 takes place at the Mission Management and Control Centre at ESA-ESOC in Germany. There are four Processing and Archiving Facilities (PAFs) located in the United Kingdom, Germany, Italy and France.

The imagery used in this study were obtained directly from ESA under a PI to K.White and A.C.Millington (UK.A02.125). The original project proposal requested monthly images spanning the time period June 1995-May 1997. Figure 3.2 shows the months for which imagery was obtained and their status in terms of cloud cover and data rate. A high data rate means all channels are present, data were collected across the full swath and full digitisation was used. These data are collected when the Wind Scatterometer on board ERS-2 is turned off. Low data rate refers to times when the Wind Scatterometer is using the X-band data capacity. The data volume is reduced as the number of detector channels and the swath width are traded off against better resolution in the remaining channels. Low data rate exists as three modes although only two modes are ever used. Mode one, 'Pixel Map 13' is used for 20 days of every



month. The infrared channels are present in the full swath but visible channels are present in only 180 km of the swath. Mode two, ‘Pixel Map 14’ occurs during the remaining 9/10 days. Infrared channels again occur in the full swath but the 550 nm channel is present in a 180 km swath and as 8 bit data in alternate pixels (Bailey, 1995, Dr Chris Mutlow, personal communication, 1998). Although high and low data rates vary in digital precision, it was considered that comparisons between them should present no problems (Dr Chris Mutlow, personal communication, 1998).

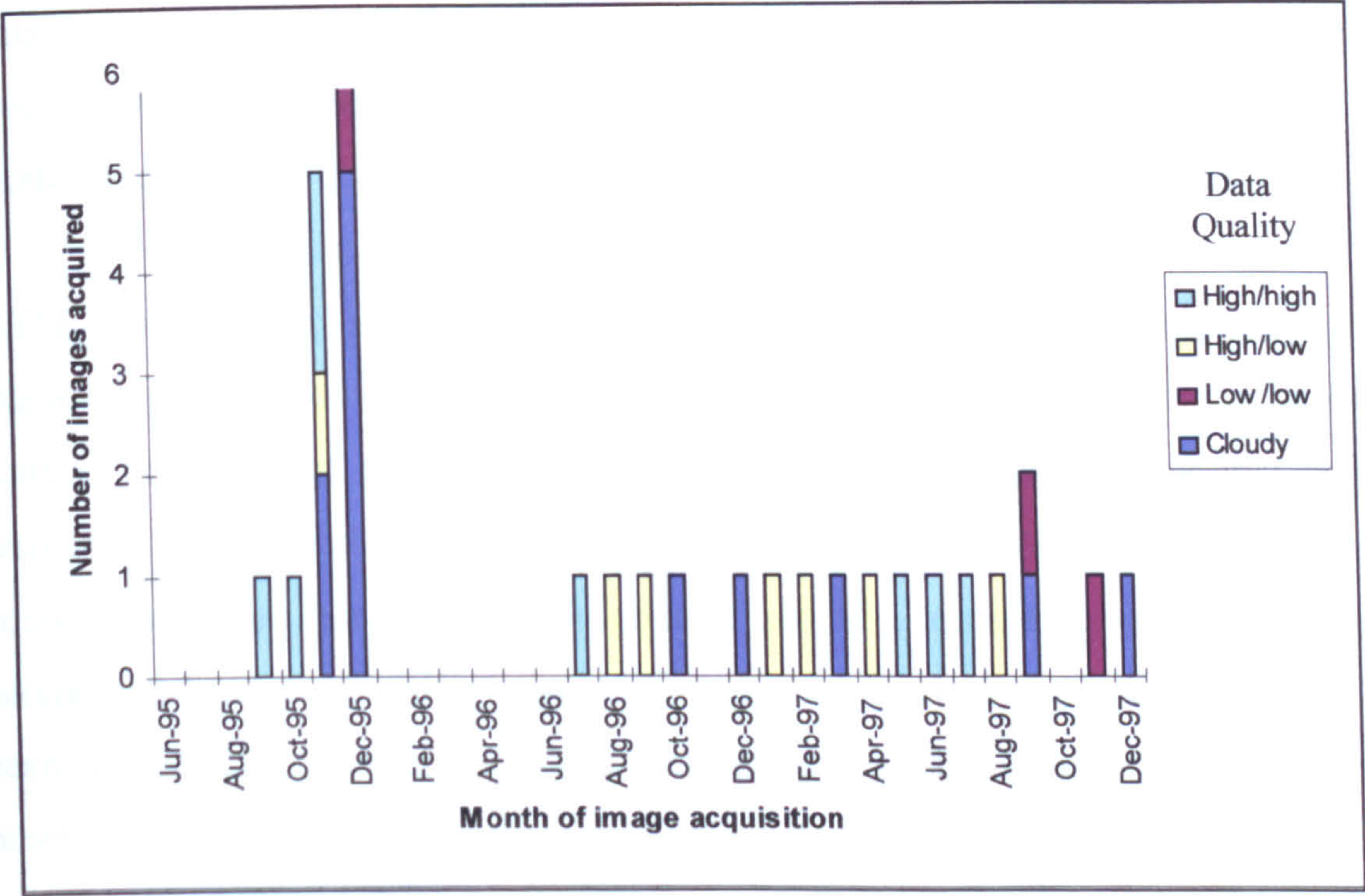


Figure 3.2: Quality of ATSR-2 images acquired in terms of data rate and the presence/absence of cloud. Only 8 of the images collected had high data rates in the nadir and forward looks (high/high).

As Figure 3.2 shows, imagery was not collected monthly for the time period specified in the original proposal. This was due to a number of reasons. Work on the project did not commence until the autumn of 1995, so images were not collected for the months of June, July and August 1995, but were collected instead for June 1995 to December 1997. This made sure a two yearly period was covered (96/97) which coincided with field work undertaken in the Jordan Valley in the autumn 1997. From January to July 1996, ATSR-2 images were unavailable. This resulted because on the 22nd December



1995, ATSR-2 was switched down to stand-by mode following problems with the scan mirror and instrument overheating. It remained switched off until 1st July 1996, when following repairs, normal operations resumed.

Figure 3.2 also shows the number of images that were cloudy. Images were designated cloudy if on visual interpretation a significant proportion of the Badia region appeared cloudy. Of 28 images collected, only 16 (57 %) were considered cloud free. Initially, images were ordered prior to their acquisition dates to coincide with periods of field data collection. Obviously at this stage it was not known if images would be cloud-free. When ESA updated their world wide web pages, images could be previewed for cloud cover. Images ordered retrospectively were viewed for cloud before ordering.

ATSR-2 imagery can be supplied in either SADIST or CEOS format and as a spatially averaged, un-gridded or gridded product (Bailey, 1995). Spatially averaged products contain imagery that has been spatially averaged to ten-arcminute or half-degree resolution. It is useful for applications covering continental or global scales where coarse resolutions are needed. Un-gridded products contain pixels in the scan geometry where nadir and forward view pixels are contemporaneous and have not been regridded or resampled. Gridded products on the other hand, contain 512 \* 512 pixel images. Forward and nadir pixels have been co-located and regridded to form pixels on a 1 km grid. Each pixel has a longitude/latitude associated with it enabling geolocation (Bailey, 1995).

For this project, ATSR-2 imagery was received in SADIST-2 format as a Gridded Brightness Temperature/reflectance product (GBT). A GBT product contains gridded, calibrated brightness temperature or reflectance images from all or some of the ATSR-2 detectors. It contrasts to GBROWSE, a gridded browse product which contains subsampled images and GSST, a Gridded Sea-Surface Temperature product containing gridded sea surface temperature images. It was decided that detailed geolocated imagery with co-located forward and nadir views would be the most useful for looking at the application of the two views to relatively distinct areas of vegetation in Jordan.



### **3.3.1 Image retrieval**

ATSR-2 imagery was received directly from ESA via File Transfer Process (FTP), or on a tape. On receiving imagery, the level 1b data were processed to convert them into a usable form. Following guidelines and sample code supplied by Rutherford Appleton Laboratories (Bailey, 1995), computer code was written to read the level 1b data and produce three files, one containing the image data, one containing the header data and one containing points in the imagery with their corresponding geolocations. The code also displayed the image, allowing visual checks for cloud. If the image appeared to contain a significant proportion of cloud over the areas of interest, it was disregarded at this stage. The code was written in Iterative Data Language (IDL) - a copy of it can be found in Appendix 2.

### **3.3.2 The Image header**

From the file supplied by ESA, the header data are read first. An example of an ATSR-2 image header can be found in Appendix 3. The header provides a wide range of information but is particularly useful in that it gives the date and time of image acquisition, (also given in the image name), and details of the illumination conditions. Solar and satellite azimuth and zenith angles are needed to run the Simulation of the Satellite Signal in the Solar Spectrum programme, '5S', for subsequent atmospheric correction (Tanré *et al.*, 1990).

### **3.3.3 Calibration and error codes**

One of the main advantages of the ATSR-2 sensor is its on-board calibration. Calibration is carried out using two stable on-board black body reference targets and the new "Viscal" system. Using an opal diffuser plate and a specially designed optical system that measures solar flux in each channel during sunset, Viscal allows the calibration of the visible channels against the sun once per orbit (Harries *et al.*, 1983).

After reading the header data, the image data were read and 'normalised count' data



converted to top-of-atmosphere fractional reflectance units by multiplying each channel by a calibration or 'Viscal' factor. These factors are calculated according to the date and time of the image acquisition and are supplied by RAL ([http://atsrw3.ag.rl.ac.uk/html/calibration\\_Table\\_html](http://atsrw3.ag.rl.ac.uk/html/calibration_Table_html), June 1996). The thermal channels are supplied as brightness temperatures and need no calibration. Following correspondence with Dr Chris Mutlow (project scientist at RAL), the 1.6  $\mu\text{m}$  channel was calibrated further by multiplying every reflectance by 1.3, and all visible reflectance channels were corrected for the sun angle by dividing by the cosine of the solar zenith.

The image data contain values from -1 to -8 which are given as error codes. These are given for the reasons outlined below (Bailey, 1995):-

- 1 Entire scan absent from telemetry
- 2 Pixel absent from telemetry
- 3 Pixel not decompressed, due to error during packet validation
- 4 No signal in channel (zero count)
- 5 Saturation in channel (maximum count)
- 6 Derived radiance outside range of calibration
- 7 Calibration parameters unavailable for pixel
- 8 Pixel unfilled (cosmetic filling algorithm unable to find nearest-neighbour pixel)

There are several ways in which to deal with error codes. They can be left as negative values, transformed into absolute values or converted to values of zero. In this instance it was decided that negative error values would be converted to values of zero. This would mean that the reasons for error would be lost, but statistical calculations could be carried out by omitting values of zero. Converting the values to their absolute equivalent may lead to confusion between erroneous pixels and pixels with low reflectance values.

Having used IDL code to separate the header data and image data, the image data were imported into ERDAS IMAGINE. ERDAS IMAGINE is the software application in which all further processing and data retrieval took place. The images were imported



as a band sequential, 512 \* 512 pixel generic binary file with 14 bands (7 nadir, 7 forward).

### 3.4 Image processing

Having imported each ATSR-2 image into ERDAS IMAGINE, they were subset in order that they just covered Jordan - the Badia, the Jordan Valley and the Dead Sea. The 512 km \* 512 km ATSR-2 scenes also covered large areas of Syria in the north, Iraq in the east and Saudi Arabia to the south, but since Jordan is the area of interest and geo-rectification information was unavailable for other countries, these were excluded at an early stage. Images were then subjected to atmospheric correction to reduce the effects of the atmosphere and allow image-to-image comparisons.

#### 3.4.1 Atmospheric correction

Cracknell and Hayes (1993) define the radiance  $L(\lambda)$  received by a sensor in a spectral channel with wavelength  $\lambda$  as:-

$$L(\lambda) = \{L_w(\lambda) + L_g(\lambda)\}T(\lambda) + L_p^A(\lambda) + L_p^R(\lambda) \quad (3.1)$$

where

$L_w(\lambda)$  = target leaving radiance

$L_g(\lambda) = L_s(\lambda) + L_d(\lambda)$  with

$L_s(\lambda)$  = sun glitter radiance

$L_d(\lambda)$  = diffused sky glitter radiance

$T(\lambda)$  = proper transmittance i.e. transmittance from target area to the sensor

$L_p^A(\lambda)$  = aerosol path radiance

$L_p^R(\lambda)$  = Rayleigh (molecular) scattering path radiance

Due to the effects of the atmosphere, only a fraction of the radiation received at the



sensor actually originates from the target. Processes of sun and sky glitter, atmospheric scattering and absorption mean that some of the radiation leaving the ground does not reach the sensor, and conversely, some of the radiation arriving at the sensor has had no contact with the target being scanned.

The multi-faceted nature of the problem is captured by Wellens (1993) who comments that the satellite received radiation can be considered to be a combination of five effects:-

- (i) direct solar radiation which has undergone only transmission by the atmosphere and is reflected by the ground towards the sensor
- (ii) diffuse solar radiation which is scattered within the atmosphere and reaches the sensor without having interacted with the Earth's surface
- (iii) diffuse solar radiation which is scattered by the atmosphere towards the ground and is then reflected to the sensor
- (iv) solar radiation which is reflected by the ground, but which then undergoes scattering within the atmosphere and reaches the sensor in the form of diffuse radiation
- (v) solar radiation which is scattered by a combination of (ii), (iii), and (iv).

The information about the target is given by (i) direct solar radiation from the ground but in order to ascertain what this is, the other processes (ii-v) must be recognised and accounted for.

Gaseous absorption and scattering by molecules and aerosols are the two main atmospheric processes affecting radiation. The effect of absorption by aerosols is usually minimal, and satellite channels tend to avoid the wavelengths at which oxygen ( $O_2$ ), carbon dioxide ( $CO_2$ ), ozone ( $O_3$ ) and water vapour ( $H_2O$ ), the main absorption gases, operate. This is true of ATSR-2. Scattering is more of a problem. Rayleigh and Mie scattering occur depending on the wavelength of the radiation and the presence of gas molecules, aerosols and particles such as dust. These scattering mechanisms have a significant effect, and vary in magnitude spatially and temporally.



Variations in atmospheric conditions both spatially and temporally mean that in order to compare surface conditions in time and space, an atmospheric correction must be applied to satellite imagery. As the atmosphere affects different wavelengths to different degrees, atmospheric corrections must be made on a band by band basis. It is often restricted to the visible and near-infrared wavelengths as these are the wavelengths which are affected most. The total contribution made by the atmosphere to radiance received at optical wavelengths has been estimated as over 50 %, maybe even approaching 80-90 % (Cracknell and Hayes, 1993). No matter which figures are used, it is a significant proportion that should be accounted for through the application of atmospheric correction routines.

Having established the need for atmospheric correction, one must decide which methodology to adopt. Several authors have developed atmospheric correction algorithms (Singh and Cracknell, 1986, Tanré *et al.*, 1990, Teillet and Fodosejevs, 1995, Vermote *et al.*, 1997, Mackay *et al.*, 1998). In this instance it was decided that the methodology proposed by Mackay and Millington (1997a) would be adopted for all images. Dr George Mackay was part of the research team at Leicester University and the work on the formulation of the atmospheric correction routine was carried out during the 1995 and 1996 field seasons. The atmospheric correction procedure was developed with the use of ATSR-2 images and within the context of the Badia environment. An overview of the method is described here. More detail and a description of the code can be found in Mackay *et al.* (1998).

Simulation of the Satellite Signal in the Solar Spectrum or 5S is a program developed by Tanré *et al.* (1990) to predict atmospheric reflectance and transmittance along the atmospheric path, given certain atmospheric parameters (i.e. the atmospheric conditions at the time of image acquisition). In order to run it and retrieve coefficients to successfully invert 5S and thus transform top-of-the-atmosphere reflectances to ground reflectances, certain parameters are needed as inputs. These are:-

- a) Illumination conditions - the solar zenith and azimuth and the view zenith and azimuth. These are usually given in image header files.
- b) A standard model for global conditions - either tropical, mid-latitude summer, mid-



latitude winter, sub-arctic summer or sub-arctic winter.

c) A standard aerosol model - either continental, urban, maritime or a user defined model.

d) Aerosol concentration in terms of visibility or aerosol optical depth at a reference wavelength of 550 nm,  $\tau^A(550)$

The standard models define the atmospheric profiles of pressure, temperature, water vapour and ozone. They estimate the amount of gaseous absorption and Rayleigh and aerosol scattering and reduce the number of variables that need to be calculated and input by the user. The factor which must be determined independently is the aerosol optical depth (AOD). This is a difficult parameter to measure because of the significant spatial and temporal variability of tropospheric aerosols and the lack of suitable information from meteorological sources (Teillet and Fedosejevs, 1995). Different methods have been used to estimate aerosol optical depth. A rough correction can be implied using standard aerosol climatology with latitudinal, longitudinal and seasonal dependences. Variables that show high correlations with aerosol optical depth can be measured at meteorological stations, ground-based measurements can be taken, or estimates can be taken directly from satellite imagery (Teillet and Fedosejevs, 1995). In the method adopted here, Mackay *et al.* (1998) use the directional data provided in the ATSR-2 spectral channels in conjunction with the 5S to estimate aerosol optical depth. 5S is then inverted to retrieve surface reflectances from those given at the top of the atmosphere.

Mackay *et al.* (1998) use 5S to simulate the top-of-atmosphere reflectances for each channel of the ATSR-2 in the forward and the nadir direction, given surface spectral reflectances. They do this repeatedly altering the aerosol concentration each time from  $\tau_1^A(550) = 0.1$  for a clear atmosphere to  $\tau_1^A(550) = 0.7$  for a turbid atmosphere. A 'shape factor', a ratio of forward to nadir reflectances, for each band is calculated, and compared between wavebands. The aerosol optical depth for the atmosphere is taken to occur where these ratios are approximately equal. For non-vegetated surfaces, this occurs for ATSR-2 channels 0.555 $\mu\text{m}$  and 0.659 $\mu\text{m}$ , whilst for vegetated surfaces, ratios are approximately equal between channels 0.555  $\mu\text{m}$  and 1.6  $\mu\text{m}$ .



Having calculated aerosol optical depth, 5S is used again to compute surface reflectances from top-of-atmosphere reflectances. Transformation coefficients  $A(\lambda)$  and  $B(\lambda)$  are defined:-

$$A(\lambda) = \frac{1}{T_g(\lambda_i, \theta_s, \theta_v) T(\lambda_i, \theta_s) T(\lambda_i, \theta_v)} \quad (3.2)$$

$$B(\lambda) = -\frac{\rho_a(\lambda_i, \theta_s, \theta_v, \phi)}{T(\lambda_i, \theta_s) T(\lambda_i, \theta_v)} \quad (3.3)$$

where

$\lambda_i$  = wavelength

$\theta_s$  = Solar zenith angle

$\theta_v$  = View zenith angle

$\phi$  = Phase angle

$T_g(\lambda_i, \theta_s, \theta_v)$  = the total gaseous transmittance associated with absorption along the sun-target-sensor atmospheric path

$T(\lambda_i, \theta_s)$  = the atmospheric scattering transmittances along the sun-target atmospheric path

$T(\lambda_i, \theta_v)$  = the atmospheric scattering transmittances along the target-sensor atmospheric path

$\rho_a(\lambda_i, \theta_s, \theta_v, \phi)$  = the atmospheric reflectance

Together with the spherical albedo,  $S$ , coefficients  $A$  and  $B$  are given by the 5S code adapted by Mackay and Millington (1997a).

The surface reflectance is then obtained using:-

$$Y(\lambda) = A(\lambda_i) \rho^*(\lambda_i) + B(\lambda_i) \quad (3.4)$$



$$\rho^*(\lambda_i) = \frac{Y(\lambda_i)}{[1 + S(\lambda_i)Y(\lambda_i)]} \quad (3.5)$$

where  $A(\lambda)$  and  $B(\lambda)$  are the transformation coefficients,  $\rho^*(\lambda_i)$  is the apparent reflectance and  $S(\lambda_i)$  is the atmospheric spherical albedo.

Mackay and Millington (1997a, 1997b) describe field experiments where aerosol optical depth was calculated directly from atmospheric field measurements taken in the study area using a LI-COR LI-1800 spectroradiometer mounted with a cosine receptor. These measurements were used to validate the method of atmospheric correction described above. Retrieved aerosol optical thicknesses, referenced at 550 nm, agreed to within 0.05 of contemporaneous ground-based measurements, and therefore support the use of the method when ground measurements are unavailable.

For the atmospheric correction carried out in this study, field measurements of AOD were used as input to the 5S to correct images in November/December 1995 (when field measurements took place), and the method described by Mackay *et al.* (1998) was used for imagery collected at other times. The other parameters used for Jordan were a continental aerosol model and mid-latitude summer or winter (depending on the image date). Illumination and viewing zenith and azimuth angles were read from the image header. Adapted 5S code gave coefficients A, B and S, and surface reflectance was then derived by writing a model using Equations 3.4 and 3.5 in ERDAS IMAGINE.

#### 3.4.1.1 Limitations of the atmospheric correction procedure

Since the commencement of this project, information on '6S', the Second Simulation of the Satellite Signal in the Solar Spectrum has been published (Vermote *et al.*, 1997). 6S was designed to refine the field of application and accuracy of the 5S code, and the authors in their defence, list the inaccuracies of the 5S, and the improvements made in 6S to overcome the problems.



5S is limited in that the user defines standard atmospheric models. This is done in the case of the seasonal global model (mid-latitude winter, mid-latitude summer etc.) and the aerosol model (continental, maritime etc.). Standard models are good in that the user often knows very little about the atmospheric conditions over which he/she is working and therefore cannot input very specific measurements, but are disadvantageous in that atmospheric conditions are approximated. It can be argued that the conditions present at the time of image acquisition are likely to fall into one of the standard models anyway or show little deviation from it, but, without accurate information, anomalies in atmospheric conditions such as those that transpire from the events of El Nino years cannot be accounted for. The 6S offers improvements over 5S in that the number of 'standard' scenarios is increased. Models for stratospheric, desertic and aerosols resulting from biomass burning are now available but the issue of modelling and accurately representing the atmosphere remains.

The 6S also improves on the 5S in its ability to treat the surface as a non-lambertian surface. In the 5S the surface is assumed to be lambertian, whether uniform or non-uniform, the target is at sea level and the sensor is space-borne. In the case of the remote sensing of Jordan using ATSR-2, the latter two conditions are true, to some extent, but the assumption of a lambertian surface is tenuous. The 6S does provide the ability to model a non-lambertian surface but as Vermote *et al.* (1997) describe, it requires the user to know and input many detailed parameters. For detailed work using BRDF with airborne satellites it is useful, but, using ATSR-2 images where viewing and illumination conditions, surface cover and pixel size vary across the scene, its use is more difficult.

At the time of data acquisition and manipulation a complete operational version of the 6S was unavailable and the 5S was therefore used. As the same atmospheric correction procedure was applied to all images, it was considered that the code worked well to reduce atmospheric effects, and subsequent comparisons between images were valid.

A further limitation with the atmospheric method adopted here is that a single



atmospheric procedure was used and applied on an image wide basis. Ideally, atmospheric correction procedures should be carried out on a pixel by pixel basis as viewing and illumination conditions change and the atmosphere varies across the swath. In practise this is difficult to achieve. Detailed information about the aerosol optical depth and viewing and illumination conditions are not available for every pixel. The method therefore relies on the difference between the forward and nadir bands of ATSR-2, differences which by fault of the processes of resampling and regridding extend further than a simple 1 km pixel square. Initially, image analysis and modelling was restricted to the area of the Badia, where field measurements of aerosol optical depth were taken, and an assumption of fairly constant desert atmospheric conditions is likely. Extension of the work to the Jordan Valley came in the latter stages of the work. As atmospheric correction had already been performed on the data, it was decided to accept the same atmospheric correction for the Jordan Valley as for the Badia. Whilst atmospheric conditions between the two very different sites may have varied considerably, by using the same atmospheric model, the pixel values may be affected by 1 or 2 %, but this would not affect the relative comparison between the sites.

### **3.4.2 Geometric correction**

Following atmospheric correction, each image was geometrically corrected. Geometric correction is needed to accurately locate field sites and undertake image-to-image comparisons. With a gridded brightness temperature product, every pixel optionally has latitude/longitude positions associated with it. These are calculated as nadir and forward pixels are resampled and co-located with each other, and are based upon an Earth-model defined by the parameters (Bailey, 1995) :-

semi-major axis: 6378.144 km

semi-minor axis: 6356.759 km

Initially, the longitude/latitude information supplied with the data were used to provide the ground control points to geometrically correct the image but, once several images were rectified, it became apparent that there were still discrepancies between



the positions of the field sites as defined by the corrected imagery, and GPS readings collected in the field. Furthermore, in some cases pixels from the forward and nadir looks were obviously mis-co-located. Since errors in geolocation and co-location have also been reported in other work using ATSR-2 (Parkes *et al.*, 1999), it was decided to geocorrect a single ATSR-2 image using ground control points collected in the field in combination with a corrected SAR image. Image to image geo-registration was then used to register all images to this 'master' image. For each image the nadir view was corrected first, and then the forward view was registered to the nadir view. This ensured that for an individual image, nadir and forward views were both geo-located and co-located. Further discussion about the errors in ATSR-2 geo-location is given in Chapter 7 (Section 7.2.1.2).

In the Badia environment ground control points are relatively easy to identify. In many areas dark basaltic lava flows form very distinct peninsulas against bright *qa'a* surfaces. Similarly, due to lines of tectonic activity running through the area, a series of small round volcanic cones can be picked out. Other ground control points include road intersections, a reservoir used for water harvesting and the Safawi field station. For all images at least 20 ground control points were chosen. This exceeds the minimum number of six points needed to perform a second order transformation given by:-

$$n = \frac{(t + 1)(t + 2)}{2} \quad (3.6)$$

where  $n$  is the minimum number of GCP's required to perform a transform of order,  $t$ , and  $t$  is the order of the transformation. Efforts were made to locate GCP's evenly over the image and the root mean square (RMS) error for a single GCP was kept to less than one pixel i.e. a positional accuracy of less than 1 km.

Geometric rectification was performed using cubic convolution resampling. It is debatable as to which resampling method is best to use as nearest neighbour, bilinear interpolation and cubic convolution all have advantages and disadvantages. Cubic



convolution is advantageous in that it is considered that the mean and standard deviation of the output pixels represent those of the input pixels more closely than the other methods (ERDAS, 1991). It is an accurate method that sharpens the image and smoothes noise (Schowengerdt, 1983). The method does result in grey level overshoot around edges as output pixels represent the interpolated value from 16 pixels but, as pixels furthest away in the 4 \* 4 window have less influence on the pixel than those near to it, and the study areas represent large homogeneous sites, it was considered that cubic convolution was a good method to use. In the absence of a preferred Jordanian system, all images were corrected to the World Geodetic System 1984 (WGS84) projection.

Following the atmospheric and geometric correction of each ATSR-2 image, they were all in a format suitable for subsequent analysis. The derivation of vegetation indices and modelling techniques using this ATSR-2 imagery are described in Chapters 5 and 6. The remainder of this chapter considers the preparation stages carried out on the AVHRR images that were used as a comparison to the ATSR-2 imagery.

### **3.5 NOAA AVHRR**

Although this project is concerned primarily with the application of ATSR-2 data to study arid land vegetation in Jordan, ATSR-2 is very similar in spatial resolution to the NOAA AVHRR, and future chapters compare the usefulness of these two sensors for the detection and monitoring of arid land vegetation. This section considers AVHRR in a similar manner to ATSR-2. Its history and specifications, image acquisition and processing and the problems associated with its use.

Due to a long history (1978 onwards), global coverage and high temporal resolution, the NOAA series of satellites have generated a great number of biophysical studies and much work has been published demonstrating their usefulness for vegetation mapping and monitoring (for example, Tucker *et al.*, 1984, Kennedy, 1989, Malingreau *et al.*, 1989, Marsh *et al.*, 1992) . Some of the information about the



instrument comes from this body of literature whilst additional detail is given in the comprehensive NOAA Polar Orbiter Data Users Guide (1997). This is available as a hard copy directly from NOAA or can be found on the NOAA web pages (reference: <http://www.saa.noaa.gov/>, July 1998)

### **3.5.1 History and specifications**

The first satellite of the National Oceanic and Atmospheric Administration (NOAA) series was called TIROS-N and was launched in October 1978. Since then, nine additional satellites named NOAA-6 to NOAA-14 have been launched. Each one has increased the amount of data available and helped in extending the lifetime of the programme to the end of the century (NOAA Polar Orbiter Data User guide, 1997). As the satellites have slightly different specifications, calibration and orbits, it is beneficial to use data from the same satellite for a study in which information from different dates is being compared. In this case, it was decided that data from NOAA-14 would be acquired and used. NOAA-14 originally called NOAA-J was launched on 30th December 1994 and is the most recent of the NOAA series of satellites. All further reference to the AVHRR refers to the sensor on board NOAA 14.

The NOAA satellite series carries on board an Advanced Very High Resolution Radiometer (AVHRR), a TIROS operational vertical sounder with a microwave sound sounding unit, a stratospheric sounding unit and a high resolution infrared radiation sounder and a search and rescue demonstration system, an Earth radiation budget experiment and a solar backscatter ultraviolet radiometer. It is the Advanced Very High Resolution Radiometer (AVHRR) providing information in the visible, near-infrared and thermal parts of the electromagnetic spectrum which is of interest here.

The general characteristics of NOAA AVHRR are presented in Table 3.2 below:-



*Table 3.2: Characteristics of the NOAA 14 AVHRR sensor*

	<b>AVHRR</b>
<b>Orbit</b>	near polar, sun synchronous
<b>Altitude</b>	833-870 km
<b>Coverage cycle</b>	9 days
<b>Swath width</b>	2700 km
<b>Spatial resolution</b>	1.16 * 1.16 km at nadir
<b>View zenith angle</b>	$\pm 55.4^\circ$
<b>Spectral bands (<math>\mu\text{m}</math>)</b>	0.580 - 0.680 red 0.725 - 1.10 near-infrared 3.55-3.93 mir/thermal 10.3-11.3 thermal 11.5-12.5 thermal

As Table 3.2 indicates, AVHRR has five bands - red, near-infrared, middle infrared and two thermal bands. Although designed to acquire data for meteorological, oceanographic and hydrological purposes, bands in the red and near-infrared mean it is also suitable for temporal studies involving land cover and vegetation (Shimabukuro *et al.*, 1997). The Normalised Difference Vegetation Index, NDVI, that has been widely used to study vegetation using many different sensors (e.g. Landsat TM, Landsat MSS), has frequently been used with AVHRR, such that this data format is often considered the *de facto* standard.

The AVHRR has a tilting scan mirror which scans  $\pm 55.4^\circ$  from nadir and produces a swath width of 2700 km. This is very wide, and due to distortions in pixel size and increased atmospheric path lengths at the extreme edges of the swath many authors recommend that only a central section of the sub-satellite path is used. It is debatable as to how large is the 'useful' part of the swath. Different authors have recommended restricting use to data from nadir  $\pm 40^\circ$  (Brown *et al.*, 1982),  $\pm 20^\circ$  (Duggin *et al.*, 1982),  $\pm 35^\circ$  (Tucker *et al.*, 1984) and  $\pm 15^\circ$  (Ehrlich *et al.*, 1994).



One of the most useful features about NOAA AVHRR is its high temporal coverage. Whilst the repeat cycle is nine days, the large swath width means that daily global coverage is achieved. Daily coverage increases the probability of obtaining cloud-free imagery or producing cloud-free composites, and is particularly useful in the study of vegetation in drylands where phenological changes can occur very quickly following rainfall.

### **3.5.2 Image acquisition**

In terms of the NOAA AVHRR ground segment, global imagery collected daily by the satellites is transmitted to the Command and Data Acquisition (CDA) stations at Wallops Island, Virginia and Fairbanks, Alaska. From there it is relayed to the National Environmental Satellite Data and Information Service (NESDIS) in Maryland for processing, archiving and further distribution.

The imagery used in this study was ordered directly from NESDIS via their Satellite Active Archive (SAA). This can be done directly over the internet. Images are selected, previewed and ordered and can be acquired via 'ftp' - file transfer processes. This service is free providing an excellent means of obtaining data in situations where financial resources for purchasing imagery are limited (as can be the case particularly in developing countries). Images are selected by date and geographic location (entered by latitude/longitude bounding co-ordinates). The satellite number can be chosen and if known, an orbit number is put in. The data can be ordered as one of three formats, GAC, LAC or HRPT:-

**GAC:** represents Global Area Coverage data. Sub-sampling of the 1.1 km data to 4 km resolution is carried out on board the satellite by averaging along-scan groups of four pixel samples out of five and skipping every third scan line. GAC is available for the whole globe on a daily basis (Robinson, 1996).

**LAC:** represents Local Area Coverage data. These are the original data that are recorded at 1.1 km resolution. LAC are recorded and stored until a CDA station is reached and they can be downloaded.

**HRPT:** represents High Resolution Picture Transfer data. Data that are readout directly



as the satellite passes over a CDA station. Each data set is 10-12 minutes in duration and requires 3 frames per channel at 1.1 km.

For this study, LAC data were ordered. Its 1.1 km nominal resolution at nadir is comparable to the 1 km resolution of ATSR-2. Images were previewed before ordering so only cloud-free images were obtained. Images were acquired for every month of 1996 and 1997, except those months when previews revealed that all images acquired by NOAA 14 were cloudy. Preference was given to images where the Badia and Jordan Valley areas fell in, or near, the central area of the swath. A complete list of ATSR-2 and AVHRR image dates can be found in Appendix 4.

### 3.5.3 Image retrieval and processing

Having received image files directly from NOAA SAA, they were imported into ERDAS IMAGINE using the NOAA AVHRR default option. This automatically reads the header data, applies a calibration and corrects for the solar zenith angle. Channels 1 and 2 are converted into apparent reflectance whilst channels 3, 4 and 5 are converted to brightness temperature values. Further details of these calibrations can be found in the NOAA Polar Orbiter Data Users Guide (1997).

For the visible channels data values are converted in albedo firstly using calibration coefficients given in the image header:-

$$A_i = S_i C + I_i \quad (3.7)$$

where  $A$  is the percent albedo measured by channel  $i$ ,  $C$  is the input data value and  $S_i$  and  $I_i$  are the scaled slope and intercept values.

From the albedo the apparent reflectance is calculated using:-

$$\rho^* (\%) = \frac{A}{\cos \theta_d} \quad (3.8)$$



where  $p^*$  is the apparent reflectance,  $d$  is the Earth-sun distance multiplication factor and  $\theta$  is the solar zenith read from the image header.

The software is not continually updated as new coefficients are calculated for features of sensor drift and degradation, and thus the coefficients used in the ERDAS software are the pre-launch values. These may be erroneous because after calculation the instrument remains on the ground before it is put into orbit, it then undergoes extreme heat, vibration and rough conditions during launch and, finally reaches an orbit where the space conditions and environment are completely different from those previously experienced. All these processes affect the calibration (Cracknell and Busu, 1995). Although there are no on-board procedures for the calibration of channels 1 and 2 of the AVHRR, scientists at NOAA/NESDIS have studied in-orbit sensor degradation and calculated post-launch calibration coefficients. These are provided on the web on a monthly basis.

As ERDAS IMAGINE uses pre-launch coefficients and post-launch coefficients are now available, a sensitivity analysis was carried out to compare the two values. A raw AVHRR image was calibrated twice, once using pre-launch coefficients and again using post-launch coefficients. Using an image from 7th February 1997, albedo values calculated using the two methods were within 1 % of each other. On the basis of these results, it was decided that the automatic correction performed within ERDAS IMAGINE using the pre-launch calibration coefficients would be adopted

The situation for channels 3,4 and 5 is more straightforward. Calibration for these channels is carried out on-board using warm internal blackbodies. The coefficients provided are thus contemporary with the corresponding data. Channels 3, 4 and 5 are converted from DN to radiance values using:-

$$E_i = S_i C + I_i \quad (3.9)$$

where  $E_i$  is the radiance value in  $\text{mW}/(\text{m}^2\text{-sr-cm}^{-1})$ ,  $C$  is the data value and  $S_i$  and  $I_i$  are the scaled slope and intercept values. Brightness temperatures are then calculated



using the Planck's function:-

$$T(E) = \frac{C_2 \nu}{\ln \left( 1 + \frac{C_1 \nu^3}{E} \right)} \quad (3.10)$$

where T is the temperature (K) for the radiance value, E,  $\nu$  is the central wavenumber of the channel ( $\text{cm}^{-1}$ ) and  $C_1$  and  $C_2$  are constants ( $C_1 = 1.1910659 \times 10^{-5} \text{ mW}/(\text{m}^2\text{-sr-cm}^{-4})$  and  $C_2 = 1.438833 \text{ cm-K}$  ).

Once each AVHRR image had been successfully imported into IMAGINE, subsets of the study area were extracted. Typically, a 2700 km swath extends over Iraq to the East and the Mediterranean and the Nile Delta to the West. Subsets were derived in order that the image was restricted to Jordan, and included the Badia, the Jordan Valley and the Dead Sea.

### 3.5.3.1 Atmospheric Correction

The atmospheric correction for AVHRR was carried out in similar manner to ATSR-2 using the 5S to retrieve parameters a, b and s. A continental aerosol model with the appropriate mid-latitude summer or winter was used, and viewing conditions were retrieved from the image header files. As the method described by Mackay *et al.* (1998) for calculating aerosol optical depth from the two views of ATSR-2 cannot be carried out with AVHRR imagery taken of a single view only, a dark target subtraction method was adopted instead (Teillet and Fedosejevs 1995).

This method assumes that the influence of the atmosphere will be revealed by pixels which are very dark and have a surface reflectance of zero i.e. deep shade or water bodies. Aerosol optical depth is determined by running the 5S atmospheric code with different aerosol optical depth values until the lowest top-of-the-atmosphere value in the image gives a surface reflectance value of near zero (Teillet and Fedosejevs 1995). The relationship between 5S input values and output values of apparent reflectance is very linear, so the correct aerosol optical depth is quickly reached. The values needed to correct ATSR-2 imagery were used as starting points. Final values of aerosol



optical depth matched those of ATSR-2 imagery, and were of the order of 0.2. Following atmospheric correction, the images were then geocorrected.

### **3.5.3.2 Geometric correction**

The AVHRR images were geocorrected in a similar manner to the ATSR-2 images with one image acting as a 'master' image and all other images being registered to it. The master image was corrected using ground control points collected in the field. At least 20 ground control points were positioned evenly over the image with an accuracy of less than one pixel. Image resampling was carried out to WGS 84 co-ordinates.

## **3.6 Problems associated with the use of imagery**

### **3.6.1 ATSR-2**

One of the main difficulties associated with the use of the ATSR-2 imagery in this study was the acquisition of cloud-free images over a two year period. The ongoing problems with the sensor's scan mirror between January and July 1996 meant that data were not available for the period 22/12/95 to 01/07/96.

A further problem with the use of ATSR-2 data was the delay between the ordering of data and their arrival in tape format. There are numerous users of ATSR-2, and ESA is often inundated with data requests. The turn around time between data acquisition and data production can be a long one (up to several months). In this research project, environment the schedule could be adjusted to accommodate delays in the arrival of imagery. In other projects or in operational and commercial settings these problems may be more crucial with critical consequences. This is especially true if operations are concerned with monitoring natural hazards and forecasting.

The problems encountered as a result of geolocation and nadir/forward co-location errors are discussed in more detail in Chapter 7, when information given in the forward look of ATSR-2 is considered. Once it was established that there were



geolocational errors, methods could be adopted to correct for the error. This increased processing time but did not lead to a degradation of data quality.

As has previously been discussed in Section 3.4.1.1, possible error could arise due to the fact that a single atmospheric correction was applied on a scene-wide basis. As has already been discussed, the differences in atmospheric conditions between areas does not appear to affect the contrast between reflectances from highly vegetated areas in the Jordan Valley and those from sparsely vegetated sites in the Badia.

### **3.6.2 NOAA AVHRR**

In general, the acquisition and use of AVHRR data was a relatively straightforward process. The NESDIS online archiving facility is excellent in that images can be previewed before ordering, and image retrieval via 'ftp' following ordering usually takes only 24 hours.

Many of the problems encountered for the ATSR-2 data are also relevant to the AVHRR. The atmospheric correction algorithm was applied on a scene wide basis resulting in generalisations over local scale variations. A further problem was that for some months cloud free images could not be obtained.

Atmospheric correction was more difficult for the AVHRR scenes as data related to viewing and illumination geometry were not always available in a header file. In these cases, viewing geometry was calculated in relation to the position of the Badia region within the image swath, and solar zenith and azimuth designated on the basis of longitude/latitude position, time of day and time of year. The method of dark target subtraction with which to extract aerosol optical depth, may have added additional errors in that suitable dark targets which are zero reflecting at ground level are difficult to find in desert areas where surfaces are very bright (Teillet and Fedosejevs 1995). Although having said that, all images did contain portions of the Dead Sea which for the purposes of this work was taken to be a near zero reflecting surface. It would have been useful to carry out the same atmospheric correction procedure for



AVHRR imagery as the ATSR-2 but the algorithm used was designed specifically for ATSR-2 and this was not possible. Arguably if atmospheric conditions are assumed to be stable on an image-wide basis, one could use two views from AVHRR (at nadir and at the extreme edges of the swath), and apply the same method as that for ATSR-2. This was not attempted on this occasion as it would need further detailed calculations, calibration, atmospheric testing and validation that were not within the scope of this study. It would make an interesting topic for further study.

### **3.7 Summary and conclusions**

This chapter has described the two sensors utilised in this project, ATSR-2 and NOAA AVHRR. Both are similar in their spatial resolution, have wavebands in the red and near-infrared regions of the electromagnetic spectrum and are suited to vegetation mapping and monitoring over large areas. Future chapters will discuss their application to the detection of sparse arid land vegetation in Jordan.

Ideally, monthly images over a two year period were required but, for both images there were gaps in the data set due to unforeseen, unavoidable problems such as instrument breakdown, poor data quality and high cloud cover. The final data set however, did contain images over a series of months and was considered an acceptable database with which to work.

ATSR-2 and AVHRR vary in data format, and individual methodologies had to be adopted for processes of data retrieval and atmospheric correction. Geometric correction procedures however were the same. All methods were selected in the light of experiences of other scientists working in the field and published literature. Although it is recognised that there are sources of error, and it is difficult to accurately account for atmospheric attenuation and geometric distortions, every effort was made to produce images that represented radiometric conditions at the ground level as accurately as possible. The next chapter moves on to consider the forward view of the ATSR-2 using a geometric optical model to simulate the effects of viewing off-nadir.



## **4.0 Bi-directional reflectance effects and the dual view of the ATSR-2**

### **4.1 Introduction**

### **4.2 Bi-directional Reflection Distribution Function (BRDF)**

### **4.3 Geometric optical modelling**

#### **4.3.1 Model design**

#### **4.3.2 Model assumptions**

#### **4.3.3 Input parameters**

### **4.4 Effect of changes in view angle**

#### **4.4.1 Change in view angle with relative azimuth**

#### **4.4.2 Change in view angle with solar zenith**

### **4.5 Model limitations**

### **4.6 Summary and conclusions**



## 4.1 Introduction

Land surfaces are very rarely lambertian in character. They usually exhibit strong anisotropic bi-directional properties (Qi *et al.*, 1994a). The radiance detected by a sensor will depend upon the angle and direction at which the surface is viewed. As was outlined in Chapter 3, one of the unique features of the ATSR-2 sensor is its ability to view the ground in two viewing directions, at nadir and at a forward look angle of 55°. This chapter aims to look more closely at the effect on reflectance of off-nadir viewing using a simple geometric optical canopy model to simulate different view angles and directional reflectance measurements collected in the field. The principles behind off-nadir viewing and the question of surface anisotropy are addressed with reference to the bi-directional reflectance distribution function. The model is then presented and results compared with those from the field data.

## 4.2 The Bi-directional Reflectance Distribution Function (BRDF)

The Bi-directional Reflectance Distribution Function or BRDF is defined by Irons *et al.* (1988), as the relationship which describes the bi-directional reflectance of a surface as a function of illuminating geometry (solar zenith and azimuth) and viewing geometry (view zenith and azimuth). It is written in equation form by Slater (1980) as:-

$$f_{\lambda}(\theta_I, \phi_I, \theta_r, \phi_r, E) = \frac{dL(\theta_I, \phi_I, \theta_r, \phi_r, E)}{dE(\theta_I, \phi_I)} sr^{-1} \quad (4.1)$$

where:-

$\theta_I$  = Solar zenith angle

$\phi_I$  = Solar azimuth angle

$\theta_r$  = View zenith angle

$\phi_r$  = View azimuth angle

$E$  = global downwelling radiance



The BRDF represents the rate of change of the directional radiance of a surface as a function of illumination angle and azimuth ( $\theta_i, \phi_i$ ), view angle and azimuth ( $\theta_r, \phi_r$ ) and the global downwelling radiance. By its definition, the BRDF is continuously defined over infinitesimally small angles and is very difficult to measure (Gauthier *et al.*, 1991). Nicodemus (1977) stated that the BRDF can never be measured directly because 'truly infinitesimal elements of solid angle do not include measurable amounts of radiant flux'. An approximation of the BRDF can be obtained by measuring bi-directional reflectance factors (BRF's) for a limited set of illumination and viewing geometries (Pinter *et al.*, 1990). Many authors have attempted to gain an understanding of the reflectance properties of different surfaces by doing this (for example, Holben *et al.*, 1986, Middleton *et al.*, 1987, Ranson *et al.*, 1994).

With respect to the ATSR-2 and the importance of the dual look, two view angles are of interest i.e. nadir and 55 °. Field measurements in Jordan were therefore taken at these two angles over a wide range of soil and vegetation surfaces.

### **4.3 Geometric optical modelling**

In order to understand the way in which reflectance of a sparsely vegetated surface changes according to illumination and viewing geometry, a simple geometric optical model was adopted. A simple model allows one to simulate the effects of changes in solar zenith, view zenith and relative azimuth which are conditions that can be difficult to reproduce in the field. Field radiometric data were collected at three view angles, nadir, 25° and 55°. Unfortunately, time restraints and solar conditions meant that it was not possible to obtain radiometric data for other viewing/illuminating conditions. Furthermore, field radiometry was only carried out over vegetation or soil as individual scene components, whereas the model allows one to simulate a sparsely vegetated landscape by combining the soil and vegetation data. Combining the results from field data in this way, a simulated model offers a good indication of the way in which a sparsely vegetated landscape responds to changes in illumination/viewing geometries.



The literature has numerous examples of models that have been designed to consider the reflectance properties of vegetated surfaces. In general, there are two main types of modelling approach. Theoretically based work aims to understand the physical basis of the interactions between downwelling irradiance and a vegetated surface, whereas empirically based work takes observations and empirical data as the starting point in an attempt to understand the processes at work. Goel (1988) splits the former into four classes: (i) turbid medium models where the canopy is represented as an infinite parallel plane with one or more homogeneous layers, (ii) geometric models where plants are approximated as geometric objects, (iii) hybrid combinations of (i) and (ii), and (iv) complex computer simulated models.

For the modelling work used here, a geometric approach was adopted. In terms of a geometric model, the landscape is broken down and considered as a series of unit blocks upon a contrasting background. These blocks, representations of trees or shrubs, usually take the form of a common geometric shape. Li and Strahler (1985) model the canopy as a series of opaque cones, Otterman (1984) develops a model for a surface covered with vertical cylinders, whilst Norman and Welles (1983), discuss a three dimensional model based on a rectangular array of ellipsoids. The geometric shape chosen will depend largely on the application involved. Coniferous forests are best approximated by cones such as those described by Li and Strahler (1985), whilst desert or semi-arid vegetation, such as that found in Jordan, is better characterised by spheres or hemispheres.

In some respects the importance of 'shape' in modelling is dependent on vegetation density. In areas of very dense vegetation, the fact that a pixel is an almost planar view of illuminated crowns is more important than the shape of an individual tree. In more sparsely vegetated areas such as Jordan, the shape of a tree will dictate the amount of shadow cast and hence the spectral response. Gauthier *et al.* (1991) argue that the average height and width of the geometric object are more important than its shape *per se*. The degree to which average height and width can be used as surrogates for shape is debatable.



As well as the geometric shape of the vegetation units, the modeller also has to decide whether to treat the 'blocks' as opaque or translucent objects. Opaque objects such as the opaque cones considered by Li and Strahler (1985) are easier to model and are appropriate in areas with dense vegetation units. In areas where vegetation units are less dense, it may be more appropriate to consider some degree of transmittance through the vegetation canopy. In the model described by Jasinski (1996), bushes are recognised as translucent spherical units, and canopy reflectance is the product of the vegetation reflectance multiplied by the canopy transmittance.

Having established the form of the model in terms of geometric representation, many models then go on to calculate the proportions of different elements within a pixel. These are often the proportions of illuminated canopy, shaded canopy, illuminated soil and shaded soil for a given percentage vegetation cover. They vary depending on the form of the model under consideration. Since these components have very different radiometric responses, their relative proportions are important and will influence the spectral response of a pixel. Li and Strahler (1985) calculate green canopy, shadow and understorey proportions using parallel ray geometry and then relate these to pixel reflectance using the Monte Carlo simulation. Rosema *et al.* (1992) adopted a slightly different and more simple approach. They used the Kootwijk forest in the Netherlands as a study area and their Forest Light Interaction Model (FLIM) considered the forest (predominantly coniferous) as a discontinuous canopy with crowns and gaps. The linear combination of shadowed and sunlit background (as viewed through the canopy), and shadowed and sunlit background (as viewed directly), are modelled in terms of biophysical parameters which can then be estimated through model inversion.

In order to understand and predict the spectral response provided by the dual view of the ATSR-2, a simple geometric optical canopy model was adopted to consider the Bi-directional Reflectance Distribution Function (BRDF) of the vegetated surfaces found in the Badia. The model was written in the 'C' programming language and followed the model by Mackay *et al.* (1996). The method is based around work done by Jupp *et al.* (1986) in the semi-arid Eucalypt woodlands of southern Queensland,



Australia. This landscape was considered to best approximate that of the Badia region when all geometric models were considered (Figure 4.2).

#### 4.3.1 Model design

In the model, the sparsely vegetated surfaces of Jordan are depicted as a series of opaque spheres upon a contrasting background. The spheres are randomly distributed and of a density such that there is no canopy overlap. As individual units, both the bushes and the soil are assumed to be lambertian reflectors. By specifying plant dimensions, fractional vegetation cover, solar and illumination geometry and soil and vegetation reflectance, the reflectance value of a pixel is calculated. Calculations are based on a 30 \* 30 m homogenous field study area. The results can be extrapolated to represent what is happening at the scale of an AVHRR or ATSR-2 pixel.

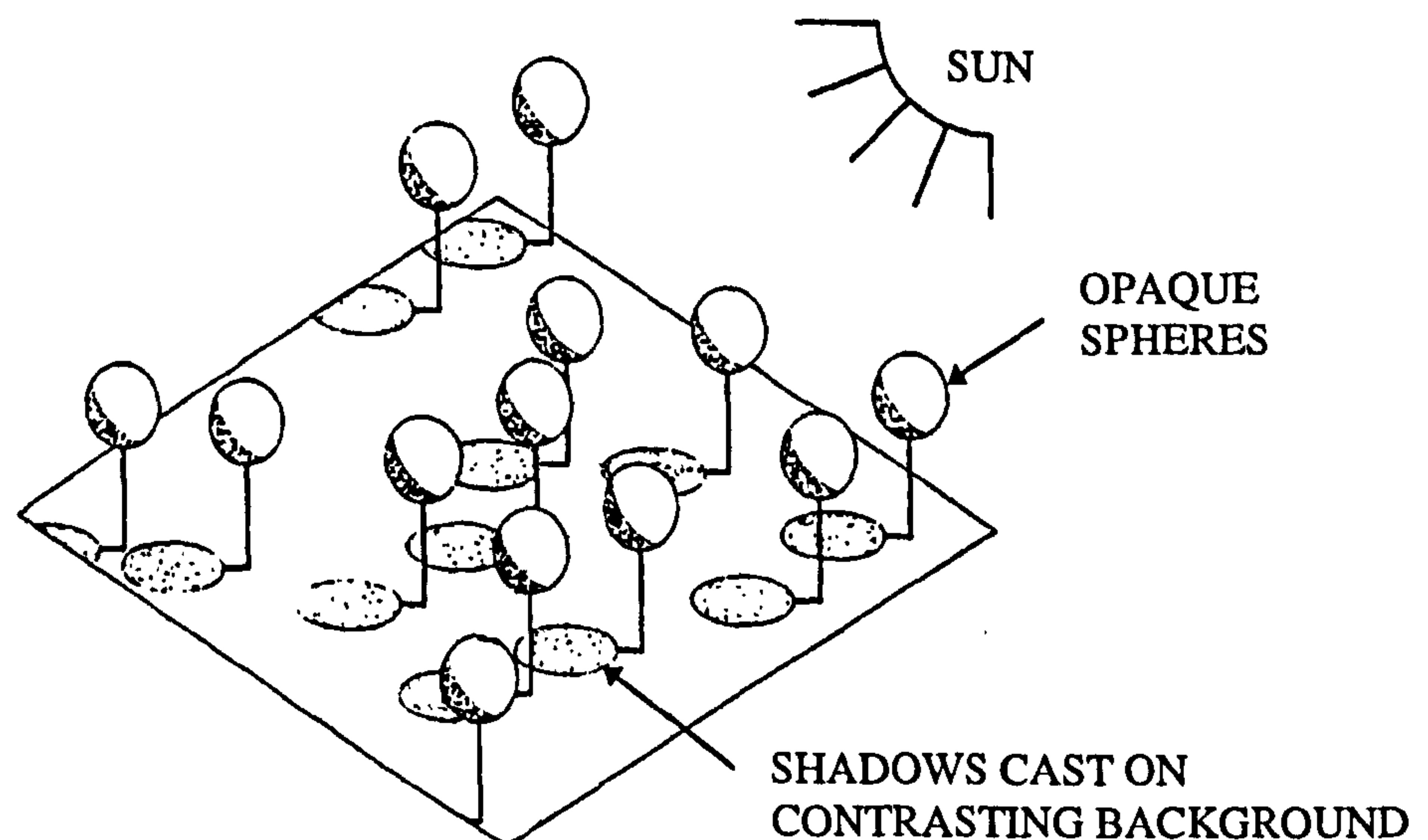


*Figure 4.1: Canopy model structure (Source: Jupp et al., 1986). The canopy is modelled as a series of opaque spheres on a flat planar background.*

The first stage of the model uses the plant geometry and solar and viewing angles to calculate the proportion of the pixel which is composed of illuminated vegetation, shaded vegetation, illuminated background and shaded background. The shaded area is calculated from the solar zenith angle and the size of the spherical bushes, and the



area obscured to the viewer is calculated from the view zenith angle. The overlap between the two can then be calculated, and the shaded area of the pixel is calculated as the shaded ellipse minus the overlap. If the phase angle equals zero, then the view angle equals the solar angle and the relative azimuth is zero. All shaded areas are obscured. At the other extreme if there is no overlap between the obscured and the shadowed surfaces, all shadowed areas are viewed and the pixel reflectance will be affected accordingly.

Having established the proportions of illuminated soil, shaded soil, illuminated canopy and shaded canopy in each pixel, the total reflectance in any given waveband is calculated by multiplying each proportion by its reflectance, and then summing all components together:

$$r_i = \sum_j R_{ij} p_j \quad (4.2)$$

where  $r_i$  = the reflectance of a pixel

$R_{ij}$  = the reflectance of component,  $j$  in band  $i$

$p_j$  = the proportion of component  $j$  visible from a specified viewing direction

As an input to the model, the illuminated canopy and illuminated soil reflectance were derived from field radiometric data, whilst shaded canopy and soil reflectance were calculated by multiplying illuminated reflectances by the fraction of diffuse illumination reaching the surface (Mackay *et al.*, 1996). Following the work by Mackay *et al.* (1996), the atmosphere radiative transfer computer code, 5S (Tanré *et al.*, 1990) was used to give estimates of diffuse illumination. An aerosol optical depth of 0.2 at 550 nm, a mid-latitude summer atmosphere and a continental model of aerosol characteristics were assumed. These parameters are those calculated for the Badia region by Mackay *et al.* (1996). A complete version of the computer code used to run the model is given in Appendix 5.



### 4.3.2 Model assumptions

A number of assumptions were made in the formulation and use of the model.

It was assumed that the plants in the Badia could be represented as spheres. As described in Chapter 2, vegetation sampling in the spring of 1996 and autumn of 1997 involved recording the shape of each plant falling on the transects. The results from that analysis indicated that of 1613 plants measured in the Badia in the autumn 1997, 1032 were considered to be spherical in shape. This represents 64 % and supports the assumption made here.

The model also assumed that plants were randomly distributed over the surface without overlap. Again this assumption can be tested with reference to the field data collected. Using the method of transect analysis, the point at which a plant overlaps the transect was recorded. As a logical consequence, the gaps between each plants were thus recorded too. In the autumn of 1995, 702 plants were measured. Of these, only on 40 occasions did two plants overlap. This represents 7 % of the sample and supports the assumption that plants are distributed without overlap.

In the model, shrubs and the soil are also assumed to be Lambertian reflectors. The model aims to test the directional properties of the landscape as a whole but, within this, each component is considered to be Lambertian i.e, an individual plant is Lambertian but, as part of a landscape casts shadows and contributes to a non-Lambertian effect. Although it is well known that most vegetation canopies are non-Lambertian (Pinter *et al.*, 1990), within a modelling context it is often assumed that leaf reflectance is Lambertian (Gauthier *et al.*, 1991). Similarly, it is equally well known that soil reflectance is non-Lambertian and varies as a function of soil properties such as surface roughness and moisture (Gauthier *et al.*, 1991). For simplicity within a modelling context, soil isotropy is assumed.



4.3.3 Input parameters

Table 4.1 below, summarises the input parameters used for running the model. The values are based on measurements made at *Wassad* in the autumn 1995 and spring 1996. Although there is species variation across the study area, the vegetation in this area had a fairly uniform structure and was considered homogenous.

*Table 4.1: Parameters used as input to the simple geometric model. These values represent those taken using field spectroscopy at the Wassad field site in the Autumn 1995. Irradiance values are calculated using the 5S model*

	Red	Near-infrared
Vegetation reflectance	0.166	0.416
Soil background reflectance	0.301	0.367
Diffuse irradiance for 30° solar angle	0.15143	0.0976
Diffuse irradiance for 50° solar angle	0.2039	0.1302
Mean vegetation diameter	26.05 cm	
Mean vegetation height	29.19 cm	

4.4 Effect of changes in view angle

There are a number of reasons why multi-view angle sensors are increasingly being used to study the Earth’s surface. Viewing off-nadir greatly increases the observational frequency of imaging an area without increasing the number of satellites in orbit (Schnetzler, 1982), and the different view afforded by looking off-nadir provides additional information about the target. In this instance, the simple geometric model enabled the effect of changes in view angle on pixel reflectance to be observed. Changes in view angle were examined in relation to changing relative azimuth and solar zenith angles.

4.4.1 Change in view angle with relative azimuth

In this context, relative azimuth refers to the angle between the position of the sun and the sensor. A relative azimuth of 180° represents instances when the sensor is looking



towards the sun in a forward scatter direction. A relative azimuth of  $0^\circ$  corresponds to when the sensor is looking in the same direction as the sun, directly away from it in a backscatter or antisolar direction. Figure 4.2 shows this relationship in diagrammatic form. Relative azimuthal angles of  $45^\circ$ ,  $90^\circ$  and  $135^\circ$  represent increments of  $45^\circ$  between forward and backscatter directions. Ground radiometric measurements were made at  $45^\circ$  intervals round the measurement sphere i.e., from 0 to  $360^\circ$  . In a modelling environment with homogeneous perfectly spherical bushes, azimuth angles of  $225^\circ$ ,  $270^\circ$  and  $315^\circ$  would produce symmetrical results to those taken looking in the opposite direction. In reality, the geometric properties of the bush are likely to vary from being perfectly spherical thus dictating the degree of symmetry about  $0^\circ$  and  $180^\circ$ .

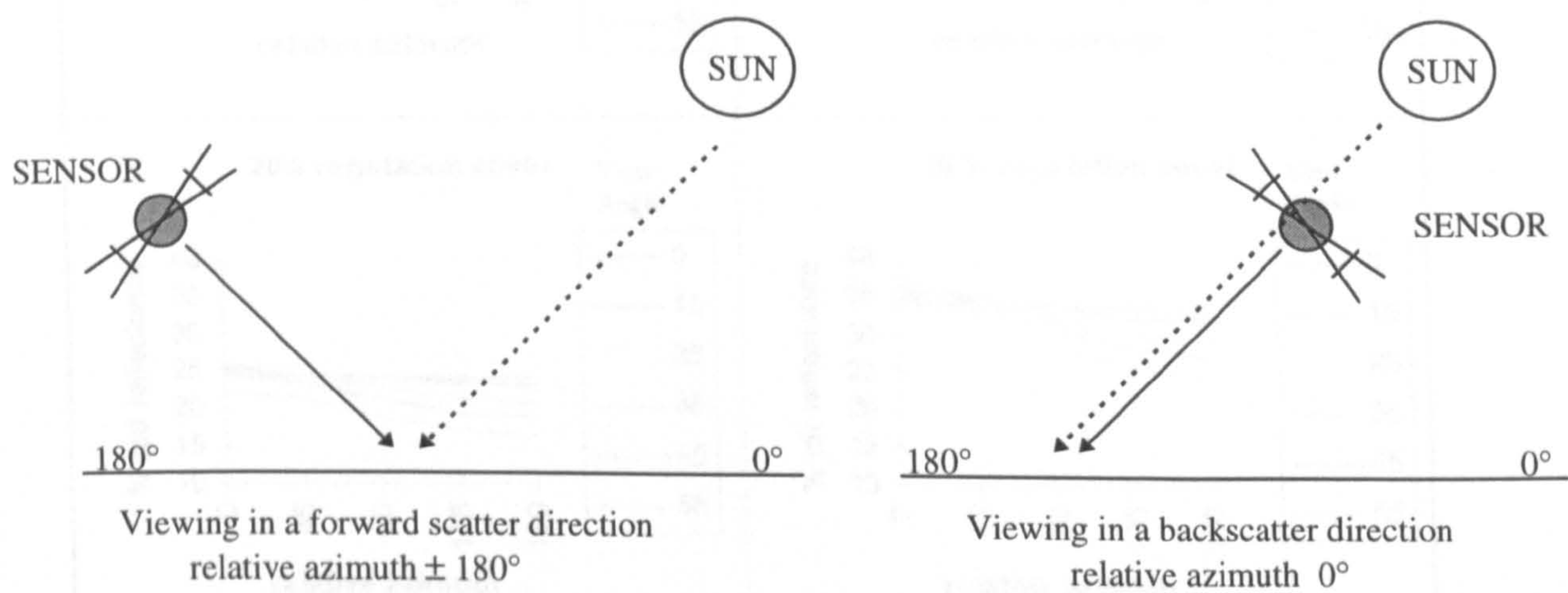


*Figure 4.2: Forward and backward scatter. For forward scatter, the sensor is looking into the sun. For backward scatter, the sensor is looking away from the sun.*

*Figure 4.3. Changes in pixel reflectance with changes in view angle and relative azimuth.*

The model was run repeatedly using view angles of  $0^\circ$ ,  $5^\circ$ ,  $15^\circ$ ,  $25^\circ$ ,  $35^\circ$ ,  $45^\circ$  and  $55^\circ$  for vegetation covers of 0, 5, 10 and 20 %, and the relative azimuth angles were changed. The resulting red and near-infrared pixel reflectance are shown in Figure 4.3.

From the results of the model, several patterns can be observed. Similar patterns are observed for both the red and the near-infrared wavelengths. In general, pixel reflectance decreases as the sensor moves from viewing in a backscatter direction to viewing in a forward scatter direction. The magnitude of change in relative azimuth varies



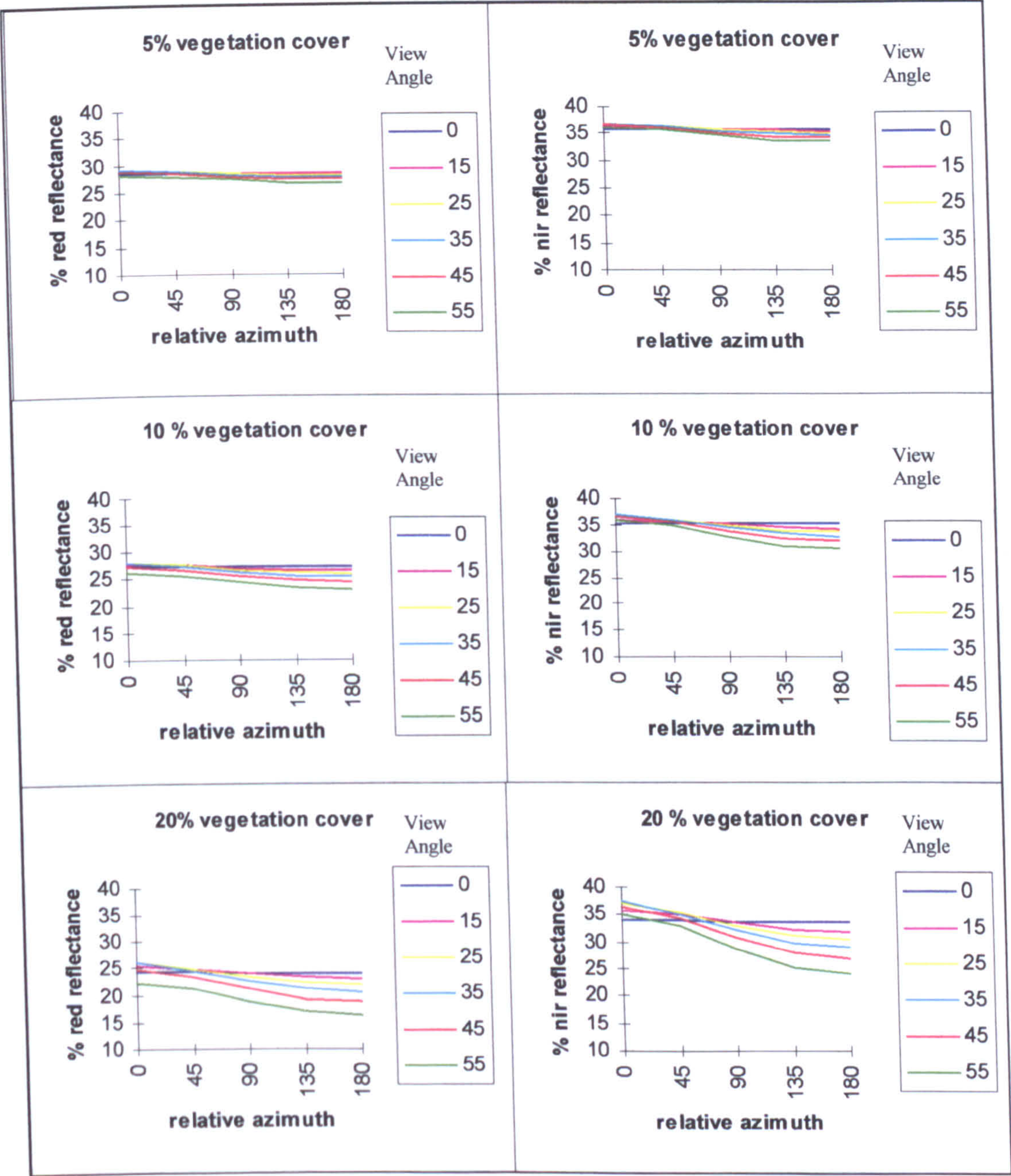


Figure 4.3: Changes in pixel reflectance with changes in relative azimuth for different view angles, and a solar zenith angle of 30°. For red and near-infrared wavelengths, reflectance decreases as the sensor moves from a backscatter to a forward scatter direction. Differences in relative azimuth have greater effects at higher coverages.

From the results of the model, several patterns can be observed. Similar patterns are observed for both the red and the near-infrared wavelengths. In general, reflectance decreases as the sensor moves from viewing in a backscatter direction to viewing in a forward scatter direction. The magnitude of changes in relative azimuth varies



according to viewing angle and increases as percentage vegetation cover increases. Each of these patterns are discussed in turn.

*(i) Surface directional reflectance decreases from a backscatter to a forward scatter direction*

This pattern is observed in both the results of the geometric optical model and radiometric measurements made in the field. The results from two non-vegetated surfaces are shown in Figure 4.4. Unfortunately, problems in the field meant that similar measurements of a vegetated surface were not taken. For both graphs, a peak or 'hotspot' is seen at a relative azimuth of 0°. The 'hotspot' is the name given to the point at which the sensor is in the principle plane as the sun and viewing from exactly the same direction - at this point shadows cast by illumination are hidden from view and reflectance is at a maximum (Strahler and Jupp, 1990). As one might expect from the nature of the surface, the effect of a change in relative azimuth is much greater at the site with large basalt boulders than the flat *qa'a* surface where any directional effect will be the result of desiccation cracks and soil components.



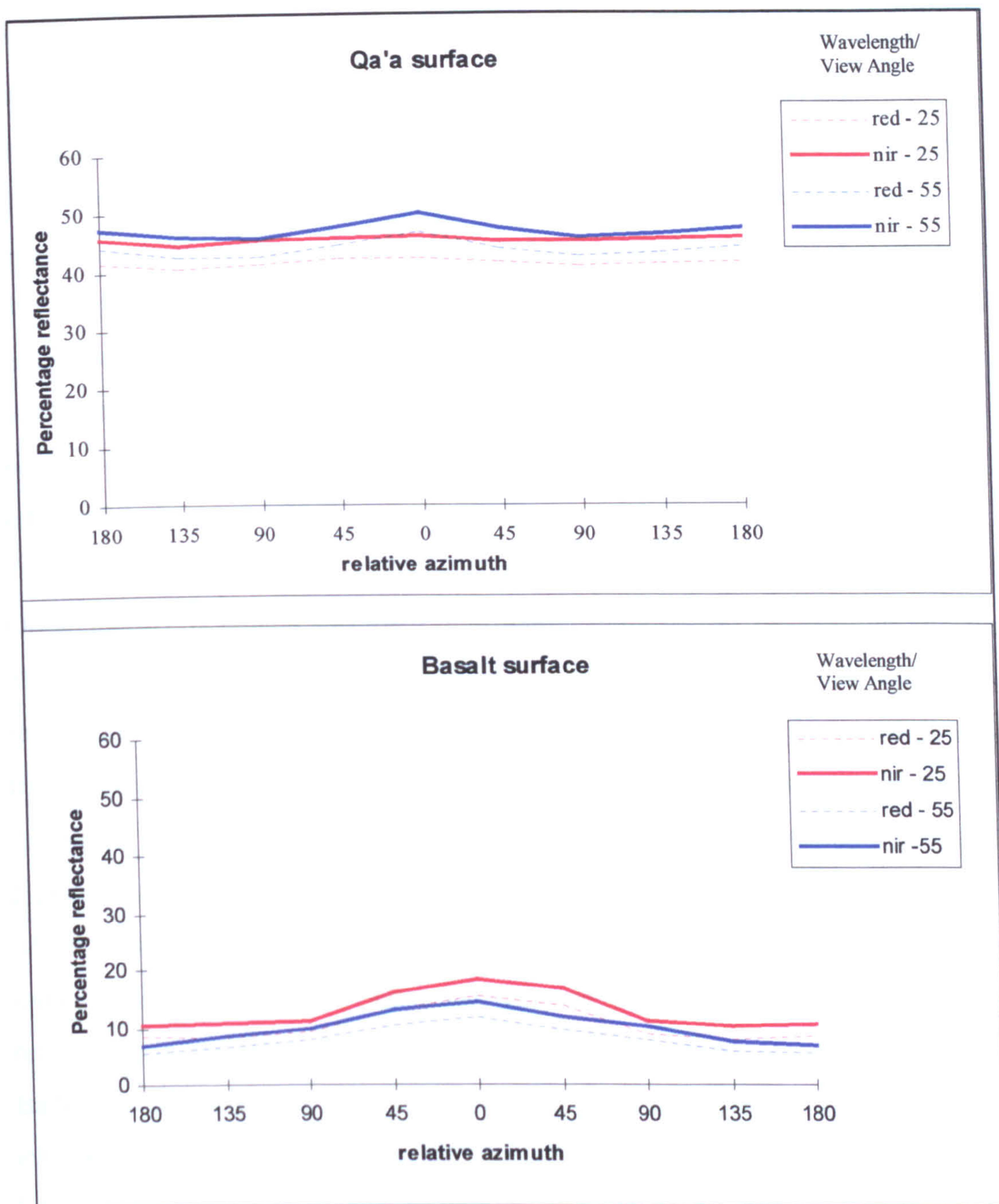


Figure 4.4: Directional reflectance at non-vegetated sites in the Badia as measured by the ASD. Reflectance is highest at a relative azimuth of  $0^{\circ}$  and a backscatter direction. Directional effects are greater for the basalt surface than the flat qa'a surface.

The shift of reflectance from a maximum in a backscatter direction to a minimum in a forward scatter direction is due to the nature of soil and vegetation reflectance and the effect of shadow. In terms of the vegetation, the sensor views a higher proportion of vegetated components that are shaded and not exposed to direct solar radiation as it



moves away from the antisolar/backscatter direction. The amount of background that is shaded by the vegetation also increases. In terms of the soil, reflectance is at a maximum in an antisolar direction due to the presence of vertical components with low transmittance (Holben *et al.*, 1986). In a backscatter direction, the front of these opaque vertical components reflect flux back towards the sensor specularly and diffusely (Kimes, 1983). As the sensor moves round, two mechanisms cause the reflectance to decrease. Firstly, in the sensors field of view, the relative proportion of shadowed surfaces increases and secondly the angle between the line of sight and the normal to the particle facets increases, thus reducing the probability of radiation being reflected to the sensor (Holben *et al.*, 1986).

On a sparsely vegetated surface it is primarily the effect of the soil that dictates the high backscatter peak (Kimes, 1983). In both the visible and the near-infrared bands the contribution of vegetation is minimal. In the visible bands, soil has a higher reflectance than vegetation and its azimuthal variation due to vertical components dominates the signal. In the near-infrared bands, although vegetation generally has a higher reflectance than the soil, the high exposure of soil fills most of the field of view of the sensor, and therefore, its reflectance is still dominant. It must be noted that the model was run with data from the *Wassad* field site. At this site, vegetation reflectance in the near-infrared is higher than soil by 4.9 %. At other field sites in the Badia, the nature of the vegetation means it often has a lower reflectance than soil even in the near-infrared bands. At *Qattafi* the reflectance of the soil in the near-infrared is 11.7% higher than that of the vegetation. In these cases the overriding effect of the soil is heightened further, and the azimuthal variations in the vegetation reflectance have little effect.

As vegetation cover increases towards complete canopy coverage one would expect the peak in backscatter reflectance to decrease. Transmittance by leaves nearly equals the reflectance and azimuthal variations are not as strong (Kimes, 1983). In the model described here, azimuthal variations increase as percentage vegetation cover increases. This could be due to the fact that the model only considered percentage vegetation coverages of up to 20 % typical of an arid environments. This is still low and the



pattern might change if the model were developed further to permit medium to high coverages, and plant overlap.

*(ii) Azimuthal variations affect different view angle by different amounts*

The sensor views different proportions of shaded and illuminated vegetation and soil at different view angles. Thus, the observation that azimuthal variations affect different view angles to different degrees is not surprising.

With reference to a vegetated scene, reflectance increases with increasing off-nadir view angle for all azimuth view directions and sun angles (Kimes *et al.* 1985). As the sensor views off-nadir the proportion of upper canopy layers (that scatter the largest amount of solar flux) seen by the sensor increases whilst the amount of lower canopy layers (scattering lower amounts of flux) decreases. The proportion of soil gap to canopy also decreases.

From the model, with a vegetation cover of 5 % (Figure 4.3), minimum reflectances are seen in a forward scatter direction but, the effect of viewing at different view angles is almost negligible. This suggests that the effect of vertical components within a canopy and the soil are of a scale that their influence is independent of viewing angle. At coverages of 10-20 % however, the model indicates that in a forward scatter direction, reflectance is influenced by the view angle. As view angle increases, reflectance decreases i.e. off nadir angles view more vegetation. In the visible bands vegetation reflectance is lower than soil reflectance and overall reflection decreases. In the near-infrared bands vegetation reflectance is higher than that of soil but reflection still decreases. This is because although the sensor is viewing more illuminated vegetation, off nadir viewing also includes more shaded vegetation and more shaded soil. Shaded surfaces have lower reflectances than equivalent vegetated surfaces.

The pattern in a backscatter direction is not as straight forward and a peak in reflection is seen slightly off nadir at view angles of 25° and 35°. Figure 4.5 indicates the



proportions of illuminated and shaded soil and canopy seen with different view angles in a backscatter direction. Although the amount of illuminated vegetation increases with view angle, the spherical geometry of the vegetation means that the amount of illuminated soil is at a maximum off nadir at 25°. In a backscatter direction maximum reflectances are therefore seen at this view angle.

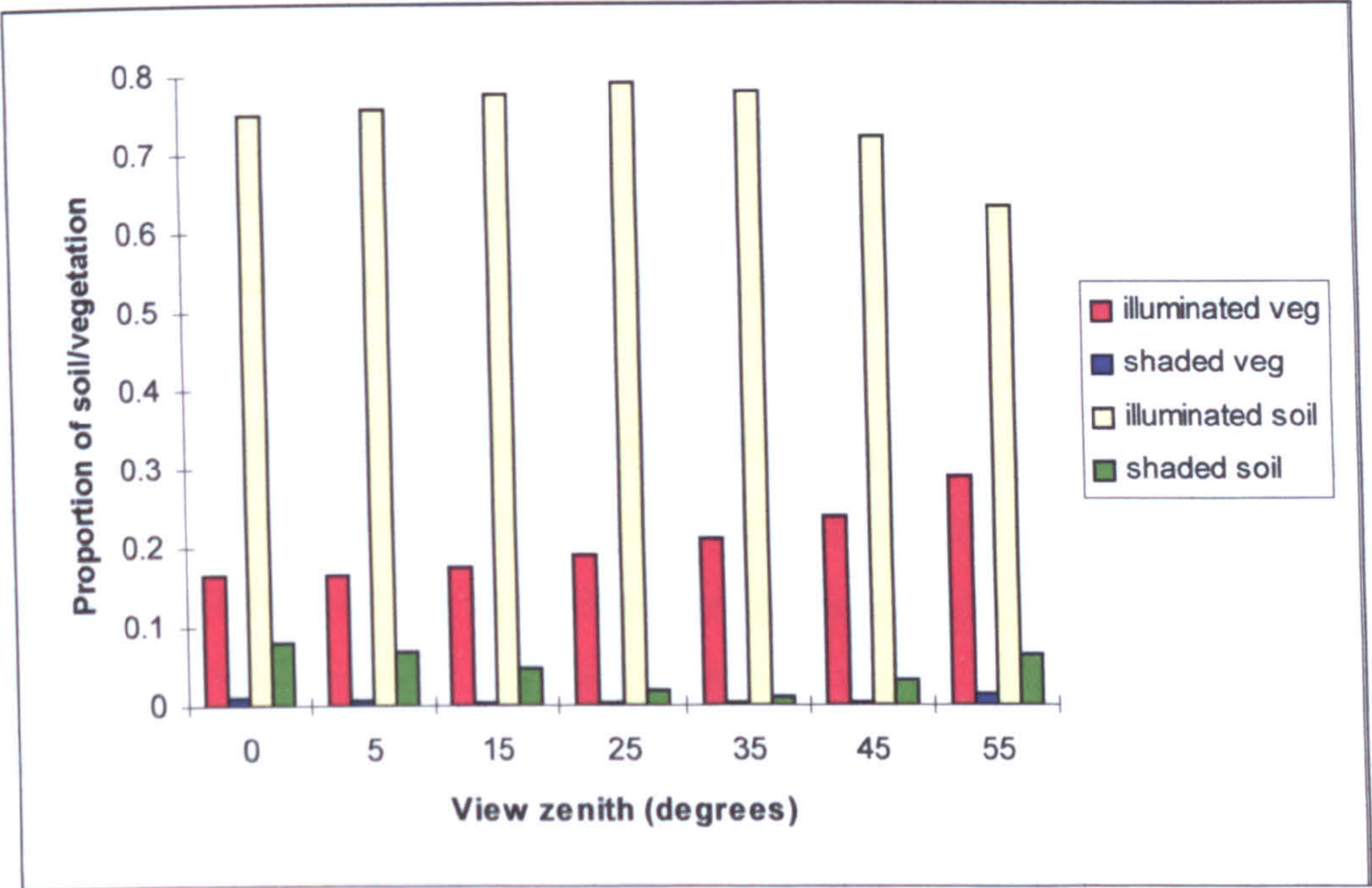


*Figure 4.5: The proportions of illuminated and shaded soil and vegetation seen as the sensor looks at different view angles, at a relative azimuth of 0° and a solar zenith angle of 30°. The highest proportion of illuminated soil is seen at a view angle of 25°. This matches the solar zenith angle.*

These results are supported by those of Qi *et al.* (1994a) who studied semi-arid vegetation at an experimental site in Arizona and found that during the dry season, the red and near-infrared reflectances reached a maximum at a solar zenith angle close to the view zenith angle. When solar and view zenith angles are similar, the sensor views more sunlit facets than when the solar and view angles are far apart. Using data from Jordan, when the model was executed with a solar zenith angle of 30°, maximum reflectance was seen at 25-35° in correspondence.



(iii) *A change in relative azimuth and off-nadir viewing influences wavelengths differentially*

Examination of multiple view angle datasets of vegetated surfaces by Barnsley (1995) revealed that a directional component accounted for 3% of the variance in the near-infrared waveband, and 21% in the red waveband. Similarly, Kirchner *et al.* (1981) comment that off nadir effects are more pronounced in the red than in the near-infrared wavebands. This is explained, due to the fact that vegetation transmits more radiation in the near-infrared wavelengths than in the red wavelengths. The effect of shadow is therefore much more pronounced in red wavelengths (Leblon *et al.*, 1996).

Figure 4.3 indicates that in sparsely vegetated areas, the effects of changes in relative azimuth and view zenith are very similar for the red and near-infrared wavelengths. Vegetation amounts are so small that the increased transmittance by leaves in the near-infrared wavelengths has little effect. Figure 4.6 shows ASD spectral measurements for the background soil at *Feidat ed Dihikiya*. As with other background surfaces in the Badia, differences between the view and azimuth angles increase as one moves to longer wavelengths. Figure 4.7 compares measurements taken at a relative azimuth of 90° at nadir and at 55° view zenith. The results suggest that whilst vegetation in the Badia follows the patterns observed by Barnsley (1995), Kirchner *et al.* (1981) and Leblon *et al.* (1996), the effect of the soil dominates.

Although there are differences in the way red and near-infrared wavelengths respond to changes in viewing and illumination conditions, band ratioing minimises the variability (Cihlar *et al.* 1994). Figure 4.8 indicates shows the NDVI as calculated for different percentage covers.



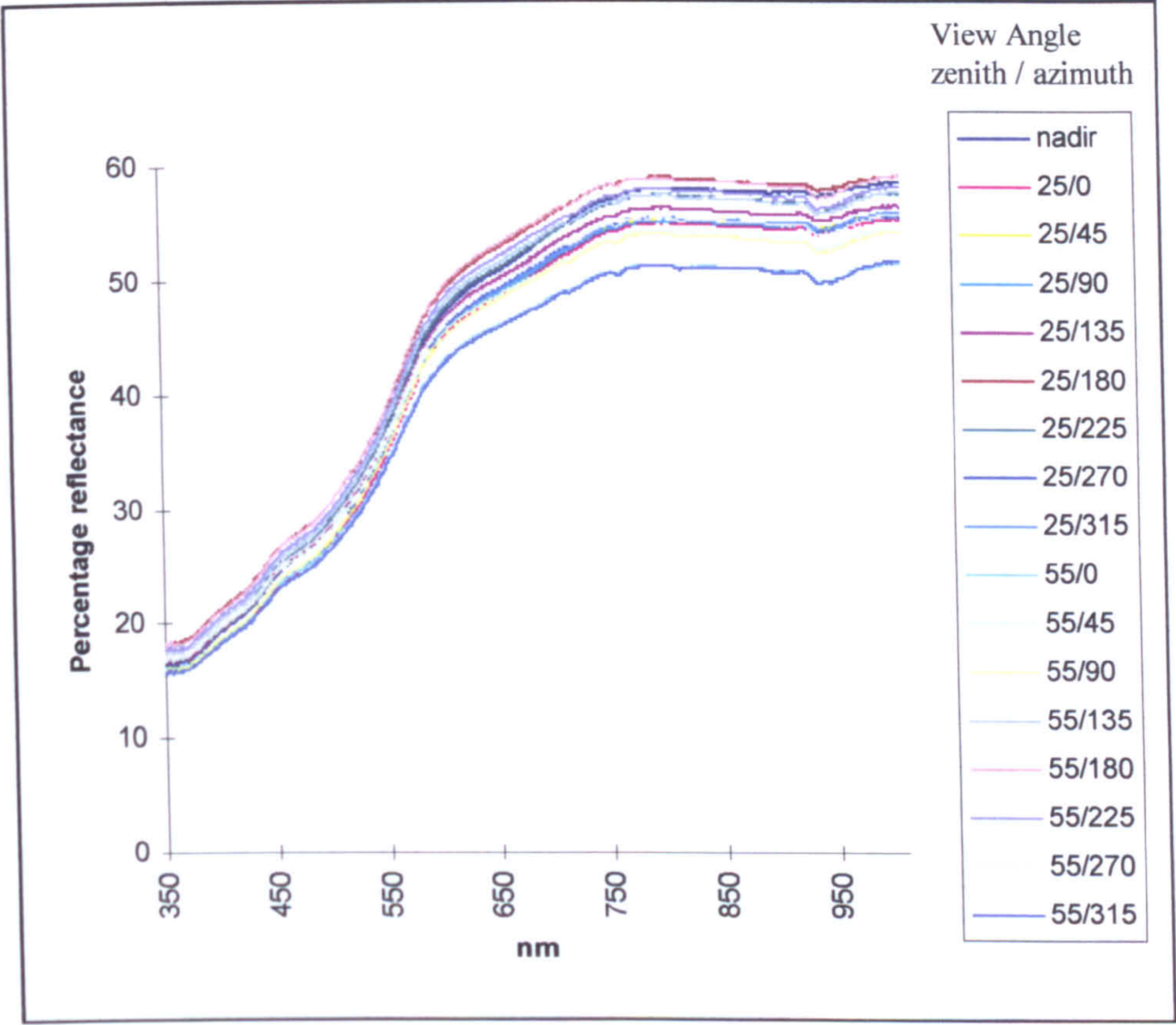


Figure 4.6: Directional reflectance measurements for the background soil at Feidat ed Dihikiya, taken with the ASD.

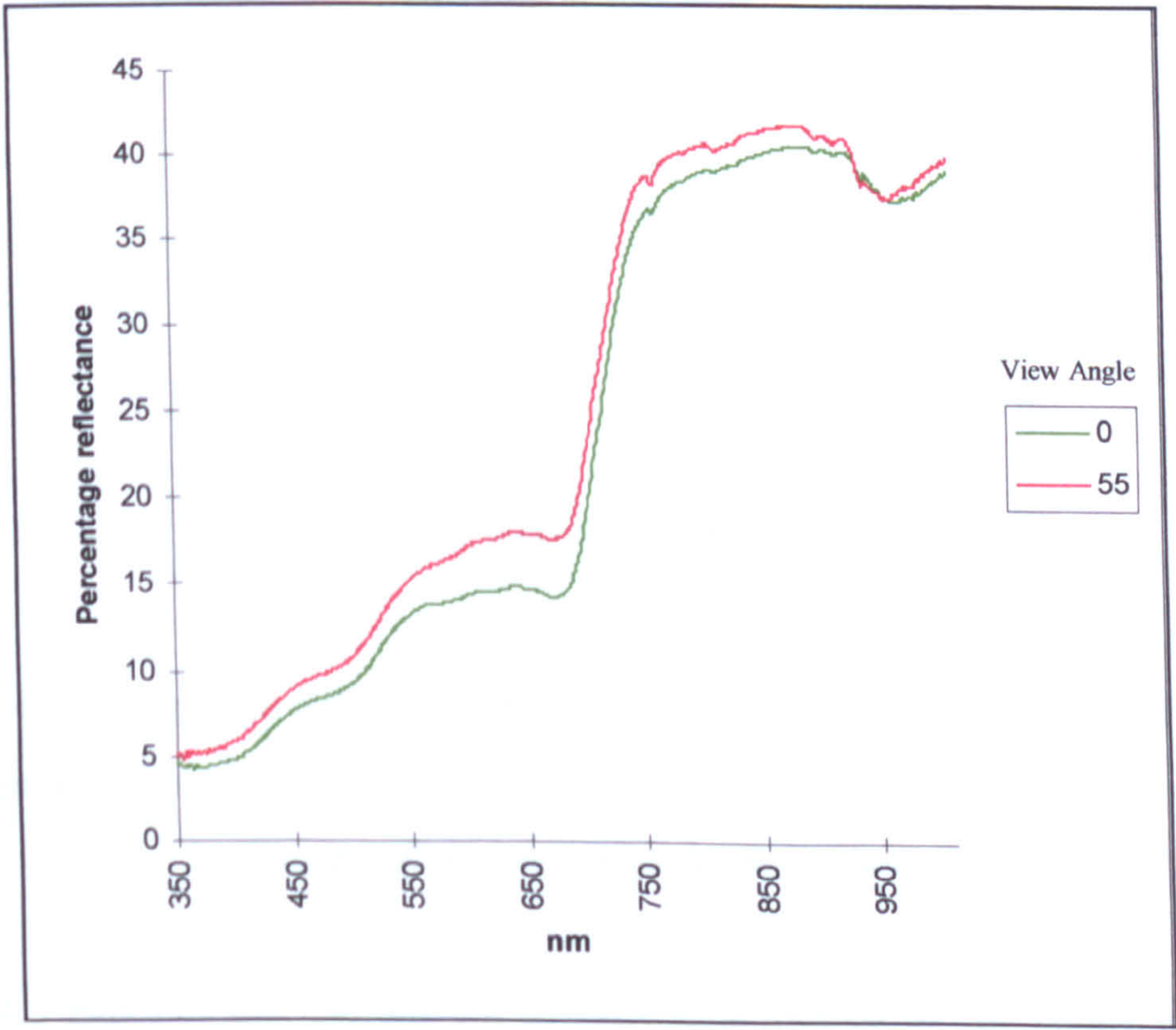


Figure 4.7: Vegetation reflectances at Wassad at two view angles taken with the ASD.



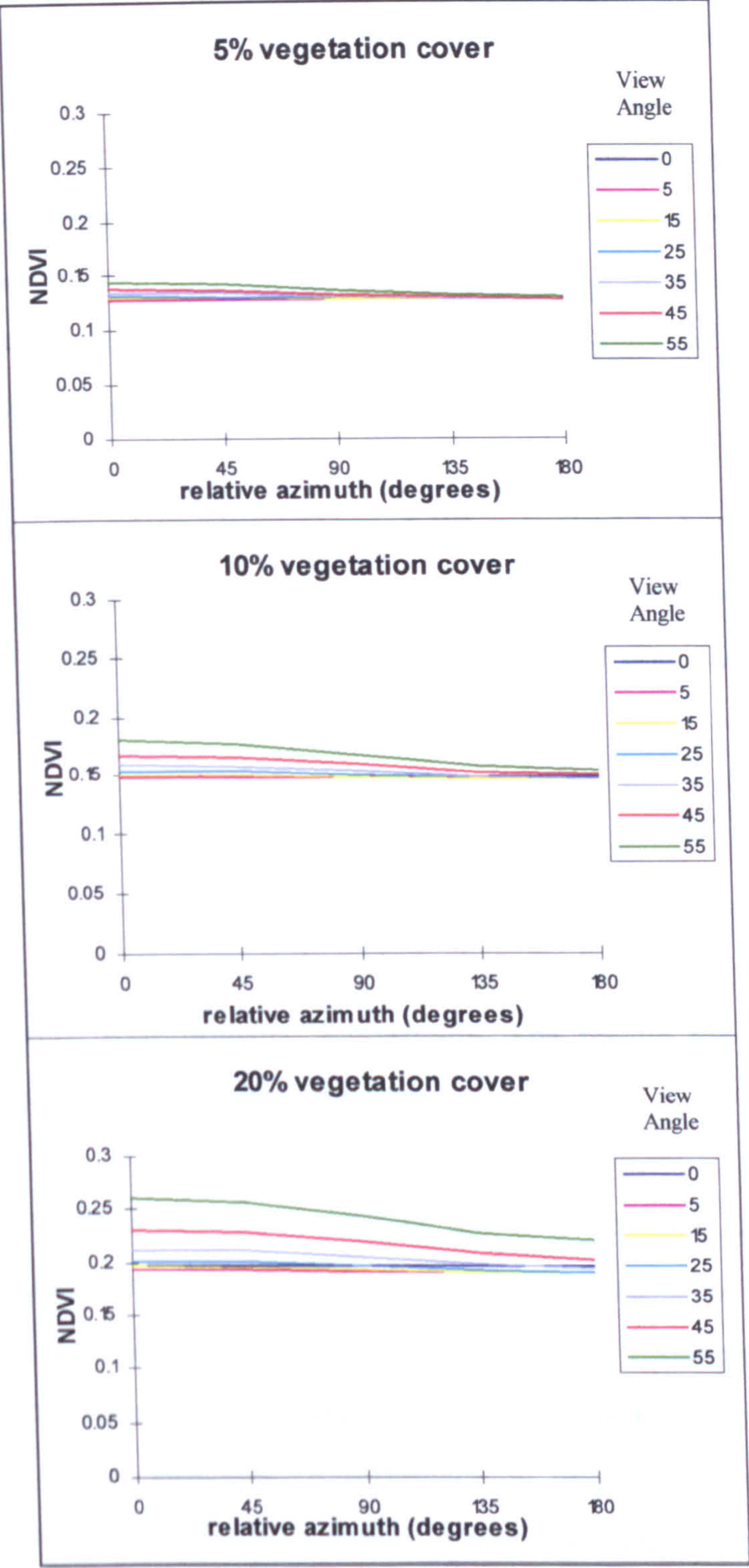


Figure 4.8: Changes in NDVI with changing relative azimuth and view angle, and a solar zenith angle of 30°. Higher NDVI values are obtained when the sensor views in the backscatter direction, and at higher view angles.

Figure 4.5 indicates that the amount of vegetation viewed by the sensor appears to increase as viewing angle increases. Figure 4.8 confirms this in that the view zenith is



directly proportional to the NDVI. The largest NDVI is recorded looking at 55° when most vegetation is seen. As Qi *et al.* (1994a) comment, if the sensor is viewing more vegetation, it will be able to provide additional information about that vegetation. In particular, the vegetation structure will dictate the amount of shadow cast. In an arid environment where the influence of the soil is very strong, an off-nadir sensor that is able to view more vegetation should be able to detect its presence better than a nadir-viewing sensor that senses less vegetation and more soil.

This said however, the relative importance of different view angles varies according to the direction of view and relative azimuth. It has been argued that when vegetation cover is low, view directional effects are more important than the magnitude of the view angle (Qi *et al.* 1994a).

#### **4.4.2 Change in view angle with solar zenith**

The model was run again using a solar zenith angle of 50° as opposed to 30°. Values of diffuse irradiance were adjusted accordingly. The results for the red and near-infrared wavelengths are shown in Figure 4.9.

From the results of the model, it can be seen that in general the same patterns apply with a solar zenith angle of 50° as 30°. Reflectance decreases as one moves from a backscatter to a forward scatter direction. Azimuthal variations affect different viewing angles to different degrees and in the forward look, reflectance was linearly related to view angle. However, a difference is observed when examining the relationship that view angle has to azimuth in the backscatter direction. With a solar zenith angle of 50° peak reflectance is obtained at a view angle of 45-55 ° rather than at 25-35° obtained with a solar zenith angle of 30°. This observation again supports the work of Qi *et al.* (1994a), who concluded that reflectances reached a maximum at the solar zenith angle closest to the view zenith angle when studying spherical vegetation in Arizona.



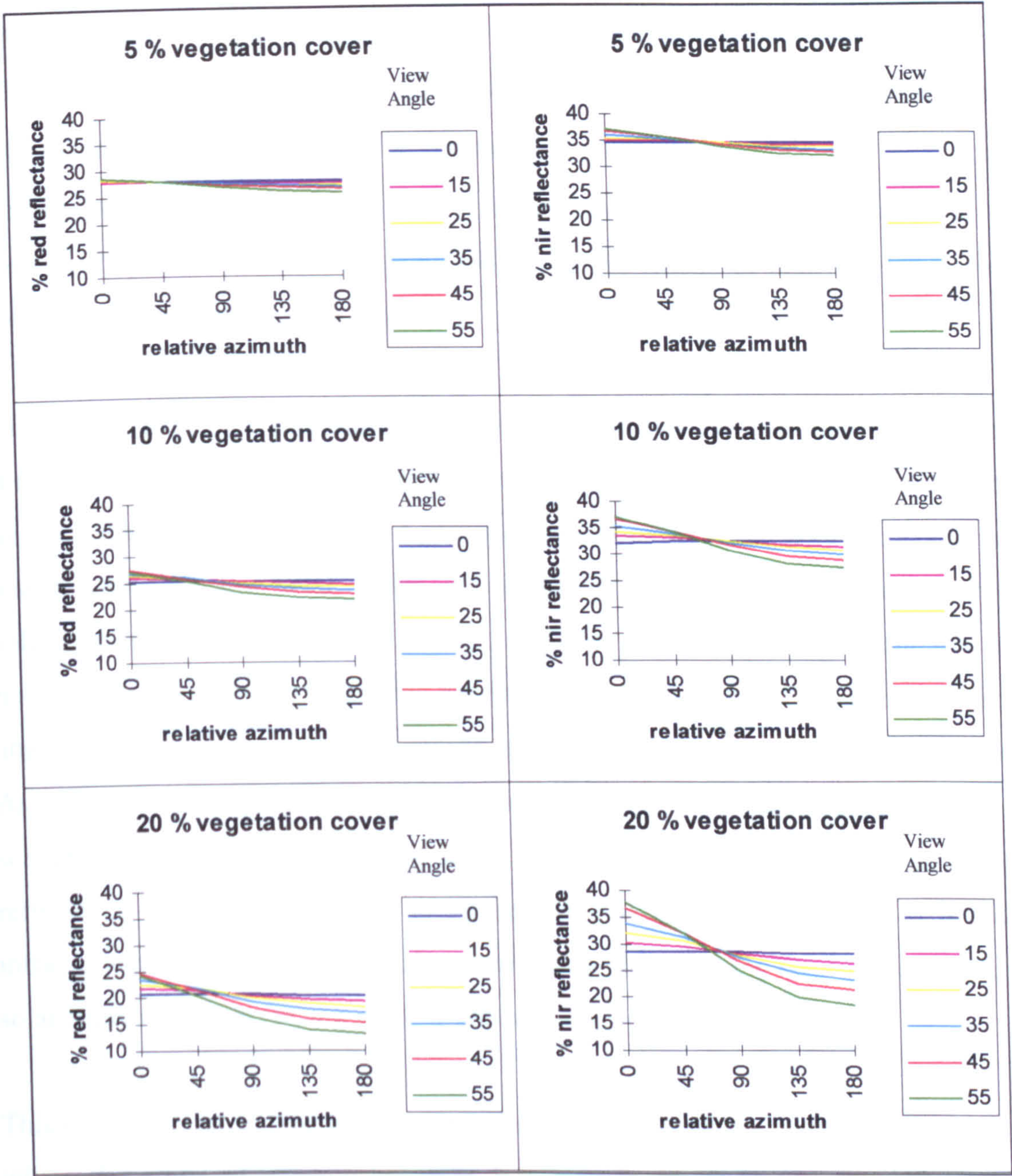


Figure 4.9: Changes in pixel reflectance with changes in relative azimuth for different view angles, and a solar zenith of 50°. Reflectance still decreases from a backscatter direction to a forward scatter direction, but the peak reflectance is now obtained with a view angle of 45-55°. This corresponds to the solar zenith angle.

Although the results from running the model at 50° show similar patterns to those obtained when the model was run with a solar zenith of 30°, the absolute reflectance values obtained for 50° are lower, and show more azimuthal variation. At 20 % cover the ground reflection in the red waveband shows a 11 % variation between extreme



forward and backscatter directions with a solar zenith of 50° and a view zenith of 55°. This compares to a 8 % variation with a solar zenith angle of 30°. In the near-infrared wavebands the variation is 19 % for the 50° solar zenith angle and 9 % for the corresponding 30° solar zenith angle. These results compare favourably to those presented by Irons *et al.* (1988), who found that the albedo of prairie grass increased by 19 % as solar zenith angle increased.

In general, it can be said that solar zenith angle has an important effect on bi-directional reflectance characteristics. The effect is most dramatic at large solar zenith angles (Whitlock *et al.*, 1987). Azimuthal variations increase with increasing solar zenith angles. At low solar angles, the azimuthal variation is small, whilst at high solar angles it is large (Kriebel, 1978). Gauthier *et al.* (1991) comment that even nominally near-lambertian surfaces can become very anisotropic at high solar zenith angles. With sparsely vegetated surfaces reflectance decreases as solar angle increases. As solar zenith angle decreases, the probability of soil gap increases, and soil scattering properties dominate the scene. In the red wavelengths soil has a higher reflectance than vegetation and so the resulting reflectance is higher. In the near-infrared wavelengths reflectance also decreases with increasing solar angle. Increasing solar angle means increasing shadow and thus decreasing reflectance.

This pattern is not true of moderately/highly vegetated areas (i.e. 30 to 100 % cover) where the effect of shadow becomes less significant. Here viewing sees the top, illuminated areas of the vegetation canopy. As the solar zenith angle increases the percentage flux reaching the soil decreases and vegetation dominates the scene reflectance. As vegetation has a higher near-infrared reflectance than soil, reflectance increases with increasing solar angle (Kimes *et al.*, 1985).

#### **4.5 Model limitations**

As with the formulation of any model, generalisations have to be made. It is recognised that whilst the model adopted here does provide a good estimation of the



changes that occur in reflectance as a result of changing illumination and viewing geometries, it is a simplification of reality and consequently has limitations.

In the model, vegetation was treated as lambertian opaque spheres on a lambertian soil background. The overall nature of the surface was treated as non-lambertian but, in reality, individual soil and vegetation units will be non-lambertian also. This is due to effects such as shadowing by vertical components of the vegetation, heterogeneity in terms of soil mineralogy, soil moisture distribution and internal canopy shadowing. Even with very dense bushes, vegetation is also unlikely to be opaque. It will have some degree of transmittance as electromagnetic energy moves down through different layers in the canopy. Transmittance is wavelength dependent. Near-infrared reflectance is less affected by a difference with solar angle than red wavelengths due to the transmittance of leaves and subsequent reflectance from lower surfaces. In the near-infrared, the difference in reflectance between shaded and sunlit leaves is less than in the visible wavelengths (Tueller and Oleson, 1989).

In an arid environment, the effects of shadow are especially important (Franklin *et al.*, 1991, Graetz and Gentle, 1982). In this model, shadow was calculated as the product of diffuse irradiance and the surface reflectance. Leblon *et al.* (1996) show that spectra measured in shadow are typical of the surface type. However, having said that, the method does fail to take account of the fact that the intensity varies as one moves from the edges towards the centre of the shadowed area. Penumbra areas are those which are characterised as being between sunlit and shadowed areas (Leblon *et al.*, 1996). They occur due to multiple shadow effects, and where the distance between the canopy and the ground is large enough that the gap diameter is less than the sun's finite angular diameter ( $0.5^\circ$ ) (Chartier *et al.*, 1973). In the Badia, where plants are relatively small, areas of penumbra shadow are unlikely to have a very significant effect. Their existence should be recognised and the possible effect on pixel reflectance values acknowledged.

The model also presents results based on reflectance measurements made at ground level. When considering measurements at a satellite level, the situation is more



complicated and affected primarily by the effects of the atmosphere. As outlined in Chapter 3, the main ways in which the atmosphere affects radiation leaving the Earth's surface are through the processes of gaseous absorption and scattering. These processes affect wavelengths differentially, and, in relation to off-nadir viewing, will differentiate between view angles depending on viewing geometry and resultant atmospheric path length.

Cihlar *et al.* (1994) studied the AVHRR response of four cover types, cropland, coniferous forest, deciduous forest and wetland, and found that angular dependence was stronger in top-of-the-atmosphere measurements than at ground measurements in the AVHRR's visible channel, but weaker in the near-infrared. Their results are supported by those of Pinter *et al.* (1990), who, comparing ground-, aircraft- and satellite-based measurements of vegetated sites in Arizona found that satellite based BRF's were nearly double those of ground based values in the visible wavelengths. Thus, to conclude, comparison of model results with ATSR-2 imagery collected at the two view angles should give similar results in terms of backscatter/forward scatter differences, although the degree of change may be different. Atmospheric correction applied to the imagery should compensate for the fact that red wavelengths are more affected by the atmosphere than near-infrared wavelengths. Ratios and vegetation indices calculated as a result should present similar patterns to those shown by the model at ground level. Chapter 5 looks at the difference between the two views of ATSR-2 and the implications for vegetation indices.

#### **4.6 Summary and conclusions**

The results of the modelling process can be summarised for sparsely vegetated surfaces as:-

- Surface directional reflectance decreases from a backscatter to a forward scatter direction. In a forward scatter direction, reflectance decreases with increasing view angle. In a backscatter direction the pattern is not as clear cut although, in general, the same is true.
- These patterns are similar for both red and near-infrared wavelengths.



- An increasing NDVI with increasing view angle reflects the fact that with increasing off-nadir view angle, vegetation fills more of the sensor's field of view. This pattern is most evident in a backscatter direction.
- Reflectance decreases with increasing solar zenith angle.

These results are important in that they indicate the results one might expect from comparing the nadir and 55° forward look of the ATSR-2 instrument. When using multi-look sensors, the results will depend on whether the ground is being viewed in a forward or backscatter direction. Reflectances should be lower viewing in a forward scatter direction, although the situation is not straightforward as the viewing geometry changes as one moves across a scan line.

From orbital parameters given in header information, it can be seen that ATSR-2 imagery recorded over Jordan was taken with the sensor moving in a descending mode and a forward scatter direction. This should be advantageous since, although individual reflectances are generally lower, differences between view zenith angles are at a maximum (Figure 4.1). Having said this, in terms of the NDVI, Figure 4.6 indicates that NDVI values are at a maximum in a backscatter rather than a forward scatter direction. View angle differences are enhanced but the use of the NDVI to detect vegetation is reduced.

Solar zenith angles also vary across a scan line. All ATSR-2 images were collected at a similar time each day (0800 - 0900 hours) but the position of the sun will vary according to the date. As Chapter 3 explains, the revisit time of ATSR-2 is 35 days. Unless images are collected 35 days apart, sites will also be at different positions within the swath. Vegetated sites will therefore have different reflectances as a result of their position across a scan line and resultant solar-sensor geometry.

Differences in illumination geometry have been seen to be problematic in the interpretation of remotely sensed data. As a result, some authors have restricted the use of imagery to those taken at or near nadir (e.g. Ehrlich *et al.*, 1994, Duggin *et al.*, 1982). Other methods have included taking a group of images and eliminating angular



variation by averaging over a specific time interval (Meyer *et al.*, 1995). The work done in this chapter has shown that images taken at different view angles can be useful in providing extra information about the target. Particularly with reference to the NDVI, it was seen that higher NDVI values were obtained viewing at 55° compared with those at nadir. It is recognised however that the relationship between reflectance and illumination geometry is a complicated one and one that is difficult to interpret. Many other factors apart from the illumination geometry affect reflectance. These factors vary spatially and temporally and again are difficult to measure and predict. The next chapter examines the detection of arid land vegetation using satellite imagery and vegetation indices. The theory investigated in this chapter should help in the interpretation of the results of the forward look of the ATSR-2.



- 5.0 Arid land vegetation analysis: comparing ground and satellite measurements using vegetation indices**
- 5.1 Introduction
- 5.2 Vegetation Indices
- 5.3 Comparing vegetation characteristics and satellite imagery
  - 5.3.1 The relationship between individual wavebands and percentage vegetation cover
    - 5.3.1.1 The relationship between reflected middle infrared and percentage vegetation cover
  - 5.3.2 Frequently used vegetation indices
  - 5.3.3 The use of 'new' vegetation indices
- 5.4 Seasonal variations detected using vegetation indices
- 5.5 Problems associated with the use of vegetation indices
- 5.6 Summary and conclusions



## 5.1 Introduction

The reflectance properties of green photosynthetically active vegetation are widely documented and well known (Belward, 1991, Tucker and Sellers, 1986). The differential response of vegetation particularly in the red and near-infrared parts of the electromagnetic spectrum has lead many people to use vegetation indices or band ratioing techniques as a means of deriving information about vegetation from satellite imagery.

This chapter describes the application and considers the usefulness of vegetation indices to the problem of the detection of vegetation in arid lands using ATSR-2 data. Vegetation indices that utilise data from ATSR-2 are investigated and correlated to ground data. The results are compared with similar indices derived from the AVHRR.

## 5.2 Vegetation indices

There is an enormous body of literature describing studies that have examined the use of vegetation indices generated from satellite imagery to derive information about surface biophysical properties. They cover a whole range of different environments from tropical forests to arctic tundra and desert rangelands, and use a variety of different sensors including Landsat TM, Landsat MSS, SPOT and NOAA AVHRR. Some indices (e.g. NDVI, the Ratio Vegetation Index) simply incorporate red and near-infrared wavebands whilst others include additional terms to take account of factors such as the influence of the background soil (e.g. SAVI) or the atmosphere (e.g. Global Environmental Monitoring Index).

Boyd *et al.* (1996) divide vegetation indices into seven categories, normalised based indices, complex division, stress related, transformed, ratio based, ratio and normalised difference. Rondeaux *et al.* (1996) divide them more simply into three classes based on their function and inclusion of additional terms. They are intrinsic indices incorporating simply red and near-infrared wavelengths, soil-line related indices and atmospheric-corrected indices. The different indices have all been found



to be useful in different situations with different satellite sensors, applications and land cover types. Given that green photosynthetically active vegetation shows a characteristic response in the red and near-infrared wavelengths, many vegetation indices concentrate on the use of these two wavebands.

Intrinsic indices as described by Rondeaux *et al.* (1996) are those which do not involve any external factor apart from the spectral reflectance. Two of the most widely used are the ratio vegetation index (RVI) and the Normalised Difference Vegetation Index (NDVI) defined as:-

$$RVI = \frac{nir}{red} \quad (5.1)$$

$$NDVI = \frac{(nir - red)}{(nir + red)} \quad (5.2)$$

where 'nir' refers to reflectance in the near-infrared wavelengths and 'red' refers to reflectance in the red wavelengths.

The NDVI has often been used with NOAA AVHRR imagery where the NDVI = channel 1 - channel 2 / channel 1 + channel 2. In ecosystems that contain up to 70 % photosynthetically active vegetation, both the NDVI and RVI have been shown to correlate well with vegetation parameters such as percentage cover, biomass and leaf area index (Tucker *et al.*, 1985a Wylie *et al.*, 1991). Over rangelands and less well vegetated areas, their success has been more variable. Kennedy (1989) studied the phenology of Tunisian grazing lands and found that whilst the NDVI could be used an indicator for monitoring inter-annual and intra-annual variations in biomass and productivity, percentage soil contribution to total recorded reflectance provided an important limiting factor and a threshold beyond which the accuracy of the index became less reliable. Tucker (1977) and Ripple (1985) found the NDVI good for estimating low levels of phytomass in blue grama and tall fescue plots in Nebraska, USA, but, Choudbury and Tucker (1987) found it was not sensitive below the 20 %



green ground cover of the Great Victoria and Great Sandy deserts in western Australia and the Kalahari desert in southern Africa. Similarly, Weiser *et al.* (1984) found good correlations between RVI and tall grass prairie phytomass but, Colwell (1974), and Pearson *et al.* (1976), comment that the RVI is unreliable with percentage green covers of less than 30 %. Reasons for the success or failure of the NDVI and RVI to estimate vegetation parameters in arid environments can be attributed to the many factors which affect the radiometric signal in an arid environment. These are summarised below.

The discussion of ground radiometric data presented in Chapter 2 outlines some of the problems associated with remote sensing of vegetation in arid regions. As Figures 2.12, 2.13 and 2.14 show, arid-zone vegetation does not always display a spectral response typical of green, photosynthetically active material. Huete and Jackson (1987) recognised that the vegetation in arid rangelands is often composed of a mixture of woody biomass, live green grass, senesced yellow grass, weathered grey litter and a large proportion of soil background. In order to overcome the problem of high soil reflectance, Richardson and Everitt (1992) examined soil adjusted vegetation indices in relation to green and brown biomass on an experimental site in Texas. They found that all gave a positive correlation with green biomass and a negative correlation with brown biomass. When applied, these two relationships will tend to work together to give poor results. Similarly Satterwhite and Henley (1987) studied vegetation and soil at 25 sites in Nevada. They concluded that red/near-infrared band ratios were effective when the surface has a high red/near-infrared band contrast, as in the case of physiologically active plants, and less effective with low band contrast, as in the case of senesced or yellow vegetation. The stage and form of vegetation growth together with the health of the vegetation will dictate the radiometric signal received and consequently the utility of vegetation indices.

The NDVI and RVI are ratio indices based on ratioing the red against the near-infrared reflectance. Another commonly used index is the Perpendicular Vegetation Index (PVI). This again, is based on the red and near-infrared wavelengths but is an orthogonal, as opposed to a ratio index. The PVI of Richardson and Wiegand (1977)



is based on the 'soil line' and the tasselled cap of Kauth and Thomas (1976). The soil line concept states that there is a linear relationship between the red and near-infrared reflectance of bare soil (Baret *et al.*, 1993). For a given area, a soil line develops as variations in soil mineralogy, texture and moisture content lead to different reflectances. Each soil has a unique soil line characterised by a slope and an intercept. Some authors assume all soils can be represented by a global soil line whilst, others (e.g. Huete *et al.*, 1984) comment that individual site-specific soil lines should be used, as each soil line describes the optical properties of the soil in question more accurately. It is argued that in the Perpendicular Vegetation Index (PVI), the variation in reflectance of developing vegetation grows perpendicularly from the plane of soils. This is shown in diagrammatic form in Figure 5.1.

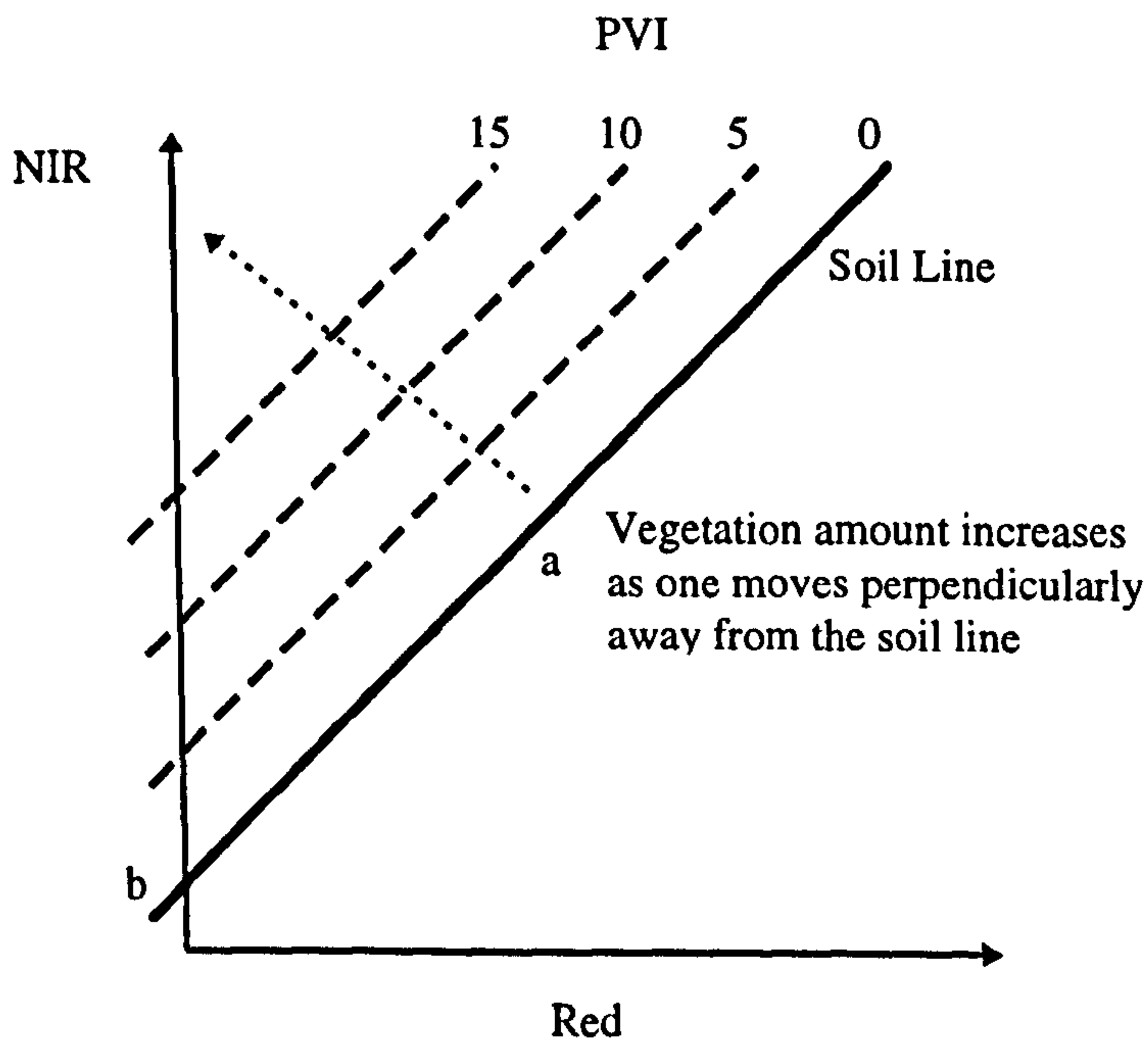


*Figure 5.1: The relation of the PVI to the soil line. The PVI increases as one moves away perpendicular to the soil line.*

The PVI is defined as:-

$$PVI = \frac{nir - ared - b}{SQRT(1 + a^2)} \quad (5.3)$$

where a and b represent the slope and the intercept of the soil line respectively, red refers to reflectance in the red wavelengths, and nir refers to reflectance in the near infrared wavelengths.



The PVI has been applied successfully in several different environments. Elvidge and Lyon (1985) examined the application of vegetation indices in assessing green biomass in the arid and semi-arid environment of the Virginia Range. They found that the PVI was the most appropriate index for studying green biomass in semi-arid areas where soil is bright and vegetation amount is low. Jackson *et al.* (1983), studying the discrimination of growth and water stress in wheat also found the PVI to give good results as it was less sensitive to the effects of the atmosphere than some of the other indices.

The influence of the background soil can be a significant problem in areas of low vegetation cover. Huete *et al.* (1984) comment that soil 'noise' can restrict the discrimination of green vegetation below 25 % cover. To address the problem indices that try to take the effects of the soil into account such as the PVI have been developed. Another index often applied is the Soil-Adjusted Vegetation Index, SAVI (Huete, 1988).

SAVI is defined as:-

$$SAVI = \left[ \frac{(nir - red)}{nir + red + L} \right] * (1 + L) \quad (5.4)$$

where L is a constant adjustment factor accounting for the influence of the soil substrate. Although L can be varied from 0 to 1 depending on the amount of vegetation cover, Huete *et al.* (1984) state that a single value of 0.5 reduces soil noise considerably for a wide range of vegetation densities. The SAVI is usefully applied on an image wide basis where vegetation of different densities may be encountered. It is however, an exact solution for bare soil only when soil line parameters have a slope of 1 and an intercept of 0. With low plant densities, it is important to reduce soil noise as much as possible (Baret and Guyot, 1991). To attempt to do this, the Transformed Soil Adjusted Index, TSAVI (Baret *et al.*, 1989) was developed. This measures the angle between the soil line and the line which joins the vegetation point and a point (S) belonging to the soil line. It was defined originally as:-



$$TSAVI = \frac{a(nir - ared - b)}{red + anir - ab} \quad (5.5)$$

where a and b give the slope and intercept of the soil line respectively, red gives reflectance in the red wavelengths and near infrared give reflectance in the near infrared wavelengths.

An improved version is given by Baret and Guyot (1991) as:-

$$TSAVI = \frac{a(nir - ared - b)}{[anir + red - ab + X(1 + a^2)]} \quad (5.6)$$

where X is the negative abscissa of the point S. TSAVI equals 0 for bare soil and 0.7 for very dense canopies.

Another soil adjusted vegetation index is the Soil Adjusted Ratio Index, SAVI<sub>2</sub> (Major *et al.*, 1990). This adds a soil background adjustment to the ratio vegetation index (RVI) and is defined as:-

$$SAVI_2 = \frac{nir}{(red + b/a)} \quad (5.7)$$

where a and b represent the slope and the intercept of the soil line respectively, red represents reflectance in the red wavelengths and nir represents reflectance in the near infrared wavelengths. It is claimed that SAVI<sub>2</sub> is less sensitive than other vegetation indices to soil background, solar zenith angle and leaf area distribution changes, but, few studies using it have been carried out (Major *et al.*, 1990, Richardson and Everitt, 1992).

The indices mentioned thus far have been concerned with reflectance in the red and near-infrared parts of the electromagnetic spectrum. Another group of indices incorporate information from the middle infrared (MIR) parts of the electromagnetic spectrum. This represents the region in which the spectral characteristics of vegetation



are influenced by water absorption bands (3.0 - 5.0  $\mu\text{m}$ ). Boyd *et al.* (1996) considered the use of middle infrared and thermal wavelengths for the detection of regeneration stages of vegetation in the Amazon rainforest. They found that indices using middle infrared wavelengths in addition to the red and near-infrared gave better results than those using red and near-infrared wavelengths alone. Similar results that indicate the usefulness of the middle infrared wavelengths have been found for other cover types such as saltmarshes (Hardisky *et al.*, 1984), cereal crops (Leamer *et al.*, 1978, Baret *et al.*, 1988), temperate coniferous forest (Boyd and Ripple, 1997) and paddy fields (Shibayama and Akiyama, 1989). In terms of an arid climate, few studies have been done. Using middle infrared wavelengths, Everitt *et al.* (1989) studied grass plots in Arizona, and concluded that middle infrared and near-infrared wavebands may be useful in estimating grass phytomass in large inaccessible rangelands. However this work was based on grass plots which had been fertilised and watered. The desert vegetation in Jordan has water as a limiting factor in plant growth. Plants have adaptations to conditions of low water availability with features such as increased cuticle thickening to prevent against water loss (McCleary, 1968), and their response in middle infrared wavelengths may be very different to that of vegetation in more temperate or humid climates. Unfortunately, field radiometric data was not measured in the middle infrared wavelength regions and so this hypothesis cannot be tested.

The final group of vegetation indices identified by Rondeaux *et al.* (1996) consists of atmospheric-corrected indices. These are indices that aim to take the effects of the atmosphere into account. Two of the more commonly used are the atmospherically resistant index, (Kaufman and Tanré, 1992), and the Global Environmental Index, (Pinty and Verstraete, 1992). The Global Environmental Index, GEMI is defined as:-

$$GEMI = \eta(1 - 0.25\eta) - \frac{red - 0.125}{1 - red} \quad (5.8)$$

where

$$\eta = \frac{2(nir^2 - red^2) + 1.5nir + 0.5red}{nir + red + 0.5}$$



GEMI ranges between 0 and +1 and is designed to reduce the effects of the atmosphere. Although it can be used for regional studies, it was designed for use with global datasets which cover a large range of different atmospheric conditions. For studies on a regional or local scale such as those discussed in this thesis, the imagery has usually already been atmospherically corrected using an atmospheric model, such that the need for atmospheric-corrected indices is reduced. Another reason for omitting the use of atmospherically resistant vegetation indices in association with areas of sparse vegetation follows from analysis of the results of other workers. Qi *et al.* (1994b) demonstrated that indices designed to minimise the effects of the atmosphere frequently have increased sensitivity to soil background variations. In an arid region with a high proportion of background soil, such increased sensitivity to soil renders atmospherically resistant vegetation indices completely unsuitable (Ray, 1995).

As this discussion has highlighted, there are many different types of vegetation index. Most use the red and near-infrared wavelengths due to the relationship that the reflectance has with photosynthetically active vegetation, but indices have been formulated that use middle infrared and thermal wavebands also. The work described in the remainder of this chapter focuses on the use of indices to detect vegetation of very low densities and percentage covers in the arid environment of Jordan. The ATSR-2 sensor has wavebands in the visible, infrared and thermal parts of the spectrum and most importantly offers the opportunity to examine the effects of off-nadir viewing. These particular characteristics will be used to investigate the utility of vegetation indices.

### **5.3 Comparing vegetation characteristics and satellite imagery**

In order to assess the utility of vegetation indices for providing information on the percentage vegetation cover on the ground, pixel reflectance values were extracted from selected ATSR-2 and AVHRR images for the individual field sites and correlated with percentage vegetation cover values derived from field observations. The ATSR-2 images used were restricted to those which were cloud free, covered



both the Badia and the Jordan Valley regions and were acquired during a period of field data collection, in the autumn of 1995 and 1997. Since ATSR-2 failed in operation during the spring of 1996, no data are available for comparison with field data collected at this time. The AVHRR images utilised date from spring 1996 and autumn 1997. Table 5.1 summarises the images used.

*Table 5.1: Images used to assess relationship between percentage vegetation cover and vegetation indices*

Sensor	Image Date
ATSR-2	06/09/95
ATSR-2	15/11/97
ATSR-2	10/09/97
AVHRR	31/03/96
AVHRR	28/04/96
AVHRR	05/05/96
AVHRR	05/09/97

Field data were collected only in the Jordan Valley on the final field trip to Jordan in autumn 1997, however, the percentage cover values collected at that time are also used to analyse autumn 1995 imagery. This is because much of the land use in the Jordan Valley is for irrigated agriculture and although fields may be left as fallow one season in every five, for example, (Jordanian farmer, personal communication, autumn 1997), this is done on a field by field basis. The overall reflectance of the area should therefore remain fairly constant.

The work described here uses imagery that had been geometrically and atmospherically corrected. Details of these procedures can be found in Chapter 3. Percentage cover calculation similarly can be found in Chapter 2.

Having selected the images to use (Table 5.1), mean pixel values for each field site were extracted. For sites in the Jordan Valley, this was done using a 3 \* 3 pixel window. For sites in the Badia where field observations indicated that vegetation in



the region covered an area smaller than 3 \* 3 km, a 2 \* 1 pixel window was used. This prevented non-vegetated areas influencing the vegetation signal. For each series of pixels extracted, the standard deviation of reflectance was checked to ensure that the field sites represented homogenous areas, and omitted any zero values or error codes.

Pixel reflectance values were extracted for each waveband and for forward and nadir view angles at every field site. The relationship between these values and percentage vegetation cover was assessed by calculating Pearson's product moment correlation coefficient (for details on Pearson's coefficient, see Ebdon, 1995). This gave an indication as to which bands explain most of the variation in percentage vegetation cover values, and suggested those which would be most useful for inclusion in a vegetation index. Two sets of correlations were performed, one using field sites across the whole of Jordan and one using only field sites in the Badia. By using only field sites in the Badia, it should be possible to test the ability of an index to discriminate between areas with very low levels of vegetation cover.

Having examined the correlations of individual bands with vegetation parameters, the NDVI and soil adjusted vegetation indices were calculated for each field site, and the results correlated with percentage vegetation cover. This approach tests the applicability of these indices in the Jordanian environment, and aims to put the work in the context of other studies which have been carried out in arid environments.

Finally, new vegetation indices were derived for the band combinations of the ATSR-2 sensor using the seven index categories described by Boyd *et al.* (1996) as a basis. Indices were produced using every combination of the first four bands of ATSR-2 and then correlated to percentage vegetation cover. As is explained in Section 5.3.3 thermal bands and individual forward bands were not included at this stage.

### **5.3.1 The relationship between individual wavebands and percentage vegetation cover**

It is debatable as to which band of ATSR-2 should be referred to as the middle infrared band. The data product description (Bailey, 1995) describes band 4 (1.58 -



1.64  $\mu\text{m}$ ) which is strictly a short wave infrared band, as being both thermal and visible thus fitting a MIR description. Band 5 (3.55 - 3.93  $\mu\text{m}$ ) that lies strictly in the MIR part of the spectrum is classed as a thermal band along with Bands 6 (10.4 - 11.3  $\mu\text{m}$ ) and 7 (11.5 - 12.5  $\mu\text{m}$ ). In this thesis, the bands will be referred to according to their wavelength position rather than following the product literature. The 1.58-1.64  $\mu\text{m}$  band is referred to as a short wave infrared band (SWIR) and the 3.55-3.93  $\mu\text{m}$  band is labelled the middle infrared band (MIR).

The results from correlating each individual ATSR-2 band with percentage vegetation cover are shown in Table 5.2. An equivalent table for AVHRR data is given in Table 5.3.

Table 5.2 *Pearson’s product moment correlation coefficients calculated for reflectance in the bands of ATSR-2 correlated against percentage vegetation cover. Significant correlations are achieved between the vegetation cover at all sites (Badia and Jordan Valley) and the first four bands of the ATSR-2. When only sites in the Badia are considered, the relationships obtained are inconsistent and often insignificant. Similar relationships occur with the nadir and forward looking bands.*

ATSR-2 ( $\mu\text{m}$ )	DATE					
	06/09/95		15/11/95		10/09/97	
	All sites	Badia only	All sites	Badia only	All sites	Badia only
Nadir -0.555	-0.626*	-0.520	-0.659*	-0.218	-0.658*	0.212
0.659	-0.826*	-0.701*	-0.838*	-0.242	-0.817*	0.145
0.865	-0.618*	-0.765*	-0.718*	-0.342	-0.675*	-0.01
1.58-1.67	-0.773*	-0.801*	-0.806*	-0.588*	-0.827*	-0.308
3.55-3.93	-0.212	-0.522	-0.138	0.430*	0.142	-0.364
10.4-11.3	0.148	0.182	-0.198	0.729*	-0.833*	0.143
11.5-12.5	missing data	missing data	0.065	-0.538	missing data	missing data
Forward, 0.555	-0.634*	-0.424	-0.656*	-0.160	-0.671*	-0.207
0.659	-0.800*	-0.533	-0.741*	-0.620*	-0.776*	-0.362
0.865	-0.597*	-0.660*	-0.531	-0.648*	-0.707*	-0.450
1.58-1.67	-0.677*	-0.518	-0.732*	-0.725*	-0.776*	-0.540
3.55-3.93	-0.914*	0.044	-0.272	0.203	0.043	-0.184
10.4-11.3	-0.053	-0.718*	0.193	0.283	0.733*	0.307
11.5-12.5	missing data	missing data	0.333	0.636*	missing data	missing data

Significant at the 95 % confidence level

\*

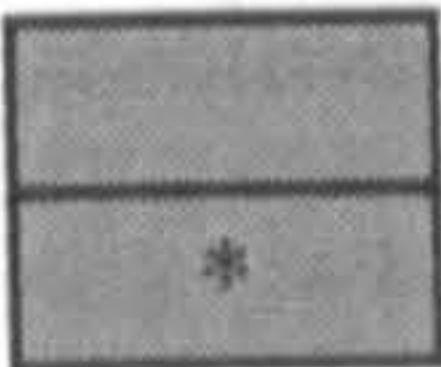
Significant at the 99 % confidence level

'missing data' denotes values where data for that band was not recorded by the sensor



Table 5.3 Pearson's product moment correlation coefficients calculated for reflectance in the bands of the AVHRR correlated against percentage vegetation cover. Significant negative relationships are obtained between percentage vegetation cover and reflectance for all bands when all sites (Jordan Valley and Badia) are considered. When only the Badia is considered, there is only one significant negative correlation.

	DATE							
	31/03/96		28/04/96		05/05/96		05/09/97	
AVHRR $\mu\text{m}$	All	Badia	All	Badia	All	Badia	All	Badia
0.58 -0.68	-0.785*	-0.349	-0.704*	-0.152	-0.781*	-0.204	-0.815*	0.125
0.725 - 1.1	-0.741*	-0.542*	-0.545*	-0.122	-0.729*	-0.339	-0.763*	-0.014
3.55 - 3.93	-0.830*	-0.189	-0.781*	0.147	-0.830*	0.085	-0.756*	-0.13
10.3 - 11.3	-0.793*	0.313	-0.554*	0.191	-0.828*	0.013	-0.748*	0.017
11.5 - 12.5	-0.805*	0.289	-0.660*	0.278	-0.820*	0.029	-0.746*	-0.14



Significant at the 99 % confidence level  
Significant at the 95 % confidence level

Table 5.2 shows that the visible, near-infrared and short wave infrared bands of ATSR-2 all gave significant negative correlations with percentage vegetation cover when sites from both the Badia and Jordan Valley are used. This is true of the nadir and the forward bands, although correlations between vegetation and reflectance in the nadir bands are generally stronger than those from the forward view. The thermal bands of ATSR-2 give low, insignificant correlations between vegetation cover and temperature across the scenes.

There are several possible explanations for these trends. As percentage vegetation cover increases, a negative correlation is observed with red reflectance. This is an anticipated result given that vegetation has a lower reflectance than soil in red wavelengths (Figure 2.14, Chapter 2). The correlation between increasing vegetation cover and the near-infrared reflectance is also negative. This contradicts expected/typical results found by most other workers. Figure 2.14 indicates that the reflectance of vegetation in the Badia in the near-infrared is lower than that of soil. Graetz and Gentle (1982) suggest the state and structure of mesophyll cells in perennial shrubs cause near-infrared reflectance to decrease as vegetation amount increases, and this helps to explain the patterns seen here. Other contributions to a negative correlation between percentage cover and near-infrared reflectance include



the work of Otterman (1974, 1975) on the infrared-paradox. This describes how, as vegetation increases, the amount of shadowing by vegetation also increases and this produces an overall decline in infrared reflectance.

The difference between the correlations between percentage vegetation cover and the forward and nadir views of ATSR-2 are largely due to sensor/sun geometry. Orbital parameters and data given in image header information indicate that the ATSR-2 is imaging Jordan in a descending mode and a forward scatter direction. As discussed in Chapter 4, viewing in a forward scatter direction produces a greater contrast between nadir and 55°, than the same area being viewed in a backscatter direction. Reflectance values are lower in the forward view and as Table 5.2 indicates, less strongly correlated with percentage vegetation cover. This is because less illuminated vegetation and more shadow (both vegetation and soil) are seen. The forward view is also not viewing exactly the same ground area as the nadir look. Forward view pixels are about 1.5 x 2 km as opposed to 1 x 1 km a nadir (Higgins, 1995). They are resampled to 1 x 1 km for registration and geolocational purposes but the pixels do not contain information about exactly the same area as those taken at nadir.

The results presented in Table 5.2 indicate that in the case of ATSR-2, relationships between thermal wavebands and vegetation cover are largely insignificant. Theoretically, vegetation cover should exhibit a negative relationship with surface brightness temperatures (Lambin and Ehrlich, 1996). An increase in biomass leads to an increase in evapotranspiration and a larger latent heat transfer. Plants also have a lower heat capacity than soil and are thus cooler during daylight hours. However, as Price (1985) comments, there are many uncertainties associated with the use of thermal infrared data and this relationship can be difficult to extract. The effects of the atmosphere can be problematic with water vapour and aerosols absorbing and transmitting radiation. The resistance factor which relates surface temperature and humidity to sensible and latent heat is also not constant. It holds a complex relationship with surface covers and is difficult to model. The ATSR-2 and AVHRR imagery used was not corrected for atmospheric effects in the thermal infrared wavebands. This is difficult to do, and the 5S code used only accounts for atmospheric



effects in the visible and near-infrared wavebands. Furthermore, the small vegetation percentage coverages found in the Badia also mean that any effects on temperature will be small and in this case, insignificant.

When only sites in the Badia region are considered, individual scenes display significant relationships but no band, except the near-infrared and short wave infrared in the forward look, produce consistent negative correlations between percentage vegetation coverage and reflectance across different scenes. In cases of low levels of vegetation cover as found in the Badia, the signal received at the sensor is highly influenced by the soil and shadow. Since the field sites differ in soil type and position in the swath, variations in reflectance due to soil and shadow are not consistent between sites. This implies that changes due to variations in vegetation cover cannot be discriminated.

As with ATSR-2, all AVHRR bands produced significant negative correlations with percentage vegetation cover when field sites in the Jordan Valley were included. When only the Badia sites were considered, none of the bands gave consistently significant results. Once again, it appears that changes in percentage vegetation cover are too small and masked by the strong influence of the soil and atmosphere to have any significant impact on the signal received.

#### **5.3.1.1 The relationship between reflected middle infrared and percentage vegetation cover**

Radiation in middle infrared wavelengths is composed of a mixture of reflected and emitted radiation. The emitted component is more sensitive to external variables such as atmospheric conditions than to the properties of the Earth's surface but recent research in tropical and temperate regions suggests that reflection in middle infrared wavelengths may be strongly related to biophysical parameters (Boyd and Curran, 1998).

Table 5.2 indicates that band 5 of the ATSR-2 (middle infrared/thermal wavelengths) shows poor, insignificant correlations with percentage vegetation cover. Using a



method by Kaufman and Remer (1994) adapted for ATSR-2 by Boyd *et al.* (1998), this 3.7  $\mu\text{m}$  band can be split into its reflected and emitted components, and percentage vegetation coverage estimates can be compared with the reflected part of the middle infrared wavelengths. This may show higher correlations to percentage vegetation cover than for the entire 3.7  $\mu\text{m}$  band radiance (Boyd *et al.*, 1998).

The method of band splitting essentially follows three steps: (i) 3.7  $\mu\text{m}$  brightness temperatures are converted to radiance values using the Planck function, (ii) radiance for the 10.5  $\mu\text{m}$  band is calculated using Planck’s function, and (iii) middle infrared reflectance is calculated using the results from (i) and (ii) (Boyd *et al.*, 1998). The equations used at each stage are given in Appendix 6.

The results of correlating percentage vegetation cover against the reflected part of the 3.7  $\mu\text{m}$  band are shown in Table 5.4. The correlation values for the 1.6  $\mu\text{m}$  band and the full 3.7  $\mu\text{m}$  band are also given for comparison.

*Table 5.4: Pearson’s product moment correlation coefficients calculated for the correlation between percentage vegetation cover and the 1.6  $\mu\text{m}$  band, the full 3.7  $\mu\text{m}$  band and the reflected part of the 3.7  $\mu\text{m}$  band of ATSR-2. The results between image dates are not consistent. Apart from the Badia sites in the 10/09/97 image, better negative correlations are obtained using the 1.6  $\mu\text{m}$  band than the reflected component of the 3.7  $\mu\text{m}$  band.*

	ATSR-2 image date					
	06/09/95		15/11/95		10/09/97	
	All sites	Badia	All sites	Badia	All sites	Badia
1.6 $\mu\text{m}$	-0.773*	-0.801*	-0.806*	-0.588*	-0.827*	-0.308
full 3.7 $\mu\text{m}$	-0.212	-0.522	-0.138	0.430	0.142	-0.364
reflected 3.7 $\mu\text{m}$	-0.765*	0.719*	0.099	0.291	-0.024	-0.920*

significant at 99 % confidence interval

\*

significant at 95 % confidence interval

The results from correlating percentage vegetation cover and the reflected portion of the 3.7  $\mu\text{m}$ , middle infrared band of ATSR-2 are inconsistent between images. In the case of the 06/09/95 image, correlations between percentage vegetation cover and



reflected middle infrared radiation are very similar to those of the short wave infrared or 1.6  $\mu\text{m}$  band. This supports the notion put forward by Boyd and Curran (1998) and Kaufman and Remer (1994), that a reduction in MIR reflectance is associated with an increase in canopy complexity and canopy water content associated with increasing vegetation cover. Similar processes appear to be occurring in the shortwave infrared region as in the reflected part of the middle infrared (Boyd *et al.*, 1998).

Results from 15/11/95 and 10/09/97 however, show very poor correlations between vegetation cover and reflected middle infrared, and the results from the 1.6  $\mu\text{m}$  and 3.7  $\mu\text{m}$  reflected region are very different. It is, therefore, very difficult to draw any general conclusions.

There are several reasons which can be put forward as an explanation to why reflected middle infrared radiation shows a poor correlation with percentage vegetation cover in arid areas. Firstly, the middle infrared reflectance is related to canopy water content (Belward, 1991). In an arid region, an increase in percentage cover does not necessarily mean a dramatic increase in canopy water content. As is explained in Section 5.5 at the end of this chapter, desert plants can be very woody and have adapted to cope with a general lack of water. Canopy water content will not necessarily increase as percentage cover increases.

The lack of consistent results also suggests there are many factors influencing middle infrared radiation that vary temporally (Boyd *et al.*, 1998). Furthermore, the method used here for calculating reflected middle infrared radiation assumed constant emissivity. At low NDVIs, background emissivity is a significant factor that should be accounted for (Oliso, 1995). Although such data were unavailable for use in this study, with additional information available on emissivity, the middle infrared radiation may show more significant results. Emissivity is, however, difficult to measure.

The method proposed by Kaufman and Remer (1994) was developed for use with dark, dense vegetation. This is appropriate for use with temperate or tropical forests



but, as the results presented here indicate, it may be of more limited use in arid regions where vegetation cover is low. The reflected part of the middle infrared produced weaker correlations with percentage vegetation cover than the more commonly used red/near-infrared based vegetation indices.

### 5.3.2 Frequently used vegetation indices

Having examined the way in which each individual waveband is related to percentage vegetation cover, vegetation indices and their usefulness for arid land vegetation detection were considered. In particular, the six indices described in Section 5.2 were investigated:- the RVI, NDVI, PVI, SAVI, TSAVI and SAVI<sub>2</sub>. Atmospherically resistant indices such as GEMI were omitted as the effects of the atmosphere had already been accounted for through the process of atmospheric correction.

In the calculation of SAVI, SAVI<sub>2</sub>, and TSAVI, values for 'a' and 'b', the slope and intercept of the soil line were required. These were calculated by plotting image reflectance values for all points in red/near-infrared feature space. The values were found to form a triangle similar to those identified by Baret *et al.* (1993), the right side of which was taken to be the soil line. Due to the changing nature of the soil across the image, it would have been ideal to have had 'a' and 'b' values for the soils at each field site. This would have required ground radiometric data of individual reflectance measurements for soil and vegetation which were not recorded at all sites. The differences in band widths, ground resolution, atmospheric effects and calibration procedures mean that the reflectance values taken from ground radiometry data cannot be directly equated with the reflectance values from imagery. Whilst it can be argued that the use of a single soil line across large areas is inappropriate (by reducing the accuracy of models designed to measure greenness (Williamson, 1989)), on an image-wide analysis it can be easily and quickly applied and provides a good option where data on individual soil types is unavailable.

Table 5.5 presents the slope and the intercept coefficients used in the calculation of vegetation indices for the selected ATSR-2 and AVHRR images. The results from



correlating each index with percentage vegetation cover are given in Tables 5.6 and 5.7.

Table 5.5: Soil line coefficients calculated from ATSR-2 and AVHRR images

	Image Date	Slope (a)	Intercept (b)
ATSR-2	06/09/95	1.0842	2.0838
	15/11/95	1.1054	0.5989
	10/09/97	1.0624	2.0201
AVHRR	31/03/96	1.0936	2.6440
	28/04/96	1.1012	2.1949
	05/05/96	1.0911	0.4322
	05/09/97	1.2140	2.7070

Table 5.6 Pearson’s product moment correlation coefficients calculated for selected vegetation indices from ATSR-2 correlated against percentage vegetation cover. Significant correlations are obtained between indices and percentage vegetation cover when all sites (Jordan Valley and Badia) are considered. Soil adjusted vegetation indices (PVI, SAVI, TSAVI and SAVI<sub>2</sub>) do not give better correlations than the RVI and NDVI.

		DATE					
ATSR-2		06/09/95 Image		15/11/95 Image		10/09/97 Image	
		All sites	Badia only	All sites	Badia only	All sites	Badia only
RVI	nadir	0.938*	-0.255	0.923*	-0.406	0.923*	-0.654*
	forward	0.899*	-0.326	0.882*	-0.254	0.760*	-0.746*
NDVI	nadir	0.937*	-0.257	0.925*	-0.410	0.915*	-0.661*
	forward	0.897*	-0.329	0.902*	-0.254	0.803*	-0.479
PVI	nadir	0.918*	-0.456	0.895*	-0.469	0.883*	-0.757*
	forward	0.906*	-0.456	0.879*	-0.338	0.796*	-0.687*
SAVI	nadir	0.938*	-0.259	0.925*	-0.411	0.915*	-0.662*
	forward	0.898*	-0.331	0.903*	-0.258	0.803*	-0.482
TSAVI	nadir	0.937*	-0.414	0.926*	-0.433	0.918*	-0.719*
	forward	0.900*	-0.428	0.904*	-0.331	0.798*	-0.667*
SAVI <sub>2</sub>	nadir	0.940*	-0.409	0.924*	-0.426	0.925*	-0.713*
	forward	0.909*	-0.425	0.925*	-0.556	0.775*	-0.771

Significant at the 95 % confidence level

\*

Significant at the 99 % confidence level



Table 5.7 Pearson's product moment correlation coefficients calculated for selected vegetation indices from AVHRR correlated against percentage vegetation cover. The results are similar to those from ATSR-2 (see Table 5.6). Significant correlations are consistently obtained when all sites (Jordan Valley and Badia) are considered.

	DATE							
	31/03/96		28/04/96		05/05/96		05/09/97	
	All	Badia	All	Badia	All	Badia	All	Badia
RVI	0.806*	-0.297	0.804*	-0.515	0.801*	-0.371	0.879*	-0.652*
NDVI	0.796*	-0.302	0.796*	-0.519	0.798*	-0.380	0.874*	-0.657*
PVI	0.743*	-0.460*	0.766*	-0.677*	0.711*	-0.494	0.811*	-0.688*
SAVI	0.796*	-0.304	0.797*	-0.525	0.789*	-0.381	0.873*	-0.658*
TSAVI	0.743*	-0.462*	0.799*	-0.687*	0.788*	-0.395	0.871*	-0.672*
SAVI <sub>2</sub>	0.813*	-0.413*	0.808*	-0.862*	0.799*	-0.385	0.876*	-0.668*

Significant at the 99 % confidence level

\*

Significant at the 95 % confidence level

From Tables 5.6 and 5.7, it appears that for studies of arid land vegetation in Jordan using ATSR-2 on the one hand and AVHRR on the other hand, there is very little difference between the use of different indices. When looking at sites in both the Badia and the Jordan Valley, the use of a soil adjusted vegetation index does not significantly enhance correlations with percentage vegetation cover. When considering only those sites in the Badia i.e. very low levels of vegetation cover, significant correlations are found across all images with soil adjusted vegetation indices (PVI, SAVI and SAVI<sub>2</sub>) but these correlations are significantly negative rather than the anticipated positive result. As percentage vegetation cover increases, the vegetation index decreases. There are several reasons which could account for this. The correlation is negative since the index is essentially sensitive to differences between the soils at the different sites, and gives little information about the vegetation characteristics. Chenopodiacea vegetation in the area consists of a high proportion of dry brown biomass as opposed to green biomass which means the reflectance of the vegetation is affected. For example, Richardson and Everitt (1992) conducting a study in the South Texas Plains found similar results. Vegetation indices were found to be significantly correlated with green and brown biomass but the relationship with brown biomass was the inverse of that for green biomass.



It is interesting to note that there is a significant relationship between percentage vegetation cover and all the vegetation indices for all images taken in autumn 1997. Reasons for these trends could be due to the fact that soil moisture values and percentage vegetation cover estimates are high during this period (Figure 2.4 and Table 2.4, Chapter 2). Richardson and Everitt (1992) also comment that the presence of soil moisture significantly improves correlations between vegetation indices and standing green biomass. Results from Jordan as a whole indicate that the vegetation index/percentage cover relationship is strongest with higher levels of vegetation cover.

When considering the whole range of sites across Jordan (i.e. in both the Jordan Valley and the Badia), correlations between percentage vegetation cover and the vegetation indices as calculated for from the ATSR-2 data were less strong with data collected at a forward view angle of  $55^\circ$  than for data collected at nadir. When considering only sites in the Badia the relationship is variable. This result confirms those found when correlating percentage vegetation cover with individual wavebands (Tables 5.2 and 5.3), and can again be attributed to the fact that in a forward scatter direction, differences between vegetation reflectance and soil reflectance are reduced due to the presence of shadow.

### **5.3.3 The use of 'new' vegetation indices**

Having investigated the application of frequently used vegetation indices to arid land vegetation detection, new indices using the bands of ATSR-2 were developed. New indices were not formulated for AVHRR wavebands since the AVHRR is a well known, extensively used sensor. The ATSR-2 offers the opportunity to assess new wavebands in the forward as well as the nadir look. In Section 5.3.1, it was found that none of the thermal bands were significantly correlated with percentage vegetation cover. Consequently, it was decided that only vegetation indices utilising the visible, near-infrared and shortwave infrared bands of ATSR-2 would be calculated. Indices were constructed using every combination of visible, near-infrared and shortwave infrared bands for, firstly, the nadir bands, secondly the forward bands and finally, the nadir bands combined with the forward bands. Combining the bands should allow



assessment of the extent to which the forward-look data added any explanation in the variance of vegetation cover. A complete list of indices investigated is given in Appendix 7 but Table 5.8 shows those which consistently gave significant correlations with percentage vegetation cover.

*Table 5.8 Pearson's product moment correlation coefficients calculated for 'new' indices from ATSR-2 data correlated against percentage vegetation cover. Significant correlations are obtained using various combinations of the green (g), red (r), near infrared (nir) and shortwave infrared (swir) bands of ATSR-2. The index,  $g/(nir*swir*r)$ , is significant when all combinations of bands are used.*

	DATE					
ATSR-2	06/09/95		15/11/95		10/09/97	
Nadir bands	All	Badia only	All	Badia only	All	Badia only
$g/(nir*swir*r)$	0.899*	0.574*	0.890*	0.922*	0.917*	0.490
Forward bands						
$r/(nir*swir*g)$	0.606*	0.525	0.590*	0.451	0.703*	0.576*
$l/(nir*swir)$	0.716*	0.547	0.731*	0.529	0.763*	0.659*
$l/(swir*r)$	0.767*	0.518	0.789*	0.488	0.718*	0.625*
$g/(nir*swir*r)$	0.822*	0.561*	0.825*	0.575*	0.801*	0.726*
$nir*r/g$	-0.665*	-0.615*	-0.832*	-0.539	-0.819*	-0.649*
$swir*r/g$	-0.784*	-0.644*	-0.810*	-0.517	-0.936*	-0.691*
Forward + nadir						
$l/(nir*swir)$	0.786*	0.646*	0.774*	0.818*	0.823*	0.486
$g/(nir*swir*r)$	0.876*	0.699*	0.869*	0.888*	0.887*	0.662*
$nir*r/g$	-0.846*	-0.634*	-0.853*	-0.675*	-0.876*	-0.625*
$swir*r/g$	-0.871*	-0.648*	-0.883*	-0.796*	-0.899*	-0.741*
$nir*swir/g$	-0.546	-0.569*	-0.668*	-0.713*	-0.746*	-0.782*

Significant at the 99 % confidence level

\*

Significant at the 95 % confidence level

As can be seen in Table 5.8, there are a number of different indices that give significant correlations with percentage vegetation cover. Unlike the NDVI and soil adjusted indices, these work well with sites in the Badia, as well as for sites across Jordan as a whole, and have relationships that work in the same direction (i.e. both negative or both positive) in both cases. The only index which showed significant correlations across all sites with nadir, forward, and nadir and forward view was  $g/(nir*swir*r)$ . From looking at the figures, the highest correlation was attained using only the nadir bands. Using the forward view bands or adding the forward view bands



to the nadir view bands resulted in lower correlations which suggests that information held in the forward bands does not aid the estimation of percentage vegetation cover. Although these 'new' indices do appear to give good correlations with percentage cover values for sites both in the Badia and the Jordan Valley, one of the problems about using 'new' vegetation indices made up with combinations of bands of ATSR-2 is that they are hard to interpret and lose their physical meaning. Unlike the NDVI, they also cannot be related to other longer archives of data.

#### **5.4 Seasonal variations detected using vegetation indices**

In order to examine seasonal variations in percentage vegetation cover as detected by ATSR-2, the NDVI was calculated for all available ATSR-2 images. The NDVI was chosen as it is the most commonly used vegetation index and results from Table 5.6 indicated that it performed as well as soil adjusted vegetation indices in terms of its relationship with percentage vegetation cover. The results presented in Tables 5.2 and 5.6 indicate that no extra information about percentage vegetation cover is attained by using the forward look, thus seasonal variations were examined with reference to measurements taken at the nadir view only. Figures 5.2 and 5.3 show the variation of the NDVI over time as calculated from ATSR-2 and AVHRR data respectively.



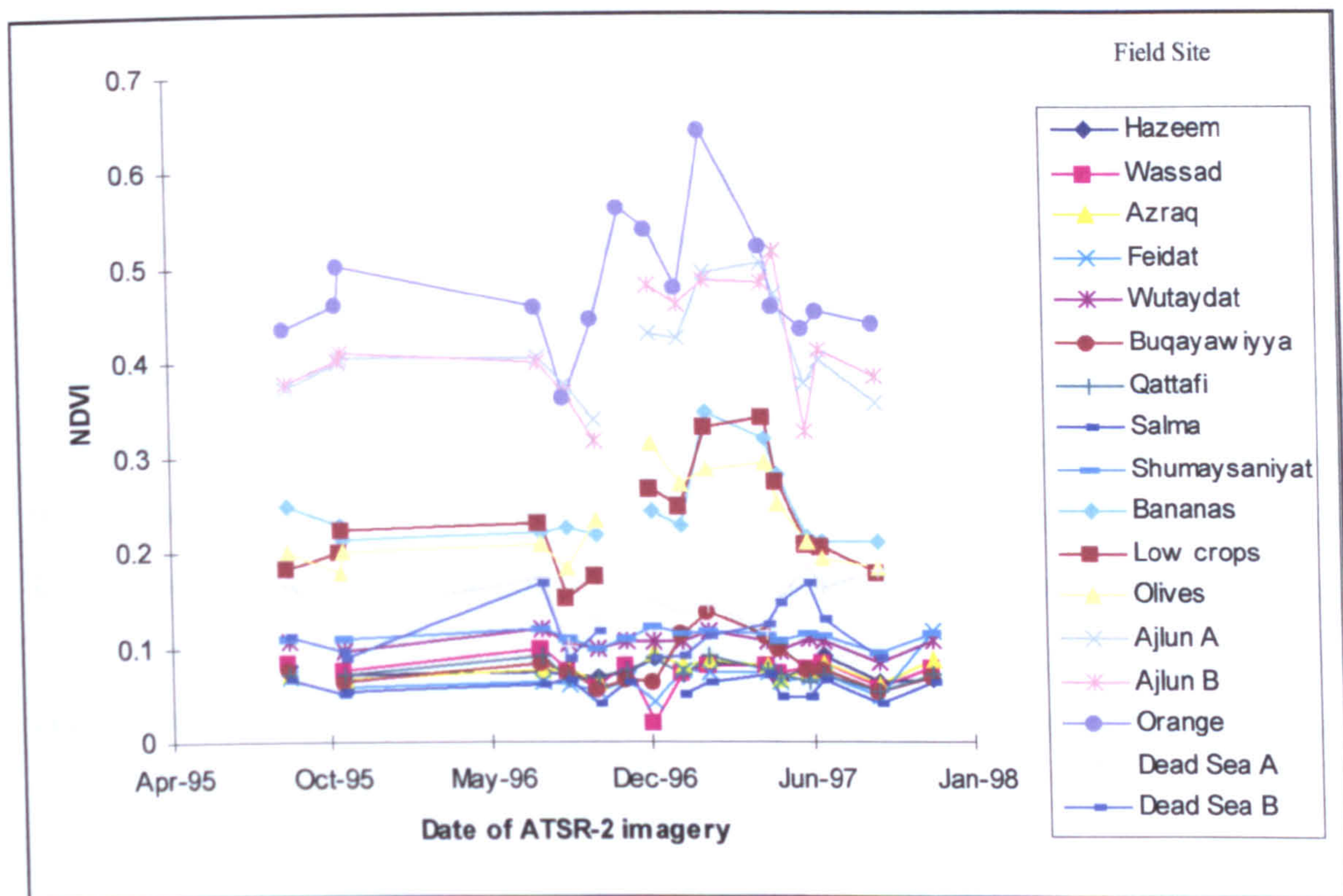


Figure 5.2: NDVI variation over time as recorded by ATSR-2 data at different field sites. Sites in the Badia show little seasonal variation. Vegetation at sites in the Jordan Valley increases over the winter months and decreases during the summer

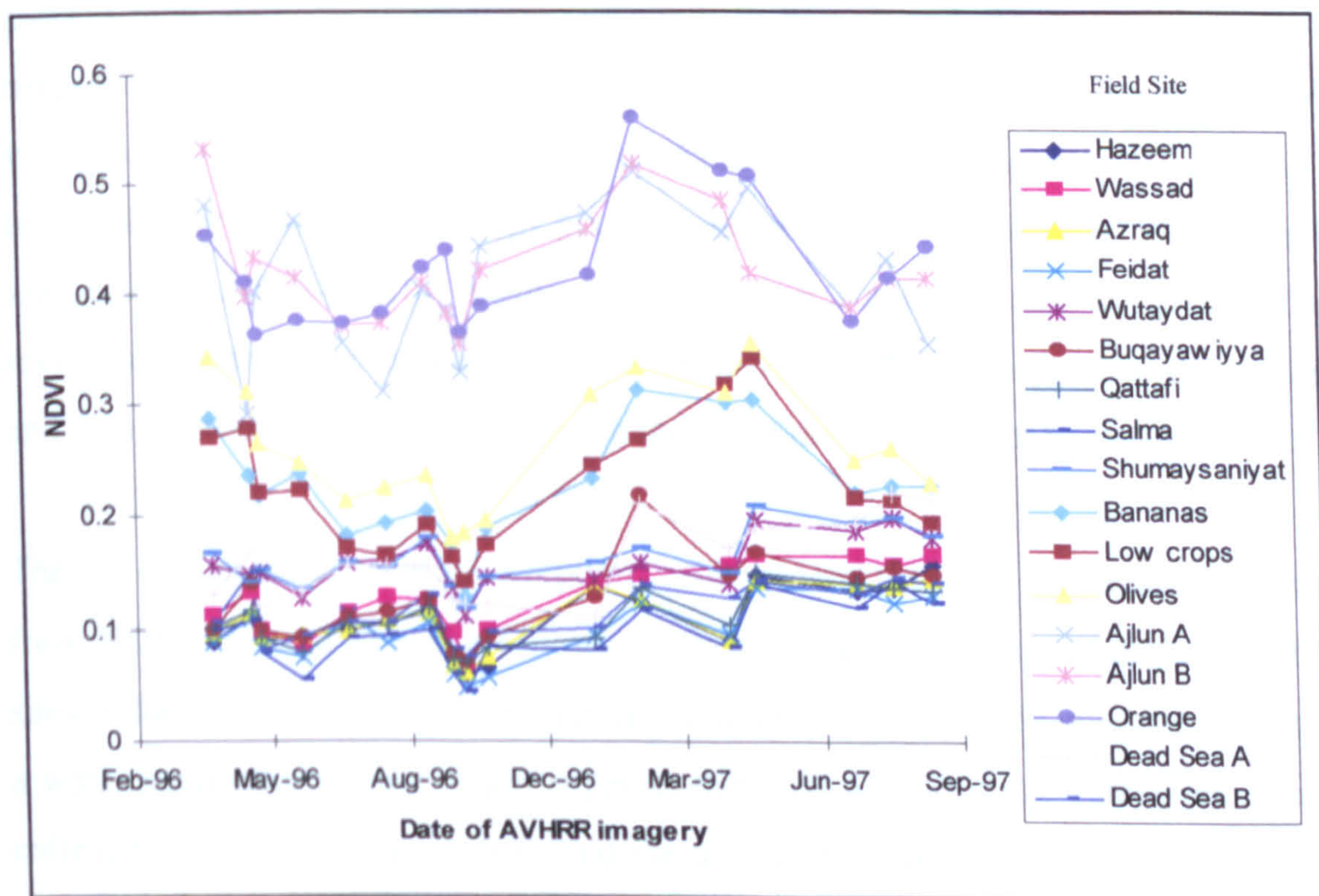


Figure 5.3: NDVI variation over time as recorded by AVHRR data at different field sites. Values are at their highest in the spring after winter rainfall and decrease during the summer.



Figure 5.2 shows the way in which NDVI varies over time. With the absence of data from spring 1996, it is hard to make generalisations about intra-annual patterns in NDVI response. However, it appears that irrigated sites in the Jordan Valley, and sites to the East of the Valley on the mountainous areas of Ajlun and Jerash, show some seasonality with an increase in NDVI during winter and early spring. Although interviews with farmers in the Jordan Valley revealed that irrigation operates throughout the year, results suggest that vegetation is also responding to increased water availability in the winter months due to rainfall and runoff and low evaporation. Irrigation equipment is mended by the farmers during the summer months. Vegetation is low during this period. NDVI values at the field sites of *Ajlun* (A and B) and Olives near Jerash are higher than those at irrigated sites in the Jordan Valley but show a similar seasonal pattern.

Sites in the Badia show little or no seasonality in terms of the NDVI. This may be due to a number of reasons. The field work results suggested that vegetation growth, even after winter rainfall is slight and can be very localised. Grazing pressure in both these areas is high. As soon as vegetation responds to rainfall and shoots appear, nomadic tribespeople move their livestock into the zone and the new shoots are eaten before vegetation can grow and re-establish itself. Furthermore, any seasonal changes may be on a scale that it is not detected by pixel-based reflectance values especially at the 1.1 km scale of ATSR-2. The results from Tables 5.2 and 5.5 also suggest that the relationship between percentage vegetation cover and NDVI is poor in desert areas and thus any seasonality associated with the vegetation should not be expected.

The site of *Buqayawiyya* is an exception to this general rule, and the trend line derived from NDVI values at this site follows the same general pattern as that derived from sites in the Jordan Valley. *Buqayawiyya* is a relatively large study area and the site of a water harvesting project which suggests that it is a good water catchment area. A colleague, Kevin Tansey, who visited the area in the Spring 1997, reported a good covering of grass associated with seasonal rainfall at this time (1998, personal communication).



Figure 5.3 displays the seasonal trends of the field sites as recorded by the AVHRR derived NDVI. As one would anticipate, temporal trends in the AVHRR data are very similar to those recorded by the ATSR-2. Absolute NDVI values are not the same due to differences in the bandwidth, calibration and resolution of the sensors.

From Figures 5.2 and 5.3, it can be said that both ATSR-2 and AVHRR indicate that field sites in the Jordan Valley show seasonal change in terms of vegetation dynamics. AVHRR also suggests that field sites in the Badia show seasonal change in NDVI, but a poor correlation with percentage vegetation cover as indicated by Table 5.6 indicates that a significant relationship between NDVI and solely vegetation cover cannot be substantiated. It could be argued, that if vegetation changes do not account for the pattern seen in the Badia field sites, then it is likely that the same pattern is not attributable to vegetational changes in the Jordan valley or Ajlun area either, but that they are a function of other factors such as sensor drift and atmospheric effects. Having said this however with similar patterns being viewed in both ATSR-2 and AVHRR data, some seasonal processes must be at work, these are likely to be vegetational in the case of the Jordan Valley, but may be background soil effects and shadow in the case of the Badia.

## **5.5 Problems associated with the use of vegetation indices**

This chapter has examined the application of vegetation indices to the mapping and monitoring of sparsely vegetated areas. The relationship between percentage vegetation cover and radiometric response has been considered in the context of individual wavebands, well known vegetation indices and new indices derived from the bands of the ATSR-2. The results have shown that whilst vegetation *per se* does show a strong correlation with spectral indices, discrimination of very low levels of vegetation as in the case of the Badia remains very difficult. This is due to a number of reasons:-

### **(i) The nature and type of arid land vegetation**

A significant problem is due to the type and nature of arid land vegetation. Both satellite sensor wavebands and vegetation indices based on red/near-infrared



wavelengths are designed with a specific spectral response of vegetation in mind. This response is representative of photosynthetically active 'green' plants such as those found in temperate or tropical climates. In 'green' plants, high leaf water content and chlorophyll pigmentation levels, together with little visible soil and stem structure, result in low reflectance in the red wavelengths due to chlorophyll absorption. Reflectance is high in near-infrared wavelengths due to the internal structure of the leaf and the reflection of energy by spongy mesophyll tissue (Ray, 1995). Figure 2.13 shows the spectral response of vegetation at sites in the Badia compared to a typical spectra of green grass (taken from USGS database, <http://speclab.cr.usgs.gov/browse.html>, July 1998).

Whilst the arid land vegetation shows characteristics of a typical vegetation spectral curve in that there is a distinctive increase in spectral response from red wavelengths to near-infrared wavelengths, the patterns in response do not show the same distinction as compared with those of green vegetation more characteristic of temperate climates. Arid vegetation has adapted to living in extreme environmental conditions. Adaptations designed to conserve water and prevent overheating, influence the reflection and absorption of solar radiation and hence the corresponding spectral response.

One of the ways in which plants cope with the scarcity of water is to reduce leaf area and transpiration as much as possible and rely on an extensive root system for moisture collection (Ray, 1995). Roots penetrate deeply into the soil drawing up on ground water reserves as well as branching widely near the surface collecting water from a large area. Reducing leaf area is problematic in that smaller leaves cannot intercept as much solar radiation - thus photosynthesis is reduced and potential production decreases. In some desert plants reduced leaf area is counterbalanced by an increased leaf thickness and more photosynthetic mesophyll (Fitter and Hay, 1987). Other adaptations to water loss include a thick coating of wax on the leaf surface, leaf loss during periods of extensive drought and the presence of leaf hair (Ray, 1995). The most extreme examples of prevention of water loss are desert plants which have no



leaves at all for most of the year but rely instead on photosynthetic tissue in their stems.

In addition to the prevention of water loss, arid plants also protect themselves against extreme temperatures. At very high temperatures metabolic processes in the plant such as photosynthesis, respiration, enzyme activity and protoplasmic streaming can begin to break down (Gates, 1980, Fitter and Hay, 1987). Prevention against high leaf temperatures include the adoption of small leaves and paraheliotropic sun tracking where leaves move and change shape to avoid excessive absorption of solar energy (Ray, 1995). Plants may also have open canopies with non-overlapping leaves enhancing convective air cooling.

Many of these affects were observed in the arid plants found in the Badia, and although these are difficult to quantify, photographic evidence and observations made in the field, allow one to use plant features in order to explain the spectral responses shown in Figure 5.4.

Plate 5.1 shows a photograph of a typical Chenopod shrub, whilst Plate 5.2 shows a photograph of grass found in the Badia just after winter rainfall. By comparing the two photographs one can appreciate that in many cases, shrubs and bushes found in arid regions are not 'green' but rather grey/green/brown in colour. A lack of chlorophyll in plant tissue and a reduction in photosynthesis produces increased reflectances in the visible part of the spectrum and means that there is no marked increase in reflectance in the near infrared wavelengths. None of the arid vegetation signatures shown in Figure 5.4 show a characteristic green peak. Furthermore, in addition to a lack of chlorophyll, increased reflectances in the visible wavelengths can also result from a secretion of salt on the surface of the leaves and the presence of leaf hairs (Ray, 1995).





*Plate 5.1: Salsola vermiculata, taken at Qattafi in the autumn 1997. This plant is woody and brown/grey/green in colour. It is not typically green and photosynthetically active.*





*Plate 5.2: Grass at Buqayawiyya, in the spring 1996. Green, photosynthetically active vegetation does grow in some areas of the Badia in the period after winter rainfall.*

Reflectance in the near-infrared part of the spectrum is controlled by internal leaf structure, particularly the amount of water within the plant leaf tissue (e.g. Belward, 1991). Arid land vegetation has limited water within cell walls and often exhibits a woody structure. Reflectance in the near-infrared wavelengths is suppressed compared with that of fresh, green vegetation such as that characteristic of wetter climates.

Although arid land vegetation does show differences in spectral response compared to green more photosynthetically active vegetation, it can be argued that it does still exhibit a significant difference between reflectance in the red and near-infrared wavelengths. This difference is too small, however, to be detected with wavebands such as those given by the ATSR-2 and AVHRR.



(ii) The background soil

In areas where vegetation is of very low densities the influence of the background soil on the spectral response of a single pixel can be significant. This is true both as soil occupies a large proportion of each pixel due to the sparsely populated nature of the area in terms of plants, and as many plants are relatively open allowing the underlying background soil to show through plant leaves and stems. Soil adjusted vegetation indices aim to compensate for the influence of the background soil but this is hard to achieve on an image-wide basis. Soils vary over small areas in mineralogy, colour, texture, surface roughness and salinity. The use of soil parameters derived from a single soil line fail to take all these variations into account. A mean soil line will adequately account for some soils but not for others. Furthermore, the difference between ground derived spectra and those derived from imagery also makes deriving individual soil lines for each field site very difficult. Thus soil must be accounted for on an image wide basis, and as a consequence the issue of background soil remains one of the biggest problems facing satellite remote sensing of vegetation in arid areas.

Figure 2.10 indicates how soils in the Badia region of Jordan are very bright and reflectance often exceeds that of vegetation in both the visible and near-infrared wavebands. A bright soil dominates the signal received from the ground, and results in an underestimation of the amount of vegetation (Elvidge and Lyon, 1985) or as this study shows results in poor correlations between percentage vegetation cover and spectral response.

The discussion in Chapter 4 highlighted how viewing the ground at an angle of  $55^\circ$  increases the amount of viewed vegetation and decreases the amount of soil viewed. As a result, one would expect the influence of background soil to be less of a problem in imagery collected off-nadir. However, the work on vegetation indices (Section 5.3.2) showed that correlations obtained between percentage vegetation cover and off-nadir imagery gave no improvement over those calculated at nadir. There were seemingly no advantages to sparse vegetation detection by viewing more vegetation and less soil. Any advantages were masked by the nature and type of vegetation (as in (i)) or the presence of shadow (iii).



### (iii) Shadow

As discussed in Chapter 4, shadow makes up a significant proportion of sparsely vegetated surfaces. This is especially true when the sun is at oblique angles or when the scene is viewed at an off-nadir angle in a forward scatter direction, such as in the case of ATSR-2 over Jordan. A high proportion of shadow in a pixel means the overall signal from the ground is darkened. Although one would expect that as vegetation increases, the amount of shadow increases and reflectance will thus still be comparable as reflectance decreases proportionally to the increase in vegetation, this situation is less straightforward and a simple relationship cannot be assumed. As vegetation increases, the amount of shadow increases to a point where plants start to overlap, at which point a further decrease occurs. Furthermore, field sites across the image vary in the amount of shadow due to positions in the swath, differences in sun-sensor geometry and variations in plant density, shape and size. Shadow also affects wavelengths differentially (Tueller and Oleson, 1989). Band ratioing does minimise this variability but due to the nature of the indices, the relationship is non linear.

When considering the correlation of vegetation indices and percentage vegetation cover on an image-wide scale, results are confused due the presence of shadow. In sparsely vegetated landscape, the contribution of shadow is significant, but its effect is not consistent and is therefore difficult to account for.

### (iv) Other factors

In this study, the vegetation parameter considered was percentage vegetation cover. In the case of Chenopod shrubs in Jordan, percentage vegetation cover was the only practical option given the nature of the vegetation, the lack of leaves and the methods and time available. Leaf Area Index, including some measure of leaf angle and orientation, may prove a better basis for studying the relationship between vegetation and remotely sensed data, in other contexts, but was not an option here. Percentage vegetation cover gives no indication of the number of photosynthetically active surfaces seen from above. As Ray (1995) comments, plants in arid and semi-arid regions often use a vertical orientation of their photosynthetic surfaces to minimise exposure to the sun. From above, this would mean that although percentage cover



might be high, reflectance may not represent that of vegetation due to the nature of the surfaces exposed to the sensor. Similarly, percentage vegetation cover can incorporate a range of different leaf area index values each of which produces a variety of spectral responses.

## **5.6 Summary and conclusions**

The results of the work discussed in this chapter indicate that:-

- Indices calculated from the ATSR-2 and AVHRR sensors both show good overall correlations with percentage vegetation cover but vegetation indices cannot be used to discriminate between low levels of cover in the Badia region. Significant correlations are obtained using the PVI but these correlations are relatively low and difficult to interpret due to the nature of the relationship changing as desert areas are selected.
- The forward look of ATSR-2 adds no advantages in terms of arid land vegetation detection. The forward view sees more vegetation but, due to the effect of shadow, correlations between percentage cover and vegetation index are reduced.
- New indices can be created using the bands of ATSR-2 and good correlations are obtained using the index  $g/(nir*r*swir)$ . However, one of the problems with the creation of new indices is that they are difficult to interpret and their physical meaning can be lost.
- Field sites in the Jordan Valley show seasonal change, with reflectance increasing during and after the winter rains due to vegetation dynamics. Poor correlations with percentage cover suggest that any seasonal change in the Badia will be the result of other factors such as soil and shadow.
- Background soil, shadow and the nature of the vegetation are all factors which contribute to the fact that arid land vegetation is difficult to detect and monitor using either ATSR-2 or AVHRR.

As Verstraete and Pinty (1996) comment, vegetation indices are good in that they present a simple solution to a complex problem. One of the problems with their use, however, is that they assume the nature and state of the target can be essentially



determined by a set of spectral observations given at the scale of a pixel. No account is made of sub-pixel processes, and any temporal variations imply that all other independent variables remain constant. In order to look at change in vegetation over time more effectively, one of the options is to adopt a modelling approach. Chapter 6 considers an alternative method for detecting and monitoring vegetation in an arid region by using a modelling approach. By modelling the surface, one can attempt to understand the way in which radiation interacts with the surface at scales smaller than the size of a single pixel (i.e. 1 km x 1 km in the case of ATSR-2). This enables one to take into account the effects of solar and viewing geometries, predict the influence of shadow, and in turn, predict percentage vegetation cover for sparsely vegetated areas from remotely sensed data.



- 6.0 Arid land vegetation analysis: a modelling approach**
- 6.1 Introduction
- 6.2 Modelling
- 6.3 Understanding surface-energy interactions using the red/ near-infrared scattergram
  - 6.3.1 Model design
  - 6.3.2 Parameter estimation
    - 6.3.2.1 Estimation of the sub-pixel fractional shadow cover
    - 6.3.2.2 Estimation of the reflectance terms
  - 6.3.3 Estimation of sub-pixel fractional canopy cover and inversion
- 6.4 Model validation
- 6.5 Seasonal variations detected using the model
- 6.6 Model assumptions and limitations
- 6.7 Summary and conclusions



## 6.1 Introduction

Chapter 4 examined the way in which the Earth's surface can be modelled by using a simple geometric optical model to predict the effect of viewing off-nadir on pixel reflectance. Chapter 5 considered the application of vegetation indices in the detection and monitoring of arid land vegetation. Results showed that whilst vegetation indices are good at distinguishing between very low and very high amounts of vegetation cover (the Badia and the Jordan Valley), the ability to discriminate between very low amounts of cover is limited. The work discussed in this chapter aims to bring together the concepts of Chapters 4 and 5, using a model that considers processes operating at a sub-pixel scale in order to interpret information at the scale of a satellite pixel (i.e. 1 x 1 km).

## 6.2 Modelling

Jasinski (1996) has commented that although the use of vegetation indices provides scientists with a mechanism for estimating regionally variable plant attributes, they do so at the expense of an understanding of the underlying physics of the behaviour of a satellite image. Recent research has recognised a need to move away from the traditional means of estimating biophysical properties from satellite imagery (through the application of vegetation indices) to a consideration of the processes occurring on a sub-pixel level, and by adopting a modelling approach to help understand these. Hall *et al.* (1995) describe a paradigm shift from a vegetation index approach to a two stage process where (i) stand level reflectance is estimated in terms of linear combinations of reflectance-invariant, spectrally distinct components, and then, (ii) radiative transfer models are used to compute biophysical characteristics values as a function of end member fractions.

The remote sensing literature has numerous examples of models which have been developed using a two stage approach. One of the most well known of these is the invertible coniferous forest canopy model of Li and Strahler (1985). Coniferous trees are considered as randomly positioned green cones upon a contrasting background. By



using Monte Carlo simulation, Li and Strahler (1985) showed that the position of a pixel within greenness-brightness feature space was directly related to the number of canopies, height:width ratio of the canopies and the reflectance of three components, sunlit canopy, shadows and sunlit background. Although designed for forest canopies, the model of Li and Strahler (1985) is a good example of a model that is invertible, i.e., a model by which pixel level measurements of reflectance are used to infer biophysical characteristics (Goel and Thompson, 1984). In an operational sense, the ability to invert a model and retrieve useful parameters such as vegetation cover is extremely important. Unfortunately however, it is difficult to achieve. The dimensionality of the remote sensing measurement must equal or exceed the number of parameters being estimated (Hall *et al.*, 1995). Li and Strahler applied their technique to brightness and greenness data collected from red fir canopies, but they found that errors in determining the canopy parameters were large, ranging up to  $\pm 100\%$  (Hall *et al.*, 1995).

The Forest Light Interaction Model (FLIM) of Rosema *et al.* (1992) is a model designed for coniferous forests. Based on the Kootwijk forest in the Netherlands as a study area, FLIM retrieves parameters such as crown ground coverage, crown Leaf Area Index and crown yellowness. It particularly takes into account the effects of shadowing and crown transmittance. The forest is modelled as a discontinuous canopy with crowns and gaps. Forest reflectance is considered as a linear combination of four elements. They are shadowed and sunlight background as viewed through the canopy, and shadowed and sunlight background as viewed directly. These elements are modelled in terms of biophysical parameters which are then estimated through model inversion.

Li and Strahler's model and the FLIM focus on forest environments. Modelling a sparsely vegetated semi-arid surface presents a different set of problems to modelling a forested landscape. Franklin and Turner (1992) adopted the methodology of Li and Strahler (1985), and applied it to the estimation of crown size and density for semi-arid shrub vegetation in Mexico using SPOT imagery. They modelled shrub vegetation as spheres on a contrasting soil background and found that predictions of



crown size and density were subject to large errors of up to 35 %. Background noise also proved problematic, and a lack of variance in the reflectance of the sample dataset contributed to poor results (Professor Janet Franklin, personal communication, 1997).

The simple geometric optical model presented in Chapter 4 is broadly based on the model designed by Jupp *et al.* (1986). Jupp *et al.* (1986) examined vegetation in a semi-arid region by considering the semi-arid Eucalypt woodlands of Wycanna, in southern Queensland, Australia using Landsat MSS data. The woodlands are depicted as a discrete three-stratum land surface. Trees in the upper and mid-strata are represented as spheres of constant diameter, depth and height, whilst the lower level is a mixture of grass, litter and soil. The proportions of illuminated and shaded ground and canopy are calculated with respect to a given set of illumination and viewing geometries. Treating the plant canopy and background as Lambertian reflectors, the total reflectance of a pixel is taken to be the area weighted sum of the reflectance of each component. The model of Jupp *et al.* (1986) is difficult to invert and requires extensive field data collection. Whilst field data collection is necessarily needed for model development and testing, in an operational sense, a model is required so that it can provide information on the surface properties without having to spend large amounts of time and resources in the field.

There are many models that one could adopt. In order to examine vegetation detection and monitoring in the sparse rangelands of Jordan, it was decided the best modelling approach was one that used sub-pixel processes to provide an understanding of the information contained in satellite images, and that was also appropriate to measuring sparse vegetation in a desert environment. Since percentage vegetation cover was the parameter collected in the field, and the best measure of vegetation in this environment, a model had to be developed that used estimates of percentage vegetation cover. Models necessitating leaf angle distribution values, or Leaf Area Index, would be inappropriate because this information was unavailable. To be useful in an operational environment it is also advantageous to have a model that uses little field data in its formulation and which can be inverted to give useful information on



vegetation characteristics as an output. The remainder of this chapter describes the model chosen, its development and its application in the Jordan environment.

### **6.3 Understanding surface-energy interactions using the red/near-infrared scattergram**

As Chapter 4 and Section 6.2 indicate, many models exist that attempt to relate pixel reflectances to biophysical parameters. In the context of this study, the model described by Jasinski (1996) was adopted. This model is invertible and uses the red/near-infrared scattergram from a multispectral satellite image to derive information on percentage ground vegetation cover i.e. the vegetation parameter of interest in this work.

Jasinski (1996) developed his model for application in two areas, a coniferous forest site in France and an experimental site called Walnut Gulch in Southeast Arizona. Walnut Gulch is a semi-arid site with vegetation similar in form and structure to that of the Badia (Professor Tony Parsons, personal communication, 1997). The success of the model in Walnut Gulch suggests its applicability to vegetation in the Badia. Jasinski (1996) bases his model on the use of a Landsat TM image. The work presented in this chapter extends the model further to consider its use with ATSR-2 and AVHRR imagery, i.e. imagery of coarser spatial resolution than that for which the model was developed and acquired at angles off-nadir (in the case of ATSR-2).

The model described in this thesis was based on the work of Jasinski (1996). Although the model was developed with advice from Michael Jasinski at the NASA Goddard Space Flight Centre, Washington, all programmes to solve the equations listed in this chapter were written at Leicester, in the C programming language.

#### **6.3.1 Model design**

The model is based around the red/near-infrared feature space of a single multispectral satellite image. Estimations of all vegetation and reflectance parameters are taken



directly from a satellite image and from personal knowledge of the form and structure of the vegetation. No ground data are needed, except for validation purposes.

As with the simple geometric optical model, the canopy is considered as randomly distributed geometric elements on a planar soil background. The elements or bushes are of a common geometric type, in this case a sphere, and cast shadows on the soil background or neighbouring bushes.

The reflectance of an individual pixel,  $\rho(\lambda)$ , is considered as a linear combination of the proportion of illuminated and shaded background and illuminated and shaded canopy multiplied by their respective reflectances:-

$$\rho(\lambda) = m_i \rho_{mi}(\lambda) + m_s \rho_{ms}(\lambda) + g_i \rho_{gi}(\lambda) + g_s \rho_{gs}(\lambda) \quad (6.1)$$

where:-

$\lambda$  = the wavelength of the band centre

$\rho_{mi}(\lambda)$  = illuminated canopy reflectance

$\rho_{ms}(\lambda)$  = shaded canopy reflectance

$\rho_{gi}(\lambda)$  = illuminated ground reflectance

$\rho_{gs}(\lambda)$  = shaded ground reflectance

$m_i, m_s$  = proportion of illuminated and shaded vegetation respectively

$g_i, g_s$  = proportion of illuminated and shaded background respectively

The total land surface reflectance consists of canopy and soil reflectance components. Bushes are not opaque but allow transmittance of radiation.

Equation 6.1 can be combined with a radiative transfer model to express the reflectance of the difference components in terms of the bulk canopy transmittance,  $\tau$ , and the canopy reflectance at zero transmittance,  $\rho_{\infty}$ . A schematic diagram of the radiative transfer model, giving terms for each reflectance component is shown in Figure 6.1.



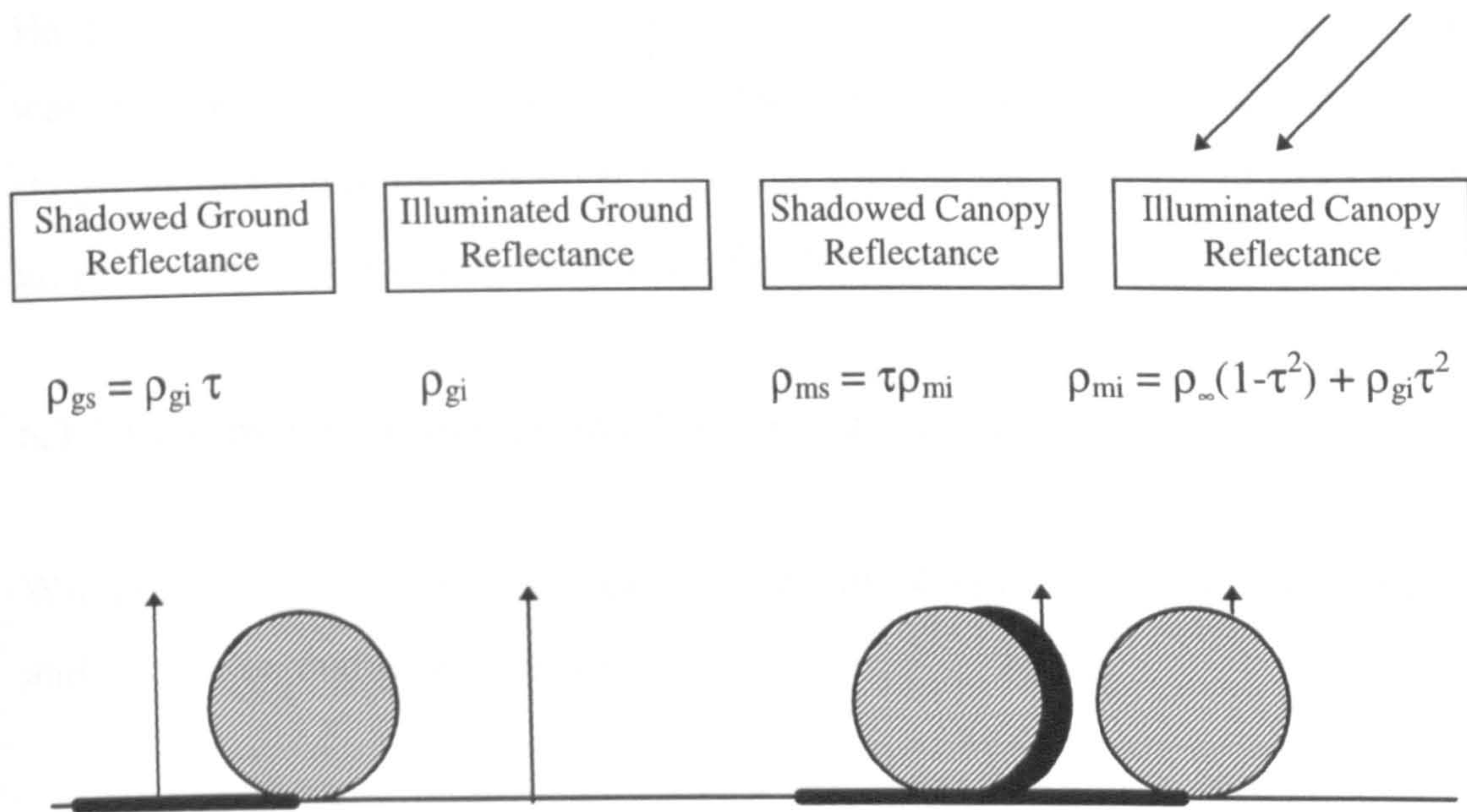


Figure 6.1: Schematic diagram showing canopy and soil reflectance model (source: Jasinski, 1996). Bushes are modelled as spheres on a flat planar background.

Reflectance is defined in terms of canopy transmittance,  $\tau$ .

Combining the radiative transfer model with Equation 6.1 gives an equation for pixel reflectance in terms of canopy transmittance (Jasinski 1996):-

$$\rho(\lambda) = [m_i + m_s \tau(\lambda)] \{ \rho_{\infty}(\lambda) [1 - \tau^2(\lambda)] + \rho_{gi}(\lambda) \tau^2(\lambda) \} + \rho_{gi}(\lambda) [g_i + g_s \tau(\lambda)] \quad (6.2)$$

where:-

$\tau$  = bulk canopy transmittance

$\lambda$  = the wavelength of the band centre

$\rho_{\infty}(\lambda)$  = canopy reflectance at zero transmittance

$\rho_{gi}(\lambda)$  = illuminated ground reflectance

$\rho_{gs}(\lambda)$  = shaded ground reflectance

$m_i, m_s$  = proportion of illuminated and shaded vegetation respectively

$g_i, g_s$  = proportion of illuminated and shaded background respectively



### 6.3.2 Parameter estimation

Having formulated an expression for pixel reflectance (Equation 6.2), the next step was to estimate the parameters contained within it. This essentially followed two main stages, estimation of the sub-pixel fractional shadow and subsequent determination of  $g_s$ ,  $g_i$ ,  $m_s$  and  $m_i$  and estimation of the reflectance terms,  $\rho_{\infty}(\lambda)$ ,  $\rho_{gi}(\lambda)$ ,  $\tau(\lambda)$  and  $\tau^2(\lambda)$ .

#### 6.3.2.1 Estimation of the sub-pixel fractional shadow cover

Within a pixel, the vegetated area ( $m$ ) consists of vegetation that is illuminated ( $m_i$ ) and vegetation that is in shade ( $m_s$ ):-

$$m = m_i + m_s \quad (6.3)$$

where:-

$m$  = total fractional vegetated cover

$m_i$  = fractional illuminated vegetation cover

$m_s$  = fractional shaded vegetation cover

Beta, ( $\beta$ ), is defined as the ratio of fractional shadowed vegetation cover to total fractional vegetation cover.

$$\beta = m_s / m \quad (6.4)$$

where:-

$\beta$  = ratio of fractional shadowed vegetation cover to total fractional vegetation cover

$m$  = total fractional vegetation cover

$m_s$  = fractional shaded vegetation cover

Jasinski (1996) determines  $\beta$  by examining the proportions of shaded and illuminated vegetation in high resolution aerial photographs. In the absence of aerial photography,



$\beta$  can be calculated graphically by taking a sphere as the basic vegetation shape and using the solar zenith angle at the time at which the image was captured. Since solar zenith angle varies across an image, the mean solar zenith angle for the whole scene was used. A sensitivity analysis was run to assess the importance of small changes in  $\beta$ . The results showed that whilst  $\beta$  is important to the model, the model is relatively insensitive to it. An accuracy of one or two decimal places obtained from calculating  $\beta$  graphically was sufficient for the purposes required here.

Having determined  $\beta$ , the amount of shaded ground for a given fractional vegetation cover was calculated as:-

$$m_s = \beta m \quad (6.5)$$

where:-

$m_s$  = fractional shaded vegetation cover

$\beta$  = ratio of fractional shadowed vegetation cover to total fractional vegetation cover

$m$  = total vegetated area

The amount of illuminated vegetation,  $m_i$ , is then simply:-

$$m_i = m - m_s \quad (6.6)$$

where:-

$m_i$  = fractional illuminated vegetation cover

$m$  = total fractional vegetation cover

$m_s$  = fractional shaded vegetation cover

Having derived expressions for the vegetation, one can then go on to examine the ground components. Jasinski (1996) shows that for a randomly distributed plant the amount of ground shadow can be related to the fractional vegetation cover by the



equation:

$$g_s = 1 - m - (1 - m)^{\eta + 1} \quad (6.7)$$

where:-

$g_s$  = fraction of shaded ground

$\eta$  = a non-dimensional solar geometric similarity parameter defined as the ratio of the mean shadow cast by a single tree,  $A_s$ , to the mean projected canopy area  $A_t$ .

$m$  = total fractional vegetation cover

$\eta$  varies according to different geometric shapes but for a sphere, it can be defined as  $\tan \theta \sin \theta$  where  $\theta$  is the solar zenith angle (Jasinski, 1990). Taking the mean solar zenith angle,  $\theta$  is assumed constant across a scene.

By default, the proportion of illuminated soil then becomes:-

$$g_i = 1 - m - g_s \quad (6.8)$$

where:-

$g_i$  = fraction of illuminated soil

$m$  = total fractional vegetation cover

$g_s$  = fraction of shaded soil

From the above discussion, it can be seen that from simply knowing the geometric shape of the vegetation units and the solar zenith angle, the proportion of the pixel in illumination and shade for any given fractional coverage can be calculated.

### 6.3.2.2 Estimation of the reflectance terms

The reflectance terms in Equation 6.2 are more difficult to estimate . The approach



used here is to apply the 'Method of Moments' to Equation 6.2, together with knowledge and interpretation of the shape and structure of the red/near-infrared scattergram. Conditional equations are written for specific regions of the feature space where reasonable assumptions can be made on the amount of fractional vegetation cover.

Following the work of many authors (e.g. Huete, 1988, Richardson and Wiegand, 1977), it is known that a vegetated area typically forms a triangular red/near-infrared scattergram. At the base of the scattergram lies a diagonal line known as the soil line representing areas of bare soil (Section 5.2). Bright soils occur to the top right, whilst darker, wetter, more organic soils lie to the bottom left. Soil reflectance thus varies in both red and near-infrared wavelengths. As one moves to the left of the soil line percentage vegetation cover increases. This is due to increased scattering within the plant in the near-infrared region and increased absorption in the red wavelengths by plant pigments (Jasinski, 1996). Eventually one reaches a point at 100 % cover where there is saturation in the red wavelengths. At this point, the scattergram forms a vertical line where red absorption is at a maximum but near-infrared reflectance still varies as a result of variations in plant architecture, leaf density and species, the amount of absorption, transmission and scattering, and variations in reflectance of the underlying soil. Figure 6.2 shows the position of the soil line and 100 % cover line.



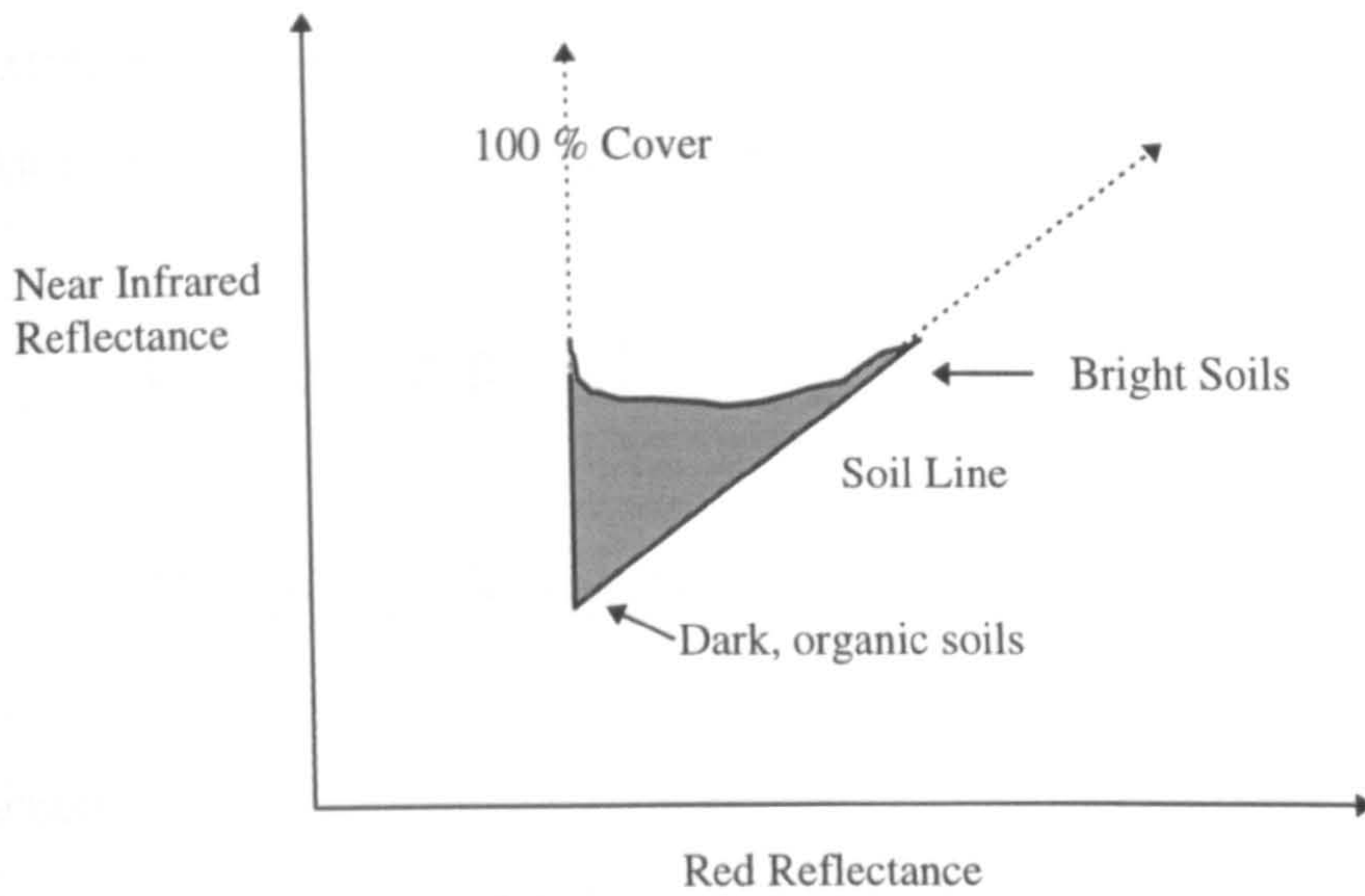


*Figure 6.2: Position of the soil line and 100 % cover line within the red/near-infrared scattergram. Pixels in a vegetated region form a triangle in the red/near infrared feature space. The 100 % cover line is a vertical line to the left whilst the soil line forms the right hand boundary.*

Estimation of the reflectance terms are derived from these two lines, the vertical 100 % cover line and the soil line. The soil line can be represented by the equation:-

$$\rho_{gi}(\lambda_{nir}) = \alpha \rho_{gi}(\lambda_{red}) + \gamma \quad (6.9)$$

where:-

$\rho_{gi}(\lambda_{nir})$  = illuminated soil reflectance in the near infrared wavelengths

$\rho_{gi}(\lambda_{red})$  = illuminated soil reflectance in the red wavelengths

$\alpha$  and  $\gamma$  = the slope and the intercept respectively.

In order for the model to be implemented, the reflectance terms,  $\alpha$  and  $\gamma$ ,  $\rho_{\infty}(\lambda)$ ,  $\rho_{gi}(\lambda)$  and  $\tau(\lambda)$  need to be estimated. The three wavelength dependent terms are found firstly for the near-infrared band and secondly for the red waveband. This sequence is important as near-infrared reflectance terms are needed for calculating red reflectance terms.



Using the scattergram, the pixels that lie along a finite width along the soil line are extracted. The equation of the soil line is calculated and hence  $\alpha$  and  $\gamma$  are found. Along the soil line too, it can be said that

$$E[\rho(\lambda)] = E[\rho_{gi}(\lambda)] \quad (6.10)$$

$$\text{Var}[\rho(\lambda)] = \text{Var}[\rho_{gi}(\lambda)] \quad (6.11)$$

where:-

$E[\rho(\lambda)]$  = the expected value of  $\rho(\lambda)$

$E[\rho_{gi}(\lambda)]$  = the expected value of  $\rho_{gi}(\lambda)$ , the illuminated soil reflectance

$\text{Var}[\rho(\lambda)]$  = the variance of  $\rho(\lambda)$ .

$\text{Var}[\rho_{gi}(\lambda)]$  = the variance of  $\rho_{gi}(\lambda)$ , the illuminated soil reflectance

Taking the expected value of the pixels along the soil line in the near-infrared band means that  $E[\rho_{gi}(\lambda_{nir})]$  is found.  $E[\rho_{gi}(\lambda_{red})]$  can be deduced from Equation 6.7 above and the relationship:-

$$E[\rho_{gi}(\lambda_{nir})] = \alpha E[\rho_{gi}(\lambda_{red})] + \gamma \quad (6.12)$$

where:-

$E[\rho_{gi}(\lambda_{nir})]$  = the expected value of the illuminated soil,  $\rho_{gi}(\lambda_{nir})$ , in the near infrared wavelengths

$E[\rho_{gi}(\lambda_{red})]$  = the expected value of the illuminated soil,  $\rho_{gi}(\lambda_{red})$ , in the red wavelengths

$\alpha$  and  $\gamma$  = slope and intercept of the soil line respectively

Having found  $\alpha$ ,  $\gamma$ ,  $E[\rho_{gi}(\lambda_{nir})]$  and  $E[\rho_{gi}(\lambda_{red})]$ , the two parameters left to find in order to use Equation 6.2 are  $\rho_{\infty}(\lambda)$  and  $\tau(\lambda)$ . These parameters are found with reference to the left hand side of the red/near-infrared scattergram and the vertical line



where vegetation coverage is approximately 100 %.

Assuming fractional cover equal to unity, Jasinski (1996) combines Equation 6.2 and 6.4, and by using a Taylor Series expansion, derives expressions for  $E[\rho(\lambda)]$  and  $\text{Var}[\rho(\lambda)]$ :-

$$E[\rho(\lambda)] = \{ 1 + \beta ( E [\tau(\lambda)] - 1 ) \} * \{ \rho_{\infty}(\lambda) + E [\tau^2 (\lambda)] (E [\rho_{gi}(\lambda)] - \rho_{\infty}(\lambda)) \} + 1/2 \text{Var} [\tau(\lambda)] \{ 6 \beta E[\tau(\lambda)] (E [\rho_{gi}(\lambda)] - \rho_{\infty}(\lambda)) + 2 (1 - \beta) (E [\rho_{gi}(\lambda)] - \rho_{\infty}(\lambda)) \} \quad (6.13)$$

$$\text{Var}[\rho(\lambda)] = \text{Var} [\rho_{gi}(\lambda)] \{ [1 + \beta ( E[\tau(\lambda)] - 1 )] E [\tau(\lambda)]^2 \} + \text{Var} [\tau(\lambda)] \{ 3 \beta E[\tau(\lambda)]^2 (E [\rho_{gi}(\lambda)] - \rho_{\infty}(\lambda)) + 2 (1 - \beta) E [\tau(\lambda)] (E [\rho_{gi}(\lambda)] - \rho_{\infty}(\lambda)) + \beta \rho_{\infty}(\lambda) \}^2 \quad (6.14)$$

where:-

$E[\rho(\lambda)]$  = expected value of  $\rho(\lambda)$ , the pixel reflectance

$\beta$  = the ratio of fractional shadowed vegetation to total fractional vegetation cover

$E [\tau(\lambda)]$  = the expected value of the bulk canopy transmittance,  $\tau$

$\rho_{\infty}(\lambda)$  = reflectance at zero transmittance

$E [\rho_{gi}(\lambda)]$  = the expected value of the illuminated soil reflectance,  $\rho_{gi}(\lambda)$

$\text{Var}[\rho(\lambda)]$  = the variance of the pixel reflectance

$\text{Var} [\rho_{gi}(\lambda)]$  = the variance of the illuminated soil reflectance

$\text{Var} [\tau(\lambda)]$  = the variance of the bulk canopy transmittance,  $\tau$

To find unknown values  $\rho_{\infty}(\lambda_{nir})$  and  $\tau(\lambda_{nir})$ , Equations 6.13 and 6.14 have to be solved simultaneously. However, by making an assumption about the variance of  $\tau$ , the computation can be made significantly quicker and easier. If the  $\text{Var} [\tau]$  is assumed to be approximately zero, Equation 6.14 reduces to:-



$$\text{Var} [\rho(\lambda)] = \text{Var} [\rho_{gi}(\lambda)] \{ [1 + \beta (E[\tau(\lambda)] - 1)] E[\tau(\lambda)] \}^2 \quad (6.15)$$

where:-

$\text{Var}[\rho(\lambda)]$  = the variance of the pixel reflectance

$\text{Var} [\rho_{gi}(\lambda)]$  = the variance of the illuminated soil reflectance

$\beta$  = the ratio of fractional shadowed vegetation to total fractional vegetation cover

$E[\tau(\lambda)]$  = the expected value of the bulk canopy transmittance,  $\tau$

Using the well known principle  $E[x^2] = \text{var} [x] + E[x]^2$ ,  $E[\tau^2]$  is equal to  $E[\tau]^2$ .

Equation 6.15 can be solved for  $E[\tau]$ .  $\beta$  is known from the plant geometry and the solar zenith angle,  $\rho_{gi}(\lambda_{nir})$  is known from the soil line and  $\text{Var} [\rho(\lambda_{nir})]$  is taken from the pixels extracted from the 100 % cover line. Solving Equation 6.14 for  $E[\tau]$  gives 3 solutions and a cubic graph. The graph only crosses the x axis in one place and so  $x$  or  $E[\tau]$  is taken as the value at this point.

Having solved Equation 6.15 to derive a value for  $E[\tau]$ , Equation 6.14 is then solved for  $\rho_{\pm}(\lambda_{nir})$ .  $E[\rho(\lambda_{nir})]$  is taken from pixels extracted from the 100 % cover line and now  $\beta$ ,  $\rho_{gi}(\lambda_{nir})$  and  $E[\tau(\lambda_{nir})]$  are known.  $\text{Var} [\tau]$  is again assumed to approximate zero.

The derivation of reflectance parameters for the red band is straight forward once values for the near-infrared band have been attained. Along the  $m = 1$  line, there is saturation in the red band and  $E[\tau(\lambda_{red})]$  and  $\text{Var}[\tau(\lambda_{red})]$  approximate zero. Equation 6.14 reduces to Equation 6.16 below and using  $E[\rho(\lambda_{red})]$  found from the 100 % cover line,  $\rho_{\pm}(\lambda_{red})$  can be found.



$$E[\rho(\lambda_{\text{red}})] = \{ 1 - \beta \} \rho_{\infty}(\lambda_{\text{red}}) \quad (6.16)$$

where:-

$E[\rho(\lambda_{\text{red}})]$  = the expected value of the pixel reflectance in the red wavelengths

$\beta$  = the ratio of fractional shadowed vegetation to total fractional vegetation cover

$\rho_{\infty}(\lambda_{\text{red}})$  = reflectance at zero transmittance in the red wavelengths

According to Jasinski (1996),  $\tau(\lambda)$  cannot be assumed to be constant at least in the near-infrared band. He formulates equations that calculate the probability mass function of  $\tau(\lambda)$  over the entire scene but finds that whilst the transmittance over a temperate forested scene is skewed towards low values, transmittance in the semiarid area of Walnut Gulch is much more uniform.  $E[\tau(\lambda)]$  can be used, and the assumption of  $\text{Var} [\tau]$  is supported.

The method explained above was carried out initially for all images which coincided with periods of field data collection. This enabled results of the model to be validated against estimates of percentage vegetation cover collected in the field.

Table 6.1 gives the results of parameter estimation for ATSR-2 images, whilst Table 6.2 gives the parameters for AVHRR.



*Table 6.1: Parameter estimation derived from the model for ATSR-2 images. These parameters are used to estimate pixel reflectance for a given percentage vegetation cover. Beta,  $\theta$ ,  $\eta$  are used to estimate the proportion of illuminated and shaded soil and vegetation. The other terms are used to estimate component reflectance. In general, parameters show little variation across scenes. The difference between nadir and forward views is most significant in the estimation of  $\beta$ .*

		06/09/95		15/11/95		10/09/97	
		Nadir	Forward	Nadir	Forward	Nadir	Forward
Beta		0.1	0.45	0.2	0.65	0.087	0.43
$\theta$		31.26	31.51	53.39	53.73	32.59	32.83
$\eta$		0.31	0.32	1.08	1.09	0.34	0.35
Red	E ( $\tau$ )	0.0	0.0	0.0	0.0	0.0	0.0
	$\rho_{\pm}$	0.059	0.095	0.0387	0.029	0.06	0.086
	Var( $\rho_{gl}$ )	0.0269	0.0179	0.021	0.0219	0.027	0.0178
	E ( $\rho_{gl}$ )	0.287	0.234	0.332	0.2789	0.247	0.292
	Var ( $\rho$ )	$2.26*10^{-6}$	$1.4 * 10^{-6}$	$1.1 *10^{-6}$	$3.29*10^{-5}$	$1.65*10^{-5}$	$3.8*10^{-6}$
NIR	E ( $\rho$ )	0.0532	0.0523	0.031	0.01	0.056	0.0493
	E ( $\tau$ )	0.62	0.45	0.56	0.36	0.47	0.64
	$\rho_{\pm}$	0.217	0.198	0.148	0.1622	0.224	0.166
	Var( $\rho_{gl}$ )	0.033	0.021	0.026	0.0255	0.03	0.0191
	E ( $\rho_{gl}$ )	0.332	0.275	0.373	0.3187	0.283	0.339
	Var ( $\rho$ )	0.0121	0.0032	0.007	0.0019	0.0063	0.0066
	E ( $\rho$ )	0.252	0.161	0.199	0.1066	0.226	0.2004
	$\alpha$	1.1052	1.08472	1.1054	1.0779	1.0624	1.1128
	$\gamma$	0.0153	0.0208	0.006	0.018	0.0202	0.0148



*Table 6.2: Parameter estimation derived from the model for AVHRR images. These parameters are used to estimate pixel reflectance for a given percentage vegetation cover. Beta,  $\theta$ ,  $\eta$  are used to estimate the proportion of illuminated and shaded soil and vegetation. The other terms are used to estimate component reflectance. The values are similar to those obtained using ATSR-2 imagery (see Table 6.1), and show little variation across scenes.*

		31/03/96	28/04/96	05/05/96	05/09/97
	<b>Beta</b>	0.1	0.075	0.075	0.095
	<b><math>\theta</math></b>	33.44	27.01	29.50	37.26
	<b><math>\eta</math></b>	0.36	0.23	0.28	0.46
<b>Red</b>	<b>E (<math>\tau</math>)</b>	0.0	0.0	0.0	0.0
	<b><math>\rho_{\pm}</math></b>	0.036	0.047	0.0122	0.0671
	<b>Var(<math>\rho_{gl}</math>)</b>	0.0125	0.0167	0.033	0.0199
	<b>E (<math>\rho_{gl}</math>)</b>	0.194	0.2574	0.316	0.2294
	<b>Var (<math>\rho</math>)</b>	$2.78 \cdot 10^{-6}$	$1.85 \cdot 10^{-5}$	$5.41 \cdot 10^{-6}$	$2.67 \cdot 10^{-5}$
	<b>E (<math>\rho</math>)</b>	0.0311	0.04390	0.01128	0.0607
<b>NIR</b>	<b>E (<math>\tau</math>)</b>	0.48	0.37	0.36	0.36
	<b><math>\rho_{\pm}</math></b>	0.152	0.1502	0.134	0.2064
	<b>Var(<math>\rho_{gl}</math>)</b>	0.01	0.0225	0.0394	0.0293
	<b>E (<math>\rho_{gl}</math>)</b>	0.238	0.3163	0.346	0.306
	<b>Var (<math>\rho</math>)</b>	0.0033	0.00286	0.0047	0.0034
	<b>E (<math>\rho</math>)</b>	0.0959	0.16481	0.1532	0.206
	<b><math>\alpha</math></b>	1.0936	1.1578	1.0911	1.214
	<b><math>\gamma</math></b>	0.0264	0.0183	0.0043	0.0279

### 6.3.3 Estimation of the sub-pixel fractional canopy cover and inversion

Once all the parameters have been estimated, the final stage of the model is to simulate red and near-infrared pixel reflectance for the whole range of percentage vegetation covers (between 0 and 100 %) and variable soil reflectance. This will determine that values of pixel reflectance are produced such that the reflectance of every pixel within the red/near-infrared scattergram will have a percentage vegetation cover associated with it. Pixel reflectance is simulated using Equation 6.2.

Model inversion can follow in two ways. Firstly, for estimating the percentage vegetation cover of an individual site, red and near-infrared reflectance from the



image as a pair, can be compared to the values given by the model. Since the model gives all combinations of red/near-infrared reflectance, percentage vegetation cover of the site is taken where the theoretical values 'match' actual red/near-infrared values.

Secondly, for inversion on a image wide basis, the model can be used to produce lines of constant fractional vegetation coverage that can be overlaid onto the red/near-infrared scattergram. The lines are estimated by using Equation 6.2 to calculate the expected value of total pixel reflectance for the red and the near-infrared band holding 'm' constant for values of 0%, 10% 20% etc., in turn, and iterating for  $\rho_{gi}(\lambda)$ . Lines are then overlaid on the red/near-infrared scattergram of an image. The areas between the percentage cover lines can then be digitised and used to form the basis of spectral signatures. All areas falling to the right of the soil line, or containing negative numbers, form the basis of one signature and represent pixels of cloud/snow/water. A supervised classification is then carried out using those signatures. As an example, Figure 6.3 shows the scattergram for the 06/09/95 image, with lines of constant percentage vegetation cover overlaid. Figure 6.4 gives the thematic map of percentage vegetation cover produced as a result of image wide inversion.



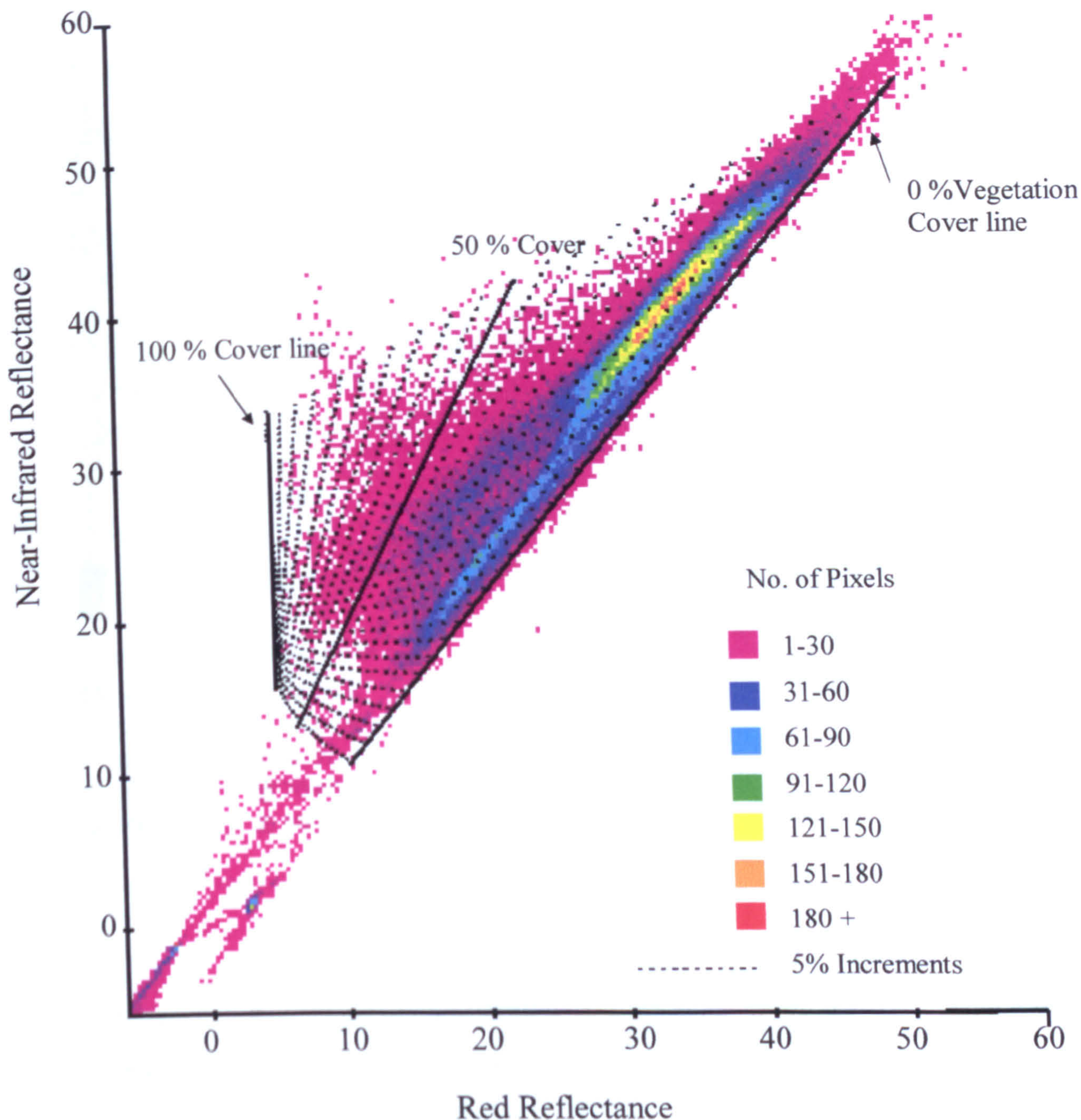
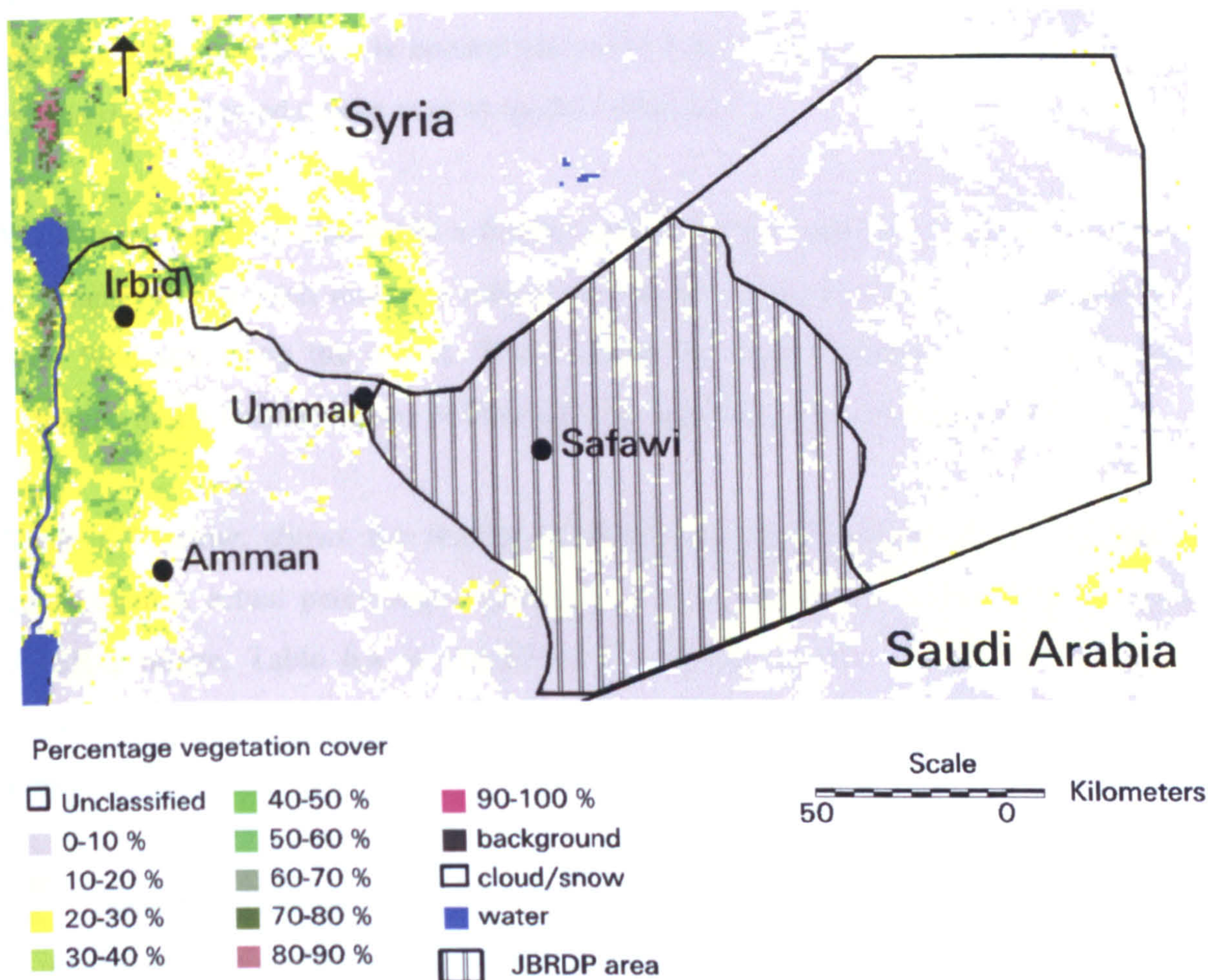


Figure 6.3: Red/near-infrared scattergram for the 06/09/95 ATSR-2 image, overlaid with lines of constant percentage vegetation cover. The lines of percentage vegetation cover are constructed using the hybrid geometric optical/empirical model. The relation of each pixel with respect to these lines, determines the percentage vegetation cover of that pixel. Plotting pixels in their geographic location then enables the construction of percentage vegetation cover maps of the area (see Figure 6.4). Within the 06/09/95 image, there are large numbers of pixels that lie close to the soil line (0% cover). These represent the desert area. Pixels with a reflectance below zero represent anomalous values and cloudy areas.





*Figure 6.4: Percentage vegetation cover map derived from the 06/09/95 ATSR-2 image using model inversion. Using the model, every pixel in the image has been assigned a percentage vegetation class based on the position of the pixel in the red/near infrared feature space. The map shows high vegetation coverages in the Jordan Valley, and low coverages (0-20%) in the Jordan Badia Research and Development Programme Area (JBRDP). Percentage vegetation cover maps were produced for all ATSR-2 and AVHRR images of the area, and will be used by the Higher Council for Science and Technology in Jordan to make informed decisions about land management in the future.*



6.4 Model validation

One of the advantages of using this model is that all values are derived from a satellite image and no ground data is needed for model formulation. This in turn means that ground data collected can be used in model validation

Validation can be carried out in a similar way as for the vegetation indices described in Chapter 5. For each image in turn, a percentage vegetation cover is estimated for each field site using the model. These values are then compared to actual values collected in the field by means of Pearson’s product moment correlation coefficient.

Table 6.3 below, shows the results of correlating modelled percentage vegetation cover against actual percentage vegetation cover as measured in the field, for each ATSR-2 image. Table 6.4 is similar but is constructed for AVHRR images. The correlation results found when field data were compared against NDVI are shown for comparison.

Table 6.3: Pearson’s product moment correlation coefficient calculated for theoretical percentage vegetation cover as predicted by the model for ATSR-2 data correlated against percentage vegetation cover values taken in the field. The correlation coefficients for NDVI against percentage vegetation cover are given for comparison. When all sites are used (Jordan Valley and Badia), the model shows good correlations with percentage vegetation cover and compares well with similar correlations for the NDVI. Data from the forward look of ATSR-2 shows poorer correlations than data collected at nadir.

		06/09/95		15/11/95		10/09/97	
		All	Badia	All	Badia	All	Badia
Model	Nadir	0.916*	-0.386	0.915*	-0.422	0.913*	-0.335
NDVI	Nadir	0.937*	-0.257	0.925*	-0.41	0.915*	-0.661*
Model	Forward	0.857*	-0.324	0.894*	0.138	0.850*	-0.294
NDVI	Forward	0.897*	-0.329	0.902*	-0.254	0.803*	-0.479

Significant at the 95 % confidence interval

\*

Significant at the 99 % confidence interval



*Table 6.4: Pearson's product moment correlation coefficient calculated for theoretical percentage vegetation cover as predicted by the model for AVHRR data correlated against percentage vegetation cover values taken in the field. The correlation coefficients for NDVI against percentage vegetation cover are given for comparison. When data from all sites is considered (Jordan Valley and Badia), the model gives significant positive correlations, comparable to those using the NDVI. When only sites in the Badia are considered, results are inconsistent and often insignificant.*

	31/03/96		28/04/96		05/05/96		05/09/97	
	All	Badia	All	Badia	All	Badia	All	Badia
Model	0.768*	-0.277	0.727*	-0.393	0.721*	-0.305	0.841*	-0.727*
NDVI	0.796*	-0.302	0.796*	-0.519	0.798*	-0.38	0.874*	-0.657*

Significant at the 95 % confidence interval

\*

Significant at the 99 % confidence interval

From Tables 6.3 and 6.4, it can be seen that correlations between modelled percentage vegetation cover and field measured percentage vegetation cover are highly significant and very similar to those obtained when considering vegetation index values such as the NDVI. As with the index values, viewing in the forward look does not enhance one's ability to detect vegetation cover, as shown by less strong correlation coefficients.

However, the results also suggest that the modelling approach does not improve ones ability to detect vegetation of very low densities compared to the use of vegetation indices. When sites in the Badia alone are considered, one cannot distinguish between the different vegetation covers found in the Badia region. Correlations are poor, insignificant and negative. Even when modelling a pixel by considering processes operating on a sub pixel scale, a bright soil background, the nature and form of vegetation and the effect of shadow remain problematic.

One of the advantages however, of using the model compared with using a vegetation index is that the model is invertible and percentage vegetation cover can be estimated without the use of field data. When using a vegetation index, a measure of a



biophysical parameter such as biomass, leaf area index or percentage vegetation cover is required in order to establish a relationship between the imagery and ground data, and assign vegetation characteristics to the index measure. Vegetation indices do not give an absolute value for a biophysical parameter.

In order to assess how well the model predicts vegetation cover without the use of field data, each image was considered in turn. Predicted values of vegetation cover as calculated using the model were plotted against actual values measured in the field and the  $x = y$  line was drawn. The mean squared residuals for the predicted  $y$  values in relation to the  $x = y$  line were then calculated (as shown by Equation 6.17 below).

In addition to examining mean squared residuals in order to indicate how well the model predicts actual vegetation cover on the ground, a line of best fit was constructed through the actual/predicted data points. This line was forced to pass through the origin in order that the model and field data both predicted zero. The equation of this line of best fit indicates how well the model fits the data. A similar equation for all images would indicate that the model is consistently over-estimating or under-estimating actual percentage cover.

Figure 6.5 shows the predicted versus the actual values as plotted for the nadir look of the 10/09/97 ATSR-2 image. The  $x = y$  line is plotted to show the residual of each point from the optimum model fit. The line of best fit for the points is also plotted. This line, passing through the origin, is represented by the equation  $y = 0.8286x$ . the points fit this line with an  $R^2$  of 0.782. Values of percentage vegetation cover are being underestimated by the model.



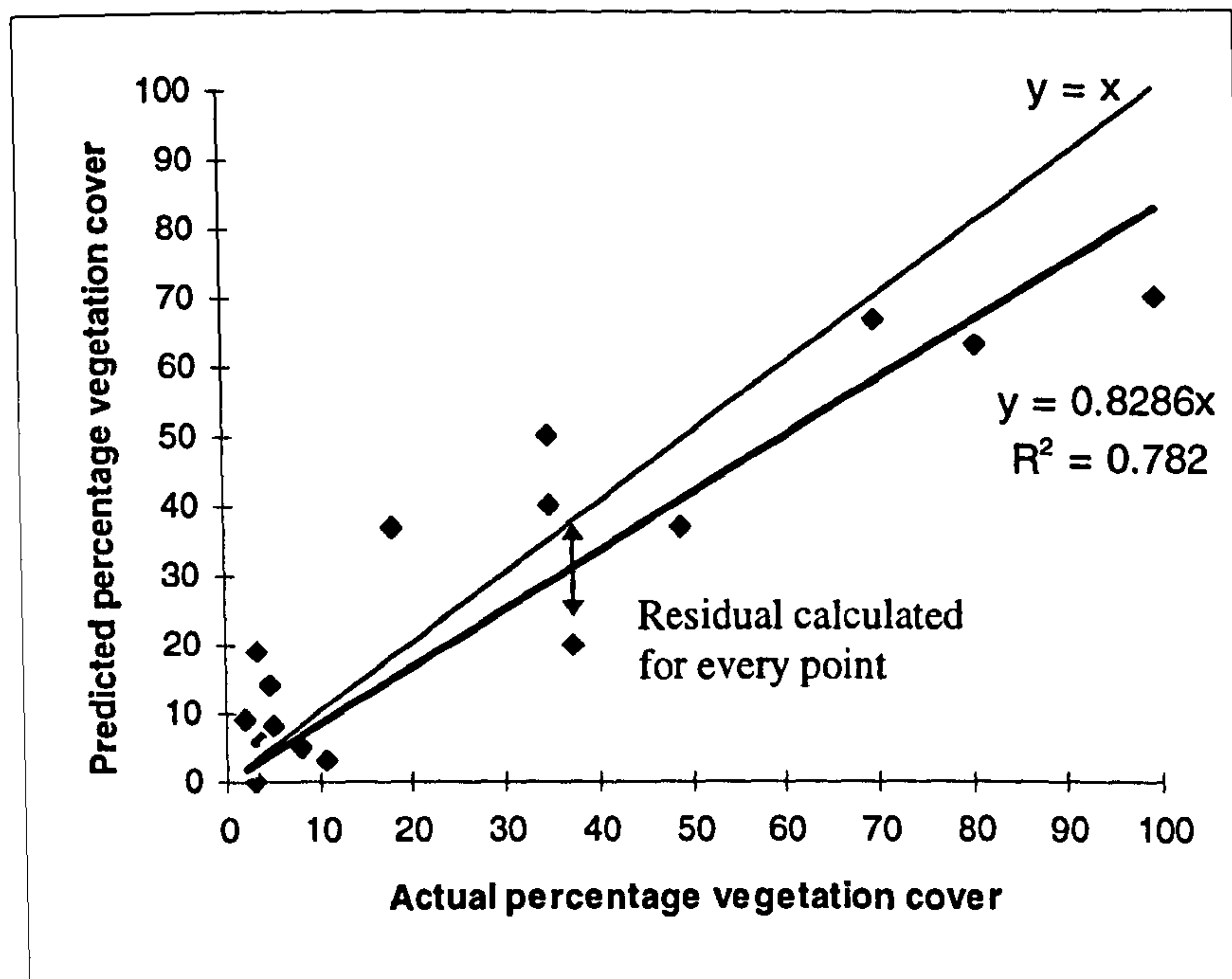


*Figure 6.5: Predicted percentage vegetation cover derived from the model for the 10/09/97 ATSR-2 image, plotted against actual percentage vegetation cover values taken in the field. The  $x = y$  line shows where the points should lie if the model is predicting percentage vegetation cover to 100% accuracy. The  $y = 0.8286x$  line shows the actual line of best fit. The model is under predicting actual percentage vegetation cover values.*

$$\text{Mean squared residual} = \frac{\sum (y - y')^2}{n} \quad (6.17)$$

where:-

$y$  = predicted percentage vegetation cover

$y'$  = actual percentage vegetation cover

$n$  = the number of observations

Mean squared residuals and lines of best fit were calculated for every image for which field data was available to validate the model. Table 6.5 presents these results.



*Table 6.5: Mean squared residuals and lines of best fit for predicted versus actual percentage vegetation cover, for imagery for which field validation data was available. In every case, the model underestimates the percentage vegetation cover. Mean square residuals are generally higher for AVHRR imagery, and lines of best fit have lower  $R^2$  values. Imagery from ATSR-2 is a better predictor of vegetation cover.*

<b>ATSR-2</b>		<b>Mean Squared Residuals</b>	<b>Line of Best Fit</b>	<b><math>R^2</math></b>
<b>Nadir</b>	<b>06/09/95</b>	0.019	$y = 0.7296x$	0.800
	<b>15/11/95</b>	0.036	$y = 0.5842x$	0.828
	<b>10/09/97</b>	0.017	$y = 0.8286x$	0.782
<b>Forward</b>	<b>06/09/95</b>	0.026	$y = 0.8089x$	0.668
	<b>15/11/95</b>	0.021	$y = 0.7901x$	0.750
	<b>10/09/97</b>	0.025	$y = 0.9522x$	0.614
<b>AVHRR</b>	<b>31/03/96</b>	0.039	$y = 0.8978x$	0.319
	<b>28/04/96</b>	0.039	$y = 0.9350 x$	0.215
	<b>05/05/96</b>	0.044	$y = 0.8469 x$	0.095
	<b>05/09/97</b>	0.027	$y = 0.8212 x$	0.477

In terms of the mean squared residuals, the lowest values are obtained with the ATSR-2 rather than the AVHRR imagery. The model appears to be a better predictor of actual vegetation coverages using ATSR-2 imagery. One of the main reasons for this may be the fact that in the three AVHRR images (with very high mean squared residual values) are those dating from the Spring 1996. Although field data did not detect a significant increase in percentage vegetation coverage in the Badia in the Spring, values of percentage cover were not taken in the Jordan Valley during this time. Results presented in Chapter 5 indicate that NDVI increases during the Spring of 1996. An increase in percentage cover will mean plants begin to overlap and a model based on the geometry of spherical plants begins to break down. Having said this however, the modelled results from all images rely on a range of covers from 0 to 100 %. At 100 % cover the geometry of a plant is less important, plants shadow adjacent plants beneath the uppermost canopy. The model seems to work well when highly vegetated sites containing plants which are not spherical, i.e. in the Jordan Valley, are used e.g. the banana site and low crop site.

From the equations of lines of best fit it can be seen that the model consistently underestimates percentage vegetation cover. The nadir look of the 15/11/95 ATSR-2 image



has the largest underestimation with  $y$  equalling  $0.5842x$ . Unfortunately underestimation is not consistent in magnitude. The slope of the line varies between  $0.5842$  (in the case of the nadir look of ATSR-2, 15/11/95) to  $0.9522$  (in the case of the forward look of ATSR-2, 10/09/97) and thus a term for this difference cannot be introduced into the model. In cases where the  $R^2$  value is low, the addition of a term to account for the real line of best fit would be inappropriate anyway.

### 6.5 Seasonal variations detected using the model

In the same way as seasonal variations can be detected using vegetation indices and the NDVI, changes in percentage vegetation cover for every field site over time can also be examined by using the modelling results over a time series of images.

Figure 6.6 shows the change in percentage vegetation cover over time as predicted by the nadir view of ATSR-2 whilst Figure 6.7 shows the change as predicted by AVHRR imagery.

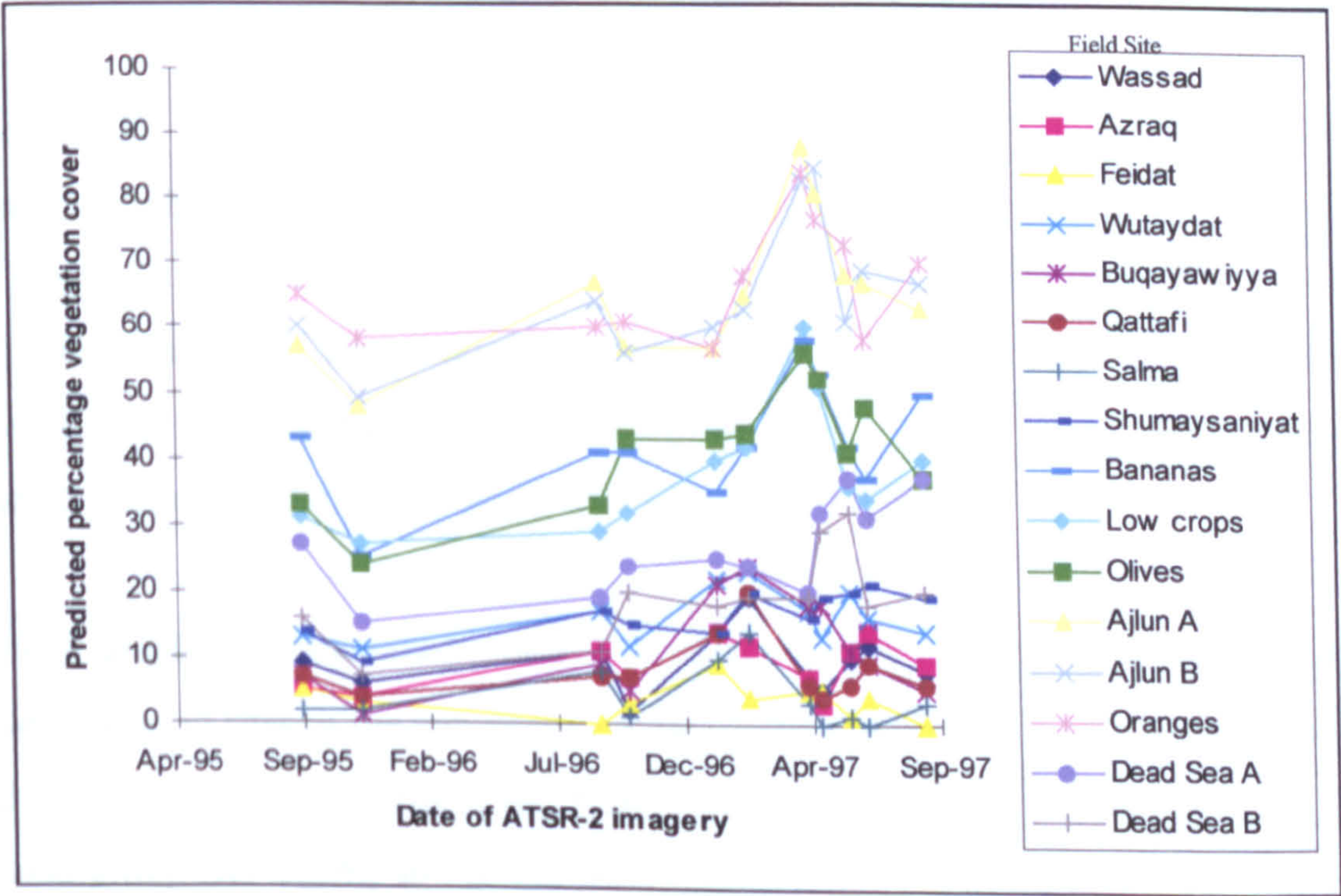
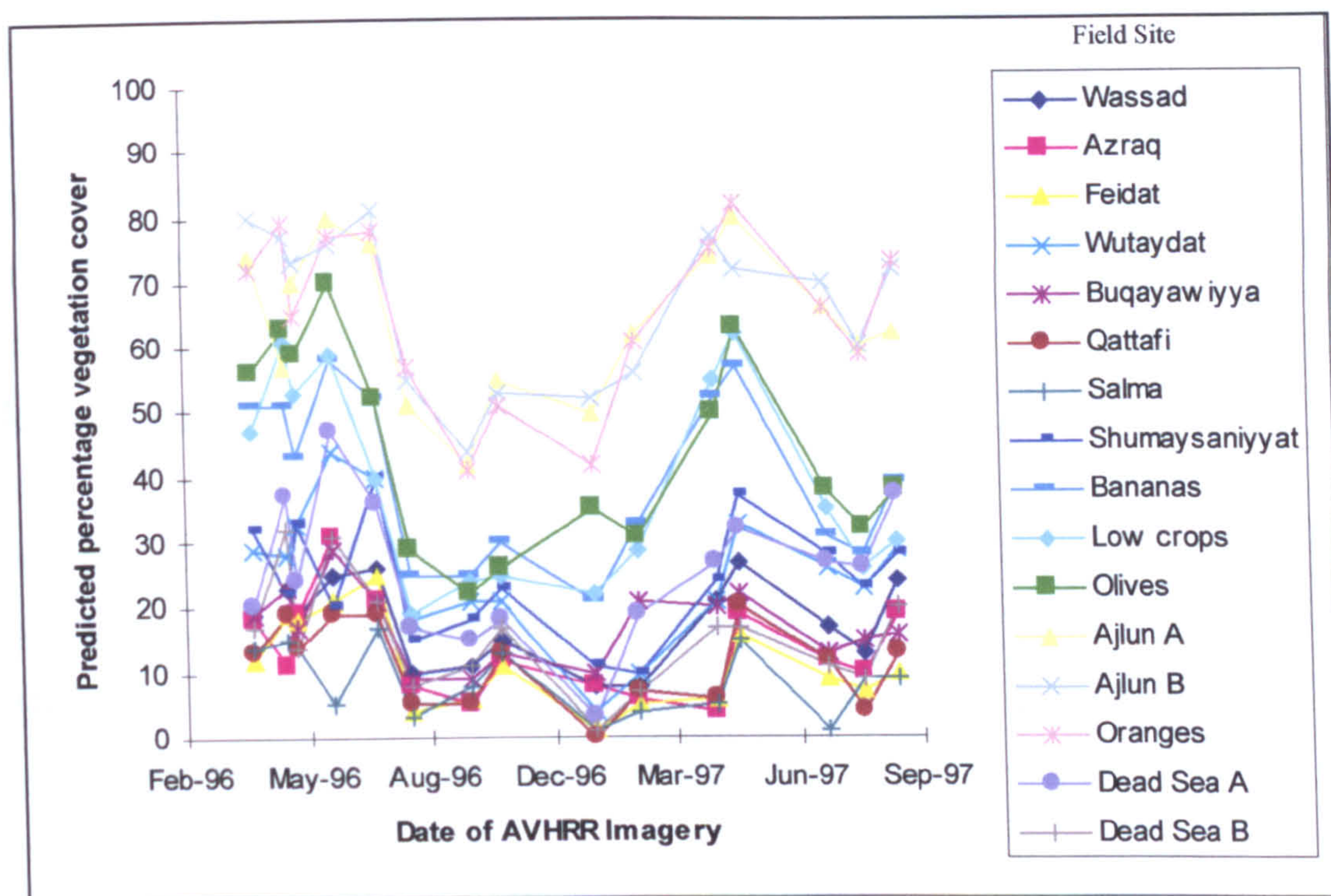


Figure 6.6: Percentage vegetation cover change over time as predicted by the model using ATSR-2 imagery





*Figure 6.7: Percentage vegetation cover change over time as predicted by the model using AVHRR imagery. In general, vegetation cover shows an increase in the spring months and a decrease during late summer.*

Allowing for the differences in image dates, both Figures 6.6 and 6.7 show similar trends to each other and to the graphs of the variation in NDVI with season (Figures 5.2 and 5.3). Percentage vegetation cover shows an increase in the spring months following periods of winter rainfall. From August to January, percentage vegetation cover is low, representing a lack of growth due to long hot dry periods and increased grazing pressure as the vegetation reserves slowly diminish.

In both graphs the vegetation cover falls into three distinct groupings. The highest cover occurs in sites in the mountainous areas surrounding the Jordan Valley, *Ajlun A* and *Ajlun B* and in the north of the Jordan Valley with intensive orange farming. The second group has slightly lower percentage coverages and is represented by irrigated sites further to the south in the Jordan Valley - bananas, olives and low crops. The two Dead Sea sites in the Valley can be grouped with areas of the Badia, which have low percentage vegetation covers. They show less of a seasonal trend and represent areas



of high grazing and no irrigation.

From the correlation results presented in Tables 6.3 and 6.4, it can be ascertained that the model does not work well in discriminating between low levels of vegetation cover, such as those found in the Badia. Although it can be said that the model indicates that sites in the Badia have low percentage vegetation coverages, there is no statistical evidence to support the variation in trends shown over the measurement period.

Figure 6.8 combines the results of Figures 6.6 and 6.7 and shows percentage vegetation cover for sites in the Jordan Valley as predicted from both ATSR-2 and AVHRR data. Because of their low annual vegetation covers that are similar to sites in the Badia, the Dead Sea sites have been omitted from the graph.

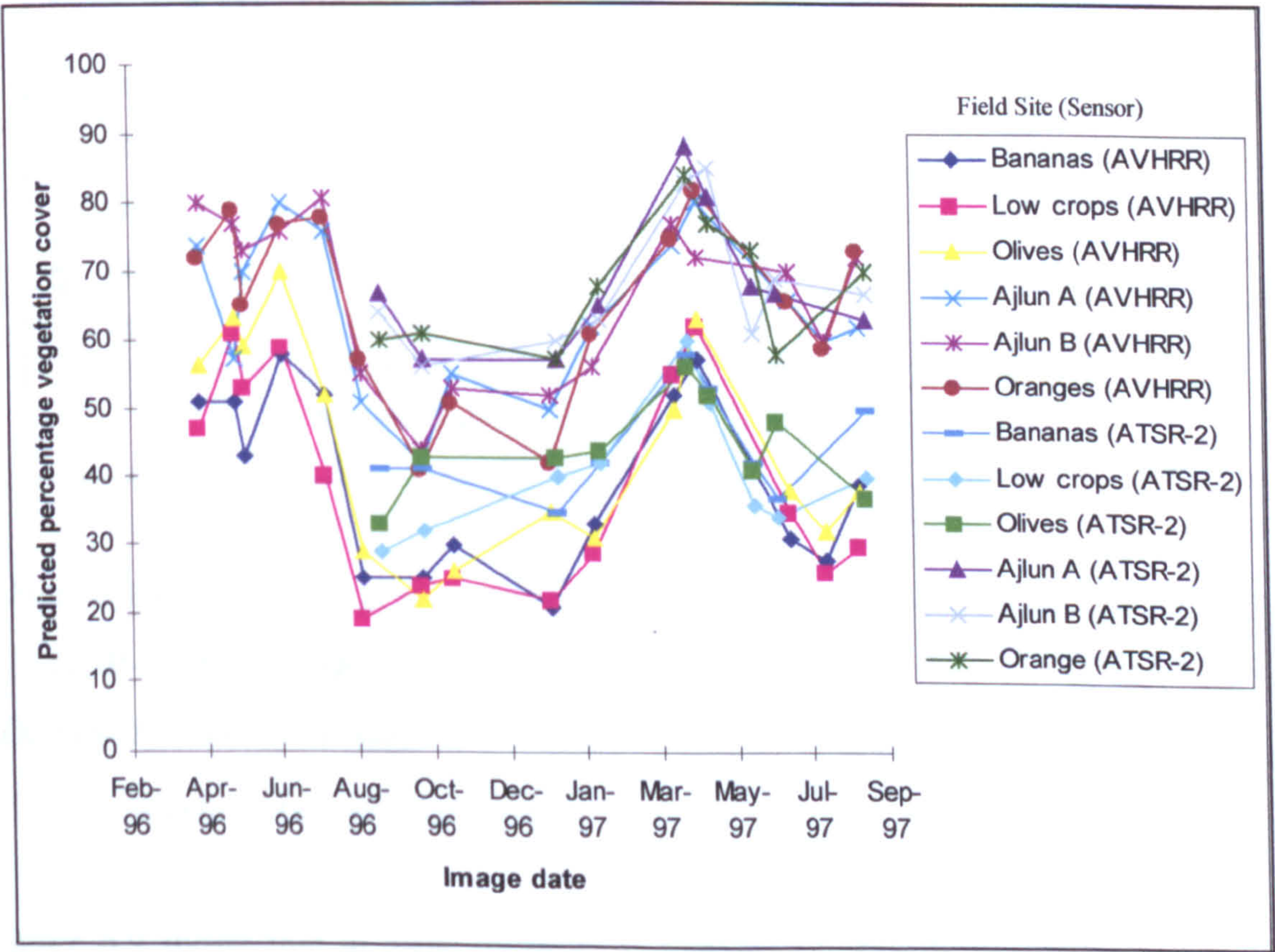


Figure 6.8: Percentage vegetation cover change over time, as predicted by the model for ATSR-2 and AVHRR imagery, for selected field sites in the Jordan Valley.



Figure 6.8 illustrates that although derived from different sensors and imagery of different dates, the seasonal patterns of percentage vegetation cover as derived from the AVHRR imagery and ATSR-2 imagery are very similar. In the spring of 1997 especially, the values produced by the model using the two types of imagery appear almost identical. The differences between percentage vegetation covers given by ATSR-2 and by AVHRR are shown in Figure 6.9, for months in which both image types were acquired.

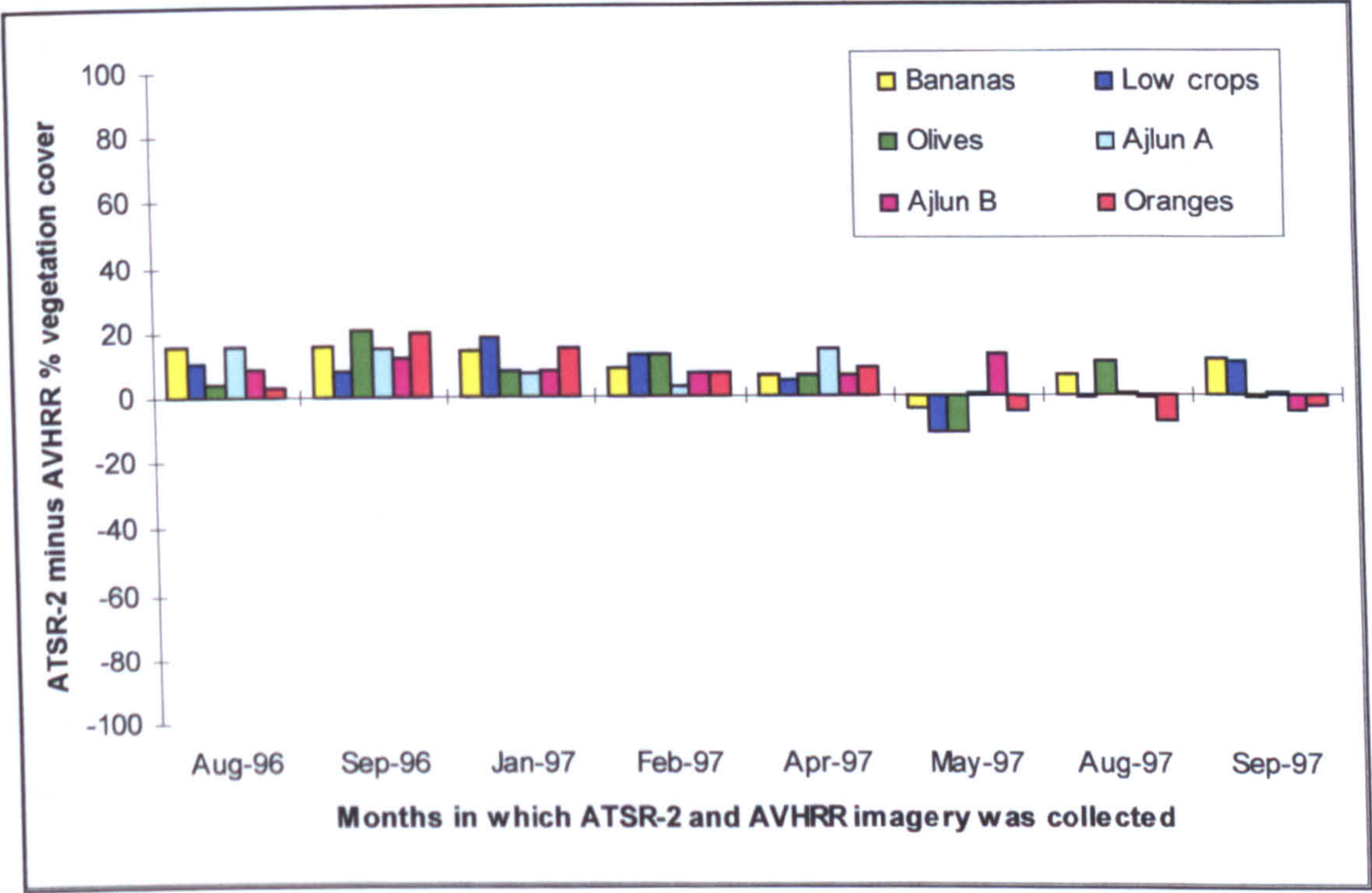


Figure 6.9: Difference in percentage vegetation cover as predicted by the model for ATSR-2 and AVHRR imagery, for months in which both imagery was collected. Despite differences in image dates, sensor calibration and specifications, percentage vegetation cover predictions from the two sensors are within  $\pm 20\%$

Figure 6.9 shows that in many cases where percentage vegetation cover is predicted from both ATSR-2 and AVHRR imagery, the values coincide to within  $\pm 5$  or  $10\%$  cover. There are larger differences particularly between the September 1996 imagery but it must be remembered that images were taken on different dates, in addition to the differences in wavebands, overpass times, spatial resolution , swath width etc.



Figure 6.10 gives a similar graph to Figure 6.9 but shows the difference in NDVI as derived from ATSR-2 and AVHRR imagery.

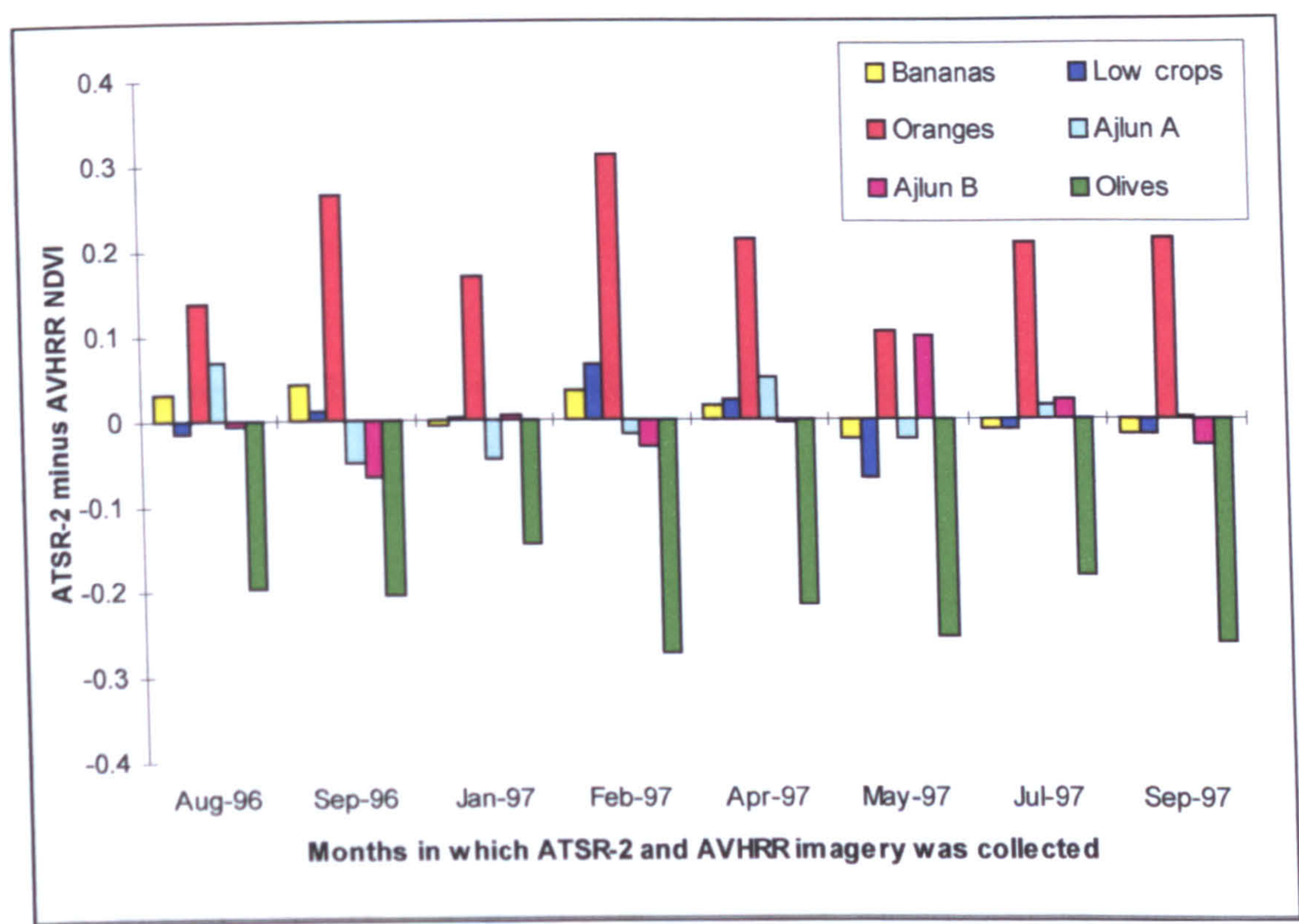


Figure 6.10: Difference in NDVI as predicted by ATSR-2 and AVHRR imagery, for months in which both image types were acquired. ATSR-2 and AVHRR data show large differences in NDVI for the orange and olive sites.

Examining differences in NDVI as shown in Figure 6.10, one can see that for the Bananas, Low crops, Ajlun A and Ajlun B sites, NDVI is very similar. For the Oranges site, ATSR-2 consistently gives a higher NDVI than the AVHRR, whilst for the Olive site the reverse is true. Although NDVI values can be very similar, using the NDVI is problematic in terms of predicting percentage vegetation coverage over a time series. NDVI is an indicator of percentage vegetation cover, and in order to invert and provide percentage vegetation cover values, values of ground percentage cover are needed. Ideally, due to sensor drift, calibration variations etc., relationships should be established on an image-by-image basis. In a time series, however, ground percentage cover values are usually not available for all months of the year.



Figure 6.11 shows the difference in percentage cover as predicted by ATSR-2 and AVHRR using NDVI values. Percentage cover values were obtained from the NDVI by establishing a regression relationship between images coincident with periods of field data collection (28/04/96 and 05/09/97 for AVHRR, and 15/11/95 and 10/09/97 for ATSR-2) and applying this regression equation to NDVI values from all other images. This was done separately for ATSR-2 images and AVHRR images using the regression equations:-

ATSR-2 imagery

% cover = (2.0449 \* NDVI) - 0.0368

(6.18)

AVHRR imagery

% cover = (2.43063 \* NDVI) - 0.1924

(6.19)

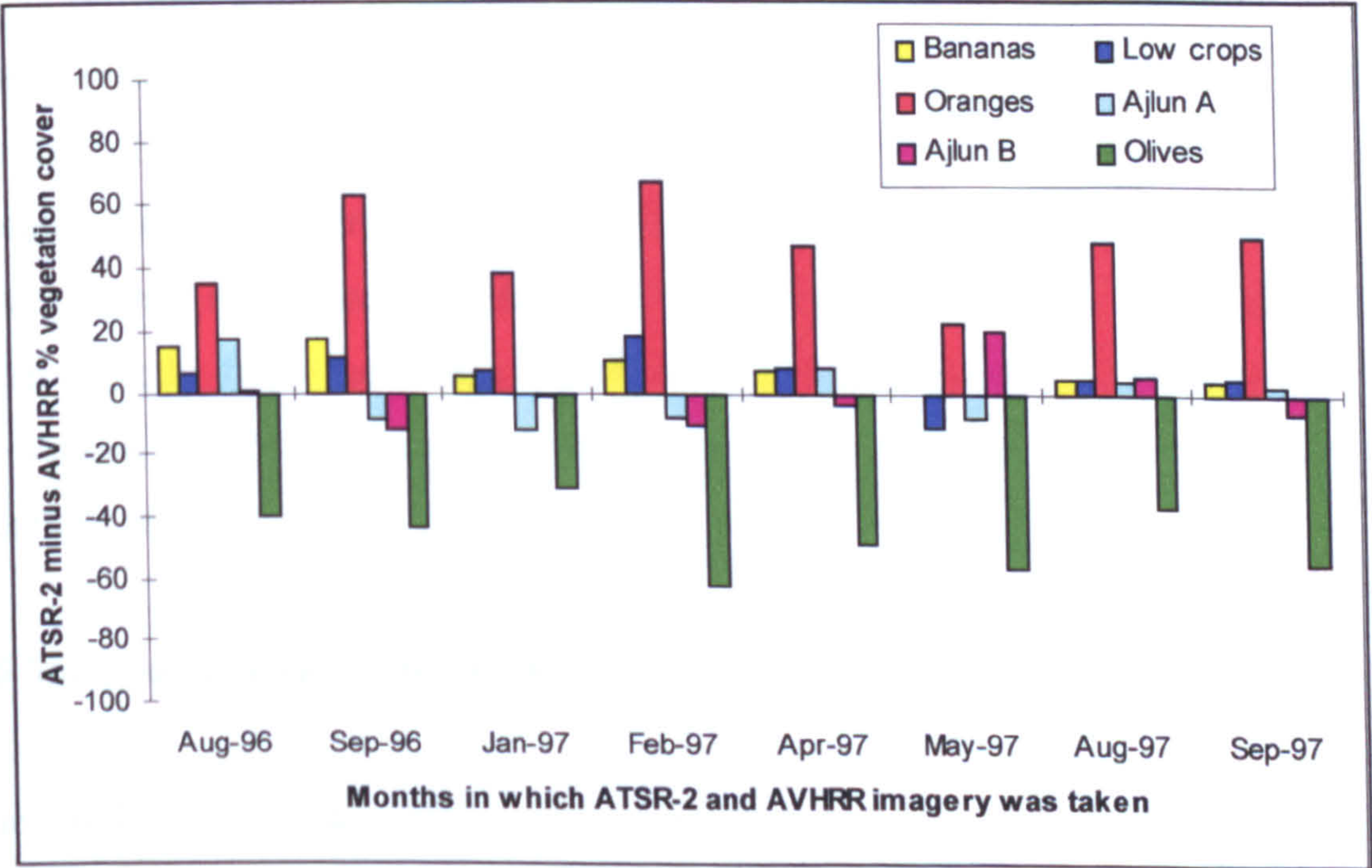


Figure 6.11: Difference in percentage vegetation cover as predicted by ATSR-2 and AVHRR from NDVI values. Predicted percentage vegetation cover is very different ( $\pm 66\%$ ) for the orange and olive field sites.

As one would expect, Figure 6.11 shows very similar patterns to Figure 6.10. Comparing Figure 6.11 with Figure 6.9, one can see that percentage vegetation cover values as calculated from the model show much less variation between the AVHRR



and the ATSR-2 images than predictions made using these images and NDVI derived cover values. All sites vary between ATSR-2 and AVHRR images by less than 20 % cover using the model but up to 66 % when using coverages derived from NDVI values. This is an interesting and significant result.

Using vegetation indices, vegetation change over time is usually monitored using images taken from the same sensor, This is because of differences in absolute radiance values between sensors caused by sensor drift and satellite calibration, spatial and spectral resolution variations. The NDVI is difficult to invert to obtain percentage vegetation cover values because large amounts of ground data are needed.

In contrast, the results presented here indicate that the red/near-infrared scattergram model provides a more robust mechanism for examining time series using different images than by using vegetation indices such as the NDVI. Temporal change within an area of relatively high vegetation coverages (i.e. greater than 20%), can be monitored using imagery from different sensors without the use of ground data. The values for the model are taken from an image. By inverting the model using values taken directly from the image means that to some degree spatial and spectral resolutions are already taken into account. Resulting percentage vegetation covers can therefore be compared.

## **6.6 Model assumptions and limitations**

The model of Jasinski (1996) applied here to AVHRR and ATSR-2 imagery is essentially a hybrid between a highly theoretical model requiring numerous input parameters (and thus extensive field data collection) on the one hand, and an empirical approach where a singular relationship between percentage vegetation cover and reflectance is hard to ascertain, on the other hand. It allows one to analyse extensive regions and thousands of pixels with little or no ground data, and has the advantage that plant and soil reflectances are estimated from the red/near-infrared scattergram without the need to define end-members.



Although the model appears to be able to predict percentage vegetation cover, it must be recognised that it was formulated using certain assumptions. In making those assumptions, limitations in the use and application of the model are introduced.

Plant centre's are assumed to be randomly distributed according to a Poisson distribution. The Poisson distribution is assumed constant within a given pixel, but can vary from pixel to pixel. All plants are assumed to be spherical in shape. As with the simple geometric model described in Chapter 2, this assumption is justified on the basis of field data, where 64 % of the plants measured in the Badia were described in the field as 'spherical'. As has already been mentioned, as one approaches higher percentage coverages, the importance of shape diminishes as plant overlap occurs and the amount of shadowed ground visible to the sensor decreases. In the case of the modelling application described here, the sites where plants were not spherical in shape (banana trees and low market gardening crops) were those in the Jordan Valley with higher percentage coverages.

The non-dimensional solar geometric similarity parameter,  $\eta$  can be defined for any plant shape but assigning it requires knowledge of the type of vegetation in the field. The model is advantageous in that field sampling is not needed for its formulation but having said this, in order to calculate  $\eta$ , some knowledge of the form and shape of the ground vegetation is needed.

Unlike many other models that use sub-pixel estimations, this model is good in that one does not have to specify the reflectance of end-members. As Baret *et al.* (1993) comment, the spatial and temporal variation of soil and vegetation reflectances are unpredictable and difficult to estimate. This is particularly true if pixels are made up of more than one cover type and are not 'pure' pixels. The model used here takes the mean and variance of soil and vegetation reflectance as input, thus allowing for the fact that both of these reflectances exhibit natural variability due to variations in soil texture, organic content, soil moisture, vegetation type, canopy height and leaf area.

One of the problems however, is that the estimates of soil and vegetation reflectance



are based upon the soil line and the  $m = 1$  or 100 % vegetation line as identified in the red/near-infrared scattergram. Firstly, this necessitates that the model can only be applied in areas where an image covers a range of percentage vegetation coverages (if possible from 0 to 100 %) and secondly, assumes that these lines can be identified from the red/near-infrared scattergram.

The existence of a soil line is relatively well established. It is recognised that the soil reflectance does vary as a result of differences in soil type, soil moisture content, mineralogy, the presence of salts etc. but in the red/near-infrared wavelengths, this variation is thought to be limited and a singular global line is generally accepted (Baret *et al.*, 1993). The inclusion of a soil reflectance variance term in model prediction means that to some extent the variability of the soil line is accounted for but on the other hand as the results from Tables 6.3 and 6.4 show distinctions between vegetation covers of less than 10 % are difficult to achieve. Baret and Guyot (1991) also state that the soil line concept is valid for the background surface in terms of senescent vegetation. In an arid region the distinction between senescent vegetation and dry brown actively growing vegetation can be difficult to make in terms of spectral response. This is especially true at very low vegetation covers where the influence of the soil background is high.

In the model, a 100 % cover line is taken as a vertical line on the left hand side of the red/near-infrared scattergram. This contradicts the assumption made by Richardson and Wiegand (1977) who developed the perpendicular vegetation index. They stated that lines of constant percentage vegetation cover fall parallel to the soil line. However, it is in agreement with the NDVI of Rouse *et al.* (1974) and the Transformed Soil Adjusted Vegetation Index of Baret *et al.* (1989) where it is assumed that brighter soils result in higher vegetation index values for a given quantity of incomplete vegetation cover. Taking the mean and variance of vegetation reflectances means to some extent that variability in vegetation reflectance is accounted for but the method does necessitate that a triangle with a vertical line to the left is present in the red/near-infrared scattergram. Pixels falling outside the red/near-infrared triangle defined by the soil line and the  $m = 1$  or 100 % cover line (i.e.



scattered pixels to the right of the soil line and the extreme bottom left) represent areas of snow, water, cloud or error pixels such as dropped image lines. The model makes no attempt to differentiate between them.

## **6.7 Summary and conclusions**

Processes occurring on a sub pixel level can be modelled using a combination of geometric optics and radiative transfer equations. The model examined in this chapter was based on the work of Jasinski (1996) although it was extended in order to consider the application of the model to AVHRR imagery and ATSR-2 imagery.

The results showed that the model produced very similar results to vegetation indices in terms of correlations with ground percentage vegetation cover values. Although considering the processes occurring on a sub-pixel level does help one to understand the physics of energy/surface interactions, in terms of distinguishing low levels of vegetation cover, the problems of confusing the vegetation signal with that of background soil still exist. As with vegetation indices, in general, the model can predict percentage vegetation cover but distinctions between very low levels of cover are difficult.

The invertible model has advantages over vegetation indices in that it does allow one to predict ground percentage vegetation cover without the need for estimates of ground vegetation cover required to draw up empirical relationships. This is advantageous because, in theory, it allows studies of changes in vegetation cover change to be made without the cost in terms of money, time and resources of field data collection. In practise, it is likely that some field data would be required to serve as verification that the model was working within known limits.

The original model was developed for use with Landsat TM and an important difference between Landsat TM and AVHRR and ATSR-2 is the spatial resolution of pixels. With a spatial resolution of 30 m pixels, one would expect Landsat TM to be more applicable to vegetation detection and monitoring than AVHRR or ATSR-2. The



results from Jasinski (1996) using Landsat TM imagery showed errors in estimated fractional cover compared to actual fractional cover to be in the order of a standard error of 0.04. The results here, gave mean squared residuals of 0.044 and below. These convert to a standard error value of 0.012 and below, and indicate that the model works as well with coarse resolution data as with finer spatial resolution data. This means it is useful for studies over large spatial areas as well as for more detailed local studies.

The model also has been shown to work well with imagery from different sensors and illustrates how different imagery can produce similar estimates of percentage vegetation cover for a given point in time. The implications of this are important for vegetation studies, since, unlike vegetation indices, a time series of vegetation change can be formulated using images from different sensors. This is important for projects where resources are limited and imagery from a particular sensor cannot be collected over a long time period.

The model described here was also applied to the forward look of ATSR-2. As was found with vegetation indices, the forward look provided no advantage when compared to the nadir look for examining areas of sparse vegetation. The increase in pixel size and the influence of increased shadow and atmospheric path length mean that relationships between surface properties and ground reflectance are more difficult to ascertain. The following chapter considers ATSR-2 and the forward look more closely. It reviews the information content of the forward look and the problems of changing spatial resolution. The spectral wavebands and the implications for arid land vegetation detection are also considered by comparing the utility of ATSR-2 to other sensors.



## **7.0 Arid land vegetation detection in Jordan using the ATSR-2**

### **7.1 Introduction**

### **7.2 Information held in the forward looking bands of the ATSR-2**

#### **7.2.1 ATSR-2 as applied to the geometric model**

##### **7.2.1.1 Reprojection and Resampling**

##### **7.2.1.2 Geolocation**

#### **7.2.2 Principal components analysis**

##### **7.2.2.1 Methodology**

##### **7.2.2.2 Visible channels**

##### **7.2.2.3 Visible plus thermal band**

##### **7.2.2.4 Forward and nadir bands combined**

##### **7.2.2.5 Summary and conclusions**

### **7.3 A comparison of ATSR-2 with other sensors**

#### **7.3.1 The importance of spectral resolution**

##### **7.3.1.1 The spectral wavebands of ATSR-2 compared to TM and AVHRR**

##### **7.3.1.2 Methodology to compare sensor waveband responses**

##### **7.3.1.3 Results and discussion**

#### **7.3.2 The importance of spatial resolution**

#### **7.3.3 The importance of temporal resolution**

#### **7.3.4 Other advantages of ATSR-2**

### **7.4 Summary and conclusions**



## **7.1 Introduction**

Chapters 5 and 6 have looked specifically at arid land vegetation analysis using vegetation indices and modelling approaches. This chapter turns its focus to the use of the ATSR-2 sensor *per se* as a tool for vegetation detection. In particular it looks more closely at some of the features of the instrument and the implications these have for its use for the mapping and monitoring of vegetation in Jordan. The first part of the chapter considers the forward view angle, the resulting data structure and its potential, whilst the second half of the chapter concentrates on the spatial, spectral and temporal resolution of ATSR-2 as compared to other sensors.

## **7.2 Information held in the forward looking bands of the ATSR-2**

### **7.2.1 ATSR-2 as applied to the geometric model**

The gridded products of ATSR-2 are defined as 512 \* 512 images where nadir and forward view pixels are co-located and regridded onto a 1 km grid (Bailey, 1995). As the conical ATSR-2 scan mechanism results in forward view pixels that are larger in size than nadir view pixels, this section examines more closely the way in which resampling and gridding takes place, and discusses some of the implications of using this method. Similarly, throughout the course of the work it became apparent that the two ATSR-2 views were not geolocated as accurately as the literature suggested. Section 7.2.1.1. considers regridding and resampling, whilst Section 7.1.2.2. examines the issue of geolocation and discusses the implications of mis-registration.

#### **7.2.1.1 Regridding and resampling**

Within the ATSR-2 product literature two terms are defined, the instrument scan and the image scan. The instrument scan represents data acquired from a single rotation of the ATSR-2 scan mirror. Instrument pixels are pixels from the instrument scan that are not co-registered. Due to the conical scan mechanism of the instrument, instrument pixels are larger in the forward view than the nadir view and, for both



views, increase in size away from the ground track. The image scan on the other hand, refers to an across track line of 512 pixels within a gridded product, which have the same along track distance. It follows that an individual image scan is made up of pixels from a number of instrument scans (Bailey, 1995).

To acquire images from instrument scans, a process of regridding and resampling has to take place. For each instrument pixel, image co-ordinates, x and y are calculated as regridding takes place. The integer parts of the co-ordinates are then used to index and arrange the image array. In the nadir view, 555 pixels are collected from the conical instrument scan. As the image represents a 512 km area, these have to be regridded and resampled into 512 places. There are no special algorithms to deal with this situation but if two instrument pixels map to the same image point, the last one to be encountered in the processing is taken, and the other is disregarded (Dr Chris Mutlow, RAL, personal communication). In the forward look the opposite is true. 370 pixels are available to fill 512 places. The 370 instrument pixels are assigned to image points, and any gaps are then cosmetically filled by taking the nearest adjacent image pixel. In this way instrument pixels are used twice

Two of the main issues regarding the question of resampling and regridding, is the difference in area between pixels obtained from the two view angles, and the repetition of information as pixels are cosmetically filled by their neighbours. Pixels recorded in the nadir look are  $1 * 1$  km in area whereas pixels recorded off-nadir at  $55^\circ$  are approximately  $1.5 * 2$  km in area. RAL argue that cosmetic filling in the forward look compensates for the difference in pixel area and to some extent this is true (Dr Chris Mutlow, personal communication 1997). However, this strategy does not work exactly. It is likely, as Godslave (1995) argues, that the distances between the ground resolution element centres for the same scan number are different for the forward and the nadir scans. The forward image will be a different sample of a different integral transform of the ground information when compared to the nadir image (Gemmell *et al.* 1995). The implications of this are important in the degree of confidence that can be placed in using correlations between the two looks as an indication of bi-directional properties of the surface or atmospheric conditions. Differences in the two



views could be as much due to different surface type and areas as any bi-directional property or atmospheric condition.

Regridding and resampling also affects the spatial stability of pixels in multi-temporal imagery. Differences in the reflectance of a field site over time may be as much due to the effects of resampling and regridding as any ground cover change.

Problems caused by differences in the area sampled will depend on the area under study. Large homogeneous areas with uniform reflectance properties will mean that slight differences in the pixel areas sampled will have little effect. Unfortunately homogeneity does not always equate with the area of interest. In Jordan, every effort was made to ensure study areas represented large homogeneous areas but due to the nature of vegetation location next to *qa'a* or basalt areas, slight variations in pixel location may mean that errors are introduced.

#### **7.2.1.2 Geo-location**

As discussed in Section 7.2.1.1, ATSR-2 gridded brightness temperature images have longitude/latitude references associated with every pixel. These can be read from the image file and used to geo-locate the image. During the early stages of the work, it became apparent that features of the image did not match longitude/latitude references taken in the field using the Garmin Global Positioning System (GPS). Although the Garmin GPS is not 100 % accurate due to downgrading in accuracy by the U.S Department of Defence, it is quoted as being accurate to within 15-100 m i.e. one ATSR-2 pixel (<http://www.garmin.com/faqs>, November 1998). In some instances also, the forward look was misregistered in relation to the nadir look.

A small study was carried out whereby *qa'as* were located on the image and their position, according to the corrected ATSR-2 imagery was compared to that taken with the GPS in the field. *Qa'a's* or mud flats were chosen as they appear on the imagery as distinct small bright features. Figure 7.1 shows a subset of the 09/05/97 ATSR-2 image with *qa'as* highlighted as bright white features.



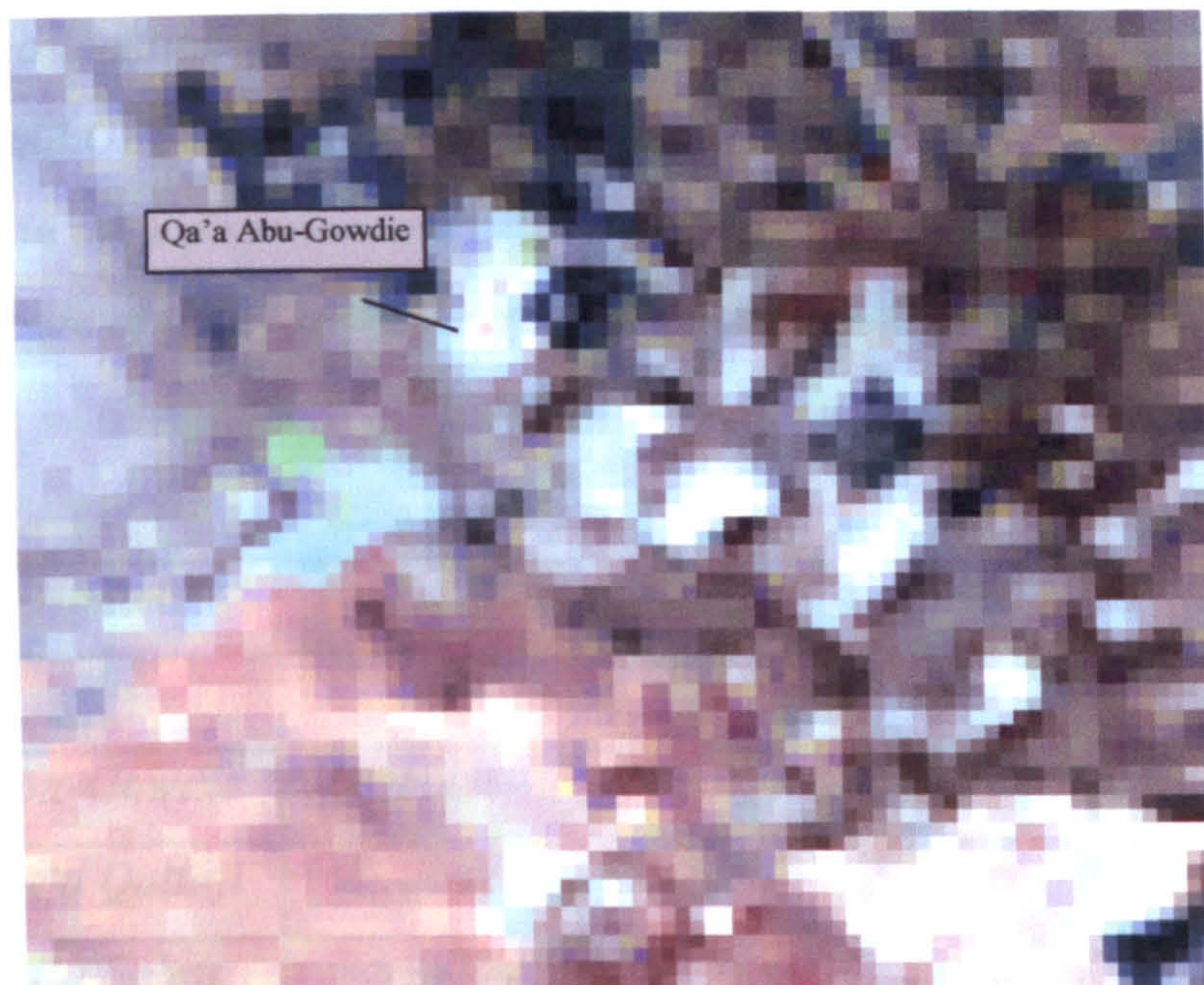


*Figure 7.1: Subset of the 05/09/97 ATSR-2 image with qa'as in white (bands 2, 3 and 4). Qa'as form good ground control points*

*Qa'a Abu-Gowdie, Qa'a Qattafi and Qa'a Salma* were located on ATSR-2 images from 06/09/95, 11/10/95 and 08/01/97 in both the nadir and the forward views. Misregistration of the imagery, as measured against the GPS was recorded in terms of x pixel displacement and y pixel displacement. A positive x displacement means the imagery is displaced to higher longitudes, a positive y displacement to higher latitudes.

The results from the study are given in Table 7.1 :-



*Table 7.1: Geo-locational differences for selected sites between the geometric model of ATSR-2 and GPS measurements taken in the field. Errors are given in terms of displacement in the x direction and displacement in the y direction (units are pixels). Mean errors are of the order of 3 pixels whilst maximum errors reach +45 in the x direction.*

Image	Site	Nadir Data Displacement		Forward Data Displacement	
		x	y	x	y
06/09/95	<i>Abu-Gowdie</i>	none	none	+42	-6
	<i>Qa'a Qattafi</i>	none	+2	+45	-2
	<i>Qa'a Salma</i>	+1	none	+44	-5
11/10/95	<i>Abu-Gowdie</i>	none	none	none	none
	<i>Qa'a Qattafi</i>	+3	none	+1	none
	<i>Qa'a Salma</i>	+1	+1	none	none
08/01/97	<i>Abu-Gowdie</i>	+1	none	none	none
	<i>Qa'a Qattafi</i>	+3	+1	none	none
	<i>Qa'a Salma</i>	none	none	+2	+2

From examination of the results presented in Table 7.1, it is apparent that there are errors and discrepancies in the geometric model applied to ATSR-2 data. These errors are not consistent over time and space and cannot be accounted for by a simple linear transformation of the imagery. Personnel communication with other ATSR-2 users (Thomas Sheasby, University of Leicester, 1998, Mark Chopping, University of Nottingham 1998) and with RAL (1996) confirmed that this was not an isolated case and other users had also experienced similar geo-location errors. Parkes *et al.* (1999) give geo-location errors of -1 in the x direction and -3 in the y direction for the forward look. They report that RAL recognises that the ERS-2 platform is not as exact as on ERS-1, and misalignment of up to 3 pixels may occur. Taking these comments into account, it is likely that the model used for the forward data for the September 1995 image producing up to 45 pixels mislocation in the x direction was erroneous. The other displacements match those described in other sources.



Shin *et al.* (1995) describe a dynamic programming algorithm designed to co-locate nadir and forward view of ERS-1 ATSR to sub-pixel accuracies. As a similar algorithm is unavailable for ATSR-2, it was decided that all imagery would be geo-located for the nadir bands, and the forward bands, using GPS points collected in the field. It is recognised that the models used by the GPS would themselves be subject to a degree of error but, at least using this method, nadir and forward bands would be co-located, and field sites located on the imagery would match those where field measurements were taken. In Jordan, there were a number of features that provided good ground control points. In an ocean based study such as Parkes *et al.* (1999), or in forests, the absence of suitable ground control points makes the accuracy of the longitude/latitude information supplied with the imagery a more critical issue.

Considering the geometric model, it can be seen that the information in the forward view is not necessarily the same as in the nadir view. Regridding and resampling means that the forward view may record slightly different information, thus adding error to the results. This is a particular problem in areas of heterogeneous land cover types. The geometric model supplied with the imagery is also erroneous and misregistration was found to occur. In this study, a better geometric correction for ATSR-2 imagery, is obtained using ground control points. In ocean or forest based studies where ground control points are difficult to locate, the geometric model supplied with the imagery would be more useful.

### **7.2.2 Principal components analysis**

Principal components analysis is a technique that has long been used in remote sensing as a means of data compression (Eastman and Fulk, 1993). Wavebands in an image often exhibit some degree of correlation (Townshend *et al.*, 1987, Li and Yeh, 1998). Principal components analysis performs a linear transformation to produce new bands, made up of proportions of the original bands that are uncorrelated and ordered in terms of the variance explained in the original data set. They are useful in that they remove redundant and duplicated information, and in the case of ATSR-2, allow one to consider the extent to which the forward bands are useful in adding any additional



explanatory information.

Principal components analysis has been performed on ATSR-2 data by Gemmell and Millington (1997) and Perrin and Millington (1997). Both studies illustrated the potential of the dual view in explaining the total data variance. The work described here adds to these studies by building on the work already done, and looking at the application of the principal components analysis in a desert area.

#### **7.2.2.1 Methodology**

Two geometrically and atmospherically corrected ATSR-2 images were chosen for this work. They were 06/09/95 representing a dry season image and 07/05/97 representing a wet season image. A prerequisite for the selection of each image was that it contained cloud free data of the Badia and Jordan Valley areas in both the forward and nadir bands. Details of image data quality and the method adopted for geometric and atmospheric correction can be found in Chapter 3.

Having selected the images, two subsets of each image were made, one containing the Jordan Valley and the other, the Badia region. These areas were selected to see the effect of a dual look on a highly vegetated area and a sparsely vegetated area, respectively. Following sub-setting, the pixel values were exported in band order from ERDAS IMAGINE to Minitab where the principal components analysis was performed. ERDAS IMAGINE does contain an algorithm for principal components analysis which was used to display the component images for interpretation purposes but Minitab was used for calculations as the eigenvectors and eigenvalues are produced in a simple tabular form.

In the literature, there is much discussion as to whether principal components analysis should be carried out using the covariance matrix or the correlation matrix (e.g. Singh and Harrison, 1985, Fung and Ledrew, 1987, Eastman and Fulk, 1993). There are advantages and disadvantages for both. The correlation and standardised matrix is usually used for the analysis of change in multi-temporal datasets (Fung and Ledrew,



1987). The covariance matrix, on the other hand, is more commonly used and justified on the basis of differences in radiometric resolution between the spectral bands of a sensor (Byrne *et al.*, 1980, Townshend, 1984, Singh and Harrison, 1985). Gemmell and Millington (1997), and Perrin and Millington (1997) use the covariance matrix and because this study looks at spectral bands with differences in radiometric resolution, it is used here for means of comparison.

Principal components analysis was performed on the desert and valley datasets for both images on the following sets of bands:-

- a) nadir visible : 0.55  $\mu\text{m}$ , 0.67  $\mu\text{m}$ . 0.87  $\mu\text{m}$ , 1.6  $\mu\text{m}$
- b) nadir visible plus thermal: 0.55  $\mu\text{m}$ , 0.67  $\mu\text{m}$ . 0.87  $\mu\text{m}$ , 1.6  $\mu\text{m}$ , 11.0  $\mu\text{m}$
- c) forward visible: 0.55  $\mu\text{m}$ , 0.67  $\mu\text{m}$ . 0.87  $\mu\text{m}$ , 1.6  $\mu\text{m}$
- d) forward visible plus thermal: : 0.55  $\mu\text{m}$ , 0.67  $\mu\text{m}$ . 0.87  $\mu\text{m}$ , 1.6  $\mu\text{m}$ , 11.0  $\mu\text{m}$
- e) nadir + forward visible plus thermal: : 0.55  $\mu\text{m}$ , 0.67  $\mu\text{m}$ . 0.87  $\mu\text{m}$ , 1.6  $\mu\text{m}$ , 11.0  $\mu\text{m}$

Bands 5 (3.7  $\mu\text{m}$ ) and 7 (11.0  $\mu\text{m}$ ) were not included in the analysis as these contain many missing pixels and pixels containing error codes in the form of negative numbers. Since the visible bands are most influential in vegetation analysis, it was considered that the omission of bands 5 and 7 was acceptable.

**7.2.2.2 Visible channels**

Table 7.2 compares the eigenstructure of the nadir and forward bands for the 09/05/97 image. Table 7.3 does the same for the dry season 06/09/95 image.



*Table 7.2: Results of the PCA carried out for two areas (Jordan Valley and Badia desert) within the 09/05/97 ATSR-2 image, using visible bands. The analysis was conducted on nadir and forward bands separately. In both areas, most of the information is contained within PC1, which is dominated by information held in band 4. Nadir and forward-looking bands give similar results in terms of individual band magnitude and the sign of the eigenvalue*

Jordan Valley								
PC	1	1	2	2	3	3	4	4
	Nad	Frd	Nad	Frd	Nad	Frd	Nad	Frd
band 1, 0.55µm	0.299	0.301	0.309	0.056	0.525	0.627	0.735	0.716
band 2, 0.67µm	0.421	0.436	0.473	0.187	0.405	0.555	-0.659	-0.683
band 3, 0.87µm	0.317	0.270	-0.824	-0.96	0.456	0.031	-0.108	-0.066
band 4, 1.6µm	0.796	0.804	-0.038	0.199	-0.593	-0.546	0.116	0.125
eigenvalue	232.8	151.7	8.06	5.23	6.09	3.55	0.35	0.14
% variance	94.1	94.4	3.3	3.3	2.5	2.2	0.1	0.1
cumulative	94.1	94.4	97.4	97.7	99.9	99.9	100	100
Badia desert								
PC	1	1	2	2	3	3	4	4
	Nad	Frd	Nad	Frd	Nad	Frd	Nad	Frd
band 1, 0.55µm	0.253	0.247	-0.555	-0.565	-0.764	-0.743	0.211	0.261
band 2, 0.67µm	0.386	0.387	-0.502	-0.499	0.295	0.250	-0.716	-0.734
band 3, 0.87µm	0.446	0.443	-0.283	-0.282	0.535	0.580	0.660	0.622
band 4, 1.6µm	0.767	0.770	0.600	0.594	-0.207	-0.221	-0.092	-0.073
eigenvalue	356.4	387.5	8.48	5.37	1.42	1.25	0.14	0.13
% variance	97.3	98.3	2.3	1.4	0.4	0.3	0.0	0.0
cumulative	97.3	98.3	99.6	99.7	100	100	100	100



*Table 7.3: Results of the PCA carried out for two areas (Jordan Valley and Badia desert) within the 06/09/95 ATSR-2 image, using visible bands. The analysis was conducted on nadir and forward bands separately. There is little difference between the two areas in terms of eigenvalue magnitude. In both areas, PC1 is dominated by band 4, whilst PC2 is a contrast between band 4 and the other 3 bands.*

Jordan Valley								
PC	1	1	2	2	3	3	4	4
	Nad	Frd	Nad	Frd	Nad	Frd	Nad	Frd
band 1, 0.55µm	0.297	0.309	-0.582	-0.444	0.298	0.55	-0.696	0.637
band 2, 0.67µm	0.399	0.408	-0.342	-0.096	0.516	0.539	0.679	-0.73
band 3, 0.87µm	0.376	0.373	-0.428	-0.692	-0.803	-0.601	0.174	-0.145
band 4. 1.6µm	0.782	0.774	0.601	0.561	0.01	-0.214	-0.165	0.201
eigenvalue	225.5	144.5	7.13	5.34	5.42	3.01	0.64	0.38
% variance	94.5	94.3	3.0	3.5	2.3	2.0	0.2	0.2
cumulative	94.5	94.3	97.5	97.8	99.8	99.8	100	100
Badia desert								
PC	1	1	2	2	3	3	4	4
	Nad	Frd	Nad	Frd	Nad	Frd	Nad	Frd
band 1, 0.55µm	0.243	0.244	-0.551	-0.613	-0.776	-0.254	0.188	0.707
band 2, 0.67µm	0.380	0.244	-0.505	-0.613	0.305	-0.254	-0.713	-0.707
band 3, 0.87µm	0.446	0.467	-0.298	-0.174	0.514	0.867	0.669	0.00
band 4, 1.6µm	0.773	0.814	0.594	0.467	-0.203	-0.345	-0.095	0.00
eigenvalue	330.9	332.6	7.03	5.55	1.24	1.14	0.09	0.00
% variance	97.5	98.0	2.1	1.7	0.4	0.3	0.00	0.00
cumulative	97.5	98.0	99.6	99.7	100	100	100	100

The results from PCA on the visible bands of ATSR-2 reveal some interesting patterns. For both images, analysis using nadir bands gives very similar results to that using the forward bands. This suggests that the components have a physical interpretation that is common to both views (Perrin and Millington, 1997). For both images, the data can be reduced to two eigenvectors with a loss of less than 3 % of the variation in the case of the Jordan valley and less than 1 % of the variation in the case of the Badia desert. A reduction to two dimensions suggests that the four original bands contain a lot of duplicate and therefore redundant information.



For the Jordan Valley, the coefficients of the first component all have the same sign, which can be interpreted as a brightness feature weighted heavily with information from the SWIR band. PC2, on the other hand, change according to the season. In the wet season image, PC2 is dominated by the near-infrared band and can be interpreted as a greenness feature. In the dry season however, the near-infrared band is less influential and PC2 can be described as being a contrast between the SWIR and the other three bands. This result supports the findings of temporal change in vegetation presented in Chapters 5 and 6. Vegetation increases over the spring months following winter rain and then decreases over the hot summer months. 'Greenness' accounts for less of the variability in the dry season than in the wet season. It is interesting to note that the near-infrared band has a negative loading in PC2 in the wet season in the Jordan Valley. This means that high biomass objects are dark in tone instead of bright in tone.

For the desert area, the results show less seasonal variation. For both images PC1 is again a brightness feature dominated by variation in band 4, the SWIR. PC2 explains less than 3 % of the variation but can be described as a difference between the SWIR on the one hand, and the other three bands on the other hand.

The results from the PCA analysis of the visible bands are similar to those described by Gemmell and Millington (1997) and Perrin and Millington (1997). In all three studies PC1 is dominated by the SWIR and for vegetated areas PC2 is described as a greenness feature. The work done here shows that in a desert area most of the variation is described by PC1 the brightness feature, most probably resulting from differences in substrate. The sparse vegetation coverages mean that variation due to greenness is very low. It appears to be described by PC3 in the 06/09/95 image, with less than 1 % variation.



### 7.2.2.3 Visible plus thermal band

Table 7.4 and 7.5 show the results from repeating the analysis but with the inclusion of the thermal band (11.0  $\mu\text{m}$ ).

With the addition of the thermal data, slight differences emerge between the desert area and the Jordan Valley. In the desert area, 99 % of the variance is still accounted for by the first two principal components. The thermal band strongly influences PC3 but this accounts for only 1-2 % of the total variance. In the Jordan Valley, the first two components account for 96-97 % of the variance and the third component accounts for slightly more, 2-3 %.

These results suggest that the thermal band adds little information to that already contained within the visible bands. Differences between the Jordan Valley and the Badia may be due to the fact that the scene from the Jordan Valley contains part of the Dead Sea. Differences in temperature between the Dead Sea and other land cover types may add to the total variation within the scene. Perrin and Millington (1997), found that the thermal data in ATSR-2 is useful for the discrimination of burned surfaces in tropical forest areas. However, with the absence of large burned areas in the images of Jordan, the role of the thermal data is limited.



*Table 7.4: Results of the PCA carried out for two areas (Jordan Valley and Badia desert) within the 09/05/97 ATSR-2 image, using visible and thermal bands. The thermal 11.0  $\mu\text{m}$  band has little influence on PC1 and PC2. It has a big effect on PC3 but this accounts for only 1-2% of the total image variance.*

Jordan Valley										
PC	1	1	2	2	3	3	4	4	5	5
	Nad	Frd	Nad	Frd	Nad	Frd	Nad	Frd	Nad	Frd
0.55 $\mu\text{m}$	-0.297	-0.298	-0.293	0.044	0.035	0.356	0.036	0.538	-0.715	-0.702
0.67 $\mu\text{m}$	-0.420	-0.432	-0.481	0.163	0.013	0.402	0.380	0.383	0.670	0.692
0.87 $\mu\text{m}$	-0.316	-0.267	-0.666	-0.937	0.605	-0.162	0.282	0.134	0.109	0.075
1.6 $\mu\text{m}$	-0.792	-0.795	0.154	0.243	-0.345	-0.427	-0.465	-0.334	-0.115	-0.12
11.0 $\mu\text{m}$	-0.093	-0.146	-0.465	-0.183	0.717	0.709	-0.496	-0.659	-0.124	-0.095
eigenvalue	234.7	154.9	8.41	5.28	7.05	3.99	5.70	3.18	0.25	0.11
% variance	91.6	92.5	3.3	3.2	2.8	2.3	2.2	0.19	0.1	0.1
cumulative	91.6	92.5	94.9	95.7	99.7	98.0	99.9	99.9	100	100
Badia desert data										
PC	1	1	2	2	3	3	4	4	5	5
	Nad	Frd	Nad	Frd	Nad	Frd	Nad	Frd	Nad	Frd
0.55 $\mu\text{m}$	-0.253	-0.247	-0.555	-0.565	0.561	-0.327	-0.522	0.669	0.205	0.255
0.67 $\mu\text{m}$	-0.386	-0.387	-0.503	-0.499	-0.172	0.047	0.258	-0.263	-0.709	-0.728
0.87 $\mu\text{m}$	-0.445	-0.443	-0.283	-0.282	-0.438	0.328	0.305	-0.479	0.661	0.623
1.6 $\mu\text{m}$	-0.766	-0.77	0.599	0.594	0.198	-0.134	-0.088	0.178	-0.087	-0.071
11.0 $\mu\text{m}$	0.049	0.024	-0.028	-0.012	0.652	-0.875	0.749	-0.471	0.107	0.11
eigenvalue	357.26	387.73	8.49	5.38	1.48	1.35	1.33	1.22	0.12	0.12
% variance	96.9	98.0	2.3	1.4	0.4	0.3	0.4	0.3	0.00	0.00
cumulative	96.9	98.0	99.2	99.4	99.6	99.7	100	100	100	100



*Table 7.5: Results of the PCA carried out for two areas (Jordan Valley and Badia desert) within the 06/09/95 ATSR-2 image, using visible and thermal bands. The thermal band has little effect on PC1. For PC2, it has a greater effect in the Jordan Valley than in the desert area. In both areas, the thermal band influences PC3.*

Jordan Valley										
PC	1	1	2	2	3	3	4	4	5	5
	Nad	Frd	Nad	Frd	Nad	Frd	Nad	Frd	Nad	Frd
0.55 μm	-0.296	-0.309	-0.531	-0.413	0.327	0.495	0.283	0.311	-0.666	0.627
0.67 μm	-0.399	-0.408	-0.201	-0.038	0.562	0.532	0.155	0.157	0.679	-0.724
0.87 μm	-0.375	-0.373	-0.536	-0.656	-0.44	-0.292	-0.602	-0.58	0.122	-0.096
1.6 μm	-0.781	-0.773	0.546	0.478	-0.228	-0.365	0.139	0.112	-0.141	0.167
11.0 μm	-0.039	-0.042	0.304	0.412	0.576	0.503	-0.717	-0.728	-0.246	0.214
eigenvalue	225.84	92.4	7.29	3.7	6.25	2.0	4.23	1.7	0.36	0.2
% variance	92.6	92.4	3.0	3.7	2.5	2.0	1.7	1.7	0.1	0.2
cumulative	92.6	92.4	95.6	96.1	98.1	98.1	99.9	99.8	100	100
Badia desert										
PC	1	1	2	2	3	3	4	4	5	5
	Nad	Frd	Nad	Frd	Nad	Frd	Nad	Frd	Nad	Frd
0.55 μm	-0.243	-0.244	0.549	0.603	-0.155	-0.138	0.762	-0.241	-0.184	0.707
0.67 μm	-0.380	-0.244	0.504	0.603	-0.013	-0.138	-0.316	-0.241	0.709	-0.707
0.87 μm	-0.446	-0.467	0.299	0.179	0.108	0.108	-0.498	0.859	-0.672	0.00
1.6 μm	-0.773	-0.814	-0.593	-0.456	0.0	0.064	0.204	-0.355	0.098	0.00
11.0 μm	-0.005	-0.036	-0.06	-0.182	-0.982	-0.973	-0.17	0.141	-0.054	0.00
eigenvalue	330.88	333.09	7.04	5.67	2.05	2.19	1.22	1.12	0.08	0.00
% variance	77.4	97.4	19.9	1.7	2.2	0.6	0.5	0.3	0.00	0.00
cumulative	77.4	97.4	97.3	99.1	99.4	99.7	100	100	100	100



7.2.2.4 Forward and nadir bands combined

In relation to the usefulness of the forward looking bands of ATSR-2, the most important analysis comes from looking at the results of combining the two views (Table 7.6 and 7.7).

*Table 7.6: Results of the PCA carried out for two areas (Jordan Valley and Badia desert) within the 09/05/97 ATSR-2 image, using visible and thermal bands, forward and nadir bands together. The forward bands have more influence in the Jordan Valley than in the Badia. PC3, PC4 and PC5 account for 5 % image variance in the Jordan Valley compared to <1 % in the Badia.*

Jordan Valley										
PC	1	2	3	4	5	6	7	8	9	10
Nadir, 0.55 µm	-0.24	0.004	-0.032	-0.086	-0.526	-0.01	0.15	-0.032	0.69	0.397
Nadir, 0.67 µm	-0.337	0.043	-0.127	0.129	-0.526	0.184	0.118	-0.534	-0.368	-0.327
Nadir, 0.87 µm	-0.242	0.333	0.643	-0.259	-0.05	-0.557	-0.12	-0.115	-0.082	-0.055
Nadir, 1.6 µm	-0.617	0.568	-0.254	0.161	0.23	0.147	-0.006	0.357	-0.041	0.047
Nadir, 11.0 µm	-0.08	-0.119	0.31	0.743	0.007	0.081	-0.534	-0.099	0.165	0.058
Frd, 0.55 µm	-0.178	-0.306	-0.001	-0.16	-0.274	-0.023	-0.257	0.535	0.153	-0.630
Frd, 0.67 µm	-0.261	-0.413	-0.064	-0.094	-0.2	-0.131	-0.206	0.249	-0.524	0.559
Frd, 0.87 µm	-0.168	-0.133	0.590	-0.216	0.110	0.708	0.189	0.068	-0.038	0.063
Frd, 1.6 µm	-0.498	-0.469	-0.142	-0.140	0.514	-0.158	0.015	-0.381	0.224	-0.087
Frd, 11.0 µm	-0.084	-0.218	0.191	0.481	0.00	-0.287	0.721	0.256	-0.065	-0.075
eigenvalues	365.9	27.4	11.45	8.77	7.37	1.18	0.76	0.49	0.27	0.03
% variance	86.4	6.5	2.6	2.1	1.7	0.3	0.2	0.1	0.1	0.0
cumulative	86.4	92.9	95.5	97.6	99.3	99.6	99.8	99.9	100	100

Table continued overleaf:-



<b>Badia desert</b>										
<b>PC</b>	<b>1</b>	<b>2</b>	<b>3</b>	<b>4</b>	<b>5</b>	<b>6</b>	<b>7</b>	<b>8</b>	<b>9</b>	<b>10</b>
Nadir, 0.55 $\mu\text{m}$	-0.175	0.201	0.432	0.476	0.242	-0.366	0.034	0.151	0.48	-0.264
Nadir, 0.67 $\mu\text{m}$	-0.266	0.307	0.375	-0.166	-0.201	-0.24	-0.216	-0.513	-0.024	0.508
Nadir, 0.87 $\mu\text{m}$	-0.307	0.362	0.193	-0.352	-0.181	-0.196	0.157	0.381	-0.483	-0.373
Nadir, 1.6 $\mu\text{m}$	-0.531	0.502	-0.508	0.181	0.049	0.375	0.051	-0.04	0.164	0.038
Nadir, 11.0 $\mu\text{m}$	0.033	-0.076	0.024	0.338	-0.621	-0.005	0.647	-0.259	-0.011	-0.08
Frd, 0.55 $\mu\text{m}$	-0.179	-0.137	0.353	0.451	0.298	0.35	0.113	0.127	-0.533	0.31
Frd, 0.67 $\mu\text{m}$	-0.279	-0.263	0.325	-0.134	-0.068	0.480	-0.235	-0.371	0.086	-0.542
Frd, 0.87 $\mu\text{m}$	-0.32	-0.299	0.201	-0.371	-0.105	0.189	0.288	0.420	0.44	0.36
Frd, 1.6 $\mu\text{m}$	-0.556	-0.546	-0.327	0.117	0.016	-0.48	-0.108	-0.073	-0.154	-0.028
Frd, 11.0 $\mu\text{m}$	0.018	-0.011	0.018	0.319	-0.612	0.099	-0.586	0.404	0.016	0.073
eigenvalue	723.8	21.31	13.13	2.63	2.38	0.67	0.25	0.20	0.08	0.02
% variance	94.7	2.8	1.7	0.3	0.3	0.1	0.1	0.0	0.0	0.0
cumulative	94.7	97.5	99.2	99.5	99.8	99.9	100	100	100	100



*Table 7.7: Results of the PCA carried out for two areas (Jordan Valley and Badia desert) within the 06/09/95 ATSR-2 image, using visible and thermal bands, forward and nadir bands together. For both areas, PC1 accounts for a large proportion of the image variance. In PC2, nadir and forward bands act in different directions.*

Jordan Valley										
PC	1	2	3	4	5	6	7	8	9	10
Nadir, 0.55 $\mu\text{m}$	-0.245	-0.015	-0.266	0.388	-0.306	-0.107	-0.26	0.042	0.585	-0.45
Nadir, 0.67 $\mu\text{m}$	-0.322	-0.136	0.031	0.509	-0.216	-0.092	-0.363	-0.296	-0.407	0.421
Nadir, 0.87 $\mu\text{m}$	-0.3	-0.189	-0.541	-0.052	0.466	-0.469	0.296	-0.227	0.00	0.045
Nadir, 1.6 $\mu\text{m}$	-0.614	-0.585	0.233	-0.255	-0.09	0.254	0.137	0.257	-0.006	-0.066
Nadir, 11.0 $\mu\text{m}$	-0.03	-0.039	0.348	0.44	0.529	0.402	0.191	-0.377	0.223	-0.118
Frd, 0.55 $\mu\text{m}$	-0.18	0.319	-0.213	0.183	-0.247	0.261	0.528	0.187	0.259	0.526
Frd, 0.67 $\mu\text{m}$	-0.243	0.369	0.045	0.201	-0.143	-0.046	0.386	0.055	-0.539	-0.545
Frd, 0.87 $\mu\text{m}$	-0.229	0.278	-0.426	-0.079	0.374	0.505	-0.439	0.251	-0.175	-0.028
Frd, 1.6 $\mu\text{m}$	-0.474	0.533	0.383	-0.362	0.062	-0.24	-0.18	-0.241	0.23	0.096
Frd, 11.0 $\mu\text{m}$	-0.024	0.045	0.292	0.344	0.359	-0.39	-0.065	0.702	0.03	0.126
eigenvalues	339.61	32.71	10.88	7.83	6.03	1.66	0.76	0.65	0.43	0.11
% variance	84.8	8.1	2.7	2.0	1.5	0.4	0.2	0.2	0.1	0.0
cumulative	84.8	92.9	95.6	97.6	99.1	99.5	99.7	99.9	100	100
Badia desert										
PC	1	2	3	4	5	6	7	8	9	10
Nadir, 0.55 $\mu\text{m}$	-0.17	0.253	0.411	-0.156	0.303	0.449	-0.307	0.57	0.036	0.0
Nadir, 0.67 $\mu\text{m}$	-0.266	0.346	0.303	-0.043	-0.356	0.095	-0.220	-0.431	-0.588	0.0
Nadir, 0.87 $\mu\text{m}$	-0.314	0.368	0.136	0.05	-0.409	-0.054	0.012	-0.122	0.748	0.0
Nadir, 1.6 $\mu\text{m}$	-0.548	0.438	-0.513	0.011	0.336	-0.215	0.204	0.127	-0.167	0.0
Nadir, 11.0 $\mu\text{m}$	-0.006	-0.069	-0.033	-0.656	-0.062	-0.577	-0.464	0.108	0.031	0.0
Frd, 0.55 $\mu\text{m}$	-0.173	-0.121	0.417	-0.021	0.373	-0.218	0.193	-0.231	0.06	-0.707
Frd, 0.67 $\mu\text{m}$	-0.173	-0.121	0.417	-0.021	0.373	-0.218	0.193	-0.231	0.06	0.707
Frd, 0.87 $\mu\text{m}$	-0.33	-0.317	0.229	0.113	-0.456	-0.241	0.348	0.540	-0.216	0.0
Frd, 1.6 $\mu\text{m}$	-0.576	-0.595	-0.226	0.016	0.021	0.315	-0.343	-0.19	0.1	0.0
Frd, 11.0 $\mu\text{m}$	-0.026	-0.035	-0.07	-0.726	-0.104	0.394	0.537	-0.108	0.013	0.0
eigenvalues	642.37	22.11	11.26	3.7	2.62	0.63	0.45	0.13	0.07	0.0
% variance	94.0	3.2	1.7	0.5	0.4	0.1	0.1	0.0	0.0	0.0
cumulative	94.0	97.2	98.9	99.4	99.8	99.9	100	100	100	100



Combining the forward and the nadir bands together changes the data structure. The general patterns apply to both areas, in both images but the influence of the forward bands are more pronounced in the Jordan Valley than in the Badia. The 10 bands can be reduced to 3 dimensions with a loss of 1 % of the variance in the case of the Badia and 5 % variance in the case of the Jordan Valley.

As before, PC1 can be described as a brightness feature dominated by the SWIR band both in the nadir and the forward look. Excluding the thermal bands, PC2 (accounting for 6-8 % of the variance in the Jordan Valley and 2-3 % of the variance in the Badia) is dominated by a contrast between the forward and the nadir data. It is interesting to note that the signs are reversed in the two areas. In the Jordan Valley the nadir bands act in a negative direction while the forward bands act in a positive direction, whilst in the Badia the reverse is true. PC3 varies for the two areas. In the Jordan Valley it can be described as a greenness feature dominated by band 3, the near-infrared band but in the Badia the near-infrared features less strongly. Again this is expected, given the low percentage vegetation cover.

#### **7.2.2.5 Summary and conclusions**

The results from principal component analysis indicate that the forward bands of ATSR-2 have the potential to add information but their use depends on the land cover types under study. In the Badia, where vegetation cover is low the difference between the two views highlighted by PC2 only accounted for 2-3 % of the total variance. This supports the work presented in Chapters 4 and 5, whereby correlations with percentage cover changed very little between the two views. The forward view adds little information in areas of sparse vegetation cover.

In conclusion, the principal components analysis performed in this chapter supports the results found in previous chapters. In general, the forward band adds explanatory information and accounts for more of the variance, but in Jordan its explanation is more applicable to areas of dense vegetation, the Jordan Valley, than the Badia. Unfortunately, one of the main problems with using unstandardised principal



components is the explanation and interpretation of the new uncorrelated wavebands. There are many differences between the two areas which might account for the differences observed in the principal components. The type and amount of vegetation is one of these, but others include soil type, elevation, the presence of water bodies and soil moisture differences. Heterogeneity and therefore spatial differences between the two looks will also result in differences between the areas (Godslave, 1995). Sparse vegetation coverages in the Badia may only be one of the reasons why the forward view seems to add little information.

### **7.3 A comparison of ATSR-2 with other sensors**

The launch of a new sensor and its subsequent use demands an enormous commitment in terms of resources. Its success is paramount and for that reason many months and years of planning go into ensuring that the sensor meets the needs of its user community, both commercial and academic. To be widely used and successful, ATSR-2 needs to have advantages over other similar sensors in terms of at least one of the following:- data quality, data availability and cost, spatial, spectral and temporal resolution.

#### **7.3.1 The importance of spectral resolution**

The spectral response of green vegetation is recognised by a dramatic transition from intense chlorophyll absorption in the red wavebands to high reflectivity in the near-infrared due to inter-cell scattering. The location and width of diagnostic bandwidths is therefore a critical issue (Elvidge *et al.* 1993, Elvidge and Chen 1995). Several studies have considered this theme, examining the movement and position of the 'red edge' (Horler *et al.* 1983) and comparing the use of broad band and narrow band vegetation indices for detecting it (Demetriades-Shah *et al.* 1990, Elvidge *et al.* 1993, Elvidge and Chen 1995).

This section aims to consider the question of the 'red edge' (the diagnostic low red/high near-infrared difference) and narrow wavebands in relation to the ATSR-2.



One of the design requirements for ATSR-2 was to provide narrow wavebands specifically for use in land surface applications (Mason and Delderfield, 1990). This section compares the response of a sparsely vegetated desert surface, typical of those found in the Badia, in ATSR-2, AVHRR and Landsat TM wavebands. Landsat TM is included here since it has very similar wavebands to the ATSR-2 and therefore provides a useful comparison. The AVHRR is included because of similarities in spatial resolution. The work concentrates on the wavebands most commonly used for vegetation detection, the red and near-infrared.

**7.3.1.1 The spectral wavebands of ATSR-2 compared to TM and AVHRR**

The sensor responses for the red and the near-infrared bands of the ATSR-2, AVHRR and Landsat TM vary in width and position. Figure 7.2 shows their positions in diagrammatic form, and Table 7.8 gives them in numeric form.

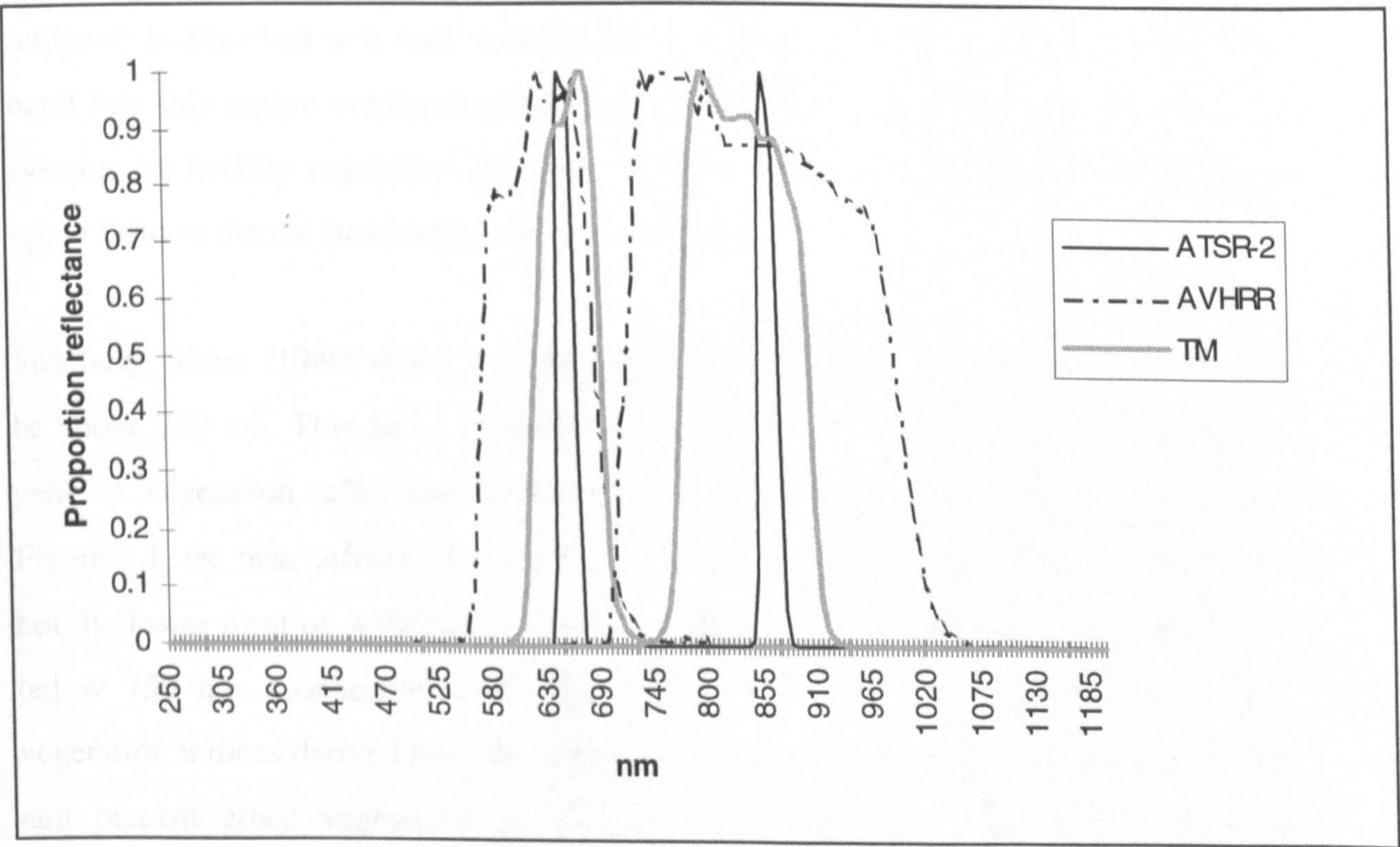


*Figure 7.2: Red and near-infrared bandwidth responses of the ATSR-2, AVHRR and Landsat TM sensors. Comparing all three, ATSR-2 has the narrowest bandwidths whilst AVHRR has the widest bandwidths.*



*Table 7.8: A comparison of the red and near-infrared bandwidths of the ATSR-2, AVHRR and Landsat TM sensors.*

	<b>ATSR-2</b>	<b>AVHRR</b>	<b>Landsat TM</b>
<b>Red waveband</b>	649 - 669 nm	580 - 680 nm	630 - 690 nm
<b>Waveband width</b>	20 nm	100 nm	60 nm
<b>Near-infrared</b>	855 - 875 nm	725 - 1100 nm	760 - 900 nm
<b>Waveband width</b>	20 nm	375 nm	140 nm

All three sensors have a 'red' band between 600 and 700 nm but on the ATSR-2 this band is 20 nm wide compared to 60 nm on the Landsat TM and 100 nm on the AVHRR sensor. As Slater (1980) comments, the lower cut off point for the 'red' band is not important but the upper one should not exceed 690 nm since the region 680-750 nm is a transition zone, where vegetation reflectance moves from a low trough where radiation is absorbed to a high peak where it is reflected. Encroachment by the 'red' band into this region confuses spectral signatures, and reduces the accuracy of such systems for healthy vegetation detection. Of the sensors considered, all three have an upper limit to the red band which lies below 690 nm.

Similarly, Slater (1980) states that the lower cut off of the near-infrared band should be above 750 nm. This again guarantees that the near-infrared band is measuring the peak of vegetation reflectance and not the transition region. As can be seen from Figure 7.1, the near-infrared wavebands of ATSR-2 and Landsat TM accord with this, but the lower limit of AVHRR (originally designed as a meteorological satellite) falls below 750 nm. Consequently AVHRR incorporates this transition zone and thus vegetation indices derived from the AVHRR should show a poorer relationship to LAI and percent green vegetation cover, than indices obtained with sensors such as Landsat TM (Elvidge and Chen, 1995).



### 7.3.1.2 Methodology to compare sensor waveband responses

In order to compare the spectral resolution of the different sensors, reflectance values of soil and vegetation taken from the field were converted into sensor waveband response, and compared. This was done using reflectance data taken across different field sites in Spring 1996 using the ASD field radiometer. Measurements recorded with the ASD were used as these provide high spectral resolution measurements, i.e. 1 nm resolution across the 300-2500 nm range, and can therefore be converted into sensor waveband responses. To convert the ASD measurements to sensor waveband responses, field reflectances were multiplied by the solar spectral radiance and the sensor spectral response. This follows the method described by Mackay *et al.* (1996), where:-

$$\rho_s(\lambda) = \frac{\sum_{i=1}^n E(\lambda_i) \rho_s(\lambda_i) \psi(\lambda_i) \Delta\lambda}{\sum_{i=1}^n E(\lambda_i) \psi(\lambda_i) \Delta\lambda} \quad (7.1)$$

where:

$\rho_s(\lambda_i)$  = Spectral reflectance

$E(\lambda_i)$  = Solar spectral irradiance

$\psi(\lambda_i)$  = Sensor spectral response

Calculations were based on ASD data at 5 nm intervals. They were performed using the waveband characteristics of each sensor separately, using the relevant spectral distribution functions. The NDVI was calculated for each sensor at every site and the results compared. The results from the sensor simulations were also input into the simple geometric model (Chapter 4). Using the model, the reflectance from a sparsely vegetated surface could be derived for each sensor and compared.

### 7.3.1.3 Results and discussion

Figure 7.3 shows the results from simulating the different sensor bands for 6 field sites.



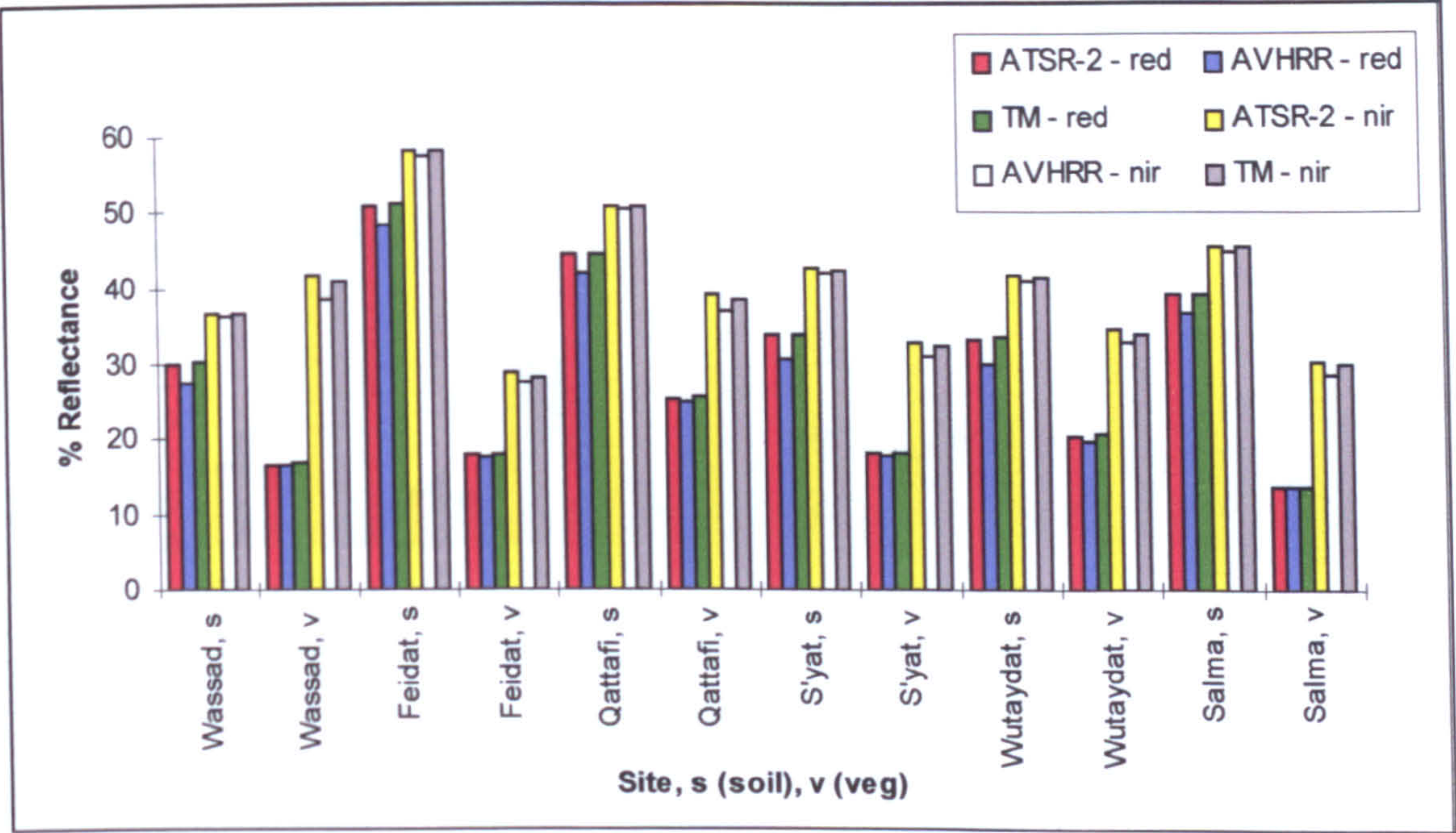


*Figure 7.3: Red and near-infrared reflectances for soil and vegetation at 6 different field sites, as measured by the ATSR-2, AVHRR and Landsat TM wavebands. Differences between the sensors are small. The greatest differential occurs between AVHRR and the other two sensors for the background soil.*

Whilst the differences between the sensors are small, it can be observed that for the background soil the differential between the AVHRR response and the other two sensors is greater in the red wavelengths than in the near-infrared wavelengths. This results in higher NDVI values. Figure 7.4 shows the NDVI values for each site simulated from the field spectra. As expected NDVI values are higher for vegetation than background soil. For the vegetated surfaces, ATSR-2 gives slightly higher NDVI values but the differences between it and other sensors are very small. For soil surfaces, AVHRR gives the higher values.



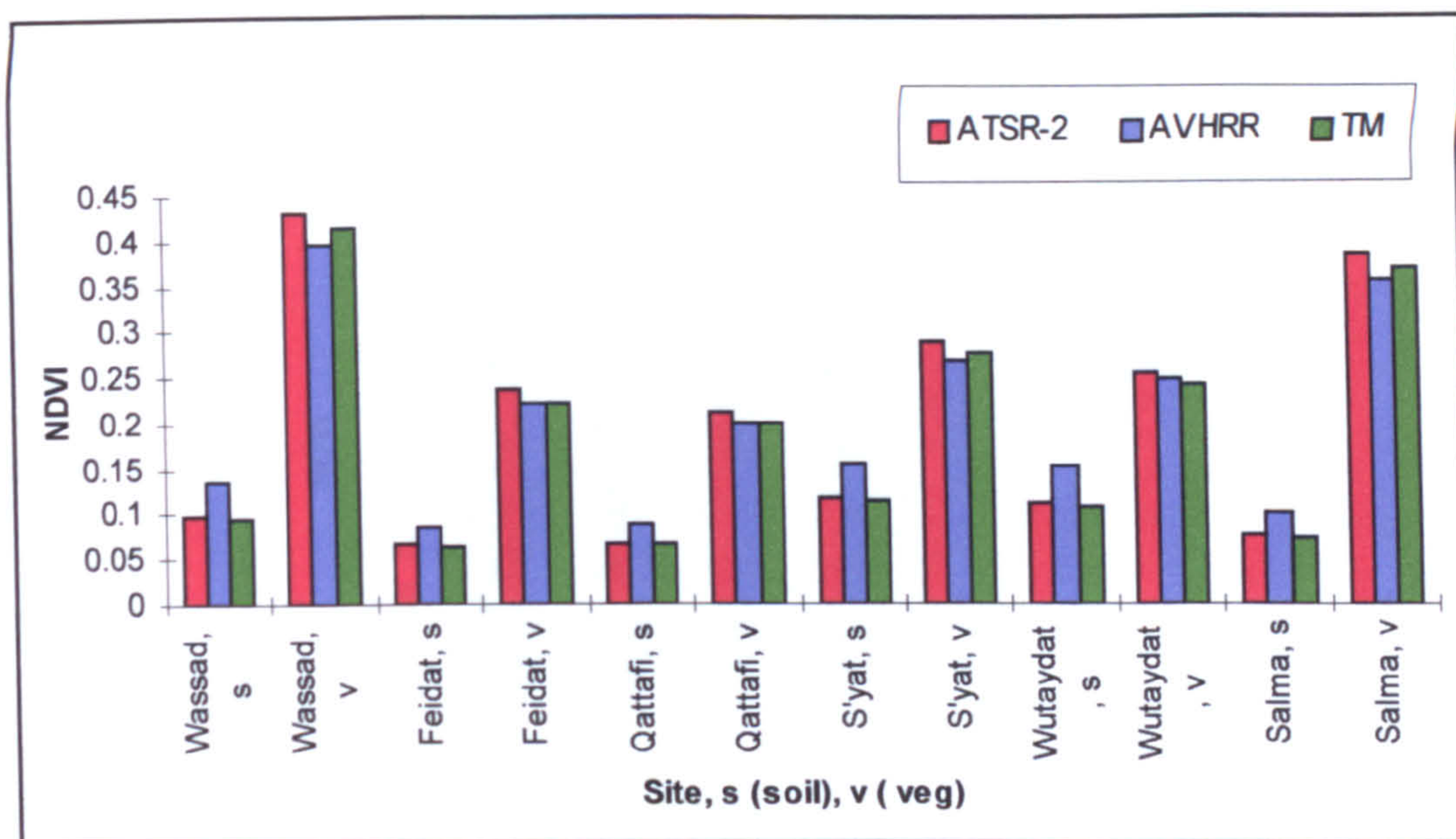


*Figure 7.4: Simulated NDVI of soil (s) and vegetation (v) at 6 field sites, calculated for the ATSR-2, AVHRR and Landsat TM wavebands using ASD field radiometry data. For soil surfaces, the AVHRR gives a consistently higher NDVI at each field site. For vegetation, the highest NDVI is achieved for the wavebands of the ATSR-2*

When the geometric model was applied to consider the spectral response of a sparsely vegetated surface, the results found in the individual band simulations were accentuated. All sites gave similar results, and Marab *Qattafi* is presented as an example in Figure 7.5. The value of 0.08 given in the graph is the fractional cover at *Qattafi* in the spring of 1996 when ASD measurements were taken. The other measurements are simulations. NDVI increases with fractional vegetation cover but due to the large amounts of background soil, the higher values are obtained with the simulated AVHRR data. Unfortunately, the model does not allow for plant overlap and the effect of increased amounts of vegetation, (i.e. above 30 % vegetation cover), could not be monitored.



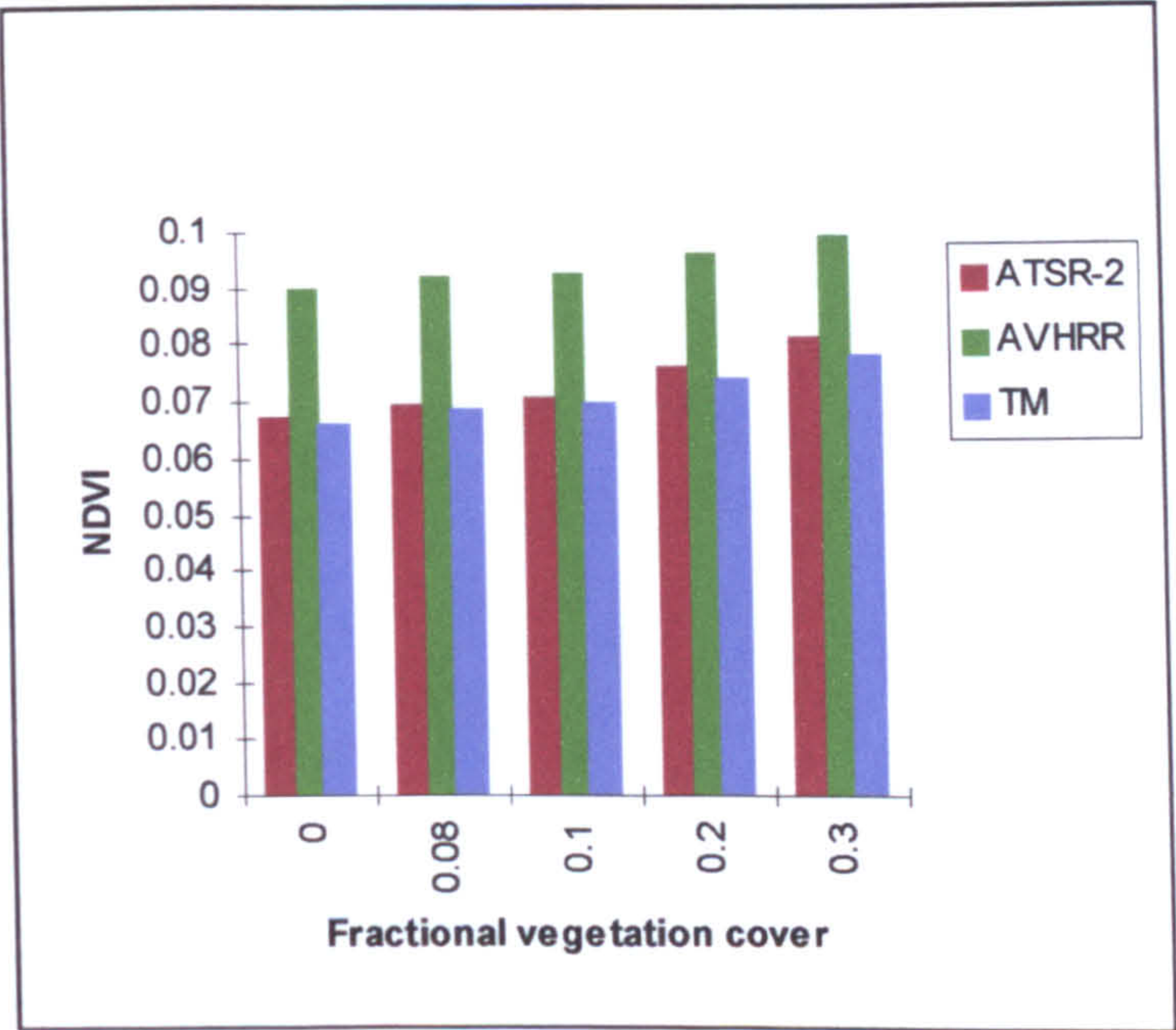


*Figure 7.5: NDVI simulated for the ATSR-2, AVHRR and Landsat TM sensors, for different fractional covers, using the simple geometric optical model (Chapter 4) and field data from Qattafi. At every fractional cover measured, the highest NDVI is given by the AVHRR wavebands.*

Figure 7.6 shows the spectral response of the background soil and the vegetation at *Qattafi*, superimposed on the graph of sensor spectral response curves. It can be used to help explain the patterns shown in Figures 7.3, 7.4 and 7.5.



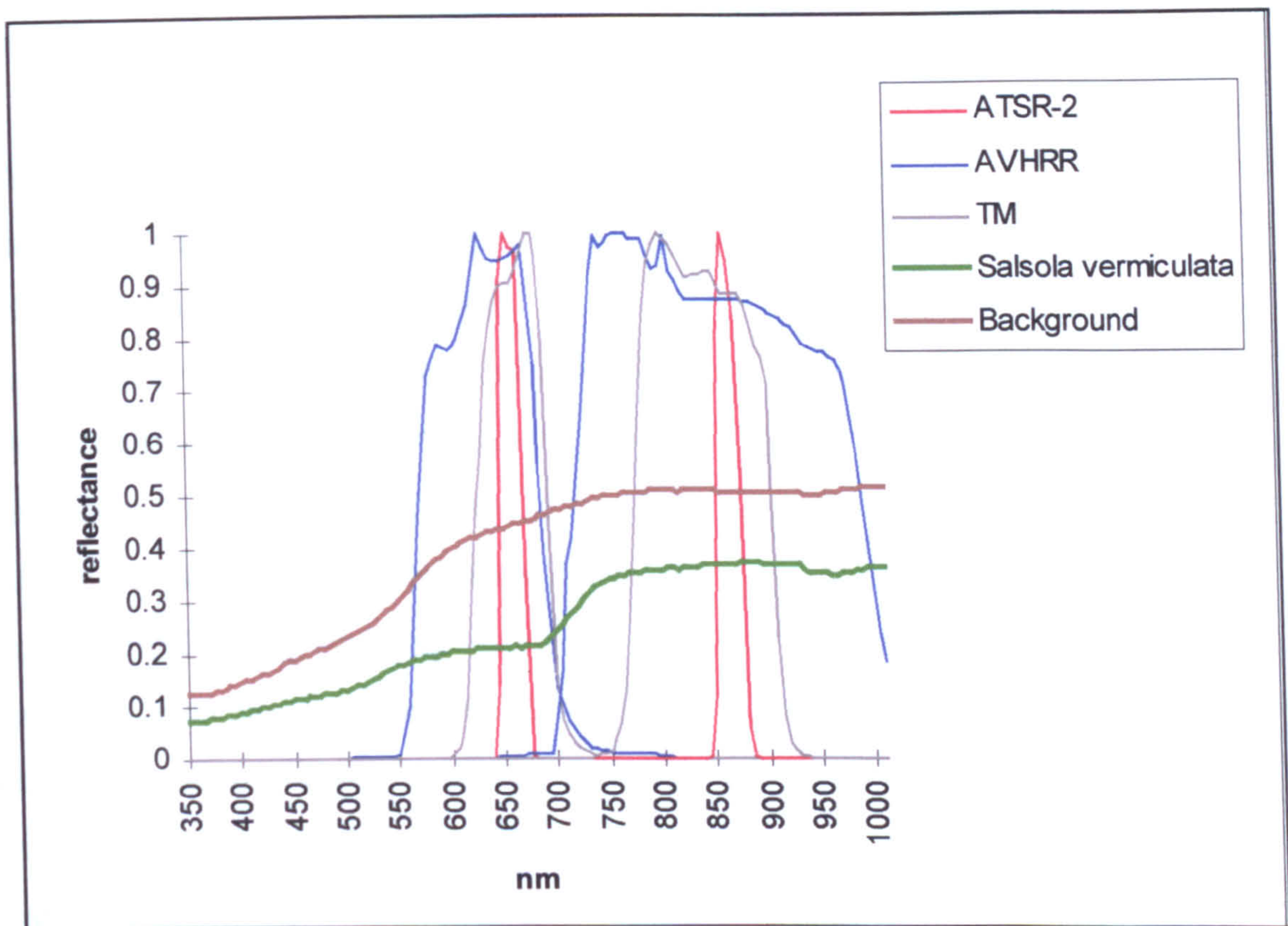


*Figure 7.6: The spectral response of Salsola vermiculata and the background soil at Qattafi superimposed on the waveband responses of the ATSR-2, AVHRR and Landsat TM sensors. The response of the AVHRR sensor appears to overlap into the 'red edge' transition zone between the low red reflectances and the high near infrared reflectances.*

AVHRR gives higher NDVI values due to the extent of the lower limit of the red band particularly in relation to the soil signature. A higher NDVI value does not necessarily mean a better correlation with % cover. As Chapter 5 demonstrated, NDVI values calculated from the AVHRR gave poorer correlations with percentage cover than those calculated with ATSR-2. From Figure 7.6 it can be seen that the ATSR-2 spectral curve is in a position so as to highlight the red edge. The narrow wavebands do not cross into the transition regions. Elvidge *et al.* (1993) describe TM as being a broad band pass sensor that cannot pick up the subtle differences in spectral signatures. The results from Figure 7.6 suggest that ATSR-2 can pick up subtle differences, but as Figures 7.4 and 7.5 indicate, the improvement against other sensors is slight. In sparse vegetated areas such as the Badia, differences in soil reflectance as measured by different sensors outweighs any advantages gained by the narrow



bandwidths of the ATSR-2 for vegetation detection and monitoring.

Chang and Collins (1983) have observed that the chlorophyll red edge is highly variable in terms of wavelength. As leaf chlorophyll levels vary between species and over seasons, the 'red edge' shifts. Narrow wavebands that may sense vegetation at one point in time may fail to sense it at a different point in time. Hall *et al.* (1990), Demetriades-Shah *et al.* (1990) and Elvidge and Chen (1995) recommend the use of derivative spectral indices for vegetation detection. These are indices based upon a continuous series of narrow bands across the chlorophyll red-edge region. In an experimental setting with high resolution spectra collected using ground or airborne spectroradiometers such as AVIRIS this is a feasible option. Using instruments on board a remote sensing satellite, the collection of numerous wavebands across wavelengths is more difficult. ATSR-2, AVHRR or Landsat TM do not provide the spectral resolution to calculate derivative spectral indices. It is hoped that in the future this need will be met. EOS MODIS will provide 36 wavebands ranging from 0.405  $\mu\text{m}$  to 14.385  $\mu\text{m}$  whilst ENVISAT due to be launched by ESA in 1999/2000 carries on board MERIS, an instrument which will provide the user with fifteen wavebands that can be programmed to detect different areas of the electromagnetic spectrum.

Furthermore, the differences between reflectances in red and near-infrared wavelengths as recorded by different sensors may also be the result of variations in solar irradiance across these wavelengths. Solar irradiance is not the same at all wavelengths. A wavelength dependent variation in irradiance and surface reflectance will result in different values as sensors measure in slightly different wavebands. Due to the distribution of solar irradiance and the integral method with which spectra were calculated, it is recognised that differences due to irradiance will be small and almost negligible.

In conclusion, it can be said that compared to Landsat TM and the AVHRR, the narrow wavebands of ATSR-2 do enhance its application to land surface studies and vegetation detection. However, in a sparsely vegetated landscape such as that of the Badia, the advantages of detecting vegetation are obscured due to the strong influence



of the background soil.

This section has only considered the spectral characteristics of ATSR-2. It must also be remembered that the narrow wavebands of ATSR-2 act in conjunction with its other features, i.e. the spatial and temporal resolution. Sections 7.3.2 and 7.3.3 consider the spatial and temporal resolution of ATSR-2 compared to Landsat TM and NOAA AVHRR.

### **7.3.2 The importance of spatial resolution**

Although the 'effective spatial resolution' of a sensor is strictly defined as the smallest object possible to separate from the background, it is often used in reference to the size of a pixel at ground level, the instantaneous field-of-view (Hyppanen, 1996). It is this latter definition that is assumed here.

According to Townshend (1980) there are four criteria for the selection of the spatial resolution of an imaging system. These are the geometric properties of the system, the ability to separate point targets, the ability to measure the periodicity of repetitive targets and the ability to measure the spectral properties of 'small' targets. With a similar spectral resolution to TM, ATSR-2 was designed to provide global coverage with a coarse spatial resolution of 1 x 1 km similar to the 1.1 x 1.1 km resolution of AVHRR (Mason and Delderfield, 1990).

In the Badia, the 1 km resolution of ATSR-2 and 500 km swath width mean that a single image covers the whole of the Badia Programme area, plus the west of the country, Amman and the Jordan Valley. By comparison, four Landsat TM or ERS SAR images are required to cover the same area. Coarse spatial resolution images such as ATSR-2 images reduce the requirement of disk space for storage and processing time, and are comparatively inexpensive when compared to products with finer spatial and temporal resolution such as SPOT data (Ehrlich *et al.*, 1994). They have a higher repeat time which is particularly useful for studies monitoring change over time. All these factors are important particularly in a developmental context



where resources are often limited (Perera and Tateishi, 1995).

Although the 30 m spatial resolution of TM is good for local and large scale studies, regional and global scale studies can only feasibly be carried out using coarse resolution imagery such as the 1.1 km of AVHRR and the 1 km of ATSR-2 (Foody *et al.*, 1997). Such data are used at the 1 km resolution or resampled to coarser resolutions for use over larger areas. AVHRR for example is frequently resampled to 15 km (the NOAA Global Vegetation Index Product) and to 4 km (Global Area Coverages). It has been applied to land cover mapping in Africa (e.g. Townshend *et al.*, 1987), tropical deforestation assessment (e.g. Malingreau *et al.*, 1985, 1989), global variability of carbon dioxide (Fung *et al.*, 1986, Tucker *et al.*, 1986) and fire monitoring (e.g. Kaufman *et al.*, 1990). ATSR-2 can be supplied as a spatially averaged product containing ten arc minute spatially averaged brightness reflectances with associated positional and confidence information. Ten bands are centred on the ERS ground track and numbered 0-9 from left to right. Each band is 50 km wide with the exception of the first and the last which are 56 km wide. The spatially averaged product is especially applicable for global studies and less suited to regional studies such as the one looked at here.

Despite the advantages listed above, coarse resolution imagery is problematic since the intrinsic scale of spatial variation in land cover is usually finer than the scale of sampling (Atkinson *et al.*, 1995). Vegetation parameters such as canopy size, leaf area and fractional canopy cover exhibit spatial scales in the order of 0.1-1.0 m, i.e. less than the resolution of most satellites (Jasinski, 1996). In the Badia, 1 km resolution data was problematic since many vegetated areas were smaller than the ATSR-2 pixel size, and therefore had to be excluded from site selection and consequent analysis. Similarly, in the Jordan Valley, 'low crops' were actually composed of individual fields of wheat, barley, onions and aubergines, crops with different physiognomic forms and bi-directional reflectance properties. The analysis of coarse resolution imagery requires techniques to allow an estimation of sub-pixel properties and the formation of models such as that described in Chapter 6, and the use of methods such as mixture modelling, artificial neural networks and unsupervised fuzzy classification



(Atkinson *et al.*, 1995).

One method by which detail can be added to coarse resolution imagery is to combine it with a finer spatial resolution imagery. Patrono (1996) discusses the advantages of combining Landsat TM with finer resolution SPOT panchromatic imagery and aerial photographs. In relation to ATSR-2, useful synergy would come about as the result of combining the ATSR-2 (with its 1 km resolution) with the 10 m finer resolution imagery of ERS SAR (synthetic aperture radar). One of the key areas in which ESA hope to use data from ENVISAT is in the synergy of AATSR with other instruments such as the ASAR and MERIS (ENVISAT meeting, DERA Farnborough, June 1998). Whether users will have the computing capacity to use all three together remains to be seen.

In conclusion, it can be said that ATSR-2 was designed to bridge the gap between global coverage and high spectral resolution. AVHRR data have been used widely for regional, continental and global scale studies, and with its comparable spatial resolution, ATSR-2 has the ability to do the same. In terms of monitoring the vegetation of the Badia, the spatial resolution of ATSR-2 is good in that it allows synoptic images of the whole region and the monitoring of small scale processes. In terms of vegetation however, processes seem to be occurring at smaller scales and monitoring using TM may enhanced the results. Unfortunately Landsat TM imagery to coinciding with periods of field data collection was not available. It would be interesting to continue this work further, and on the one hand look at vegetation detection using Landsat TM, and on the other hand, combine the dual look and optical properties of ATSR-2, with the finer spatial resolution and soil moisture determinant capacity of ERS SAR.

### **7.3.3 The importance of temporal resolution**

NOAA AVHRR images have been widely used for global studies due to their low cost, suitable wavebands and of discussion here, their high temporal resolution (Shimabukuro *et al.*, 1997). With daily coverage, the AVHRR is ideal for temporal



studies (Ehrlich *et al.*, 1996). Compared to the daily coverage of AVHRR and the 16 day repeat cycle of Landsat TM, the ATSR-2 with a near polar sun synchronous orbit has a repeat cycle of six days. This is still a relatively high coverage and in theory provides the means for temporal studies of a particular area.

In terms of arid land vegetation detection, a six day repeat cycle should capture important physiognomic and physiological changes. After a period of rainfall plants respond quickly, and it is likely that the a 6 day period would capture the greening up. However, as with any set of images, a given revisit period does not necessarily equate with the acquisition of useful imagery. This project aimed to receive monthly images over a two year period enabling inter and intra-annual comparisons to be made. Unfortunately, (as Section 3.3 in Chapter 3 details), some of the images received could not be used in a time series due to the presence of cloud, or the absence of data in one or more bands. Further problems were also encountered due to the failure of the mirror scan and shut down of the instrument between 22/12/95 and 01/07/96. Problems such as these were unforeseen and have to be accepted as an integral part of any research programme.

#### **7.3.4 Other advantages of ATSR-2**

One of the advantages that the ATSR-2 has over AVHRR is that it has continuous on-board calibration. Unfortunately channels 1 and 2 of the AVHRR instrument contain no in-flight calibration other than space viewing. To obtain up-to-date estimates of calibration coefficients, pre-launch calibration coefficients which were calculated before the instrument was subjected to extreme heat, vibration and rough conditions during launch, must be used in association with knowledge of in-orbit sensor degradation (Cracknell and Busu, 1995). In comparison, the ATSR-2 has two black bodies on-board at known temperatures. Radiation from these is measured during each scan and a continuous calibration of the instrument is undertaken. On-board calibration means that images taken over a significant period of time are less subject to influences of sensor degradation, and are therefore more directly comparable over a long period.



An important issue in relation to temporal resolution is the storing and archiving of data. One of the best known for AVHRR data is the archive at Dundee, Scotland which contains data from late 1978 to the present time (Cracknell and Busu, 1995). For the ATSR-2, data is available from a number sources, the UK processing and archiving facility (PAF), is at the National Remote Sensing Centre (NRSC). Archived images can also be viewed and ordered from the European Space Agency via their comprehensive web pages. In terms of data continuity, ATSR-2 carried on from the ATSR and is to be succeeded by the AASTR - the Advanced Along Track Scanning Radiometer. All three data sources vary slightly, but, in the same way as the NOAA satellite series, they provide a continuous series of instruments with which land surface properties can be monitored over long periods of time.

#### **7.4 Summary and conclusions**

This chapter has examined some of the features of the ATSR-2 instrument and from it a number of conclusions can be drawn:-

- Due to the processes of re-gridding and re-sampling, the ground area represented by a pixel in the forward look is not necessarily the same as that represented in the nadir look. Any differences between the looks could therefore be as much due to differences in ground area as bi-directional reflectance properties.
- Confidence in the longitude/latitude data given with the imagery can only be made to within 3 pixels. Accurate geometric correction of ATSR-2 should be made with reference to additional information such as ground control points.
- Principal components analysis suggests that in areas of low vegetation cover such as the Badia, the forward look adds little in the way of additional information. In areas of high vegetation cover, the forward look does add information and PC2 can be used to pick out areas of 'greenness'.
- The narrow wavebands of ATSR-2 are favourable for vegetation detection but with sparse vegetation cover in an arid environment, any advantages the ATSR-2 has over broader band sensors are lost, due to the over-riding influence of the background soil.
- The spatial resolution of the ATSR-2 is appropriate for large scale studies and



comparable to the more widely used AVHRR. In conjunction with vegetation detection in the Badia however, a finer spatial resolution would be more useful as changes occur at scales smaller than 1 km.

- With a 6 day repeat cycle, ATSR-2 provides good temporal coverage. Problems with data quality and cloud cover however, mean that many images have to be disregarded. A daily cycle, such as that provided by NOAA AVHRR, increases the probability of obtaining cloud-free images and enables one to detect rapid temporal changes in vegetation.

This study is concerned with the application of ATSR-2 at the extreme limits of low vegetation cover. Several features contribute to the fact that at very low cover, vegetation is very difficult to detect using the ATSR-2. It must be remembered that the ATSR-2 meets a number of pre-determined applications. It came as a successor to ATSR which was designed primarily for oceanographic and climatic research and provided the accurate determination of sea surface temperatures for input into climate models (Zavody *et al.*, 1994). In the quest to meet several applications, it is inevitable that the instrument will work better for some applications than others. The work done here suggests that ATSR-2 does not work particularly well for the detection of sparse vegetation coverages as in the Badia but it can detect higher coverages such as those present in the Jordan Valley. Arid land vegetation is very difficult to map and monitor *per se* and enhanced spatial, temporal and spectral resolution found on other sensors may still not provide the means necessary to detect it.



## **8.0 Conclusions**

### **8.1 Introduction**

### **8.2 Summary**

#### **8.2.1 Arid land vegetation detection**

#### **8.2.2 ATSR-2 as a tool for arid land vegetation detection**

### **8.3 Application to the Jordan Badia Research and Development Programme**

#### **8.3.1 Integration of data sources**

#### **8.3.2 Remote sensing in development**

### **8.4 Problems associated with arid land vegetation detection and monitoring**

### **8.5 Suggestions for further work**



## **8.1 Introduction**

This thesis has attempted to examine the utility of ATSR-2 as a tool for the detection and monitoring of arid land vegetation in the Badia region of Jordan. Throughout the course of the research, it became apparent that in essence two issues were being considered, the question of the detection and monitoring of arid land vegetation *per se* and the problems associated with this aspect, and the ability of ATSR-2 as a sensor to address this question. More particularly, in addressing the question as to whether the specific features of ATSR-2 that make it distinct from other optical sensors, particularly its dual look and narrow bandwidths, make it suitable for the study of vegetation in arid areas ?

This final chapter summarises the findings of the work and attempts to put it back into the context of the Badia Research and Development Programme. Problems encountered throughout the project are discussed, and suggestions for further study, made.

## **8.2 Summary**

### **8.2.1 Arid land vegetation detection**

The work carried out looking at arid land vegetation detection and monitoring in the Badia region of Jordan supports claims by other authors that the detection of very low levels of vegetation cover is very difficult to achieve especially in arid environments where soil background reflectance is often very high. Both vegetation indices and a modelling approach using either ATSR-2 or AVHRR data, one can differentiate high levels of vegetation cover, such as those found in the Jordan Valley from low levels of cover such as those found in the Badia, but distinguishing between very low levels of vegetation cover cannot be achieved.

One of the biggest problems is the influence of the background soil. Soil adjusted vegetation indices include constant terms to take account of the soil but a single



constant applied on an image wide basis fails to recognise local variations in soil properties and soil reflectance. Soil is confused with vegetation as a result. Using the red/near-infrared scattergram model, it is possible to recognise variations in soil reflectance since it is formulated using the mean and variance of the soil line. However, on inversion, difficulties are still encountered when distinguishing between low levels of cover.

In addition to the background soil, another difficulty in distinguishing low levels of vegetation cover stems from the fact that pixels containing low levels of cover include a high proportion of shadow. Shadow darkens the reflected signal and affects wavelengths differentially. It suppresses the red/near-infrared spectral difference that is characteristic of the spectral reflectance of vegetation making soil/vegetation distinctions more difficult.

A further point of consideration is the nature of the vegetation itself in a desert region. Although plants grown for commercial use in the Jordan Valley are very green and photosynthetically active due to irrigation, those in the Badia region are often dry and green/grey/brown in colour. They are specially adapted to reduce water loss and photosynthetic activity. These characteristics affect the plant's spectral properties, decreasing the red/near-infrared difference which again makes the distinction between soil and vegetation less pronounced.

The background soil, nature of the vegetation and shadow mean that traditional vegetation indices cannot detect small amounts of vegetation. These factors also apply to the model applied in this study. Although concerned with processes occurring on a sub-pixel scale, the model is still based on the red/near-infrared scattergram of an image. Interpretation of this scattergram relies on the fact that certain properties can be associated with the position of pixels within it. This necessarily dictates that the spectral properties of both soil and green vegetation can be assumed. Departure away from these assumptions as in the case of arid land vegetation, which does not fit a 'typical' vegetation response in the red and near infrared makes application of the model difficult, particularly in the case of low vegetation cover.



Despite the fact that both AVHRR and ATSR-2 data cannot distinguish between very low levels of vegetation as found in the Badia region of Jordan, they can be used to look at seasonal responses of vegetation across this region and the Jordan Valley. Using both vegetation indices and the modelling approach, it can be seen that vegetation covers are lowest in the hot dry summer months, and increase in the period after winter rainfall. Given the lack of precipitation and irrigation activity in the summer and the response of vegetation to increased water availability in the late winter/early spring months, this pattern is expected and readily explained. The comparison of AVHRR and ATSR-2 imagery showed that the red/near-infrared scattergram model can be used successfully on imagery from different sensors, illustrated by the similarity of the results. This is an important result, indicating the potential of the model to monitor vegetation over a significant period of time with a time series of images acquired from different sensors.

### **8.2.2 ATSR-2 as a tool for arid land vegetation detection**

In addition to investigating and comparing the use of ATSR-2 and AVHRR for arid land vegetation detection and monitoring. This thesis aimed to consider the utility of ATSR-2 as an instrument for arid land vegetation detection. This placed particular emphasis on properties unique to the ATSR-2 - namely its forward look and narrow bandwidths.

Results from the simple geometric optical model, image analysis in Chapters 5 and 6 and principal components analysis have showed that the forward view of the ATSR-2 seemingly offers no advantages to arid land vegetation detection. This is due primarily to the fact that images of Jordan in the forward look of ATSR-2 are taken in a descending mode and a forward scatter direction. A forward scatter direction, although increasing the difference in reflectance between view angles, means that shadow becomes an important component of any pixel. This means that any advantages in vegetation detection due to 'seeing' more of the vegetation off-nadir do not translate into an increased ability to detect and monitor vegetation using spectral responses given from the surface and received at the sensor.



In addition to viewing in a forward scatter direction, viewing the ground off-nadir also means that the size of the pixel is increased. Resampling and regriding results in a comparable 1 km resolution image to the nadir look but for purposes of comparison it must be recognised that the images do not represent the same area on the ground. Imagery can be compared with ground data, but nadir and forward view comparisons are limited since each represents different ground areas.

In terms of the utility of the narrow bandwidths of ATSR-2, this work has shown that narrow bandwidths are favourable for vegetation detection, even in the case of arid land vegetation where the difference between the red and near-infrared wavelengths can be slight. However, for vegetation detection on the scale of a 1 x 1 km pixel, the advantages are outweighed by the overriding influence of the background soil. ATSR-2 has therefore no advantages over the broader bandwidths of the AVHRR sensor in terms of arid land vegetation detection.

### **8.3 Application to the Jordan Badia Research and Development Programme**

#### **8.3.1 Integration of data sources**

To place this study within the context of a wider real-time application, this work was carried out as part of the Jordan Badia Research and Development Programme. Initially, it was hoped that the study may be able to provide information on grazing potential and the way in which grazing patterns change seasonally, and from year to year. Throughout the course of the work it became apparent that the difficulties in arid land vegetation detection, and the inability of ATSR-2 to distinguish between very low levels of vegetation cover would render this task difficult, if not impossible.

As an alternative, it was decided that images from the model could be provided to the JBRDP terms of dry and wet season images. Whilst not being accurate in terms of absolute percentage vegetation cover values, these would give an idea of areas of high and low vegetation cover within the Programme area, and indicate the way in which



the Badia region differs to that of the more vegetated regions of the Jordan Valley. These images will be presented as percentage vegetation cover images as calculated using the red/near-infrared scattergram image (e.g. Figure 6.4)

The Centre for Overseas Research and Development (CORD) at the University of Durham provides the headquarters for Badia Programme involvement in the UK. At CORD, they are bringing together information collected by different researchers to form a Geographical Information System (GIS) covering the spatial area of the Badia Programme area, and including information layers on both aspects of the human and physical geography of the area e.g. the soils, geology, geomorphology, topography, hydrology and settlement pattern. A thematic map of percentage vegetation cover, the result of this work, forms an input layer to the GIS.

It is envisaged that the Badia GIS will provide the information needed to make informed decisions regarding future sustainable development and resource management in the region. It is also hoped that it will increase general awareness about the region of the Badia both in Jordan and overseas.

### **8.3.2 Remote Sensing in development**

This study was undertaken primarily to research the utility of ATSR-2 as a tool for the study of arid land vegetation. Set within a development programme, it also provides the opportunity to comment on the issue of remote sensing in development.

Remote sensing within a development programme is a potentially contentious issue. As a resource intensive methodology, it could be argued that the resources used in the acquisition of imagery and undertaking of fieldwork could be better spent in the implementation of development projects. In the case of Bedouin in the Badia region of Jordan, it could also be argued that although remote sensing can give decision makers up-to-date information regarding the temporal and spatial information of vegetation cover and state, the relevance of this to the Bedouin themselves is debatable.



Despite these arguments, Agenda 21, reports at the United Nations and World Bank consider remote sensing to be a necessity in developing countries (Kabbaj and Mehrez, 1994). Like Jordan, many developing countries face major environmental problems such as desertification, deforestation, drought and flooding. Remote sensing offers the only practical means of obtaining information on natural resources quickly, at relatively low cost and for inaccessible areas (Kabbaj and Mehrez, 1994, Perera and Tateishi, 1995).

While there are problems of remote sensing implementation in developed countries, these are heightened in the developing world. With low national incomes and low resource allocation to the national education system, some of the difficulties faced include the cost of computer resources and data, trained users, software development, leadership, organisation and funding (Yeh, 1991, Saunders and Culter, 1994).

Having said this, attempts can be made to make remote sensing more appropriate and attractive in a developmental context. In terms of low economic strength, techniques can be adopted that are not computer intensive in terms of resources. Classification using visual interpretation by SPOT panchromatic imagery, for example, can produce the same results in terms of accuracy as automated methods (Edwards, 1995). Imagery can also be used that is cheap or freely available such as the AVHRR. The Badia Programme is fortunate to have government sponsorship and international collaboration. In many developing countries it is economically difficult to implement GIS and remote sensing laboratories without the use of foreign aid (Perera and Tateishi, 1995).

In terms of educational barriers, training can be given at a local level in national universities or at an international level. The International Institute for Aerospace Survey and Earth Sciences (ITC), the Groupement pour le Developpement de al Teledetection Aerospatiale (GDTA) and the European Space Agency are just some of the organisations in Europe that have offered training in remote sensing for developing countries (Kabbaj and Mehrez, 1994). In terms of the Badia Programme, the work is very much a collaboration between researchers from universities in the



UK and researchers in Jordan. Several Jordanian researchers have spent time at universities in the UK and *vice versa*. The GIS being constructed at CORD, will be placed at the field centre at Safawi in the Badia for use within the development programme there.

The Badia Programme is a good example of the way in which remote sensing can be applied to a developmental context. At the present time, the information produced as a result of this project and the parallel work by Tansey (1999) has been made available to project administrators and managers. The extent to which it is used in the future to address regional development, and the problems of overgrazing and desertification in the Badia region remains to be seen.

#### **8.4 Problems associated with arid land vegetation detection and monitoring**

Section 8.2 has already mentioned some of the problems encountered when considering arid land vegetation detection and monitoring, i.e. the influence of the soil background, the nature and type of vegetation and the influence of shadow. This section comments on the methodology adopted and evaluates some of the problems experienced.

The vegetation parameter adopted to act as a comparison with remotely sensed data was that of percentage vegetation cover. Whilst in the circumstances available in the field, other measures such as leaf area index or biomass could not be taken, percentage vegetation cover is limiting in that it gives no indication as to the number and orientation of leaf surfaces visible to the sensor, factors which directly influence radiance values received.

Correlating reflectance values from ATSR-2 and AVHRR, with a broad vegetation measure such as percentage cover also gives no information on the species present. In the context of grazing, information on species is useful in that species vary in their palatability such that the presence or absence of certain species could give an indication of the level of grazing which could be supported. With the use of models



predicting plant structure, some inclusion of particular species type can be made but in general this is very difficult to achieve. The large spatial scale of ATSR-2 and AVHRR restricts the extent to which vegetation parameters can be determined.

Given that the study looked primarily at the way in which reflectance values changed with percentage vegetation cover, it would have been good to have a situation in which in a given reference area percentage vegetation cover values ranged from 0 to 100 % in unit blocks on a similar soil background. This would enable one to assess directly the effect of changing coverages, eliminating common factors such as soil type, topography, climatic variables etc. In reality however, this situation is unlikely to occur except in a designed experimental capacity. In order to encompass a range of coverages in Jordan, sites in Jordan had to be taken from two very different regions, the desert of the Badia region and the fertile Jordan Valley. These areas differ in geology, soils, topography and climate and add more variables to the vegetation/surface reflectance equation. However, in an operational setting these are typical problems and have to be accepted and accounted for.

As with any regional temporal study, observations are also constrained by the imagery and information available. With the use of optical sensors, the weather plays a significant role dictating the availability of cloud-free scenes. Technological difficulties in sensor operation although unforeseen and unfortunate, severely limits imagery availability and consequent analysis. Similarly, administrative and logistical problems encountered during fieldwork meant that the project had to be tailored accordingly. When using remote sensing as a tool for environmental analysis, this situation is acceptable, and taken as a common and integral part of applying a technology to a real-time application.



## 8.5 Suggestions for further work

This study aimed to address several questions. Firstly to look at the use of both the ATSR-2 and the AVHRR for arid land vegetation detection and monitoring, to assess the utility of the forward view of ATSR-2 and to consider the implications of its narrow bandwidths. Using several methodologies the work attempted to answer these questions using the Jordan Badia Research and Development Programme as a geographical site for data collection and analysis. In answering these questions, the study posed new ones. Suggestions for further work can be made.

ATSR-2 was one of the first of a new generation of sensors developing off-nadir viewing. Since its launch in 1995, other sensors have been developed which will view the Earth's surface at view angles away from nadir. They include the joint French/Japanese sensor POLDER (POLarisation and Directionality of Earth Reflectance), SPOT VEGETATION and the NASA satellites MISR (Multiangle Imaging SpectroRadiometer) and MODIS (MODerate resolution Imaging Spectroradiometer).

At the present time, preparations are being made by ESA for the launch of a new satellite, ENVISAT. As an Earth observing satellite, ENVISAT is planned as a successor to ERS-1 and ERS-2 offering new instruments and the continuation of old ones. In relation to global vegetation monitoring, ENVISAT carries on-board three instruments, ASAR, AATSR and MERIS. ASAR and AATSR as the names suggest, are continuations of the SAR and ATSR-2 on-board ERS-2 whilst MERIS is a new instrument capable of gathering information in 15 programmable wavebands in the visible and near-infrared at resolutions of 300 m or 1200 m (ESA, 1998). Whilst AATSR offers the opportunity to examine again the significance of a dual view, MERIS, with programmable narrow wavebands will enable one to investigate further the importance of spectral resolution and narrow wavebands. In relation to arid land vegetation detection and monitoring, this is particularly significant.



Another sensor with narrow bandwidths is SPOT VEGETATION or SPOT 4. Launched on 24th March 1998, SPOT 4 was designed specifically for studies of the biosphere. In the visible and near-infrared regions SPOT 4 provides 4 wavebands in its multi-spectral mode, taken at angles up to 27° from nadir and at 20 m resolution. Designed specifically to enhance the study of vegetation and the red/near-infrared difference, wavebands are narrow, 0.5-0.59  $\mu\text{m}$ , 0.61-0.68  $\mu\text{m}$ , 0.79-0.89  $\mu\text{m}$  and 1.58-1.75  $\mu\text{m}$ . Despite this however, initial studies carried out using ASD field data in Jordan show that, as with ATSR-2, these narrow wavebands still do not enhance the ability to detect arid land vegetation. 'Vegetation' sensors are designed around the archetypal reflectance curve of green photosynthetically active vegetation - desert vegetation does not necessarily conform to this pattern and problems in its detection result. Further work could include the use of airborne hyperspectral data. This gives numerous narrow wavebands and would allow the detection of very small red and near-infrared differences.

It would be interesting to compare images from ATSR-2 with those of AATSR, as well as to look at images collected using MERIS and SPOT 4 instruments. In terms of application of the red/near-infrared scattergram model, the question of whether similar results are consistently obtained using images collected using different sensors is an important one, that would be good to investigate further. This does not require off-nadir viewing sensors but could be carried out using more traditional imagery such as that from Landsat TM, MSS and SPOT.

The effect of finer spatial resolution, both on the applicability of the model, and the question of the detection and monitoring of arid land vegetation using off nadir sensors also needs further investigation. It would also be useful to test the robustness of the model by applying it to similar areas in other parts of the world e.g. the arid rangelands of Tunisia.

Although the results from this study are taken to be generally applicable to the detection and monitoring of vegetation in arid areas, it would be interesting to conduct a similar study in an arid area in another location. More research is needed on the



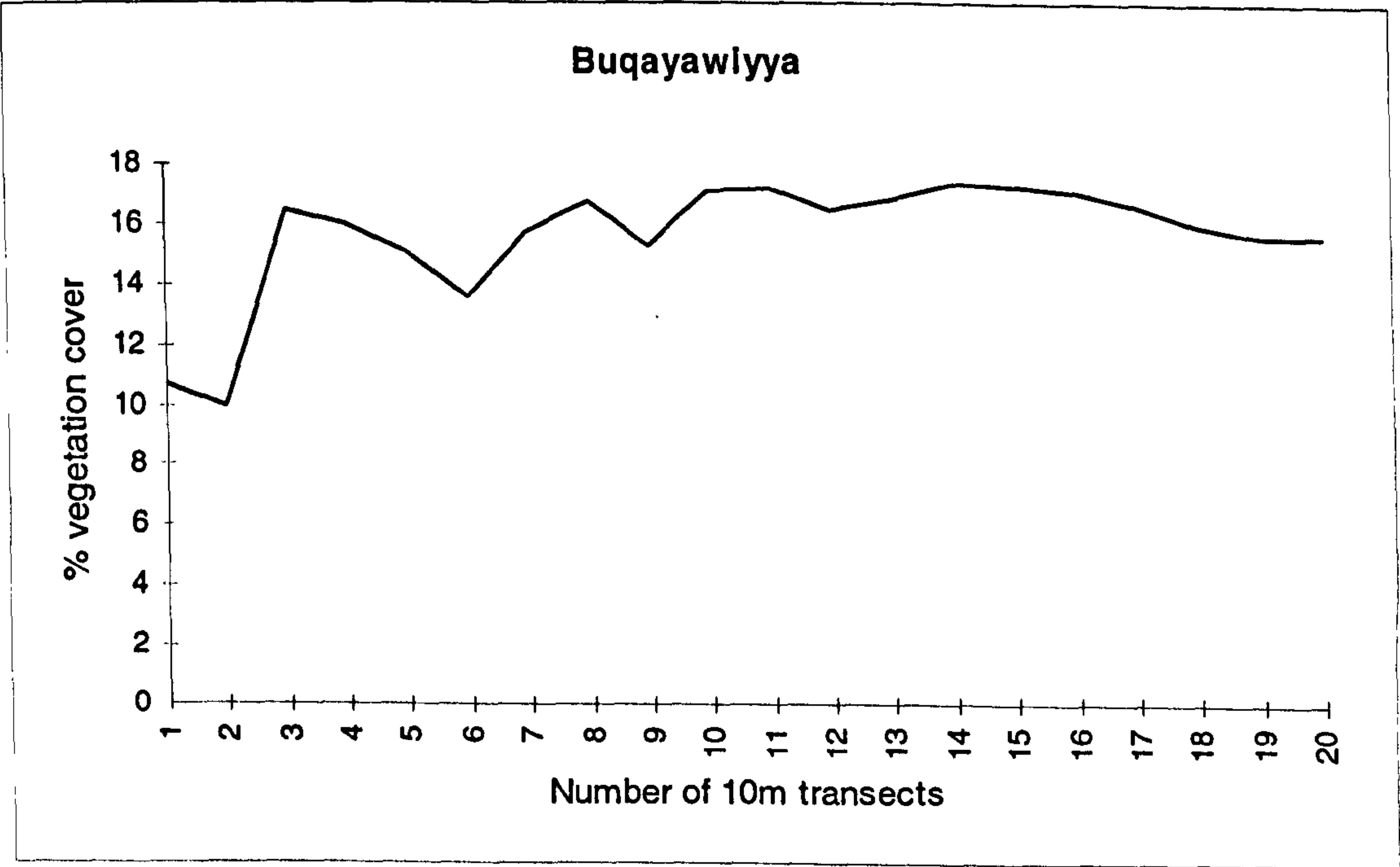
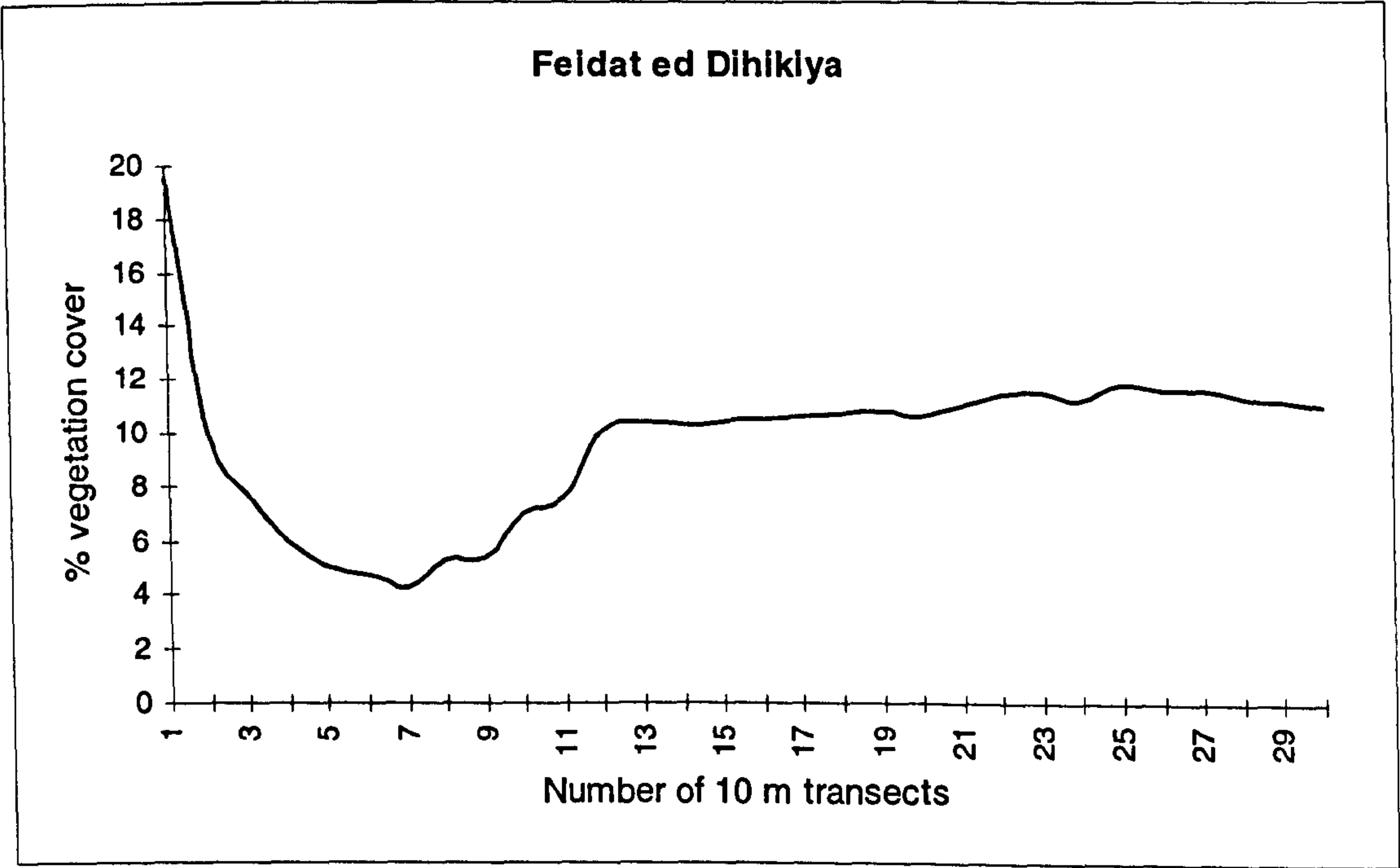
importance of the locational position of a study site in relation to the forward look of the ATSR-2. A study area chosen so the sensor viewed in a backscatter direction may dramatically change the results and importance of the forward look.

Despite the fact that this study suggests that the forward look and narrow wavebands of ATSR-2 do not aid in the ability to detect and monitor arid land vegetation using remote sensing, the work has been useful in that it has highlighted the importance of bandwidth and some of the problems that can result from off nadir viewing. These are increased spatial resolution, changing across scene illumination/viewing geometries and geolocational difficulties. It has also illustrated the potential of a model which based on the red/near-infrared scattergram allows one to obtain information on ground percentage vegetation cover from different sensors in a time series, and without the use of field data. The potential of a model of this kind in terms of providing biophysical information about a large area at low cost is considerable, and especially relevant to remote sensing in a development context. Further research on this aspect is clearly needed.



**APPENDIX 1**

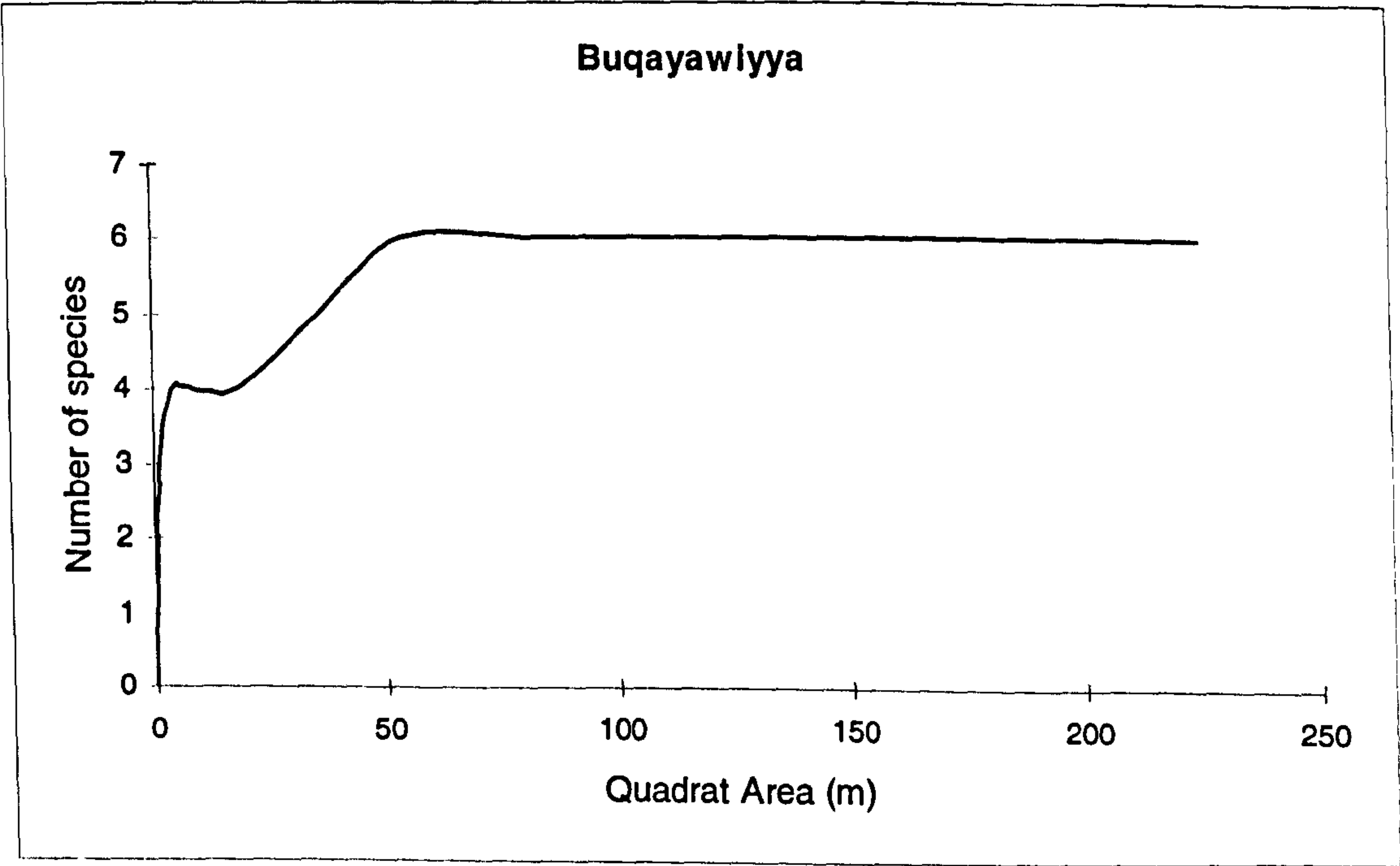
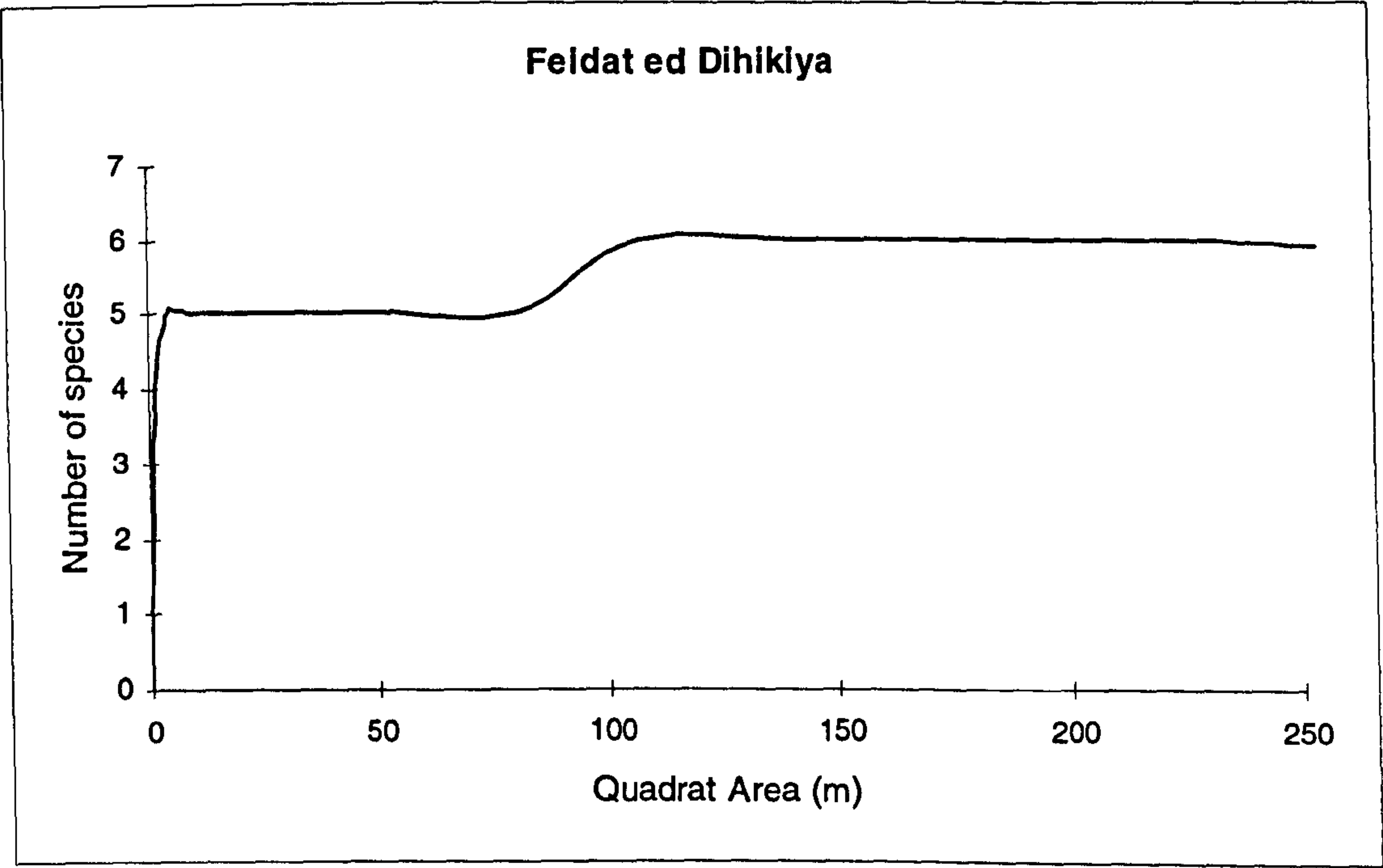
**Minimum Transect Lengths needed to accurately estimate percentage vegetation cover at two field sites, *Feidat ed Dihikiya* and *Buqayawiyya***





APPENDIX 1

Species-area curves for two field sites, *Feidat ed Dihikiya* and *Buqayawiyya*





## APPENDIX 2

### IDL code used to read level 1b ATSR-2 files

```

; /* IDL code to read Level 1b GBT ATSR-2 images */
; /* This code is adapted from IDL given by the product literature, see Bailey 1995 */
; /* Marianne Edwards, 1st June 1996 */

; /* The code follows three main stages:-
; Firstly, the image header is read, displayed on the screen and written to a file.
; Secondly, the image data is read and calibrated using the visible calibration information. It
is ; written to a file.
; Thirdly, the image is displayed on the screen. Using the mouse, latitude/longitude
; geolocal information can be read for chosen ground control points. These are stored in
; a file and can be optionally used to geocorrect the image at a later stage */

; /* To use the code, the name of the ATSR-2 images to be read must be edited. Visible
calibration
; coefficients must also be entered. The code should be edited directly */

; /* Structures for reading the data are defined */

; /*-----*/
;
; Function: get_string_from_header
;
; Extracts sub-string from general byte-array HEADER, starting
; at character START (where first character is #0), and
; continuing for LENGTH characters.
;
;
;
; /*-----*/

function get_string_from_header, header, start, length
return, string(header(start : (start + length) - 1))

end

; /*-----*/
;
; Function: get_int_from_header
;
; Extracts sub-string from general byte-array HEADER, starting
; at character START (where first character is #0), and
; continuing for LENGTH characters.
;
; Returns conversion of sub-string to two-byte integer.
;
;
;
; /*-----*/

function get_int_from_header, header, start, length

```



```

return, fix(string(header(start : (start + length) - 1)))

end

/*-----*/
;
; Function: get_long_from_header
;
; Extracts sub-string from general byte-array HEADER, starting
; at character START (where first character is #0), and
; continuing for LENGTH characters.
;
; Returns conversion of sub-string to four-byte integer.
;
;
/*-----*/

function get_long_from_header, header, start, length

return, long(string(header(start : (start + length) - 1)))

end

/*-----*/
;
; Function: get_float_from_header
;
; Extracts sub-string from general byte-array HEADER, starting
; at character START (where first character is #0), and
; continuing for LENGTH characters.
;
; Returns conversion of sub-string to single-precision
; floating-point value.
;
;
/*-----*/

function get_float_from_header, header, start, length

return, float(string(header(start : (start + length) - 1)))

end

/*-----*/
;
; Function: get_double_from_header
;
; Extracts sub-string from general byte-array HEADER, starting
; at character START (where first character is #0), and
; continuing for LENGTH characters.
;
; Returns conversion of sub-string to double-precision
; floating-point value.
;
;
```



```

;
; /*-----*/

function get_double_from_header, header, start, length

    return, double(string(header(start : (start + length) - 1)))

end

; /* The subroutine: sadist_header is defined. This will read the image header */

; /*-----*/
;
; Subroutine: get_sadist2_header.pro
;
; Reads the SADIST-2 product header from FILE, which has a record
; length of RECORD_LENGTH.
;
; Converts header contents to internal representation, where appropriate,
; and returns interpreted header structure HEADER.
;
; Interprets first two bytes of header as byte-order word. Returns
; flag BYTE_SWAP_NEEDED, which identifies whether local system is
; big-endian, and therefore whether byte-swapping is required.
;
;
; /*-----*/

pro get_sadist2_header, file, record_length, header, byte_swap_needed

; /* Defining the byte-order word and a byte-array into which the SADIST-2 product
; header (minus the byte-order word) will be read. */

number_of_header_records = fix(4096 / record_length)

if ((number_of_header_records * record_length) ne 4096) then $
    number_of_header_records = number_of_header_records + 1

byte_order = 0
temp = bytarr((number_of_header_records * record_length) - 2)

; /* Defining the structure which will be returned by this subroutine. All header
; contents are converted to the appropriate type. */

header = { file_name: ", instrument: ", $
    vec_type: ", vec_time: 0.0d, vec_utc: ", $
    vec_pos: dblarr(3), vec_vel: dblarr(3), vec_long: 0.0d, $
    clock_ut: 0.0d, clock_bin: 0.0d, clock_period: 0.0d, $
    options: intarr(6), $
    atd: lonarr(2), acq_time: strarr(2), $
    latitude: fltarr(4), longitude: fltarr(4), $
    nad_psm1: 0, nad_psm2: 0, nad_psm_change: 0l, $
    for_psm1: 0, for_psm2: 0, for_psm_change: 0l, $
    nad_rate1: ", nad_rate_change: 0l, $
    for_rate1: ", for_rate_change: 0l, $
    min_temps: fltarr(6), max_temps: fltarr(6), $
    nad_sol_elev_start: fltarr(11), nad_sol_elev_end: fltarr(11), $

```



```

nad_sat_elev_start: fltarr(11), nad_sat_elev_end: fltarr(11), $
nad_sol_azim_start: fltarr(11), nad_sol_azim_end: fltarr(11), $
nad_sat_azim_start: fltarr(11), nad_sat_azim_end: fltarr(11), $
for_sol_elev_start: fltarr(11), for_sol_elev_end: fltarr(11), $
for_sat_elev_start: fltarr(11), for_sat_elev_end: fltarr(11), $
for_sol_azim_start: fltarr(11), for_sol_azim_end: fltarr(11), $
for_sat_azim_start: fltarr(11), for_sat_azim_end: fltarr(11), $
nad_platform: lonarr(6), for_platform: lonarr(6), $
nad_pcd: lonarr(8), for_pcd: lonarr(8), $
nad_invalid: lonarr(10), for_invalid: lonarr(10), $
max_error: 0 }

```

```

; /* Read the SADIST-2 header (including the byte-order word) into the temporary array.
;    Interpret the byte-order word to decide whether system is little- or big-endian.
;    The header information is written to the screen and to a file called header.dat. This may be
;    needed for atmospheric and radiometric correction at a later stage */

```

```

openw,2, 'header.dat'
readu, file, byte_order, temp
if (byte_order eq 16961) then byte_swap_needed = 0 else byte_swap_needed = 1
printf,2, format = '(a30, i)', 'Byte_order: ', byte_order
printf,2, format = '(a30, i)', 'Byte-swap needed: ', byte_swap_needed

```

```

; /* The header is read in various stages. These are commented below. */
; /* Read and display the SADIST-2 product file-name and the ATSR instrument name. */

```

```

header.file_name = get_string_from_header(temp, 0, 60)
printf,2, format = '(a30, a60)', 'File-name: ', header.file_name

```

```

header.instrument = get_string_from_header(temp, 60, 6)
printf,2, format = '(a30, a6)', 'Instrument: ', header.instrument

```

```

; /* Read and display the ERS state vector information. Contents are:
;    type (MPH, ORPD or ORRE); time (MJD from 1950); converted time (UTC format);
;    longitude (degrees East); position vector (km); velocity vector (km/s). */

```

```

header.vec_type = get_string_from_header(temp, 66, 5)
printf,2, format = '(a30, a5)', 'State vector (type): ', header.vec_type

```

```

header.vec_time = get_double_from_header(temp, 71, 16)
printf,2, format = '(a30, f16.8)', '(MJD time): ', header.vec_time

```

```

header.vec_utc = get_string_from_header(temp, 87, 25)
printf,2, format = '(a30, a25)', '(UTC time): ', header.vec_utc

```

```

header.vec_long = get_double_from_header(temp, 178, 11)
printf,2, format = '(a30, f11.5)', '(longitude): ', header.vec_long

```

```

for i = 0, 2 do begin
    header.vec_pos(i) = get_double_from_header(temp, 112 + (i * 13), 13)
    header.vec_vel(i) = get_double_from_header(temp, 151 + (i * 9), 9)
endfor

```

```

printf,2, format = '(a30, 3f13.5)', '(x/y/z position): ', header.vec_pos
printf,2, format = '(a30, 3f9.5)', '(x/y/z velocity): ', header.vec_vel

```



```

;/* Read and display the ERS clock calibration parameters. Contents are:
;   reference Universal Time (MJD from 1950); reference ERS satellite binary;
;   ERS clock period (ns). */

header.clock_ut = get_double_from_header(temp, 189, 16)
header.clock_bin = get_double_from_header(temp, 205, 13)
header.clock_period = get_double_from_header(temp, 218, 13)

printf,2, format = '(a30, f16.8, f13.0, f13.0)', 'Clock calibration: ', $
        header.clock_ut, header.clock_bin, header.clock_period


;/* Read and display the product options. Order is:
;   nadir only (N); thermal (T); visible (V); latitude/longitude (L);
;   x/y offsets (X); cloud/land (C). */

for i = 0, 5 do begin
    header.options(i) = get_int_from_header(temp, 231 + (i * 2), 2)
endfor

printf,2, format = '(a30, 6i2)', 'Options (NTVLXC): ', header.options


;/* Read and display the along-track distances (km or relative scan number) and
;   acquisition times for the start and end of the product. */

for i = 0, 1 do begin
    header.atd(i) = get_long_from_header(temp, 243 + (i * 6), 6)
    header.acq_time(i) = get_string_from_header(temp, 255 + (i * 25), 25)
endfor

printf,2, format = '(a30, 2i6)', 'Along-track distance: ', header.atd
printf,2, format = '(a30, 2a25)', 'Acquisition time: ', header.acq_time


;/* Read and display the latitudes and longitudes of the product corner-points.
;   Order is: LHS at start; RHS at start; LHS at end; RHS at end. */

for i = 0, 3 do begin
    header.latitude(i) = get_float_from_header(temp, 305 + (i * 8), 8)
    header.longitude(i) = get_float_from_header(temp, 337 + (i * 9), 9)
endfor

printf,2, format = '(a30, 4f8.3)', 'Latitude: ', header.latitude
printf,2, format = '(a30, 4f9.3)', 'Longitude: ', header.longitude


;/* Read and display the pixel-selection-map (PSM) information: first PSM number;
;   second PSM number; distance or relative scan number or first PSM change. */

header.nad_psm1 = get_int_from_header(temp, 373, 3)
header.nad_psm2 = get_int_from_header(temp, 376, 3)
header.nad_psm_change = get_long_from_header(temp, 379, 6)

printf,2, format = '(a30, i3, i3, i6)', 'Nadir-view PSM: ', $
        header.nad_psm1, header.nad_psm2, header.nad_psm_change

header.for_psm1 = get_int_from_header(temp, 385, 3)

```



```

header.for_psm2 = get_int_from_header(temp, 388, 3)
header.for_psm_change = get_long_from_header(temp, 391, 6)

printf,2, format = '(a30, i3, i3, i6)', 'Forward-view PSM: ', $
    header.for_psm1, header.for_psm2, header.for_psm_change

; /* Read and display the ATSR-2 data-rate information: rate at start of product (L or H);
;    distance or relative scan number of first rate change. */

header.nad_rate1 = get_string_from_header(temp, 397, 2)
header.nad_rate_change = get_long_from_header(temp, 399, 6)

printf,2, format = '(a30, a2, i6)', 'Nadir-view ATSR-2 rate: ', header.nad_rate1,
header.nad_rate_change

header.for_rate1 = get_string_from_header(temp, 405, 2)
header.for_rate_change = get_long_from_header(temp, 407, 6)

printf,2, format = '(a30, a2, i6)', 'Forward-view ATSR-2 rate: ', header.for_rate1,
header.for_rate_change

; /* Read and display the minimum and maximum auxiliary temperatures: The six temperatures
;    provided are: SCC cold-tip (tm.z556); 12.0um detector (tm.z565); 11.0um detector (tm.z564);
;    3.7um detector (tm.z563); 1.6um detector (tm.z562); 0.870um detector (tm.z567). */

for i = 0, 5 do begin
    header.min_temps(i) = get_float_from_header(temp, 413 + (i * 8), 8)
    header.max_temps(i) = get_float_from_header(temp, 461 + (i * 8), 8)
endfor

printf,2, format = '(a30, 6f8.3)', 'Minimum temperatures: ', header.min_temps
printf,2, format = '(a30, 6f8.3)', 'Maximum temperatures: ', header.max_temps

; /* Read and display the solar and viewing angles for nadir and forward views, at the
;    start and end of the product. Solar elevation and azimuth, and satellite elevation
;    and azimuth, are all measured from the pixel. */

for i = 0, 10 do begin
    header.nad_sol_elev_start(i) = get_float_from_header(temp, 509 + (i * 9), 9)
    header.nad_sol_elev_end(i) = get_float_from_header(temp, 608 + (i * 9), 9)
    header.nad_sat_elev_start(i) = get_float_from_header(temp, 707 + (i * 9), 9)
    header.nad_sat_elev_end(i) = get_float_from_header(temp, 806 + (i * 9), 9)
    header.nad_sol_azim_start(i) = get_float_from_header(temp, 905 + (i * 9), 9)
    header.nad_sol_azim_end(i) = get_float_from_header(temp, 1004 + (i * 9), 9)
    header.nad_sat_azim_start(i) = get_float_from_header(temp, 1103 + (i * 9), 9)
    header.nad_sat_azim_end(i) = get_float_from_header(temp, 1202 + (i * 9), 9)
    header.for_sol_elev_start(i) = get_float_from_header(temp, 1301 + (i * 9), 9)
    header.for_sol_elev_end(i) = get_float_from_header(temp, 1400 + (i * 9), 9)
    header.for_sat_elev_start(i) = get_float_from_header(temp, 1499 + (i * 9), 9)
    header.for_sat_elev_end(i) = get_float_from_header(temp, 1598 + (i * 9), 9)
    header.for_sol_azim_start(i) = get_float_from_header(temp, 1697 + (i * 9), 9)
    header.for_sol_azim_end(i) = get_float_from_header(temp, 1796 + (i * 9), 9)
    header.for_sat_azim_start(i) = get_float_from_header(temp, 1895 + (i * 9), 9)
    header.for_sat_azim_end(i) = get_float_from_header(temp, 1994 + (i * 9), 9)
endfor

```



```

printf,2, format = '(a30, 11f9.3)', 'Nadir-view sol-elev (start): ', header.nad_sol_elev_start
printf,2, format = '(a30, 11f9.3)', ' (end): ', header.nad_sol_elev_end
printf,2, format = '(a30, 11f9.3)', 'Nadir-view sat-elev (start): ', header.nad_sat_elev_start
printf,2, format = '(a30, 11f9.3)', ' (end): ', header.nad_sat_elev_end
printf,2, format = '(a30, 11f9.3)', 'Nadir-view sol-azim (start): ', header.nad_sol_azim_start
printf,2, format = '(a30, 11f9.3)', ' (end): ', header.nad_sol_azim_end
printf,2, format = '(a30, 11f9.3)', 'Nadir-view sat-azim (start): ', header.nad_sat_azim_start
printf,2, format = '(a30, 11f9.3)', ' (end): ', header.nad_sat_azim_end
printf,2, format = '(a30, 11f9.3)', 'Frwr-view sol-elev (start): ', header.for_sol_elev_start
printf,2, format = '(a30, 11f9.3)', ' (end): ', header.for_sol_elev_end
printf,2, format = '(a30, 11f9.3)', 'Frwr-view sat-elev (start): ', header.for_sat_elev_start
printf,2, format = '(a30, 11f9.3)', ' (end): ', header.for_sat_elev_end
printf,2, format = '(a30, 11f9.3)', 'Frwr-view sol-azim (start): ', header.for_sol_azim_start
printf,2, format = '(a30, 11f9.3)', ' (end): ', header.for_sol_azim_end
printf,2, format = '(a30, 11f9.3)', 'Frwr-view sat-azim (start): ', header.for_sat_azim_start
printf,2, format = '(a30, 11f9.3)', ' (end): ', header.for_sat_azim_end

```

```

; /* Read and display the ERS platform mode counters for the nadir and forward views.
;   Order is: YSM; FCM, OCM, FPM, RTMM, RTMC. */

```

```

for i = 0, 5 do begin
    header.nad_platform(i) = get_long_from_header(temp, 2093 + (i * 6), 6)
    header.for_platform(i) = get_long_from_header(temp, 2129 + (i * 6), 6)
endfor

```

```

printf,2, format = '(a30, 6i6)', 'Nadir-view platform mode: ', header.nad_platform
printf,2, format = '(a30, 6i6)', 'Frwr-view platform mode: ', header.for_platform

```

```

; /* Read and display the product confidence data (PCD) counters for the nadir and
;   forward views. */

```

```

for i = 0, 7 do begin
    header.nad_pcd(i) = get_long_from_header(temp, 2165 + (i * 6), 6)
    header.for_pcd(i) = get_long_from_header(temp, 2213 + (i * 6), 6)
endfor

```

```

printf,2, format = '(a30, 8i6)', 'Nadir-view PCD: ', header.nad_pcd
printf,2, format = '(a30, 8i6)', 'Frwr-view PCD: ', header.for_pcd

```

```

; /* Read and display the SADIST-2 packet validity counters for the nadir and
;   forward views. Order is: null packet; basic validation; crc error;
;   buffer full error; scan jitter; nibble shift; 3 * unused; other errors. */

```

```

for i = 0, 9 do begin
    header.nad_invalid(i) = get_long_from_header(temp, 2261 + (i * 6), 6)
    header.for_invalid(i) = get_long_from_header(temp, 2321 + (i * 6), 6)
endfor

```

```

printf,2, format = '(a30, 10i6)', 'Nadir-view validity: ', header.nad_invalid
printf,2, format = '(a30, 10i6)', 'Frwr-view validity: ', header.for_invalid

```

```

; /* Read and display the value of the maximum single pixel error. */

```

```

header.max_error = get_int_from_header(temp, 2381, 4)
printf,2, format = '(a30, i4)', 'Max single-pixel error: ', header.max_error

```



```

close,2
end

```

```

/* This is the code to read the visible calibration coefficients for calibrating the image data.
; The image data can be calibrated using a file of calibration coefficients, or alternatively,
; by typing the coefficients in directly (see code further down). This is useful as coefficients
; are constantly being updated, but can become tedious if a lot of images are being processed.
; This version of the code is written so calibration coefficients are typed in manually. */

```

```

/*-----*/

```

```

; AUTHOR: P.D.WATTS
; computes number of days since beginning of year
; from given month,day,year. Uses JULDAY
; Then reads vis calibration file and gets calibration
; slopes from nearest possible day.
;-----

```

```

pro get_vcal,mon,day,year,slope,dayno

```

```

; mon ENTRY month
; day ENTRY day
; year ENTRY year
; slope EXIT calibration slope for 4 channels
; dayno EXIT day number of year

```

```

;-----
;for a given month, day and year calculate the number of days since Jan 1st 1995
dayno=julday(mon,day,year)-julday(1,1,1995)

```

```

;-----
; read visible channel calibration file
day = fltarr(5,365) ;days since 1-1-95
cal_level = fltarr(5,365) ;detector counts normalised to unit gain
cal_error = fltarr(5,365) ;standard dev
cal_slope = fltarr(5,365) ;calibration slope Reflectance/Count
cal_signal = fltarr(5,365) ;Detector sensitivity nW/Count - used for
;engineering purposes
cal_input = fltarr(5,365) ;Solar input at each channel
np = [-1,-1,-1,-1,-1] ;number of valid calibration points

```

```

;array indices :-
;0 = Viscal Monitor ;1 = 1.6um ;2 = 555nm ;3 = 659nm ;4 = 870nm
close,1

```

```

;openr,1,'/disk/u/mcel/calibs2.dat' ;open data file
;a = fltarr(26) ;input array
;while (not eof(1)) do begin ;read data
;for cnt=0,258 do begin ;(modified 1/12/95)
; readf,1,a
; for j = 0, 4 do begin
; if(a(1+5*j))then begin ;if the data is valid
; np(j) = np(j) + 1 ;sort data into arrays
; i = np(j)
; day(j,i) = a(0)
; cal_level(j,i) = a(1+5*j)
; cal_error(j,i) = a(2+5*j)
; cal_slope(j,i) = a(3+5*j)
; cal_signal(j,i) = a(4+5*j)
; cal_input(j,i) = a(5+5*j)

```



```

; endif
; endfor
;endfor
;endwhile
;close,1
                                ;close file

;-----
slope=fltarr(4)    ; extract slopes for closest days possible
for ic=0,3 do begin
dayn=dayno        ; (save day number because it may get changed)
a:
z=where(fix(day(ic+1,*)) eq dayn,ct)
if ct gt 0 then slope(ic)=cal_slope(ic+1,z(0))
if ct eq 0 then begin & dayn=dayn-1 & goto,a & end
endfor

;rescale slope for a gain setting of 20.0 (to bring into line with SADIST-2)
slope = slope/ (20.0 *4096/50)

print, slope
print, dayno
return
end

;/* Now the programs for reading in the header and calibrating the visible bands have been
; defined, imagery can now be processed.
; Main Program */

;/*-----*/
;
; Program: get_sadist2_gbt.pro
;
; Reads SADIST-2 gridded brightness temperature product (GBT)
; into memory, byte-swapping where necessary.
;
; Copes with all combinations of the nadir-only (N), thermal (T),
; visible (V), latitude/longitude (L), x/y (X) and cloud/land (C)
; product options.
;
;
;
;
;/*-----*/

; Close any open files
close, 1

;/* Where are your images ? Enter a string of text for the default data path, and define your
; images */

path = '/disk/temp/mce1/atsr2/'
; gbt_name = '9703190741-16214-970418-2av100.gbt'
; gbt_name = '9510110741-16214-970416-2av100.gbt'
; gbt_name = '9511150741-16214-970416-2av100.gbt'
; gbt_name = '9512200741-16214-970416-2av100.gbt'
; gbt_name = '9607170741-16214-970416-2av100.gbt'
; wrong area gbt_name = '9607170922-16214-970416-2av100.gbt'
; gbt_name = '9609250741-16214-970416-2av100.gbt'
; gbt_name = '9610300741-16214-970416-2av100.gbt'

```



```

; gbt_name = '9612040741-16214-970416-2av100.gbt'
; gbt_name = '9511120735-16214-970416-2av100.gbt'
; gbt_name = '9511180747-16214-970418-2av100.gbt'
; gbt_name = '9511210753-16214-970418-2av100.gbt'
; gbt_name = '9511250727-16214-970418-2av100.gbt'
; gbt_name = '9511180747-16214-970418-2av100.gbt'
; gbt_name = '9511210753-16214-970418-2av100.gbt'
; gbt_name = '9511250727-16214-970418-2av100.gbt'
; gbt_name = '9512040744-16214-970418-2av100.gbt'
; gbt_name = '9512070750-16214-970418-2av100.gbt'
; gbt_name = '9512170735-16414-960215-2t100.gbt'
; gbt_name = '9511280735-16414-960215-2t100.gbt'
; gbt_name = '9512010738-16414-960326-2t100.gbt'
; gbt_name = '9512140730-16414-960215-2t100.gbt'
; gbt_name = '9701080741-16214-970425-2av100.gbt'
; gbt_name = '9702120741-16214-970612-2av100.gbt'
; gbt_name = '9509060741-16214-970807-2av200.gbt'
; gbt_name = '9608210741-16214-980409-2av201.gbt'
; gbt_name = '9704230741-16214-980409-2av201.gbt'
; gbt_name = '9705090738-16214-980409-2av201.gbt'
; gbt_name = '9706130738-16214-980409-2av201.gbt'
; gbt_name = '9707020741-16214-980409-2av201.gbt'
; gbt_name = '9708060741-16214-980409-2av201.gbt'
; gbt_name = '9709100741-16214-980409-2av201.gbt'
; gbt_name = '9709290744-16214-980409-2av201.gbt'
; gbt_name = '9711160735-16214-980409-2av201.gbt'
; gbt_name = '9712050738-16214-980409-2av201.gbt'

```

**;/\* Enter the file name to open \*/**

```

; gbt_name = ""
; read, 'File name: ', gbt_name

```

**;/\* Combine path and file name \*/**

```
full_name = path+gbt_name
```

```
print, 'Processing ', full_name
```

**;/\* Define the output file names. Output names are defined based on input image names \*/**

```
pos_of_hyph = strpos(gbt_name, '-') /* Position of 1st hyphen */
output_main = strmid(gbt_name, 2, pos_of_hyph-6)
```

**;/\* Open the product file and read/display the contents of the product header. \*/**

```
openr, 1, full_name, /fixed, 1024
get_sadist2_header, 1, 1024, gbt_header, byte_swap_needed
```

**;/\* Works with the true file name to find the marker \*/**

```
file_name = string(gbt_header.file_name)
file_name = strtrim(file_name)
```

```
/* mark_hyph = strpos(file_name, '-1')
; lake_id = strmid(file_name, mark_hyph, 4) */
```



```

; date_marker = strpos(file_name, '-95')
; date_marker = strpos(file_name, '-96')
date_marker = strpos(file_name, '-97')
name_month = strmid(file_name, (date_marker+3), 2)
name_day = strmid(file_name, (date_marker+5), 2)
name_year = strmid(file_name, (date_marker+1), 2)

print,name_year
print,name_day
print,name_month

/* Reading in the image data */

/* If the thermal (T) option has been selected, define the nadir-view 12.0um,
; 11.0um and 3.7um image arrays, and read from the product file. Byte-swap
; if necessary. */

if (gbt_header.options(1)) then begin

    nadir_ir12 = intarr(512, 512)
    readu, 1, nadir_ir12

    nadir_ir11 = intarr(512, 512)
    readu, 1, nadir_ir11

    nadir_ir37 = intarr(512, 512)
    readu, 1, nadir_ir37

    if (byte_swap_needed) then byteorder, nadir_ir12, nadir_ir11, nadir_ir37, /sswap

endif

/* If the thermal (T) or visible (V) options have been selected, define the
; nadir-view 1.6um image array, and read from the product file. Byte-swap if
; necessary. */

if (gbt_header.options(1) or gbt_header.options(2)) then begin

    nadir_v16 = intarr(512, 512)
    readu, 1, nadir_v16

    if (byte_swap_needed) then byteorder, nadir_v16, /sswap

endif

/* If the visible (V) option has been selected, define the nadir-view 0.870um,
; 0.670um and 0.555um image arrays, and read from the product file. Byte-swap
; if necessary. */

if (gbt_header.options(2)) then begin

    nadir_v870 = intarr(512, 512)
    readu, 1, nadir_v870

    nadir_v670 = intarr(512, 512)

```



```

readu, 1, nadir_v670

nadir_v555 = intarr(512, 512)
readu, 1, nadir_v555

if (byte_swap_needed) then byteorder, nadir_v870, nadir_v670, nadir_v555, /sswap

endif

; /* Read the forward-view image arrays only if the nadir-only (N) option has
;   not been selected. */

if (not gbt_header.options(0)) then begin

; /* If the thermal (T) option has been selected, define the forward-view 12.0um,
;   11.0um and 3.7um image arrays, and read from the product file. Byte-swap if
;   necessary. */

if (gbt_header.options(1)) then begin

    frwrdr_ir12 = intarr(512, 512)
    readu, 1, frwrdr_ir12

    frwrdr_ir11 = intarr(512, 512)
    readu, 1, frwrdr_ir11

    frwrdr_ir37 = intarr(512, 512)
    readu, 1, frwrdr_ir37

    if (byte_swap_needed) then byteorder, frwrdr_ir12, frwrdr_ir11, frwrdr_ir37, /sswap

endif

; /* If the thermal (T) or visible (V) options have been selected, define the
;   forward-view 1.6um image array, and read from the product file. Byte-swap
;   if necessary. */

if (gbt_header.options(1) or gbt_header.options(2)) then begin

    frwrdr_v16 = intarr(512, 512)
    readu, 1, frwrdr_v16

    if (byte_swap_needed) then byteorder, frwrdr_v16, /sswap

endif

; /* If the visible (V) option has been selected, define the forward-view 0.870um,
;   0.670um and 0.555um image arrays, and read from the product file. Byte-swap
;   if necessary. */

if (gbt_header.options(2)) then begin

    frwrdr_v870 = intarr(512, 512)
    readu, 1, frwrdr_v870

```



```

    frwrд_v670 = intarr(512, 512)
    readu, 1, frwrд_v670

    frwrд_v555 = intarr(512, 512)
    readu, 1, frwrд_v555

    if (byte_swap_needed) then byteorder, frwrд_v870, frwrд_v670, frwrд_v555, /sswap

endif

endif

; /* If the latitude/longitude (L) option has been selected, define the latitude
;    and longitude arrays, and read from the product file. Convert the latitudes
;    and longitudes to a floating-point representation, with units of degrees. Note
;    that byte-swapping must be performed *before* conversion. */

if (gbt_header.options(3)) then begin

    temp_grid = lonarr(512, 512)

    readu, 1, temp_grid
    if (byte_swap_needed) then byteorder, temp_grid, /lswap

    latitude_grid = fltarr(512, 512)
    latitude_grid = float(temp_grid) / 1000.0

    readu, 1, temp_grid
    if (byte_swap_needed) then byteorder, temp_grid, /lswap

    longitude_grid = fltarr(512, 512)
    longitude_grid = float(temp_grid) / 1000.0

endif

; /* If the x/y (X) option has been selected, define the x/y offset arrays, and
;    read from the product file. Note that the x/y offsets are *unsigned* bytes. */

if (gbt_header.options(4)) then begin

    nadir_x_offset = bytarr(512, 512)
    readu, 1, nadir_x_offset

    nadir_y_offset = bytarr(512, 512)
    readu, 1, nadir_y_offset

; /* Read the forward-view x/y offsets only if the nadir-only (N) option has not
;    been selected. */

if (not gbt_header.options(0)) then begin

    frwrд_x_offset = bytarr(512, 512)
    readu, 1, frwrд_x_offset

    frwrд_y_offset = bytarr(512, 512)
    readu, 1, frwrд_y_offset

```



```

endif

endif

; /* If the cloud/land (C) option has been selected, define the nadir- and forward-view
;   cloud/land flag arrays, and read from the product file. Byte-swap if necessary. */

if (gbt_header.options(5)) then begin

    nadir_cloud_flags = intarr(512, 512)
    readu, 1, nadir_cloud_flags

    if (byte_swap_needed) then byteorder, nadir_cloud_flags, /sswap

; /* Read the forward-view cloud/land flags only if the nadir-only (N) option has not
;   been selected. Byte-swap if necessary. */

    if (not gbt_header.options(0)) then begin

        frwrд_cloud_flags = intarr(512, 512)
        readu, 1, frwrд_cloud_flags

        if (byte_swap_needed) then byteorder, frwrд_cloud_flags, /sswap

    endif

endif

close, 1

output_main = string(output_main)
geoffs_days = intarr(1,1)

; /* Remove flagging. This gets rid of error values in the image - all negative error values are made
;   positive, and then set to zero. This will depend on what you want to do with the imagery */

    abs_nadir_v16 = abs(nadir_v16)
    abs_nadir_v870 = abs(nadir_v870)
    abs_nadir_v670 = abs(nadir_v670)
    abs_nadir_v555 = abs(nadir_v555)
    abs_nadir_ir11 = abs(nadir_ir11)
    abs_nadir_ir12 = abs(nadir_ir12)
    abs_nadir_ir37 = abs(nadir_ir37)

    abs_frwrд_v16 = abs(frwrд_v16)
    abs_frwrд_v870 = abs(frwrд_v870)
    abs_frwrд_v670 = abs(frwrд_v670)
    abs_frwrд_v555 = abs(frwrд_v555)
    abs_frwrд_ir11 = abs(frwrд_ir11)
    abs_frwrд_ir12 = abs(frwrд_ir12)
    abs_frwrд_ir37 = abs(frwrд_ir37)

; /* setting the error values to zero */
; /* defining new arrays and multiplying by the values */

```



```

for i=0,511 do begin
  for j=0,511 do begin
    if (abs_nadir_v16 (i,j) le 8) then begin
      abs_nadir_v16 (i,j)= 0.0
    endif
    if (abs_nadir_v870 (i,j) le 8) then begin
      abs_nadir_v870 (i,j)= 0.0
    endif
    if (abs_nadir_v670 (i,j) le 8) then begin
      abs_nadir_v670 (i,j)= 0.0
    endif
    if (abs_nadir_v555 (i,j) le 8) then begin
      abs_nadir_v555 (i,j)= 0.0
    endif
    if (abs_nadir_ir11 (i,j) le 8) then begin
      abs_nadir_ir11 (i,j)= 0.0
    endif
    if (abs_nadir_ir12 (i,j) le 8) then begin
      abs_nadir_ir12 (i,j)= 0.0
    endif
    if (abs_nadir_ir37 (i,j) le 8) then begin
      abs_nadir_ir37 (i,j)= 0.0
    endif
    if (abs_frwr_v16 (i,j) le 8) then begin
      abs_frwr_v16 (i,j)= 0.0
    endif
    if (abs_frwr_v870 (i,j) le 8) then begin
      abs_frwr_v870 (i,j)= 0.0
    endif
    if (abs_frwr_v670 (i,j) le 8) then begin
      abs_frwr_v670 (i,j)= 0.0
    endif
    if (abs_frwr_v555 (i,j) le 8) then begin
      abs_frwr_v555 (i,j)= 0.0
    endif
    if (abs_frwr_ir11 (i,j) le 8) then begin
      abs_frwr_ir11 (i,j)= 0.0
    endif
    if (abs_frwr_ir12 (i,j) le 8) then begin
      abs_frwr_ir12 (i,j)= 0.0
    endif
    if (abs_frwr_ir37 (i,j) le 8) then begin
      abs_frwr_ir37 (i,j)= 0.0
    endif
  endfor
endfor

```

```

/* The imagery has been read in, error values have been accounted for. The data is now
; calibrated */
/* Returning date data from file name for viscal calibration */

```

```

;   years = 1995
;   years = 1996
;   years = 1997
;   month = strmid(output_main, 0, 2)
;   geoffs_days = strmid(output_main, 2, 2)
print,geoffs_days
print,month

```



```

    print,years

;/* Returning visible calibration data into string called visible_calibration*/

    get_vcal,month,geoffs_days,years,vis_cal
;    get_vcal,name_month,name_day,name_year,vis_cal

;    print,vis_cal

;/* Dissect the string to individual values */

;    fix_16 = vis_cal(0)
;    fix_555 = vis_cal(1)
;    fix_670 = vis_cal(2)
;    fix_870 = vis_cal(3)
;    fix_16 = 0.00003184
;    fix_555 = 0.0000581
;    fix_670 = 0.0000414
;    fix_870 = 0.00004978

;/* 01/12/95 */
;    fix_16 = 0.00004485
;    fix_555 = 0.00004912
;    fix_670 = 0.00004120
;    fix_870 = 0.00005789

;/* typing in the calibration values for the visible calibration */

;/* 11/10/95 */
;    fix_16 = 0.00004597
;    fix_555 = 0.00005911
;    fix_670 = 0.00004177
;    fix_870 = 0.00004956

;/* 15/11/95 */
;    fix_16 = 0.00004510
;    fix_555 = 0.00005827
;    fix_670 = 0.00004175
;    fix_870 = 0.00004982

;/* 20/12/95 */
;    fix_16 = 0.00004491
;    fix_555 = 0.00005814
;    fix_670 = 0.00004135
;    fix_870 = 0.00005002

;/* 17/07/96 */
;    fix_16 = 0.00004914
;    fix_555 = 0.00006604
;    fix_670 = 0.00004697
;    fix_870 = 0.00005682

;/* 12/11/95 */
;    fix_16 = 0.00004513
;    fix_555 = 0.00005800
;    fix_670 = 0.00004162
;    fix_870 = 0.00004943

;/* 18/11/95 */

```



```

;      fix_16 = 0.00004497
;      fix_555 = 0.00005845
;      fix_670 = 0.00004171
;      fix_870 = 0.00005007

; /* 21/11/95 */
;      fix_16 = 0.00004497
;      fix_555 = 0.00005837
;      fix_670 = 0.00004154
;      fix_870 = 0.00005018

; /* 25/11/95 */
;      fix_16 = 0.00004496
;      fix_555 = 0.00005803
;      fix_670 = 0.00004130
;      fix_870 = 0.00004996

; /* 04/12/95 */
;      fix_16 = 0.00004482
;      fix_555 = 0.00005800
;      fix_670 = 0.00004127
;      fix_870 = 0.00004896

; /* 07/12/95 */
;      fix_16 = 0.00004484
;      fix_555 = 0.00005828
;      fix_670 = 0.00004148
;      fix_870 = 0.00004884

; /* 17/12/95 */
;      fix_16 = 0.00004489
;      fix_555 = 0.00005810
;      fix_670 = 0.00004140
;      fix_870 = 0.00004978

; /* 21/08/96 */
;      fix_16 = 0.00004742
;      fix_555 = 0.00006294
;      fix_670 = 0.00004353
;      fix_870 = 0.00005338

; /* 25/09/96 */
;      fix_16 = 0.00004671
;      fix_555 = 0.00006186
;      fix_670 = 0.00004480
;      fix_870 = 0.00005184

; /* 30/10/96 */
;      fix_16 = 0.00004585
;      fix_555 = 0.00006261
;      fix_670 = 0.00004274
;      fix_870 = 0.00005382

; /* 04/12/96 */
;      fix_16 = 0.00004501
;      fix_555 = 0.00006108
;      fix_670 = 0.00004251
;      fix_870 = 0.00005027

```



```

; /* 19/03/97 */
;      fix_16 = 0.00004612
;      fix_555 = 0.00006419
;      fix_670 = 0.00004510
;      fix_870 = 0.00005493

; /* 08/01/97 */
;      fix_16 = 0.000045
;      fix_555 = 0.00005888
;      fix_670 = 0.00004213
;      fix_870 = 0.00005329

; /* 12/02/97 */
;      fix_16 = 0.00004556
;      fix_555 = 0.00006159
;      fix_670 = 0.00004189
;      fix_870 = 0.00004990

; /* 23/04/97 */
;      fix_16 = 0.00004742
;      fix_555 = 0.00006395
;      fix_670 = 0.00004475
;      fix_870 = 0.00005639

; /* 09/05/97 */
;      fix_16 = 0.00004787
;      fix_555 = 0.00006623
;      fix_670 = 0.00004502
;      fix_870 = 0.00005535

; /* 13/06/97 */
;      fix_16 = 0.00004868
;      fix_555 = 0.00006929
;      fix_670 = 0.00004756
;      fix_870 = 0.00005430

; /* 02/07/97 */
;      fix_16 = 0.00004868
;      fix_555 = 0.00006810
;      fix_670 = 0.00004817
;      fix_870 = 0.00005517

; /* 06/08/97 */
;      fix_16 = 0.00004823
;      fix_555 = 0.00006778
;      fix_670 = 0.00004672
;      fix_870 = 0.00005759

; /* 10/09/97 */
;      fix_16 = 0.00004735
;      fix_555 = 0.00006744
;      fix_670 = 0.0000459
;      fix_870 = 0.00005402

; /* 29/09/97 */

```



```

;      fix_16 = 0.00004687
;      fix_555 = 0.00006855
;      fix_670 = 0.00004666
;      fix_870 = 0.00005548

; /* 16/11/97 */
;      fix_16 = 0.00004576
;      fix_555 = 0.00006470
;      fix_670 = 0.00004496
;      fix_870 = 0.00005620

; /* 05/12/97 */
;      fix_16 = 0.00004538
;      fix_555 = 0.00006646
;      fix_670 = 0.00004472
;      fix_870 = 0.00005254

; /* 06/09/95 */
;      fix_16 = 0.00004666
;      fix_555 = 0.00006013
;      fix_670 = 0.00004275
;      fix_870 = 0.00004902

; print, fix_16
; print, fix_555
; print, fix_670
; print, fix_870

; /* The imagery is calibrated further. Correcting Imagery - multiplying by slope and 1.6 by 1.3 */

print, 'Correcting to top of the atmosphere reflectance '
; corr_abs_frwr_v16 = abs_frwr_v16*fix_16*1.3
; corr_abs_frwr_v870 = abs_frwr_v870*fix_870
; corr_abs_frwr_v670 = abs_frwr_v670*fix_670
; corr_abs_frwr_v555 = abs_frwr_v555*fix_555

; corr_abs_nadir_v16 = abs_nadir_v16*fix_16*1.3
; corr_abs_nadir_v870 = abs_nadir_v870*fix_870
; corr_abs_nadir_v670 = abs_nadir_v670*fix_670
; corr_abs_nadir_v555 = abs_nadir_v555*fix_555

; /* Dividing by the cosine of the solar zenith angle - from the header */

print, 'Dividing by the cosine of the solar zenith '
; sol_el = (median(gbt_header.nad_sol_elev_end)) + (median(gbt_header.nad_sol_elev_start))
; sol_el = sol_el/2
; sol_zenith = 90 - sol_el

; /*convert to radians before using cos() */

; sol_zen = sol_zenith/180 * 3.1415926
; sol_fact = cos(sol_zen)

; corr_abs_frwr_v16 = corr_abs_frwr_v16/sol_fact
; corr_abs_frwr_v870 = corr_abs_frwr_v870/sol_fact
; corr_abs_frwr_v670 = corr_abs_frwr_v670/sol_fact
; corr_abs_frwr_v555 = corr_abs_frwr_v555/sol_fact

```



```

corr_abs_nadir_v16 = corr_abs_nadir_v16/sol_fact
corr_abs_nadir_v870 = corr_abs_nadir_v870/sol_fact
corr_abs_nadir_v670 = corr_abs_nadir_v670/sol_fact
corr_abs_nadir_v555 = corr_abs_nadir_v555/sol_fact

; /* Multiplying by 10,000 to produce useable imagery */
; /* arrays are converted to LONGWORD types */

print, 'Converting to LONGWORD arrays '
    long_abs_frwr_v16 = corr_abs_frwr_v16*10000
    long_abs_frwr_v870 = corr_abs_frwr_v870*10000
    long_abs_frwr_v670 = corr_abs_frwr_v670*10000
    long_abs_frwr_v555 = corr_abs_frwr_v555*10000

    long_abs_nadir_v16 = corr_abs_nadir_v16*10000
    long_abs_nadir_v870 = corr_abs_nadir_v870*10000
    long_abs_nadir_v670 = corr_abs_nadir_v670*10000
    long_abs_nadir_v555 = corr_abs_nadir_v555*10000

; /* Converting back to INTEGER arrays using FIX command */

print, 'Fixing and returning to integers '
    fixed_abs_frwr_v16 = fix(long_abs_frwr_v16)
    fixed_abs_frwr_v870 = fix(long_abs_frwr_v870)
    fixed_abs_frwr_v670 = fix(long_abs_frwr_v670)
    fixed_abs_frwr_v555 = fix(long_abs_frwr_v555)

    fixed_abs_nadir_v16 = fix(long_abs_nadir_v16)
    fixed_abs_nadir_v870 = fix(long_abs_nadir_v870)
    fixed_abs_nadir_v670 = fix(long_abs_nadir_v670)
    fixed_abs_nadir_v555 = fix(long_abs_nadir_v555)

; /* Rotating imagery */

print, 'Rotating imagery '
    rotd_fixed_abs_frwr_v16 = rotate(fixed_abs_frwr_v16,5)
    rotd_fixed_abs_frwr_v870 = rotate(fixed_abs_frwr_v870,5)
    rotd_fixed_abs_frwr_v670 = rotate(fixed_abs_frwr_v670,5)
    rotd_fixed_abs_frwr_v555 = rotate(fixed_abs_frwr_v555,5)
    rotd_fixed_abs_frwr_ir11 = rotate(abs_frwr_ir11,5)
    rotd_fixed_abs_frwr_ir12 = rotate(abs_frwr_ir12,5)
    rotd_fixed_abs_frwr_ir37 = rotate(abs_frwr_ir37,5)

    rotd_fixed_abs_nadir_v16 = rotate(fixed_abs_nadir_v16,5)
    rotd_fixed_abs_nadir_v870 = rotate(fixed_abs_nadir_v870,5)
    rotd_fixed_abs_nadir_v670 = rotate(fixed_abs_nadir_v670,5)
    rotd_fixed_abs_nadir_v555 = rotate(fixed_abs_nadir_v555,5)
    rotd_fixed_abs_nadir_ir11 = rotate(abs_nadir_ir11,5)
    rotd_fixed_abs_nadir_ir12 = rotate(abs_nadir_ir12,5)
    rotd_fixed_abs_nadir_ir37 = rotate(abs_nadir_ir37,5)

; /* Rotating long and lat arrays to produce a grid of the same
; orientation as that used in IMAGINE. This is to allow the
; data points to have the same coordinates as the imagine image

```



**; for geometric rectification.**

```
    rotd_long = rotate(longitude_grid,2)
    rotd_lat = rotate(latitude_grid,2)
```

**;/\* Displaying the image on the screen. Bytescaling for nadir channels for tiff file \*/**

```
;    bsd_n870 = bytscl(rotd_fixed_abs_nadir_v870)
;    bsd_n670 = bytscl(rotd_fixed_abs_nadir_v670)
;    bsd_n555 = bytscl(rotd_fixed_abs_nadir_v555)
```

**;/\* Defining and producing tiff array \*/**

```
;    tiff_array = bytarr(3,512,512)

;    tiff_array(0,*,*) = bsd_n555
;    tiff_array(1,*,*) = bsd_n670
;    tiff_array(2,*,*) = bsd_n870
```

**;/\* Formatting File Names for output \*/**

```
    vis_raw = '.dat'
    tiff_file = '.tif'
;    maskd = '.msk'

    vis_chans = path+name_month+name_day+vis_raw
;    byte_scaled = path+lake+name_month+name_day+tiff_file
;    masked_file = path+lake+name_month+name_day+maskd
```

**;/\* Transpose the lat and long arrays so values can be extracted  
; from them for GCP'S**

```
    lat_5 = rotate(latitude_grid, 5)
    lon_5 = rotate(longitude_grid, 5)
```

**;/\* The mouse is used to define GCP's. Latitude/longitude values are read at each point \*/**

```
    window, xsize=512, ysize=512, title=file_name
    tv, rotate(bytscl(abs_nadir_v670), 2)
```

```
    print, 'GCP 1:'
    cursor, x1, y1, /device
    col1 = x1
    row1 = 512 - y1
    lat1 = lat_5(col1, row1)
    lon1 = lon_5(col1, row1)
    print, 'GCP 1 = ', col1, y1, lat1, lon1
```

```
    print, 'GCP 2:'
    cursor, x2, y2, /device
    col2 = x2
    row2 = 512 - y2
    lat2 = lat_5(col2, row2)
    lon2 = lon_5(col2, row2)
    print, 'GCP 2 = ', col2, y2, lat2, lon2
```



```

print, 'GCP 3:'
cursor, x3, y3, /device
col3 = x3
row3 = 512 - y3
lat3 = lat_5(col3, row3)
lon3 = lon_5(col3, row3)
print, 'GCP 3 = ', col3, y3, lat3, lon3

print, 'GCP 4:'
cursor, x4, y4, /device
col4 = x4
row4 = 512 - y4
lat4 = lat_5(col4, row4)
lon4 = lon_5(col4, row4)
print, 'GCP 4 = ', col4, y4, lat4, lon4

print, 'GCP 5:'
cursor, x5, y5, /device
col5 = x5
row5 = 512 - y5
lat5 = lat_5(col5, row5)
lon5 = lon_5(col5, row5)
print, 'GCP 5 = ', col5, y5, lat5, lon5

print, 'GCP 6:'
cursor, x6, y6, /device
col6 = x6
row6 = 512 - y6
lat6 = lat_5(col6, row6)
lon6 = lon_5(col6, row6)
print, 'GCP 6 = ', col6, y6, lat6, lon6

print, 'GCP 7:'
cursor, x7, y7, /device
col7 = x7
row7 = 512-y7
lat7 = lat_5(col7, row7)
lon7 = lon_5(col7, row7)
print, 'GCP 7 = ', col7, y7, lat7, lon7

print, 'GCP 8:'
cursor, x8, y8, /device
col8 = x8
row8 = 512-y8
lat8 = lat_5(col8, row8)
lon8 = lon_5(col8, row8)
print, 'GCP 8 = ', col8, y8, lat8, lon8

print, 'GCP 9:'
cursor, x9, y9, /device
col9 = x9
row9 = 512-y9
lat9 = lat_5(col9, row9)
lon9 = lon_5(col9, row9)
print, 'GCP 9 = ', col9, y9, lat9, lon9

```



```

print, 'GCP 10:'
cursor, x10, y10, /device
col10 = x10
row10 = 512-y10
lat10 = lat_5(col10, row10)
lon10 = lon_5(col10, row10)
print, 'GCP 10 = ', col10, y10, lat10, lon10

```

**;/\* Having read the data, it is then written to raw data files \*/**

```

print, 'Writing nadir channels: '

openw, 1, vis_chans

writeu, 1, rotd_fixed_abs_nadir_v555
writeu, 1, rotd_fixed_abs_nadir_v670
writeu, 1, rotd_fixed_abs_nadir_v870
writeu, 1, rotd_fixed_abs_nadir_v16
writeu, 1, rotd_fixed_abs_nadir_ir11
writeu, 1, rotd_fixed_abs_nadir_ir12
writeu, 1, rotd_fixed_abs_nadir_ir37

print, 'Writing forward channels (same order) '

writeu, 1, rotd_fixed_abs_frwrд_v555
writeu, 1, rotd_fixed_abs_frwrд_v670
writeu, 1, rotd_fixed_abs_frwrд_v870
writeu, 1, rotd_fixed_abs_frwrд_v16
writeu, 1, rotd_fixed_abs_frwrд_ir11
writeu, 1, rotd_fixed_abs_frwrд_ir12
writeu, 1, rotd_fixed_abs_frwrд_ir37

close, 1

```

**; /\* The file containg GCP information is written.**

```

gcp_txt = '.txt'
gcp_file = path+name_month+name_day+gcp_txt
openw, 1, gcp_file
; openw, 1, 'click.txt'

printf, 1, 'File name = :', file_name
printf, 1, 'Products written =: '
printf, 1, vis_chans
; printf, 1, byte_scaled
; printf, 1, masked_file

printf, 1, 'GCP points = :
Printf, 1, 'No.      ', 'x      ', 'y      ', 'Lon.  ', 'Lat.'

printf, 1, '1', col1, y1, lon1, lat1
printf, 1, '2', col2, y2, lon2, lat2
printf, 1, '3', col3, y3, lon3, lat3
printf, 1, '4', col4, y4, lon4, lat4
printf, 1, '5', col5, y5, lon5, lat5
printf, 1, '6', col6, y6, lon6, lat6

```



```

printf, 1, '7', col7, y7, lon7, lat7
printf, 1, '8', col8, y8, lon8, lat8
printf, 1, '9', col9, y9, lon9, lat9
printf, 1, '10', col10, y10, lon10, lat10

```

```

close, 1

```

```

print, 'Files Written = '
print, '          ', vis_chans
;print, '          ', byte_scaled
;print, '          ', masked_file
print, '          ', gcp_file
print, "

```

**/\* In addition to selecting GCP's on screen, latitude and longitude locations of pixels can be read  
; directly from the header. These are written to a file called coord.dat. \*/**

```

cord_txt = '.cord'
cord_file = path+name_month+name_day+cord_txt
openw, 1, cord_file
printf, 1, 'Coordinates for points within the imagery : '
printf, 1, 'Top left (0,511)    = ', rotd_long(0,511), ', ', rotd_lat(0,511)
printf, 1, 'Top right (511,511) = ', rotd_long(511,511), ', ', rotd_lat(511,511)
printf, 1, 'Bot. left (0,0)      = ', rotd_long(0,0), ', ', rotd_lat(0,0)
printf, 1, 'Bot. right (511,0)   = ', rotd_long(511,0), ', ', rotd_lat(511,0)
printf, 1, 'Middle (256,256)     = ', rotd_long(256,256), ', ', rotd_lat(256,256)
printf, 1, '0,63                = ', rotd_long(0,63), ', ', rotd_lat(0,63)
printf, 1, '0,127               = ', rotd_long(0,127), ', ', rotd_lat(0,127)
printf, 1, '0,191               = ', rotd_long(0,191), ', ', rotd_lat(0,191)
printf, 1, '0,255               = ', rotd_long(0,255), ', ', rotd_lat(0,255)
printf, 1, '0,319               = ', rotd_long(0,319), ', ', rotd_lat(0,319)
printf, 1, '0,383               = ', rotd_long(0,383), ', ', rotd_lat(0,383)
printf, 1, '0,444               = ', rotd_long(0,444), ', ', rotd_lat(0,444)
printf, 1, '63,0                = ', rotd_long(63,0), ', ', rotd_lat(63,0)
printf, 1, '63,63               = ', rotd_long(63,63), ', ', rotd_lat(63,63)
printf, 1, '63,127              = ', rotd_long(63,127), ', ', rotd_lat(63,127)
printf, 1, '63,191              = ', rotd_long(63,191), ', ', rotd_lat(63,191)
printf, 1, '63,255              = ', rotd_long(63,255), ', ', rotd_lat(63,255)
printf, 1, '63,319              = ', rotd_long(63,319), ', ', rotd_lat(63,319)
printf, 1, '63,383              = ', rotd_long(63,383), ', ', rotd_lat(63,383)
printf, 1, '63,444              = ', rotd_long(63,444), ', ', rotd_lat(63,444)
printf, 1, '63,511              = ', rotd_long(63,511), ', ', rotd_lat(63,511)
printf, 1, '127,0               = ', rotd_long(127,0), ', ', rotd_lat(127,0)
printf, 1, '127,63              = ', rotd_long(127,63), ', ', rotd_lat(127,63)
printf, 1, '127,127             = ', rotd_long(127,127), ', ', rotd_lat(127,127)
printf, 1, '127,191             = ', rotd_long(127,191), ', ', rotd_lat(127,191)
printf, 1, '127,255             = ', rotd_long(127,255), ', ', rotd_lat(127,255)
printf, 1, '127,319             = ', rotd_long(127,319), ', ', rotd_lat(127,319)
printf, 1, '127,383             = ', rotd_long(127,383), ', ', rotd_lat(127,383)
printf, 1, '127,444             = ', rotd_long(127,444), ', ', rotd_lat(127,444)
printf, 1, '127,511             = ', rotd_long(127,511), ', ', rotd_lat(127,511)
printf, 1, '191,0               = ', rotd_long(191,0), ', ', rotd_lat(191,0)
printf, 1, '191,63              = ', rotd_long(191,63), ', ', rotd_lat(191,63)
printf, 1, '191,127             = ', rotd_long(191,127), ', ', rotd_lat(191,127)
printf, 1, '191,191             = ', rotd_long(191,191), ', ', rotd_lat(191,191)
printf, 1, '191,255             = ', rotd_long(191,255), ', ', rotd_lat(191,255)
printf, 1, '191,319             = ', rotd_long(191,319), ', ', rotd_lat(191,319)
printf, 1, '191,383             = ', rotd_long(191,383), ', ', rotd_lat(191,383)
printf, 1, '191,444             = ', rotd_long(191,444), ', ', rotd_lat(191,444)

```



```

printf,1, '191,511      = ',rotd_long(191,511),  ', ' ,rotd_lat(191,511)
printf,1, '255,0        = ',rotd_long(255,0),    ', ' ,rotd_lat(255,0)
printf,1, '255,63       = ',rotd_long(255,63),    ', ' ,rotd_lat(255,63)
printf,1, '255,127      = ',rotd_long(255,127),   ', ' ,rotd_lat(255,127)
printf,1, '255,191      = ',rotd_long(255,191),   ', ' ,rotd_lat(255,191)
printf,1, '255,255      = ',rotd_long(255,255),   ', ' ,rotd_lat(255,255)
printf,1, '255,319      = ',rotd_long(255,319),   ', ' ,rotd_lat(255,319)
printf,1, '255,383      = ',rotd_long(255,383),   ', ' ,rotd_lat(255,383)
printf,1, '255,444      = ',rotd_long(255,444),   ', ' ,rotd_lat(255,444)
printf,1, '255,511      = ',rotd_long(255,511),   ', ' ,rotd_lat(255,511)
printf,1, '319,0        = ',rotd_long(319,0),    ', ' ,rotd_lat(319,0)
printf,1, '319,63       = ',rotd_long(319,63),    ', ' ,rotd_lat(319,63)
printf,1, '319,127      = ',rotd_long(319,127),   ', ' ,rotd_lat(319,127)
printf,1, '319,191      = ',rotd_long(319,191),   ', ' ,rotd_lat(319,191)
printf,1, '319,255      = ',rotd_long(319,255),   ', ' ,rotd_lat(319,255)
printf,1, '319,319      = ',rotd_long(319,319),   ', ' ,rotd_lat(319,319)
printf,1, '319,383      = ',rotd_long(319,383),   ', ' ,rotd_lat(319,383)
printf,1, '319,444      = ',rotd_long(319,444),   ', ' ,rotd_lat(319,444)
printf,1, '319,511      = ',rotd_long(319,511),   ', ' ,rotd_lat(319,511)
printf,1, '383,0        = ',rotd_long(383,0),    ', ' ,rotd_lat(383,0)
printf,1, '383,63       = ',rotd_long(383,63),    ', ' ,rotd_lat(383,63)
printf,1, '383,127      = ',rotd_long(383,127),   ', ' ,rotd_lat(383,127)
printf,1, '383,191      = ',rotd_long(383,191),   ', ' ,rotd_lat(383,191)
printf,1, '383,255      = ',rotd_long(383,255),   ', ' ,rotd_lat(383,255)
printf,1, '383,319      = ',rotd_long(383,319),   ', ' ,rotd_lat(383,319)
printf,1, '383,383      = ',rotd_long(383,383),   ', ' ,rotd_lat(383,383)
printf,1, '383,444      = ',rotd_long(383,444),   ', ' ,rotd_lat(383,444)
printf,1, '383,511      = ',rotd_long(383,511),   ', ' ,rotd_lat(383,511)
printf,1, '444,0        = ',rotd_long(444,0),    ', ' ,rotd_lat(444,0)
printf,1, '444,63       = ',rotd_long(444,63),    ', ' ,rotd_lat(444,63)
printf,1, '444,127      = ',rotd_long(444,127),   ', ' ,rotd_lat(444,127)
printf,1, '444,191      = ',rotd_long(444,191),   ', ' ,rotd_lat(444,191)
printf,1, '444,255      = ',rotd_long(444,255),   ', ' ,rotd_lat(444,255)
printf,1, '444,319      = ',rotd_long(444,319),   ', ' ,rotd_lat(444,319)
printf,1, '444,383      = ',rotd_long(444,383),   ', ' ,rotd_lat(444,383)
printf,1, '444,444      = ',rotd_long(444,444),   ', ' ,rotd_lat(444,444)
printf,1, '444,511      = ',rotd_long(444,511),   ', ' ,rotd_lat(444,511)
printf,1, '511,63       = ',rotd_long(511,63),    ', ' ,rotd_lat(511,63)
printf,1, '511,127      = ',rotd_long(511,127),   ', ' ,rotd_lat(511,127)
printf,1, '511,191      = ',rotd_long(511,191),   ', ' ,rotd_lat(511,191)
printf,1, '511,255      = ',rotd_long(511,255),   ', ' ,rotd_lat(511,255)
printf,1, '511,319      = ',rotd_long(511,319),   ', ' ,rotd_lat(511,319)
printf,1, '511,383      = ',rotd_long(511,383),   ', ' ,rotd_lat(511,383)
printf,1, '94,408       = ',rotd_long(94,408),    ', ' ,rotd_lat(94,408)
printf,1, '265,422      = ',rotd_long(265,422),   ', ' ,rotd_lat(265,422)
printf,1, '452,421      = ',rotd_long(452,421),   ', ' ,rotd_lat(452,421)
printf,1, '452,283      = ',rotd_long(452,283),   ', ' ,rotd_lat(452,283)
printf,1, '263,261      = ',rotd_long(263,261),   ', ' ,rotd_lat(263,261)

```

```
close,1
```

```
wait, 5
wdelete
end
```



## APPENDIX 3

### Example of Header data from an ATSR-2 image

Byte\_order: 16706  
Byte swap needed: 1  
File-name: 02053803-9706130738-16214-980409-2aV201.GBT-TVLXC  
Instrument: ATSR2  
State vector (type): ORRE  
(MJD time): 17330.38833642  
(UTC time): 13-JUN-1997 09:19:12.266  
(longitude): -162.26281  
(x/y/z position): -6824.61426 -2182.89359 0.00123  
(x/y/z velocity): -0.48854 1.55588 7.37749  
Clock calibration: 17330.40483978 175224320. 3906250.  
Options (NTVLXC): 0 1 1 1 1 1  
Along-track distance: 16214 16725  
Acquisition time: 13-JUN-1997 08:18:46.117 13-JUN-1997 08:20:02.020  
Latitude: 35.123 36.212 30.666 31.729  
Longitude: 41.737 36.259 40.325 35.112  
Nadir-view PSM: 13 -1 -1  
Forward-view PSM: 13 -1 -1  
Nadir-view ATSR-2 rate: H -1  
Forward-view ATSR-2 rate: H -1  
Minimum temperatures: 80.495 81.356 81.111 81.916 81.917 252.450  
Maximum temperatures: 80.636 82.047 81.802 82.990 82.812 253.750  
Nadir-view sol-elev (start): 72.643 72.242 71.840 71.431 71.026 70.600 70.182 69.757  
69.326 68.891 68.452  
(end): 74.159 73.734 73.307 72.877 72.438 71.990 71.544 71.099 70.644 70.183 69.715  
Nadir-view sat-elev (start): 68.259 72.856 77.174 81.402 85.431 89.448 86.350 82.315  
78.152 73.890 69.485  
(end): 68.262 72.858 77.176 81.324 85.432 89.448 86.350 82.316 78.154 73.892 69.413  
Nadir-view sol-azim (start): 128.585 127.790 126.990 126.180 125.411 124.644 123.864  
123.139 122.383 121.633 120.921  
(end): 113.597 113.126 112.668 112.224 111.774 111.303 110.856 110.406 109.945 109.508  
109.050  
Nadir-view sat-azim (start): -50.142 -55.314 -59.868 -63.839 -66.048 18.303 95.479 93.287  
89.364 84.846 79.858  
(end): -50.733 -55.862 -60.370 -64.226 -66.458 17.924 95.171 93.027 89.156 84.689  
79.670  
Frwr-view sol-elev (start): 72.367 71.930 71.494 71.073 70.648 70.215 69.794 69.384  
68.965 68.545 68.136  
(end): 73.819 73.352 72.896 72.436 71.986 71.542 71.100 70.656 70.219 69.780 69.355  
Frwr-view sat-elev (start): 38.089 37.033 36.302 35.839 35.565 35.468 35.543 35.785  
36.221 36.901 37.869  
(end): 38.100 37.044 36.330 35.851 35.577 35.480 35.550 35.797 36.232 36.913 37.880  
Frwr-view sol-azim (start): 127.682 126.798 125.921 125.130 124.355 123.583 122.875  
122.186 121.511 120.827 120.201  
(end): 112.892 112.355 111.872 111.384 110.937 110.500 110.088 109.676 109.281 108.868  
108.501  
Frwr-view sat-azim (start): -2.273 1.406 4.715 7.669 10.529 13.390 16.168 18.955  
21.930 25.188 28.738  
(end): -2.812 0.916 4.188 7.278 10.188 13.011 15.837 18.760 21.784 25.090 28.688  
Nadir-view platform mode: 512 0 0 0 0 0  
Frwr-view platform mode: 512 0 0 0 0 0  
Nadir-view PCD: 0 0 0 0 0 0 0 0  
Frwr-view PCD: 0 0 0 0 0 0 0 0



Nadir-view validity: 0 0 0 0 0 0 0 0 0 0  
Frwrd-view validity: 0 0 119 0 0 0 0 0 0 0  
Max single-pixel error: 8



## APPENDIX 4

### ATSR-2 and AVHRR imagery obtained

#### ATSR-2

Full Image name: Image date is given in the first 6 digits in bold in the form yymmdd

**970319**0741-16214-970418-2av100.gbt-tvlx  
**951011**0741-16214-970416-2av100.gbt-tvlx  
**951115**0741-16214-970416-2av100.gbt-tvlx  
**951220**0741-16214-970416-2av100.gbt-tvlx  
**960717**0741-16214-970416-2av100.gbt-tvlx  
**960925**0741-16214-970416-2av100.gbt-tvlx  
**961030**0741-16214-970416-2av100.gbt-tvlx  
**961204**0741-16214-970416-2av100.gbt-tvlx  
**951112**0735-16214-970416-2av100.gbt-tvlx  
**951125**0727-16214-970418-2av100.gbt-tvlx  
**951204**0744-16214-970418-2av100.gbt-tvlx  
**951207**0750-16214-970418-2av100.gbt-tvlx  
**951217**0735-16414-960215-2t100.gbt-tvlx  
**951128**0735-16414-960215-2t100.gbt-tvlx  
**951201**0738-16414-960326-2t100.gbt-tvlx  
**951214**0730-16414-960215-2t100.gbt-tvlx  
**970108**0741-16214-970425-2av100.gbt-tvlx  
**970212**0741-16214-970612-2av100.gbt-tvlx  
**950906**0741-16214-970807-2av200.gbt-tvlx  
**960821**0741-16214-980409-2av201.gbt-tvlx  
**970423**0741-16214-980409-2av201.gbt-tvlx  
**970509**0738-16214-980409-2av201.gbt-tvlx  
**970613**0738-16214-980409-2av201.gbt-tvlx  
**970702**0741-16214-980409-2av201.gbt-tvlx  
**970806**0741-16214-980409-2av201.gbt-tvlx  
**970910**0741-16214-980409-2av201.gbt-tvlx  
**970929**0744-16214-980409-2av201.gbt-tvlx  
**971116**0735-16214-980409-2av201.gbt-tvlx  
**971205**0738-16214-980409-2av201.gbt-tvlx

#### AVHRR

Image name in the form ALssmmddyyhhmmss where ss = sensor number, and mmddyy is the date

AL14020596105232  
AL14033196105923  
AL14061296111742  
AL14070996111919  
AL14080696111628  
AL14090596105010  
AL14092396105516  
AL14100196111649  
AL14101896112504  
AL14110796110800  
AL14010397104923  
AL14020797110947  
AL14041297112156  
AL14050197110759  
AL14060697112321  
AL14071297113123  
AL14080997112607  
AL14090597112901  
AL14121497113017



## APPENDIX 5

### C programme used to run the simple geometric optical model, Chapter 4

```
/* Model based on the work of Jupp et al. 1986. Journal of Environmental Management 23. 35-  
; 57. The code takes vegetation measurements (input directly from the keyboard or from a file),  
; and calculates red and near-infrared pixel reflectance based on user defined illumination  
; conditions */  
/* Marianne Edwards 21/05/97 */
```

```
#include <stdio.h>  
#include <math.h>
```

```
float pi;  
float yy,rr;  
float xmus, xmuv;  
float rfrac;  
float solzen, viwzen;  
float test, test2, gg, phi, phase;  
float relaz;  
float xx1, xx2, lx2, ox1, ox2, lx1, rx;  
float area, areabush, area1, area2, rad1, rad2, ao, bang, aang, aa3, pp;  
float vs, vi, areai, areas, rnum;  
float fvi, fvs, fss, fsh, diffred, diffnir, rvegred, rvegnir, rback;  
float rsbakred,rsvegred, rsbaknir, rbacknir,rbaknir, rsvegnir,rtotnir,rtotred;  
float diam,hght,diameter,height;  
float aa,bb,rr;  
float lambda;  
float NDVI;  
int data;
```

```
char fraction[4];  
char solzenith[10];  
char viewzenith[10];  
char relazimuth[10];  
char shrub[10];  
char density[10];  
char vegred[10];  
char vegnir[10];  
char background[10];  
char irradred[10];  
char irradnir[10];  
char input[10];  
char infile[10];  
char file[40];  
char diamet[10];  
char heigh[10];  
char output[10];  
char out[10];  
char filename[10];  
char fileout[10];
```

```
main ()  
{  
    FILE *fpointer;
```



```

FILE *fptr;
FILE *filein;

/* Define the output file for the results of the model */

printf("Enter the output filename: \n");
gets(output);
sscanf(output,"%s",out);

fpointer = fopen(out,"w");

printf("Enter filename for data: \n");
gets(filename);
sscanf(filename,"%s",fileout);

fptr = fopen(fileout,"w");

pi=3.141592654;

/* Shrub height and diameter are input from a file [1], or from the keyboard [2] */

printf("Input data source: [1] - shrub diameter and height file \n");
printf("          [2] - operator input \n");
gets(input);
sscanf(input,"%d",&data);

if (data==1)
{
    printf("Input file for shrub diameter and height: \n");
    gets(infile);
    sscanf(infile,"%s",file);

    filein=fopen("file","r");
    if (filein==NULL)
        printf("Error opening data file \n");

    while (!feof(filein))
    {
        fscanf(filein,"%f, %f",&diameter,&height);
        rnum = rnum + 1.0;
        diam = diam + diameter;
        hght = hght + height;
    }

    diam=diam/rnum;
    hght=hght/rnum;

}

else if (data==2)
{
    printf("Average plant diameter: (cm) \n");
    gets(diamet);
    sscanf(diamet,"%f",&diam);

    printf("Average plant height: (cm) \n");
    gets(heigh);
    sscanf(heigh,"%f",&hght);
}

```



```

    }

    diam=diam/100;
    hght=hght/100;

    aa=hght/2;
    bb=diam/2;
    rr=sqrt(aa*bb);
    area=pi*bb*bb;

/* The area of the vegetation for a given pixel, is calculated from the fractional cover */

    printf("The area of the vegetation is : %f\n", area);

    printf("Enter the fraction of vegetation cover: \n");
    gets(fraction);
    sscanf(fraction,"%f",&rfrac);

/*
    if (data==1)
/*
    {
        rnum=(rfrac*30*30)/area;
/*
    }

/*
    else if (data==2)
/*
    {
        lambda=rnum/(30*30);
        rfrac=area*lambda;
/*
    }

/* The user defines the illumination conditions */

    printf("Please enter the solar zenith: \n");
    gets(solzenith);
    sscanf(solzenith,"%f",&solzen);

    printf("Please enter the view zenith: \n");
    gets(viewzenith);
    sscanf(viewzenith,"%f",&viwzen);

    printf("Please enter the relative azimuth: \n");
    gets(relazimuth);
    sscanf(relazimuth,"%f",&relaz);

    xmus=solzen*(pi/180);
    xmuv=viwzen*(pi/180);
    phi=relaz*(pi/180);

/* compute phase angle gg */
    gg=acos(cos(xmus)*cos(xmuv)+sin(xmus)*sin(xmuv)*cos(phi));
    test=(cos(xmus)*cos(xmuv))+(sin(xmus)*sin(xmuv)*cos(phi));
    test2=acos(test);
    gg=test2;
    printf("test=%f\n",test);
    printf("test2=%f\n",test2);
    printf("gg=%f\n",gg);
    phase=gg*(180/pi);

/* writing the information to a file */

```



```

        fprintf(fpointer, "Viewing and illumination angles are: \n");
        fprintf(fpointer, "Solar zenith = %f \n", solzen);
        fprintf(fpointer, "View zenith = %f \n", viwzen);
        fprintf(fpointer, "Relative Azimuth = %f \n", relaz);
        fprintf(fpointer, "xmus = %f \n", xmus);
        fprintf(fpointer, "xmuv = %f \n", xmuv);
        fprintf(fpointer, "phi = %f \n", phi);
        fprintf(fpointer, "gg = %f \n", gg);
        fprintf(fpointer, "Phase Angle = %f \n", phase);

    /***/

    /* part of the program to compute shadow centre and shadow length assuming */
    /* sphere of radius rr */
    /* yy is the vertical distance from the origin to the tangent of the */
    /* illumination beam at zenith (xmus - solar zenith) */
    /***/

        yy = rr*sin(xmus);
        xx1 = (rr-yy)*tan(xmus);
        xx2 = (rr+yy)*tan(xmus);

    /* lx2 is length of the elongated semi-axis for solar projection (shadow) */

        lx2=((xx2+(2*rr*cos(xmus)))-xx1)/2;

        fprintf(fpointer, "yy=%f, xx1=%f, xx2 = %f, lx2=%f \n\n", yy, xx1, xx2, lx2);

    /* shift of the centre */

        ox2=(xx1+lx2)-(rr*cos(xmus));

    /* repeat for obscured surface area using view zenith (xmuv) */

        yy = rr*sin(xmuv);
        xx1 = (rr-yy)*tan(xmuv);
        xx2 = (rr+yy)*tan(xmuv);

        fprintf(fpointer, "ox2=%f, yy=%f, xx1=%f, xx2=%f \n\n", ox2, yy, xx1, xx2);

    /* lxl is length of elongated semi-axis for view projection (obscured) */

        lxl = ((xx2+(2*rr*cos(xmuv)))-xx1)/2;

    /* shift of the centre */

        ox1=(xx1+lxl)-(rr*cos(xmuv));

    /* projected areas - use rr as one axis and lxl, lx2 */

        area1=pi*rr*lxl;
        area2=pi*rr*lx2;

        fprintf(fpointer, "lxl=%f, ox1=%f, area1=%f, area2=%f \n", lxl, ox1, area1, area2);

        fprintf(fpointer, "Projection onto surface: \n");

```



```

        fprintf(fpointer,"Elongated semi-axes: \n");
        fprintf(fpointer,"Obscured [view] projection %f \n",lx1);
        fprintf(fpointer,"Shadow [solar] projection %f \n",lx2);
        fprintf(fpointer,"Obscured projected area %f \n",area1);
        fprintf(fpointer,"Shadow projected area %f \n\n",area2);

/* determine equivalent circle radius to approximate projected ellipses */
/* approximate radius of equivalent circles from projected ellipses */

        rad1=sqrt(area1/pi);
        rad2=sqrt(area2/pi);

/* compute distance between the centres of projected ellipses: use formula in */
/* Bronshtein and Semendyayev a guidebook to mathematics given sides a[ox1], */
/* b[ox2] and intervening angle C[phi] - compute c[aa3]*/

/*first check phase angle - if phase angle is zero then view zenith is equal */
/* to solar zenith and relative azimuth is equal to naut - therefore area of */
/* overlap equals shaded area equals obscured area */

        if (gg<0.0001)
        {
            ao=area1;
            printf("ao=%f \n", ao);
            fprintf(fpointer,"Phase angle = zero: shaded areas are obscured. \n");
        }
        else if (gg>0.0001)
        {
            if (relaz>0.01 && relaz<179.9)
            {
                bang=((180-relaz)-((atan(((ox1-ox2)/(ox1+ox2))*(1/tan((phi/2)))))*(360/pi)))/2;
                aang=(180-relaz)-bang;
                printf("aang=%f, bang=%f \n",aang,bang);
                aa3=(ox1*sin(phi))/sin((aang*pi/180));
            }
            else if (relaz<0.01)
            {
                printf("ox1=%f,ox2=%f \n",ox1,ox2);
                aa3=(ox1-ox2)*-1;
                printf("aa3=%f \n",aa3);
            }
            else if (relaz>179.9)
            {
                aa3=ox1+ox2;
            }

            fprintf(fpointer, "rad1=%f , rad2 = %f \n",rad1,rad2);
            fprintf(fpointer,"aa3=%f \n",aa3);

/* check if there is overlap between obscured disk and shadowed disk */

            if (rad1+rad2<aa3)
            {
/* no overlap */
                ao = 0.0;
                fprintf(fpointer, "No overlap between obscured and shadowed surfaces \n");
            }
            else if (rad1+rad2>aa3)

```



```

{

/* compute overlap using alternative method */
/* have length aa3 between centre of obscured and shaded projected circles */
/* now obtain half angle at origin to intersection of circles */
/* have 3 sides of triangle a[rad1],b[rad2],c[aa3, compute opposite angles */
/* A[aang], B[bang] */
        pp=0.5*(rad1+rad2+aa3);
        rx=sqrt(((pp-rad1)*(pp-rad2)*(pp-aa3))/pp);
        aang=2*(atan((rx/(pp-rad1))));
        bang=2*(atan((rx/(pp-rad2))));

        printf("rad1=%f,rad2=%f,rx=%f\n",rad1,rad2,rx);
        fprintf(fpointer,"pp=%f,rx=%f,aang=%f,bang=%f\n",pp,rx,aang,bang);

/* compute overlap in 2 sections from intersecting cord */
/* [area of segment minus area of triangle to cord in each circle ] */
        ao=((aang*rad2*rad2)-((rad2*cos(aang))*(rad2*sin(aang))))+((bang*rad1*rad1)-
        ((rad1*cos(bang))*(rad1*sin(bang))));
        fprintf(fpointer,"Area of overlap: %f\n",ao);
    }
}

/* area of observed surface in shadow is equal to shaded ellipse minus overlap */
        area2=area2-ao;

/* line put in to test calculation */
        printf("area2=%f\n",area2);

/* additional code to determine fraction of observed vegetation which is */
/* illuminated and fraction which is in shadow using phase angle (gg) */
/* compute fraction of spherical quadrant in shadow assuming that */
/* if (gg.le.pi/2) then - other observed spherical quadrant is illuminated */
/* if (gg.gt.pi/2) then - other observed quadrant is shaded */
/* as gg increases shade encroaches across observed hemisphere from the */
/* extremity of the hemisphere */

/* fraction of observed hemisphere in shade */
        if (gg<(pi/2))
        {
                vs=(1 - sin((pi/2)-gg))/2;
        }
        else if (gg>(pi/2))
        {
                vs=(1+sin(gg-(pi/2)))/2;
        }

/* fraction illuminated */
        vi=1-vs;
        areai=area1*vi;
        areas=area1*vs;

/* now have area per plant: illuminated veg [areai] */
/* shaded vegetation [areas] */
/* surface shadow [area2] */
/* surface area per plant [1/lambda] */

        fprintf(fpointer,"area of illum. veg = %f\n",areai);
        fprintf(fpointer,"shaded veg. = %f\n",areas);
        fprintf(fpointer,"surface shadow = %f\n", area2);

```



```

        area=(30*30)/rnum;
/*      area = 1/lambda;  */

        fprintf(fpointer,"Area of vegetation = %f\n",area);

/* The irradiance, vegetation and soil reflectances are input by the user */

        printf("Enter fraction of diffuse irradiance in red band\n");
        gets(irradred);
        sscanf(irradred,"%f",&diffred);

        printf("Enter fraction of diffuse irradiance in nir band\n");
        gets(irradnir);
        sscanf(irradnir,"%f",&diffnir);

        printf("Enter vegetation reflectance (fraction) in red band\n");
        gets(vegred);
        sscanf(vegred,"%f",&rvegred);

        printf("Enter vegetation reflectance (fraction) in nir band\n");
        gets(vegnir);
        sscanf(vegnir,"%f",&rvegnir);

/* can obtain fractions of illuminated background */
/*      shaded background      */
/*      illuminated vegetation */
/*      shaded vegetation      */

/* composite scene reflectance */
/* fvi = fraction of illuminated vegetation visible */
/* fvs = fraction of shaded vegetation visible      */
/* fss = fraction of sunlit background visible      */
/* fsh = fraction of shaded background visible      */

        fvi=areai/area;
        fvs=areas/area;
        fss=(area-(areas+areai+area2))/area;
        fsh=area2/area;

        fprintf(fpointer,"Fractional projected coverage observed for %f\n",rfrac);
        fprintf(fpointer,"Illuminated vegetation: %f\n", fvi);
        fprintf(fpointer,"Shaded vegetation: %f\n", fvs);
        fprintf(fpointer,"Sunlit background: %f\n",fss);
        fprintf(fpointer,"shaded background: %f\n",fsh);

/* rveg = shrub reflectance */
/* rback = sunlit background reflectance */
/* rsveg = shaded shrub reflectance */
/* rsbak = shaded background reflectance */

        printf("Enter background reflectance for red band\n");
        gets(background);
        sscanf(background,"%f",&rback);

/* increment the soil reflectance for the red band */

```



```

rsbakred=rback*diffred;
rsvegred=rvegred*diffred;
rtotred=(rvegred*fvi)+(rsvegred*fvs)+(rback*fss)+(rsbakred*fsh);

printf("Enter background reflectance for rnir band \n");
gets(background);
sscanf(background,"%f",&rbacknir);

/* Model output: Soil and Vegetation reflectance for a givn pixel, given a certain percentage
vegetation cover and illumination conditions */

rsbaknir=rbacknir*diffnir;
rsvegnir=rvegnir*diffnir;
rtotnir=(rvegnir*fvi)+(rsvegnir*fvs)+(rbacknir*fss)+(rsbaknir*fsh);
printf("The soil reflectance in the red is %f \n",rsbakred);
printf("The soil reflectance in the nir is %f \n",rsbaknir);
printf("The veg reflectance in the nir is %f \n",rsvegnir);
printf("The veg reflectance in the red is %f \n",rsvegred);
printf("The total reflectance in the nir is %f \n",rtotnir);
printf("%f,%f,%f,%f\n",fvi,fvs,fss,fsh);

/*      NDVI=(rtotnir-rtotred)/(rtotnir*rtotred);      */

fprintf(fpointer,"Component reflectances: \n");
fprintf(fpointer,"Illuminated vegetation: %f \n", rvegnir);
fprintf(fpointer,"Shaded vegetation: %f \n", rsvegnir);
fprintf(fpointer,"Illuminated background: %f \n", rbacknir);
fprintf(fpointer,"Shaded background: %f \n", rsbaknir);
fprintf(fpointer, "Surface reflectance: %f \n", rtotnir);

fprintf(fptr,"%f,%f,%f,%f,",rfrac,solzen,viwzen,relaz);
fprintf(fptr,"%f,%f,%f,%f,",fvi,fvs,fss,fsh);
fprintf(fptr,"%f,%f\n",rtotnir,rtotred);
printf("%f,%f,%f,%f \n",rfrac,rback,rtotnir,rtotred);

}

```



## APPENDIX 6

### Splitting the 3.7 µm band

The 3.7 µm middle infrared band of ATSR-2 can be split into thermal and reflected components parts using the method outlined by Kaufman and Remer (1994) adapted for ATSR-2 (Boyd *et al.*, 1998). Essentially three steps are followed:-

- i) 3.7 µm brightness temperatures are converted to radiance values using the Planck function

$$Radiance = \frac{C_1 nu^3}{\left[ \exp\left(\left(\frac{C_2 nu}{T_{3.7}}\right) - 1\right) \right]} \quad (5.1)$$

where

$$C_1 = 1.191064 * 10^{-5}$$

$$C_2 = 1.43883$$

nu = central wavenumber

$T_{3.7}$  = brightness temperature for 3.7 µm band

- ii) Radiance for the 10.5 µm band is calculated using Planck's function. This is used as values for the emitted radiation of the 3.7 µm band are calculated using the 10.5 µm band.

$$Radiance = \frac{C_1 nu^3}{\left[ \exp\left(\left(\frac{C_2 nu}{T_{10.5}}\right) - 1\right) \right]} \quad (5.2)$$

where

$$C_1 = 1.191064 * 10^{-5}$$

$$C_2 = 1.43883$$



$\nu$  = central wavenumber

$T_{10.5}$  = brightness temperature for 10.5  $\mu\text{m}$  band

- iii) Middle infrared reflectance is calculated using the results from i) and ii) above and the equation given by Kaufman and Remer (1994)

$$\rho_{3.75} = \frac{L_{3.75} - t_{3.75} B_{3.75}(T)}{t'_{3.75} \frac{F_0 \mu_0}{\pi} - t_{3.75} B_{3.75}(T)} \quad (5.3)$$

where

$\rho_{3.75}$  = reflection in the middle infrared

$L_{3.75}$  = radiance in middle infrared wavelengths (from Equation 5.1)

$B_{3.75}(T)$  = radiance in band 10.5  $\mu\text{m}$  (from Equation 5.2)

$F_0$  = incident solar radiance at the top of the atmosphere

$\mu_0$  = cosine of the solar zenith angle

$t_{3.75}$  = one way transmission function through the atmosphere

$t'_{3.75}$  = two way transmission function through the atmosphere

Following the results of sensitivity studies carried out by Kaufman and Remer (1994),  $t_{3.75}$  was assigned a value of 0.92 and  $t'_{3.75}$  a value of 0.9.



## APPENDIX 7

### Full list of vegetation indices correlated against percentage vegetation cover estimates

Indices were calculated for the nadir bands of ATSR-2. Bands listed under 'index calculated' refer to:

- 'g' = ATSR-2 Band 1, 0.545-0.565  $\mu\text{m}$
- 'r' = ATSR-2 Band 2, 0.649 - 0.669  $\mu\text{m}$
- 'nir' = ATSR-2 Band 3, 0.855 - 0.875  $\mu\text{m}$
- 'mir' = ATSR-2 Band 4, 1.58-1.64  $\mu\text{m}$

Index Group	Index Calculated
<b>Normalised Based Indices</b>	$\text{mir}-(\text{r}+\text{nir})/\text{mir}+(\text{r}+\text{nir})$
	$\text{mir}-(\text{r}+\text{g})/\text{mir}+(\text{r}+\text{g})$
	$\text{mir}-(\text{g}+\text{nir})/\text{mir}+(\text{g}+\text{nir})$
	$\text{g}-(\text{r}+\text{nir})/\text{g}+(\text{r}+\text{nir})$
	$\text{g}-(\text{r}+\text{mir})/\text{g}+(\text{r}+\text{mir})$
	$\text{g}-(\text{nir}+\text{mir})/(\text{g}+(\text{nir}+\text{mir}))$
	$\text{r}-(\text{nir}+\text{g})/\text{r}+(\text{nir}+\text{g})$
	$\text{r}-(\text{nir}+\text{mir})/\text{r}+(\text{nir}+\text{mir})$
	$\text{r}-(\text{mir}+\text{g})/\text{r}+(\text{mir}+\text{g})$
	$\text{nir}-(\text{mir}+\text{g})/\text{nir}+(\text{mir}+\text{g})$
	$\text{nir}-(\text{mir}+\text{r})/\text{nir}+(\text{mir}+\text{r})$
	$\text{nir}-(\text{r}+\text{g})/\text{nir}+(\text{r}+\text{g})$
<b>Complex Division Indices</b>	$\text{mir}/(\text{g}*\text{r}*\text{mir})$
	$\text{mir}/(\text{g}*\text{r}*\text{nir})$
	$\text{mir}/(\text{mir}*\text{nir}*\text{g})$
	$\text{mir}/(\text{mir}*\text{nir}*\text{r})$
	$\text{r}/(\text{nir}*\text{mir}*\text{g})$
	$\text{r}/(\text{nir}*\text{mir}*\text{r})$
	$\text{r}/(\text{r}*\text{g}*\text{mir})$
	$\text{r}/(\text{r}*\text{g}*\text{nir})$
	$\text{nir}/(\text{nir}*\text{mir}*\text{r})$
	$\text{nir}/(\text{nir}*\text{mir}*\text{g})$
	$\text{nir}/(\text{r}*\text{g}*\text{mir})$
	$\text{nir}/(\text{r}*\text{g}*\text{nir})$
	$\text{g}/(\text{r}*\text{g}*\text{nir})$
	$\text{g}/(\text{r}*\text{g}*\text{mir})$
	$\text{g}/(\text{nir}*\text{mir}*\text{r})$
	$\text{g}/(\text{nir}*\text{mir}*\text{g})$
<b>Stress related indices</b>	$\text{g}*\text{r}/\text{nir}$
	$\text{g}*\text{r}/\text{mir}$
	$\text{nir}*\text{r}/\text{g}$
	$\text{nir}*\text{r}/\text{mir}$



	$\text{mir} \cdot \text{r} / \text{g}$
	$\text{mir} \cdot \text{r} / \text{nir}$
	$\text{nir} \cdot \text{mir} / \text{g}$
	$\text{nir} \cdot \text{mir} / \text{r}$
	$\text{mir} \cdot \text{g} / \text{r}$
	$\text{mir} \cdot \text{g} / \text{nir}$
	$\text{nir} \cdot \text{g} / \text{r}$
	$\text{nir} \cdot \text{g} / \text{nir}$
<b>Ratio based indices</b>	$\text{g} / (\text{r} + \text{nir})$
	$\text{g} / (\text{r} + \text{mir})$
	$\text{g} / (\text{mir} + \text{nir})$
	$\text{g} / (\text{nir} + \text{g})$
	$\text{g} / (\text{mir} + \text{g})$
	$\text{g} / (\text{g} + \text{r})$
	$\text{r} / (\text{g} + \text{r})$
	$\text{r} / (\text{g} + \text{nir})$
	$\text{r} / (\text{g} + \text{mir})$
	$\text{r} / (\text{nir} + \text{mir})$
	$\text{r} / (\text{nir} + \text{r})$
	$\text{r} / (\text{mir} + \text{r})$
	$\text{nir} / (\text{g} + \text{r})$
	$\text{nir} / (\text{g} + \text{nir})$
	$\text{nir} / (\text{g} + \text{mir})$
	$\text{nir} / (\text{mir} + \text{nir})$
	$\text{nir} / (\text{mir} + \text{r})$
	$\text{nir} / (\text{nir} + \text{r})$
	$\text{mir} / (\text{g} + \text{r})$
	$\text{mir} / (\text{g} + \text{nir})$
	$\text{mir} / (\text{g} + \text{mir})$
	$\text{mir} / (\text{nir} + \text{mir})$
	$\text{mir} / (\text{mir} + \text{r})$
	$\text{mir} / (\text{nir} + \text{r})$
<b>Simple ratio indices</b>	$\text{g} / \text{r}$
	$\text{g} / \text{nir}$
	$\text{g} / \text{mir}$
	$\text{r} / \text{g}$
	$\text{r} / \text{nir}$
	$\text{r} / \text{mir}$
	$\text{nir} / \text{r}$
	$\text{nir} / \text{g}$
	$\text{nir} / \text{mir}$
	$\text{mir} / \text{g}$
	$\text{mir} / \text{r}$
	$\text{mir} / \text{nir}$
<b>Transformed indices</b>	$(\text{r} - \text{nir}) / (\text{r} + \text{nir} + 0.5)$
	$(\text{g} - \text{r}) / (\text{g} + \text{r} + 0.5)$
	$(\text{g} - \text{nir}) / (\text{g} + \text{nir} + 0.5)$
	$(\text{g} - \text{mir}) / (\text{mir} + \text{g} + 0.5)$
	$(\text{r} - \text{mir}) / (\text{r} + \text{mir} + 0.5)$
	$(\text{mir} - \text{nir}) / (\text{mir} + \text{nir} + 0.5)$



## References

- Abu-Awwad, A.M., and Shatanawi, M.R. (1997) Water harvesting and infiltration in arid areas affected by surface crust: examples from Jordan. *Journal of Arid Environments* **37**, pp. 443-452.
- Abu-Irmaileh, B.E. (1994) Al-Mowaqqar, a model for arid rangelands in Jordan: botanical composition and productivity. *Journal of Arid Environments* **28**, pp. 155-162.
- Abu-Taleb, M.F., Deason, J.P., Salameh, E., and Kefaya, B. (1992) Water resources planning and development in Jordan: problems, future scenarios and recommendations. *World Bank Technical Paper* **175**, pp. 119-127.
- Aldakheel, Y.Y., and Danson, F.M. (1997) Spectral reflectance of dehydrating leaves: measurements and modelling. *International Journal of Remote Sensing* **18**, No. 17, pp. 3683-3690.
- Al-Eisawi, D.M.H. (1985) Vegetation in Jordan In *Studies in the history and archaeology of Jordan II* edited by A.Hadid, Department of Antiquities, Amman. Hashemite Kingdom of Jordan, pp. 45-57.
- Al-Eisawi, D.M.H., and Hatough, A.M. (1987) Ecological analysis of the vegetation of Shaumari Reserve in Jordan. *Dirasat* **XIV**, No. 12, pp 81-94.
- Al-Fataftah, A.A. (1991) *Towards science and technology strategies and policies in the agriculture and water sector* A sectorial report. The Higher Council for Science and Technology, Amman, Jordan, July 1991.
- Al-Homoud, A.S., Allison, R.J., Sunna, B.F., and White, K. (1996) A study on geology, geomorphology, hydrology, groundwater and physical resources of the desertified Badia environment in Jordan towards sustainable development.



*Environmental Geology* 27, pp. 198-209.

Allison, R.J., Higgitt, D.L., Kirk, A.J., Warbuton, J., Al-Homoud, A.S., Sunna, B., and White, K. (1998) Geology, Geomorphology, Hydrology, Groundwater and Physical Resources pp. 21-44 in *Arid Land Resources and their management: Jordan's desert margin*, edited by R.W.Dutton, J.I.Clarke and A.M.Battikihi. Keegan Paul International. London.

Atkinson, P.M., Cutler, M.E.J., Lewis, H. (1995) Mapping subpixel variation in land cover in the UK from AVHRR imagery. *Proceedings of the 21st Annual Conference of the Remote Sensing Society*. 11-14th September, University of Southampton. pp. 58-65.

Bailey, P. (1995) *SADIST-2 v100 Products ER-TN-RAL-AT-2164* Rutherford Appleton Laboratories.

Ball, D.F. (1986) Site and soils. Chapter 5, pp. 215-284, in *Methods in Plant Ecology* edited by P.D.Moore and S.B.Chapman. Blackwell Scientific Publications. Oxford

Baret, F., Guyot, G., Begue, A., Maurel, P., and Podaire, A. (1988) Complementarity of middle-infrared with visible and near-infrared reflectance for monitoring wheat canopies. *Remote Sensing of Environment* 26, pp. 213-225.

Baret, F., Guyot, G., and Major, D. (1989) TSAVI: a vegetation index which minimises soil brightness effects on LAI and APAR estimation, in *12th Canadian symposium on remote sensing and IGARSS'90* Vancouver, Canada. 10-14th July, 1989.

Baret, F., and Guyot, G. (1991) Potentials and limits of vegetation indices for LAI and APAR assessment. *Remote Sensing of Environment* 35, pp. 161-173.

Baret, F., Jacquemond, S., and Hanocq, J.F. (1993) The soil line concept in remote



sensing. *Remote Sensing Reviews* 7, pp. 65-82.

Barham, N., and Mensching, H. (1988) Pressure on the pastureland in Jordan. *Applied Geography and Development* 31, pp. 37-53.

Barnsley, M.J. (1985) The implications of view angle effects on the use of multispectral data for vegetation studies. Paper presented at a conference on the application of remote sensing to aid range management September 1983, Silsoe College, Bedford.

Barnsley, M.J., Allison, D., and Lewis, P. (1997) On the information content of multiple view angle (MVA) images. *International Journal of Remote Sensing* 18, No. 9, pp. 1937-1960.

Barton, I.J., and Prata, A.J., (1995), Satellite-derived Sea-Surface Temperature data sets for climate applications. *Advances in Space Research* 16, No. 10, pp. 127-136.

Belward, A.S. (1991) Spectral characteristics of vegetation, soil and water invisible, near infrared and middle-infrared wavelengths. pp. 31-53 in *Remote sensing and geographical information systems of resource management in developing countries* edited by A.S.Belward and C.R.Valenzuela. Dordrecht. Kluwer Academic

Boyd, D.S., Foody, G.M., Curran, P.J., Lucas, R.M., and Honzak. (1996) An assessment of radiance in Landsat TM middle and thermal infrared wavebands for the detection of tropical forest regeneration. *International Journal of Remote sensing* 17, No. 2, pp. 249-261.

Boyd, D.S., and Ripple. W.J. (1997) Potential vegetation indices for determining global forest cover. *International Journal of Remote Sensing* 18, No. 6, pp. 1395-1401.

Boyd, D.S., and Curran, P.J. (1998) Using remote sensing to reduce uncertainties in



the global carbon budget: the potential of radiation acquired in the middle infrared wavelengths. *Remote Sensing Reviews* **16**, pp. 293-327.

Boyd, D.S., Edwards, M.C., and Wellens, J. (1998) Analysis of ERS ATSR-2 shortwave infrared (1.5-3.0  $\mu\text{m}$ ) and reflected middle infrared (3.0-5.0  $\mu\text{m}$ ) response of dryland vegetation. pp 371-377 in *Proceedings of the 24th annual conference and exhibition of the Remote Sensing Society*, University of Greenwich, 9-11 September 1998.

Brown, R.J., Bernier, M., and Fedosejevs, G. (1982) Geometric and radiometric considerations of NOAA AVHRR imagery. *Proceedings of the 8th International Symposium on machine processing of remotely sensed data*. Purdue University, Indiana, pp. 374-381.

Bryne, G.F., Crapper, P.F., and Mayo, K.K. (1980) Monitoring land cover change by principal component analysis of multitemporal Landsat data. *Remote Sensing of Environment* **10**, pp. 175-184.

Burdon, D.J. (1959) *Handbook of the geology of Jordan* 82 pp. Government of the Hashemite Kingdom of Jordan.

Chang, S.H., and Collins, W. (1983) Confirmation of the airborne biogeochemical mineral exploitation technique using laboratory methods. *Economic Geology* **78**, pp. 723-736.

Chartier, R., Becker, M., Bonhomme, R., and Bony, R.P (1973) Effects physiologiques et caractéristaion du rayonnement solaire dans le cadre d'une methode d'aménagement sylvicole en foret dense africaine *Revue Bois Forets Tropiques* **152**, pp. 19-35.

Choudbury, B.J., and Tucker, C.J. (1987) Satellite observed seasonal and inter annual variation of vegetation over the Kalahari, The Great Victoria Desert and the Great



Sandy Desert 1979-1984. *Remote Sensing of Environment* **23**, pp. 233-241.

Cihlar, J., Manak, D., and Voisin, N. (1994) AVHRR Bi-directional reflectance effects and compositing. *Remote Sensing of Environment* **48**, pp. 77-88.

Colwell, J.E. (1974) Vegetation canopy reflectance. *Remote Sensing of Environment* **3**, pp. 175-183.

Cope, T.A, and Al-Eisawi, D. (1998) Checklist of the flora, pp 183-188 in *Arid land resources and their management, Jordan's desert margin* edited by R.W.Dutton, J.I.Clark and A.M.Batikki. John Wiley and Sons. Chichester.

Cracknell, A.P, and Hayes, L.W.B. (1993) *Introduction to Remote Sensing*, Taylor and Francis, London.

Cracknell, A.P., and Busu, I. (1995) Archives of AVHRR data: the correction of systematic errors due to sensor degradation. *Proceedings of the 21st Annual Conference of the Remote Sensing Society*. 11-14th September, University of Southampton. pp. 615-623.

Curran, P.J. (1980) Multispectral photographic remote sensing of vegetation amount and productivity. *Proceedings of the 14th International Symposium on Remote Sensing of the Environment*, Ann Arbor, Michigan, pp. 623-637.

Delta-T Devices (1995) *ThetaProbe Soil Moisture Sensor User Manual* ML1-UM-1

Demetriades-Shah, T.H., Steven, M.D., and Clark, J.A. (1990) High resolution derivative spectra in remote sensing. *Remote Sensing of Environment* **33**, pp. 55-64.

Diallo, O., Diouf, A., Hanan, N.P., Ndiaye, A., and Prevost, Y. (1991) AVHRR monitoring of savanna primary production in Senegal, West Africa: 1987-1988. *International Journal of Remote Sensing* **12**, pp. 1259-1280.



Dotteridge, J., and Gibbs, B.R. (1998) Water for sustainable development, pp 111-118 in *Arid Land Resources and their management: Jordan's desert margin*, edited by R.W.Dutton, J.I.Clarke and A.M.Battikihi. Keegan Paul International. London.

Dotteridge, J. (1998) Water resources quality, sustainability and development, pp 67-78 in *Arid Land Resources and their management: Jordan's desert margin*, edited by R.W.Dutton, J.I.Clarke and A.M.Battikihi. Keegan Paul International. London

Duggin, M.J., Piwinski, D., Whitehead, V., Ryland, G. (1982) Evaluation of NOAA-AVHRR data for crop assessment. *Applied Optics* **21**, pp. 1873.

Dutton, R.W. (1998) Population, environment and development, pp 3-20 in *Arid Land Resources and their management: Jordan's desert margin* edited by R.W.Dutton, J.I.Clarke and A.M.Battikihi. Keegan Paul International. London.

Eastman, J.R., and Fulk, M. (1993) Long sequence time series evaluation using standardised principal components. *Photogrammetric Engineering and Remote Sensing* **59**, No. 6, pp. 991-996.

Ebdon, D. (1985) *Statistics in Geography*. Second Edition. Blackwell, Oxford.

Edwards, M.C. (1995) *Visual interpretation of SPOT panchromatic imagery for land cover mapping in Nigeria*. Unpublished MSc thesis, Silsoe College.

Edwards, T., Browning, R., Delderfield, J., Lee, D.J., Lidiard, K.A., Milborrow, R.S., McPherson, P.H., Peskett, S.C., Toplis, G.M., Taylor, H.S., Mason, I., Mason, G., Smith, A., Stringer, S., (1990) The Along Track Scanning Radiometer measurement of sea-surface temperature from ERS-1, *Journal of the British Interplanary Society* **43**, pp. 160-180.

Ehrlich, D., Estes, J.E., and Singh, A. (1994) Review Article: Applications of NOAA-AVHRR 1 km data for environmental monitoring. *International Journal of Remote Sensing* **15**, No. 1. pp. 145-161.



Elvidge, C.D, and Lyon, R.J.P. (1985) Influence of rock-soil spectral variation on the assessment of green biomass. *Remote Sensing of Environment* 17, pp. 265-279.

Elvidge, C.D., Chen, Z., and Groeneveld, D.P. (1993) Detection of trace quantities of green vegetation in 1990 AVIRIS data. *Remote Sensing of Environment* 44, pp. 271-279.

Elvidge, C.D., and Chen, Z. (1995) Comparison of broad-band and narrow-band red and near infrared vegetation indices. *Remote Sensing of Environment* 54, pp. 38-48.

ERDAS (1991) *Field Guide* ERDAS. USA

European Space Agency (1998) *ENVISAT Mission: Opportunities for Science and Applications SP-1218*.

Everitt, J.H., Escobar, D.E., and Richardson, A.J. (1989) Estimating grassland phytomass production with near-infrared and mid-infrared spectral variables. *Remote Sensing of Environment* 30, pp. 257-261.

Fitter, A.H., and Hay, R.K.M. (1987) *Environmental Physiology of Plants* 2nd Edition, Academic Press, London. 423 pp.

Foody, G.M., Lucas, R.M., Curran, P.J., and Honzak, M. (1997) Mapping tropical forest fractional cover from coarse spatial resolution imagery. *Plant Ecology* 131-132, pp. 143-154.

Foran, B.D. (1987) Detection of yearly cover change with Landsat MSS on pastoral landscapes in central Australia. *Remote Sensing of Environment* 23, pp 333-350.

Forrester, T.N., and Challenor, P.G., (1995) Validation of ATSR sea-surface temperatures in the Faeroes region. *International Journal of Remote Sensing* 16, No. 15, pp. 2741-2753.



Franklin, J., Prince, S.D., Strahler, A.H., Hanan, N.P., and Simonett, D.S. (1991) Reflectance and transmittance properties of West African savanna trees from ground radiometric measurements. *International Journal of Remote Sensing* 12, No. 6, pp. 1369-1385.

Franklin, J., and Turner, D.L. (1992) The application of a geometric optical canopy reflectance model to semiarid shrub vegetation. *IEEE Transactions on Geoscience and Remote Sensing* 30, No. 2, pp. 293-301.

Fung, I.Y., Tucker, C.J., and Prentice, K.C. (1986) On the applicability of the AVHRR vegetation index to study the atmosphere-biosphere exchange of CO<sub>2</sub>. *Journal of geophysical Research* 92, pp. 2999-3015.

Fung, T., and Ledrew, E. (1987) Application of principal components analysis to change detection. *Photogrammetric Engineering and Remote Sensing* 53, No. 12, pp. 1649-1658.

Gao, B., and Goetz, A.F.H. (1994) Extraction of dry leaf spectral features from reflectance spectra of green vegetation. *Remote Sensing of Environment* 47, pp. 369-374.

Gates, D.M. (1980) *Biophysical Ecology*, Springer-Verlag, New York, Heidelberg, Berlin, 611 pp.

Gauthier, R.P., Ahern, F.J., Teillet, P.M., and Fedosejevs, G. (1991) *Report on the specialist meeting on the derivation of bi-directional reflectance distribution functions for various ground cover types* Report of a workshop held November 1990, Arizona. Canada Centre for Remote Sensing, June 1991

Gemmell, F., Millington, A.C., Wellens, J., Wyatt, B.K., and Gerard, F. (1995) An assessment of the combined use of ATSR-2 and Landsat TM data for mapping humid tropical forest types in Bolivia. in *Proceedings of the 21st Annual Conference of the Remote Sensing Society* 11-14th September, University of Southampton pp. 829-838.



Gemmell, F., and Millington, A.C. (1997) Initial assessment of ATSR-2 structure for land surface applications. *International Journal of Remote Sensing* 18, No.2, pp. 461-466.

Gertsl, S.A., Simmer, C., and Powers, B.J. (1986) The canopy hot-spot as a crop identifier. *Proceedings of the International Symposium on remote sensing for resources development and environmental management*, edited by M.C.Damen, G Sicco Smit and M.Th.Verstappen (Rotterdam/Boston: A.A.Balkema) pp. 261-263.

Godslave, C. (1995) Bi-directional reflectance sampling by ATSR-2: a combined orbit and scan model. *International Journal of Remote Sensing* 16, No. 2, pp. 269-300.

Goel, N.S., and Thompson, R.L. (1984) Inversion of vegetation canopy reflectance models for estimating agronomic variables. V: Estimation of LAI and average leaf angle using measured canopy reflectances. *Remote Sensing of Environment* 16, pp. 69-85.

Goel, N.S. (1988) Models of vegetation canopy reflectance and their use in the estimation of biophysical parameters from reflectance data. *Remote Sensing Reviews* 3, pp. 1-212.

Graetz, R.D., and Gentle, M.R. (1982) The relationships between reflectance in the Landsat wavebands and the composition of an Australian semi-arid shrub rangeland. *Photogrammetric Engineering and Remote Sensing* 48, No. 11, pp. 1721-1730.

Graetz, R.D. (1987) Satellite remote sensing of Australian rangelands. *Remote Sensing of Environment* 23, pp. 313-331.

Greig-Smith, P. (1983) *Quantitative Plant Ecology*, Blackwell Scientific Publications. Oxford.

Grove, K and Quegan, S. (1999) Quantitative estimation of tropical forest cover by SAR. *IEEE Transactions on Geoscience and Remote Sensing* 37, No. 1, pp. 479-490.



Hall, F.G., Huemmrich, K.F., and Goward, S.N. (1990) Use of narrow-band spectra to estimate the fraction of absorbed photosynthetically active radiation. *Remote Sensing of Environment* **32**, pp. 47-54.

Hall, F.G., Shimabukaro, Y.E., and Huemmrich, K.F. (1995) Remote sensing of forest biophysical structure using mixture decomposition and geometric reflectance models. *Ecological Applications* **5**, No. 4, pp. 993-1013.

Hapke, B. (1986) The extinction coefficient and the opposition effect. *Icarus* **67**, pp. 264-280.

Hardisky, M.A., Daiber, F.C., Roman, C.T., and Klemas, V. (1984) Remote sensing of biomass and annual net aerial primary productivity of a saltmarsh. *Remote Sensing of Environment* **16**, pp. 91-106.

Harries, J.E., Llewellyn-Jones, D.T., Minnett, P.J., Saunders, R.W., and Zavody, A.M. (1983) Observations of sea surface temperatures for climate research. *Philosophical Transactions of the Royal Society* **A309**, pp. 381-394.

Hatough, A.M., Al-Eisawi, D.M., and Disi, A.M. (1986) The effect of conservation on wildlife in Jordan. *Environmental Conservation* **13**, No. 4, pp. 331-335.

Higgins, N.A. (1995) Potential of the ERS-2 ATSR-2 for monitoring land cover change. *Proceedings of the 21st Annual Conference of the Remote Sensing Society*. 11-14th September, University of Southampton, pp 320-324.

Hobbs, T.J., Sparrow, A.D., Landsberg, J.J. (1994) A model of soil moisture balance and herbage growth in the arid rangelands of central Australia. *Journal of Arid Environments* **28**, pp. 281-298.

Hobbs, T.J. (1995) The use of NOAA-AVHRR NDVI data to assess herbage production in the arid rangelands of Central Australia. *International Journal of*



*Remote Sensing* **16**, No. 7, pp. 1289-1302.

Holben, B., Kimes, D., and Fraser, R.S. (1986) Directional reflectance response in AVHRR red and near infrared bands for 3 cover types and varying atmospheric conditions. *Remote Sensing of Environment* **19**, pp. 213-236.

Horler, D.N.H., Dockray, M., and Barber, J. (1983) The red edge of plant leaf reflectance. *International Journal of Remote Sensing* **4**, No. 2, pp. 273-288.

Huete, A.R., Post, D.F., and Jackson, R.D. (1984) Soil spectral effects on 4-space vegetation discrimination. *Remote Sensing of Environment* **15**, pp. 155-165.

Huete, A.R., and Jackson, R.D. (1987) Suitability of spectral indices for evaluating vegetation characteristics on arid rangelands. *Remote Sensing of Environment* **23**, pp. 213-232.

Huete, A.R. (1988) A soil-adjusted vegetation index (SAVI). *Remote sensing of Environment* **25**, pp. 295-309.

Hyppanen, H. (1996) Spatial autocorrelation and optimal spatial resolution of optical remote sensing data in boreal forest environment. *International Journal of Remote Sensing* **17**, No. 17. pp. 3441-3452.

Irons, J.R., Ranson, K.J., and Daugherty, C.S.T. (1988) Estimating big bluestem albedo from directional reflectance measurements. *Remote Sensing of Environment* **25**, pp. 185-199.

Jackson, R.D., Slater, P.N., and Pinter, P.J.Jr. (1983) Discrimination of growth and water stress in wheat by various vegetation indices through clear and turbid atmospheres. *Remote Sensing of Environment* **13**, pp. 187-208.

Jasinski, M.F., and Eagleson, P.S. (1990) Estimation of subpixel vegetation cover



using red infrared scattergrams. *IEEE Transactions on Geoscience and Remote Sensing* **28**, No. 2, pp. 253-267.

Jasinski, M.F. (1996) Estimation of subpixel vegetation density of natural regions using satellite multispectral imagery. *IEEE Transactions on Geoscience and Remote Sensing* **34**, No. 3, pp. 804-813.

Jupp, D.L.B., Walker, J., and Penridge, L.K. (1986) Interpretation of a vegetation structure in Landsat MSS imagery: a case study in disturbed semi-arid eucalypt woodlands. Part 2. Model based analysis. *Journal of Environmental Management* **23**, pp. 35-57.

Justice, C.O. (1978) *The effect of ground conditions on Landsat multispectral scanner data for an area of complex terrain in southern Italy* Unpublished PhD thesis, University of Reading, UK.

Justice, C.O., and Townshend, J.R.G. (1981) Integrating ground data with remote sensing in *Terrain analysis and Remote Sensing*, edited by J.R.G., Townshend, George Allen and Unwin: London, pp. 38-58.

Justice, C.O., and Hiernaux, P.H.Y. (1986) Monitoring the grasslands of the Sahel using NOAA AVHRR data - Niger 1983. *International Journal of Remote Sensing* **7**, No. 11, pp. 1475-1497.

Kabbaj, M.M., and Mehrez, M.B. (1994) Remote Sensing and developing countries, training and technology transfer Europe-Africa. *International Journal of Remote Sensing* **15**, No. 15, pp. 3003-3016.

Kasapligil, B. (1956) *An ecological survey of vegetation in relation to forestry and grazing*. Report to the government of the Hashemite Kingdom of Jordan FAO/5691 7164 Rome.



- Kaufman, Y.J., Setzer, A., Justice, C., Tucker, C.J., Pereira, M.C., and Fung, I. (1990) Remote sensing of biomass burning in the tropics. pp 371-299 in *Fire in the Tropical Biota: Ecosystem and global challenges*, edited by J.G. Goldammer, Berlin: Springer-verlag.
- Kaufman, Y.J., and Tanré, D. (1992) Atmospherically resistant vegetation index (ARVI) for EOS-MODIS. *IEEE Transactions on Geoscience and Remote Sensing* 30, No. 2, pp. 261-270.
- Kaufman, Y.J., and Remer, L.A. (1994) Detection of forests using mid-IR reflectance: an application for aerosol studies. *IEEE Transactions on Geoscience and Remote Sensing* 32. pp. 672-683.
- Kauth, R.J., and Thomas, G.S. (1976) The Tasselled-cap - a graphic description of the spectral-temporal development of agricultural crops as seen by Landsat. *Proceedings of a Symposium of Machine Processing of Remotely Sensed Data*. Purdue University, West Lafayette, pp. 41-51.
- Kennedy, P.J. (1989) Monitoring the phenology of Tunisian grazing lands. *International Journal of Remote Sensing* 10, No. 4, pp. 835-845.
- Kent, M., and Coker, P. (1994) *Vegetation description and analysis: a practical approach*. John Wiley and Sons, Chichester.
- Kimes, D.S. (1983) Dynamics of directional reflectance factor distributions for vegetation canopies. *Applied Optics* 22, No. 9, pp. 1364-1372.
- Kimes, D.S., Holben, B.N., Tucker, C.J., and Newcomb, W.W. (1984) Optimal directional view angles for remote sensing missions. *International Journal of Remote Sensing* 5, No. 6, pp. 887-908.
- Kimes, D.S., Newcomb, W.W., Tucker, C.J., Zonneveld, I.S., Van Wijngaarden, W.,



De Leeuw, J., Epema, G.F. (1985) Directional reflectance factor distributions for cover types of Northern Africa. *Remote Sensing of Environment* **18**, pp. 1-19.

Kimes, D.S., and Sellers, P.J. (1985) Inferring hemispherical reflectance of the earth's surface for global energy budgets from remotely sensed nadir or directional values. *Remote Sensing of Environment* **18**, pp. 205-223.

Kirchner, J.A., Schnetzler, C.C., and Smith, J.A. (1981) Simulated directional radiances of vegetation from satellite platforms. *International Journal of Remote Sensing* **2**, No. 3, pp. 253-264.

Kirk, A. (1998) A synthesis of the climatic data with specific interest in the precipitation record, pp 47-66 in *Arid Land Resources and their management: Jordan's desert margin*, edited by R.W. Dutton, J.I. Clarke and A.M. Battikihi. Keegan Paul International. London.

Kriebel, K.T. (1978) Measured spectral bi-directional reflection properties of four vegetated surfaces. *Applied Optics* **17**, No. 2, pp. 253-259.

Lambin, E.F., and Ehrlich, D. (1996) The surface temperature-vegetation index space for land cover change analysis. *International Journal of Remote Sensing* **17**, No. 3, pp. 463-487.

Leamer, R.W., Noriega, J.R., and Wiegand, C.L. (1978) Seasonal changes in reflectance of two wheat cultivators. *Agronomy Journal* **70**, pp. 113-118.

Leblon, B., Gallant, L., and Granberg, H. (1996) Effects of shadowing types on ground-measured visible and near infrared shadow reflectances. *Remote Sensing of Environment* **58**, pp. 322-328.

Le Houerou, H.N. (1984) Rain use efficiency: a unifying concept in arid land ecology *Journal of Arid Environments* **7**, pp. 212-247.



Li, X., and Strahler, A.H. (1985) Geometric-optical modelling of a conifer forest canopy. *IEEE Transactions on Geoscience and Remote Sensing* **GE-23**, No. 5, pp. 705-721.

Li, X., and Strahler, A.H. (1986) Geometrical-optical bi-directional reflectance modelling of a conifer forest canopy *IEEE Transactions on Geoscience and Remote Sensing* **24**, pp. 906-919.

Li, X and Yeh, A.G.O. (1998) Principal component analysis of stacked multitemporal images for the monitoring of rapid urban expansion in the Pearl River Delta. *International Journal of Remote Sensing* **19**, No. 8, pp. 1501-1518.

Maani, M., Hunaiti, H. and Findlay, A.M. (1998) Demographic change and population projections, pp 1976-2013, in *Arid Land Resources and Their Management: Jordan's Desert Margin*, edited by R.W.Dutton, J.I.Clark and A.M.Batikki. John Wiley and Sons. Chichester.

Mackay, G., Millington, A., and White, K. (1996) Directional reflectance properties of desert surfaces, the Eastern Badia, Jordan. *Proceedings of the 22nd annual conference of the Remote Sensing Society* 11-14 September, Durham. pp. 37-42.

Mackay, G., Steven, M.D., and Clark, J.A. (1998) An atmospheric correction procedure for the ATSR-2 visible and near infrared land surface data. *International Journal of Remote Sensing* **19**, No. 15, pp 2949-2968

Mackay, G., and Millington, A.C. (1997a) Application of a dual-angle atmospheric correction for ATSR-2 solar reflecting channels. *International Journal of Remote Sensing* in press

Mackay, G. and Millington, A.C. (1997b) Validation of surface conditions for the atmospheric correction of ATSR-2 solar reflecting data over desert surfaces. *International Journal of Remote Sensing*. in press



Major, D.J., Baret, F., and Guyot, G. (1990) A ratio vegetation index adjusted for soil brightness. *International Journal of Remote Sensing* **11**, No. 5, pp. 7227-7240.

Malingreau, J.P., Stevens, G., and Fellows, C. (1985) 1982-83 forest fire of Kalimantan and North Borneo: Satellite observations for detection and monitoring. *Ambio* **14**, pp. 314-346.

Malingreau, J.P., Tucker, C.J., and Laporte, N. (1989) AVHRR for monitoring global tropical deforestation. *International Journal of Remote Sensing* **10**, pp. 855-867.

Marsh, S.E., Walsh, J.L., Lee, C.T., Beck, L.Rl., and Hutchinson, C.F. (1992) Comparison of multi-temporal NOAA-AVHRR and SPOT-XS satellite data for mapping land cover dynamics in the west African Sahel. *International Journal of Remote Sensing* **13**, No. 16, pp. 2997-3016.

Mason, I.M., and Delderfield, J. (1990) *Scientific requirements specification for the ATSR-2 on ERS-2* Rutherford Appleton Labs Technical Report ER-RS-MSL-AT-2001 Issue 2C

McCleary, J.A. (1968) The biology of desert plants. pp. 141-194 in *Desert Biology* edited by G.W.Brown, Jr. Academic Press. New York.

Meyer, D., Verstraete, M., and Pinty, B. (1995) The effect of surface anisotropy and viewing geometry on the estimation of NDVI from AVHRR. *Remote Sensing Reviews* **12** pp. 3-27.

Middleton, E.M., Deering, D.W., and Ahmad, N.P. (1987) Surface anisotropy and hemispheric reflectance for a semiarid ecosystem. *Remote Sensing of Environment* **23**, pp. 193-212.

Milton, E.J. (1987) Principles of field spectroscopy. *International Journal of Remote Sensing* **8**, pp. 1807-1827.



Moore, P.D., and Chapman, S.B. (1986) *Methods in Plant Ecology*. Blackwell Scientific Publications, Oxford

Nicodemus, F.E., Richmond, J.C., Hsia, J.J., Ginsberg, I.W., and Limperis, T. (1977) Geometrical considerations and nomenclature for reflectance. *NBS Monograph 160*, 52 pp.

Norman, J.M., and Welles, J.M. (1983) Radiative transfer in an array of canopies. *Agronomy Journal 75* pp. 481-488.

NOAA Polar Orbiter Data Users Guide (1997) US Department of Commerce National Oceanic and atmospheric administration

Oliosio, A. (1995) Simulating the relationship between thermal emissivity and the normalised difference vegetation index. *International Journal of Remote Sensing 16*, pp. 3211-3216.

Otterman, J. (1974) Bearing high albedo soils by overgrazing: a hypothesised desertification mechanism. *Science 186*, pp. 531-533.

Otterman, J. (1975) Correspondence. *Science 189*, pp. 1013.

Otterman, J., Waisel, Y., and Rosenberg, E. (1975) Western Negev and Sinai ecosystems: comparative study of vegetation, albedo and temperatures. *Agro-ecosystems 2*, No 1, pp. 47-59.

Otterman, J. (1981) Satellite and field studies of man's impact on the surface in arid regions. *Tellus 33*, pp. 68-77.

Otterman, J. (1984) Albedo of a forest modelled as a plane with dense protrusions. *Journal of Climate and Applied Meteorology 23*, pp. 297-307.



Otterman, J. (1996) Desert-scrub as the cause of reduced reflectances in protected versus impacted sandy arid regions *International Journal of Remote Sensing* 17, No. 3, pp. 615-619.

Paltridge, G.W., and Mitchell, R.M. (1990) Atmospheric and viewing angle correction of vegetation indices and grassland fuel moisture content derived from NOAA/AVHRR *Remote Sensing of Environment* 31, pp. 121-135.

Parkes, I.M., Sheasby, T.N., Llewellyn-Jones, D.T., Nightingale, T.J., Zavody, A.M., Mutlow, C.T., Yokoyama, R., Tamba, A.S., Donlon, C.J. (1999) The MUTSU experiment - validation of ATSR-1 and ATSR-2 sea surface temperature (SST) in Mutsu Bay, Japan during July and August 1996. *International Journal of Remote Sensing* in press

Patrono, A. (1996) Synergism of remotely sensed data for land cover mapping in heterogeneous alpine areas: an example combining accuracy and resolution. *ITC Journal* 1/2, pp. 101-109.

Pears, N. (1985) *Basis Biogeography*. Longman Scientific and Technical.

Pearson, R.L., Tucker, C.J., and Miller, L.D. (1976) Spectral Mapping of short grass prairie biomass *Photogrammetric Engineering and Remote Sensing* 42, pp. 317-324.

Pech, R.P., Graetz, R.D., and Davis, A.W. (1986) Reflectance modelling and the derivation of vegetation indices for an Australian semi-arid shrubland *International Journal of Remote Sensing* 7, No. 3, pp. 389-403.

Perera, L.K., and Tateishi, R. (1995) Do remote sensing and GIS have a practical applicability in developing countries ? (including some Sri Lankan experiences) *International Journal of Remote Sensing* 16, No. 1, pp. 35-51.

Perrin, M., and Millington, A.C. (1997) ATSR-2 data for burned area detection. RSS97 Observations and Interactions. 23rd Annual conference and exhibition of the



*Remote Sensing Society* pp. 165-170.

Perry, A. (1981) Mediterranean Climate - a synoptic reappraisal. *Progress in Physical Geography* **5**, pp. 107-113.

Pickup, G. (1989) New land degradation survey techniques for arid Australia - problems and prospects *Australian Rangeland Journal* **11**, pp. 74-82.

Pinker, R.T., and Karnieli, A. (1995) Characteristic spectral reflectance of a semi-arid environment. *International Journal of Remote Sensing* **16**, No 7, pp. 1341-1363.

Pinter, P.J., Jackson, R.D., and Moran, M.S. (1990) Bi-directional reflectance factors of agricultural targets: a comparison of ground-, aircraft- and satellite-based observations *Remote Sensing of Environment* **32**, pp. 215-228.

Pinty, B., and Verstraete, M.M. (1992) GEMI: a non-linear index to monitor global vegetation from satellites *Vegetatio* **101**, pp. 15-20.

Price, J.C. (1985) On the analysis of thermal infrared imagery: the limited utility of apparent thermal inertia. *Remote Sensing of Environment* **18**, pp. 59-73.

Price, J.C. (1992) Estimating vegetation amount from visible and near infrared reflectances. *Remote Sensing of Environment* **41**, pp. 29-34.

Qi, J., Huete, A.R., Cabot, F., and Chehnouni, A. (1994a) Bi-directional properties and utilisations of high-resolution spectra from a semiarid watershed. *Water Resources Research* **30**, No. 5, pp. 1271-1279.

Qi, J., Chehbouni, Al., Huete, A.R., Kerr, Y.H., and Sorooshian, S. (1994b) A modified soil adjusted vegetation index (MSAVI) *Remote Sensing of Environment* **48**, pp. 119-126.



- Ranson, K.J., Irons, J.R., and Williams, D.L. (1994) Multispectral bi-directional reflectance of northern forest canopies with the advanced solid-state array spectroradiometer (ASAS). *Remote Sensing of Environment* **47**, pp. 276-289.
- Ray, T.W. (1995) *Remote monitoring of land degradation in arid/semi-arid regions*. PhD thesis, California Institute of Technology 415 pp
- Ribbles, F., and leToan, T. (1999) Rice field mapping and monitoring with Radarsat data. *International Journal of Remote Sensing* **20**, No. 4, pp 745-765.
- Richardson, A.J., and Wiegand, C.L. (1977) Distinguishing vegetation from soil background information. *Photogrammetric Engineering and Remote Sensing* **43**, pp. 1541-1552.
- Richardson, A.J., and Everitt, J.H. (1992) Using spectral vegetation indices to estimate rangeland productivity. *Geocarto International* **1**, pp. 63-69.
- Ringrose, S., and Matheson, W. (1987) Spectral assessment of indicators of range degradation in the Botswana hardveld environment. *Remote Sensing of Environment* **23**, pp. 379-396.
- Ringrose, S., Matheson, W., Mogotsi, B., and Tempest, F. (1989) The darkening effect in drought affected savanna woodland environments relative to soil reflectance in Landsat and SPOT wavebands. *Remote Sensing of Environment* **30**, pp. 1-19.
- Ripple, W.J. (1985) Asymptotic reflectance characteristics of grass vegetation. *Photogrammetric Engineering and Remote Sensing* **51**, pp. 1915-1921.
- Robinson, T.P. (1996) Spatial and temporal resolution products of NOAA-AVHRR NDVI data. *International Journal of Remote Sensing* **17**, No. 12, pp. 2303-2321.
- Rondeaux, G., Steven, S., Baret, F. (1996) Optimisation of soil-adjusted vegetation indices. *Remote Sensing of Environment* **55**, pp.95-107.



- Rosema, A., Verhoef, W., Noorbergen, H., and Borgesius, J.J. (1992) A new forest light interaction model in support of forest monitoring. *Remote Sensing of Environment* **42**, pp. 23-41.
- Rouse, J.W., Haas, R.H., Schell. J.A., Deering, D.W., and Harlan, J.C. (1974) *Monitoring the vernal advancement of retrogradation of natural vegetation*, NASA/GCFC Type III Final Report, Greenbelt, MD. 371 pp.
- Satterwhite, M.B., and Henley, J. P. (1987) Spectral characteristics of selected soils and vegetation in Northern Nevada and their discrimination using band ratioing techniques. *Remote Sensing of Environment* **23**, pp. 155-175.
- Saunders, J and Culter, J. (1994) *GIS and remote sensing for developing countries Geographic Information 1994 The Source Book of GIS* , Taylor and Francis, London
- Schnetzler, C.C. (1982) On the use of off-nadir pointing for increased temporal resolution of earth observing satellite systems. *NASA technical paper* **82139**, 27 pp.
- Schowengerdt, R.A. (1983) *Techniques for image processing and classification in remote sensing*, Academic Press, New York.
- Shimabukuro, Y.E., Carvalho, V.C., and Rudorff, B.F.T. (1997) NOAA-AVHRR data processing for the mapping of vegetation cover *International Journal of Remote Sensing* **18**, No. 3, pp. 671-677.
- Shibayama, M., and Akiyama, T. (1989) Seasonal visible, near infrared and mid infrared spectra of rice canopies in relation to LAI and above-ground dry phytomass. . *Remote Sensing of Environment* **27**, pp. 119-127.
- Shin, D., Pollard, J.K., and Muller, J. (1995) Dynamic programming for fine co-location of ATSR images. *Applied Signal Processing* **2**, pp. 108-116.
- Singh, A., and Harrison, A. (1985) Standardised Principal Components *International*



*Journal of Remote Sensing* 6, No. 6, pp. 883-896.

Singh, S.M., and Cracknell, A.P. (1986) The estimation of atmospheric effects for SPOT using AVHRR channel-1 data. *International Journal of Remote Sensing* 7, pp. 361-377.

Slater, P.N. (1980) *Remote sensing: Optics and optical systems* Addison-Wesley Publishing Company. Reading, Massachusetts.

Smartt, P.F.M, Meacock.S.E., and Lambert, J.M. (1974) Investigations into the properties of quantitative vegetational data I Pilot Study *Journal of Ecology* 62, pp. 735-759.

Smartt, P.F.M, Meacock.S.E., and Lambert, J.M. (1976) Investigations into the properties of quantitative vegetational data II Further data type compactions *Journal of Ecology* 64, pp. 41-78.

Strahler, A.H., and Jupp, D.L.B. (1990) Modelling bi-directional reflectance of forests and woodlands using Boolean models and geometric optics. *Remote Sensing of Environment* 34, pp. 153-166.

Taimeh, A.Y. (1985) Relationship between air and soil temperature in the semi-arid-subhumid region of Jordan. *Dirasat* 12, No. 4, pp. 87-104.

Tanré, D., Deroo, C., Duhaut, P., Herman, M., Morecette, J.J., and Deschamps, P.Y. (1990) Description of a computer code to simulate the satellite signal in the solar spectrum. the 5S code. *International Journal of Remote Sensing* 11, pp. 659-668.

Tansey, K. (1999) *Modelling dryland soil moisture dynamics using ERS SAR data* Unpublished PhD thesis, University of Leicester

Teillet, P.M., and Fedosejevs, G. (1995) On the dark target approach to atmospheric



correction of remotely sensed data. 1995. *Canadian Journal of Remote Sensing* **21**, No. 4, pp. 374-387.

Townshend, J.R.G. (1980) The spatial resolving power of earth resources satellites: A review. *Progress in Physical Geography* **5**, pp. 32-55.

Townshend, J.R.G. (1984) Agricultural land cover discrimination using thematic mapper spectral bands. *International Journal of Remote Sensing* **5**, No. 4, pp. 681-698.

Townshend, J.R.G., Justice, C.O., and Klab, V.T. (1987) Characterisation and classification of South American land cover types using satellite data. *International Journal of Remote Sensing* **8**, pp. 1189-1207.

Tucker, C.J. (1977) Asymptotic nature of grass canopy spectral reflectance. *Applied Optics* **6**, pp. 1151-1156.

Tucker, C.J., Holben, B.N., Elgin, J.H., and McMurtrey, J.E. (1981) Remote Sensing of total dry matter accumulation in winter wheat. *Remote Sensing of Environment*, **11**, pp. 171-189.

Tucker, C.J., Gatlin, J.A., Schneider, S.R., and Kuchinos, M.A. (1984) Monitoring of vegetation in the Nile Delta with NOAA-6 and NOAA-7 AVHRR imagery. *Photogrammetric Engineering and Remote Sensing* **50**, pp. 53-61.

Tucker, C.J., Townshend, J.R.G., and Goff, T.E. (1985a) African land cover classification using satellite data. *Science* **227**, pp. 369-375.

Tucker, C.J., Vanpraet, C.L., Sharman, M.J., and Van Ittersum, G. (1985b) Satellite remote sensing of total herbaceous biomass production in the Senegalese Sahel: 1980-1984. *Remote Sensing of Environment* **17**, pp. 233-249.

Tucker, C.J., and Sellers, P.J. (1986) Satellite remote sensing of primary production



*International Journal of Remote Sensing* 7, pp. 1395-1416.

Tucker, C.J., Fung, I.Y., Keeling, C.D., and Gammon, R.H. (1986) Relationship between atmospheric CO<sub>2</sub> variation and a satellite-derived vegetation index. *Nature* 319, pp. 195-199.

Tueller, P.T. (1987) Remote Sensing Science applications in arid environments *Remote Sensing of Environment* 23, pp. 143-154.

Tueller, P.T., and Oleson, S.G. (1989) Diurnal radiance and shadow fluctuations in a cold desert shrub plant community. *Remote Sensing of Environment* 29, pp. 1-13.

Uresk, D.W., Gilbert, R.O., and Richard, W.H. (1977) Sampling big sagebrush for phytomass. *Journal of Range Management* 30, pp. 311-314.

Vermote, E.F., Tanre, D., Deuze, J., Herman, M., Morcrette, J. (1997) Second Simulation of the satellite signal in the solar spectrum, 6S: an overview. *IEEE Transactions on Geoscience and Remote Sensing* 35, No. 3, pp. 675-686.

Verstraete, M.M., and Pinty, B., 1996, Designing optimal spectral indices for remote sensing applications. *IEEE Transactions on Geoscience and Remote Sensing* 34, No. 5, pp 1254-1264

Weiser, R.L., Asrar, G., Miller, G.P. and Kanemasu, E.T. (1984) Assessing grassland biophysical characteristics from spectral measurements. *Proceedings of the tenth International Symposium of Machine Processing of Remote Sensing Data* Purdue University West Lafayette In. pp. 357-361.

Wellens, J. (1993) *Monitoring and modelling rangeland vegetation in Tunisia using satellite and meteorological data* Unpublished PhD thesis, University of Reading

Whitlock, C.H., Purgold, G.C., and LeCroy, S.R. (1987) Surface bi-directional reflectance properties of two Southwest Arizona deserts for wavelengths between 0.4



and 2.2 micrometers. *NASA Technical Paper 2643*

Williamson, H.D. (1989) Reflectance from shrubs and under-shrub soil in a semiarid environment. *Remote Sensing of Environment* **29**, pp. 263-271.

Wilson, R.O., and Tueller, P.T. (1987) Aerial and ground spectral characteristics of rangeland plant communities in Nevada. *Remote Sensing of Environment* **23**, pp. 177-191.

Wooster, M.J., Rothery, D.A, Kaneko, T., Carlton, R.W.T. (1997) Thermal monitoring of high temperature fumaroles on volcanic lava domes: case studies using shortwave infrared data from ERS Along Track Scanning Radiometer. *RSS97 Observations and Interactions. 23rd Annual conference and exhibition of the Remote Sensing Society*. pp. 79-84. Reading

Wylie, B.K., Harrington, J.A., Prince, S.D., and Denda, I. (1991) Satellite and ground based pasture production assessment in Niger 1986-1988 *International Journal of Remote Sensing* **12**, pp. 1281-1300.

Yeh, A.G.O. (1991) The development and application of geographical information system for urban and regional planning in developing countries. *International Journal of Geographical Information Systems* **5**, pp. 5-28.

Zohary, M. (1962) *Plant Life of Palestine*, New York, Ronald Press Co.

Zohary, M. (1973) *Geobotanical Foundation of the Middle East*, Amsterdam. Swets and Zeitlinger

Zavody, A.M., Gorman, M.R., Lee, D.J., Eccles, D., Mutlow, C.T., and Llewellyn-Jones, D.T. (1994) The ATSR data processing scheme for the EODC *International Journal of Remote Sensing* **15**, pp. 827-843.